

AD-A269 823



2



**High Frequency Analysis of EM Scattering
from a Circular Conducting Cylinder
with Dielectric/Ferrite Coating**

S DTIC
ELECTE
SEP 14 1993
A **D**

Hyo-Tae Kim

Nan Wang

The Ohio State University

ElectroScience Laboratory

Department of Electrical Engineering
Columbus, Ohio 43212

Technical Report 717674-4

Contract No. N60530-85-C-0249

January, 1987

This document has been approved
for public release and sale; its
distribution is unlimited.

Naval Weapons Center
China Lake, California 93555

93-21436



18598
~~93-21436~~

93 9 14 11 T

REPORT DOCUMENTATION PAGE	1. REPORT NO.	2.	3. Recipient's Accession No.
4. Title and Subtitle High Frequency Analysis of EM Scattering from a Circular Conducting Cylinder with Dielectric/Ferrite Coating			5. Report Date January 1987
7. Author(s) Hyo-Tae Kim and Nan Wang			6.
9. Performing Organization Name and Address The Ohio State University ElectroScience Laboratory 1320 Kinnear Road Columbus, Ohio 43212			8. Performing Organization Rept. No. 717674-4
12. Sponsoring Organization Name and Address Naval Weapons Center China Lake, California 93555			10. Project/Task/Work Unit No.
15. Supplementary Notes			11. Contract(C) or Grant(G) No. (C) N60530-85-C-0249 (G)
16. Abstract (Limit: 200 words) An approximate asymptotic high-frequency solution is obtained for the field exterior to a two-dimensional circular conducting cylinder with a thin dielectric/ferrite coating. The formal integral representation for the field is evaluated asymptotically via the stationary phase method for the field in lit region and via the residue theorem for the field in shadow region. The obtained solution is cast in the format of the geometrical theory of diffraction (GTD). In the lit region, the geometrical optics (GO) solution consists of the direct incident ray and the reflected ray. The ray picture associated with the reflected ray for the coated cylinder remains the same as that for the conducting cylinder without coating. The reflection coefficient for the field reflected at the specular reflection point on the coated circular surface is approximated by the reflection coefficient for a grounded planar dielectric/ferrite slab with a plane wave incidence. In the shadow region, the residue series solution can be interpreted as the usual creeping wave diffraction of the GTD solution with the same ray path as the diffracted field associated with the conducting cylinder without coating. In the transition regions adjacent to the shadow boundaries where the pure ray-optical solution fails, a 'universal' transition integral of the uniform GTD (UTD) is employed to obtain the uniform solution. Numerical data for the essential transition integral is deduced, via a heuristic approach, from the exact eigenfunction solution together with the GTD solutions for the coated cylinder. The solution is convenient for the engineering applications due to its simple ray format. Numerical results obtained from the UTD solution for the cylinder with thin coating show excellent agreement with the exact eigenfunction results.			13. Type of Report & Period Covered Technical
17. Document Analysis a. Descriptors			14.
b. Identifiers/Open-Ended Terms			
c. COSATI Field/Group			
18. Availability Statement	19. Security Class (This Report) Unclassified	21. No of Pages 188	
	20. Security Class (This Page) Unclassified	22. Price	

TABLE OF CONTENTS

LIST OF FIGURES		vi
LIST OF TABLES		xi
I. INTRODUCTION		1
1.1 Outline		1
1.2 Literature survey		3
II. EIGENFUNCTION SERIES SOLUTION		6
2.1 The canonical problem		7
2.2 Impedance Cylinder		10
2.2.1 TM_z case		10
2.2.2 TE_z case		12
2.3 Coated Cylinder		14
2.3.1 TM_z case		14
2.3.2 TE_z case		17
2.4 Examples and the discussion		19
III. GTD SOLUTION		30
3.1 Integral Representation of the Field		33
3.2 Field in the deep lit region - G.O. field		36
3.2.1 Evaluation of u_1^o		36

Availability Codes	
Dist	Avail and/or Special
A-1	

3.2.2	Evaluation of u_2^0	42
3.2.3	Incident field	46
3.2.4	Evaluation of I_2	47
3.2.5	Reflected Field	53
3.3	Field in the deep shadow region	61
3.3.1	Residue series solution	61
3.3.2	Diffracted field	64
3.3.3	Equivalent impedance associated with the creeping wave of the coated cylinder	72
3.4	Numerical results and discussion	73
3.4.1	Numerical results	73
3.4.2	Discussion	75
IV.	CHARACTERISTICS OF THE CREEPING WAVES	89
4.1	Propagation and Attenuation Constants	90
4.1.1	Impedance cylinder	92
4.1.2	Coated cylinder	102
4.2	Dominance of Creeping Wave Modes	109
4.3	Creeping waves on a large cylinder	116
V.	FIELD IN THE TRANSITION REGION	124
5.1	Uniform GTD solution for the impedance and the coated cylinder	126
5.1.1	Lit region	126
5.1.2	Shadow region	129
5.2	Transition function	132
5.3	Numerical results and discussion	143

VI. SUMMARY AND CONCLUSIONS	156
APPENDIX	
A. WATSON'S TRANSFORMATION	159
A.1 Watson's Transformation	159
A.2 Integral representation	159
A.3 Residue series representation	161
B. REFLECTION COEFFICIENT	164
B.1 TM_z case	164
B.2 TE_z case	169
REFERENCES	172

LIST OF FIGURES

2.1	The geometry of the problem	9
2.2	Normalized bistatic scattering pattern of impedance cylinder . . .	20
2.3	Normalized bistatic scattering pattern of impedance cylinder . . .	20
2.4	Normalized bistatic scattering pattern of impedance cylinder . . .	21
2.5	Normalized bistatic scattering pattern of impedance cylinder . . .	21
2.6	Normalized bistatic scattering pattern of impedance cylinder . . .	22
2.7	Normalized bistatic scattering pattern of impedance cylinder . . .	22
2.8	Normalized bistatic scattering pattern of impedance cylinder . . .	23
2.9	Normalized bistatic scattering pattern of impedance cylinder . . .	23
2.10	Normalized bistatic scattering pattern of coated cylinder : TM_z case	24
2.11	Normalized bistatic scattering pattern of coated cylinder : TM_z case	24
2.12	Normalized bistatic scattering pattern of coated cylinder : TM_z case	25
2.13	Normalized bistatic scattering pattern of coated cylinder : TM_z case	25
2.14	Normalized bistatic scattering pattern of coated cylinder : TM_z case	26
2.15	Normalized bistatic scattering pattern of coated cylinder : TM_z case	26
2.16	Normalized bistatic scattering pattern of coated cylinder : TE_z case	27
2.17	Normalized bistatic scattering pattern of coated cylinder : TE_z case	27
2.18	Normalized bistatic scattering pattern of coated cylinder : TE_z case	28
2.19	Normalized bistatic scattering pattern of coated cylinder : TE_z case	28
2.20	Normalized bistatic scattering pattern of coated cylinder : TE_z case	29
2.21	Normalized bistatic scattering pattern of coated cylinder : TE_z case	29

3.1	The geometric optical domains	32
3.2	The contours C_1 and C_2	38
3.3	Physical meaning of the stationary point	40
3.4	Physical meaning of the stationary point	45
3.5	Physical meaning of the stationary point	51
3.6	Reflection field	55
3.7	Reflection Coefficient	59
3.8	Reflection Coefficient	60
3.9	The contour of the integral	62
3.10	Field in the shadow region	65
3.11	Ray encirclements associated with the summation index p	71
3.12	Ray paths employed for the UTD solution	74
3.13	Normalized bistatic scattering pattern of impedance cylinder	77
3.14	Normalized bistatic scattering pattern of impedance cylinder	77
3.15	Normalized bistatic scattering pattern of impedance cylinder	78
3.16	Normalized bistatic scattering pattern of impedance cylinder	78
3.17	Normalized bistatic scattering pattern of coated cylinder : TM_z case	79
3.18	Normalized bistatic scattering pattern of coated cylinder : TE_z case	79
3.19	Normalized bistatic scattering pattern of coated cylinder : TM_z case	80
3.20	Normalized bistatic scattering pattern of coated cylinder : TE_z case	80
3.21	Normalized bistatic scattering pattern of coated cylinder : TM_z case	81
3.22	Normalized bistatic scattering pattern of coated cylinder : TE_z case	81
3.23	Normalized bistatic scattering pattern of coated cylinder : TM_z case	82
3.24	Normalized bistatic scattering pattern of coated cylinder : TE_z case	82
3.25	Normalized bistatic scattering pattern of coated cylinder : TM_z case	83
3.26	Normalized bistatic scattering pattern of coated cylinder : TE_z case	83

3.27	Normalized bistatic scattering pattern of coated cylinder : TM_z case	84
3.28	Normalized bistatic scattering pattern of coated cylinder : TE_z case	84
3.29	Normalized bistatic scattering pattern of coated cylinder : TM_z case	85
3.30	Normalized bistatic scattering pattern of coated cylinder : TE_z case	85
3.31	Normalized bistatic scattering pattern of coated cylinder : TM_z case	86
3.32	Normalized bistatic scattering pattern of coated cylinder : TE_z case	86
3.33	Normalized bistatic scattering pattern of coated cylinder : TM_z case	87
3.34	Normalized bistatic scattering pattern of coated cylinder : TE_z case	87
3.35	Normalized bistatic scattering pattern of coated cylinder : TM_z case	88
3.36	Normalized bistatic scattering pattern of coated cylinder : TE_z case	88
4.1	Creeping wave	91
4.2	The roots of the transcendental equation for the impedance cylinder	94
4.3	The roots of the transcendental equation for the impedance cylinder using Equation (4.12)	98
4.4	Field pattern obtained using the ν_n in Figure 4.3	99
4.5	Field pattern obtained using the ν_n in Figure 4.2	99
4.6	Field pattern obtained using the ν_n in Figure 4.3	100
4.7	Field pattern obtained using the ν_n in Figure 4.2	100
4.8	Field pattern obtained using the ν_n in Figure 4.3	101
4.9	Field pattern obtained using the ν_n in Figure 4.2	101
4.10	The roots of the transcendental equation	104
4.11	The roots of the transcendental equation	105
4.12	The roots of the transcendental equation	106
4.13	The roots of the transcendental equation	107
4.14	The relative phase velocity and the attenuation	108
4.15	Normalized backscattering width of a coated cylinder	112

4.16	Diffraction coefficient	112
4.17	Propagation and the attenuation constant	113
4.18	Normalized backscattering width of a coated cylinder	114
4.19	Diffraction coefficient	114
4.20	Propagation and the attenuation constant	115
4.21	Trajectory of roots	118
4.22	Attenuation per meter	119
4.23	Diffraction coefficient	120
4.24	Trajectory of roots	121
4.25	Attenuation per meter	122
4.26	Diffraction coefficient	123
5.1	Field in the lit part of transition region	127
5.2	Field in the shadow part of transition region	130
5.3	The transition integral $p^*(\xi, q)e^{-j\pi/4}$ or $q^*(\xi, q)e^{-j\pi/4}$: Impedance Cylinder	135
5.4	The transition integral $p^*(\xi, q)e^{-j\pi/4}$ or $q^*(\xi, q)e^{-j\pi/4}$: Impedance Cylinder	136
5.5	The transition integral $e^{-j\pi/4}p^*(x, q)$: Coated Cylinder	137
5.6	The transition integral $e^{-j\pi/4}p^*(x, q)$: Coated Cylinder	138
5.7	The transition integral $e^{-j\pi/4}p^*(x, q)$ or $q^*(\xi, q)e^{-j\pi/4}$: Impedance cylinder	139
5.8	The transition integral $e^{-j\pi/4}q^*(x, q)$: Coated Cylinder	140
5.9	The transition integral $e^{-j\pi/4}q^*(x, q)$: Coated Cylinder	141
5.10	The transition integral $e^{-j\pi/4}p^*(x, q)$ or $q^*(\xi, q)e^{-j\pi/4}$: Impedance cylinder	142
5.11	Normalized bistatic scattering pattern of impedance cylinder	144

5.12	Normalized bistatic scattering pattern of impedance cylinder . . .	144
5.13	Normalized bistatic scattering pattern of impedance cylinder . . .	145
5.14	Normalized bistatic scattering pattern of impedance cylinder . . .	145
5.15	Normalized bistatic scattering pattern of coated cylinder : TM_z case	146
5.16	Normalized bistatic scattering pattern of coated cylinder : TE_z case	146
5.17	Normalized bistatic scattering pattern of coated cylinder : TM_z case	147
5.18	Normalized bistatic scattering pattern of coated cylinder : TE_z case	147
5.19	Normalized bistatic scattering pattern of coated cylinder : TM_z case	148
5.20	Normalized bistatic scattering pattern of coated cylinder : TE_z case	148
5.21	Normalized bistatic scattering pattern of coated cylinder : TM_z case	149
5.22	Normalized bistatic scattering pattern of coated cylinder : TE_z case	149
5.23	Normalized bistatic scattering pattern of coated cylinder : TM_z case	150
5.24	Normalized bistatic scattering pattern of coated cylinder : TE_z case	150
5.25	Normalized bistatic scattering pattern of coated cylinder : TM_z case	151
5.26	Normalized bistatic scattering pattern of coated cylinder : TE_z case	151
5.27	Normalized bistatic scattering pattern of coated cylinder : TM_z case	152
5.28	Normalized bistatic scattering pattern of coated cylinder : TE_z case	152
5.29	Normalized bistatic scattering pattern of coated cylinder : TM_z case	153
5.30	Normalized bistatic scattering pattern of coated cylinder : TE_z case	153
5.31	Normalized bistatic scattering pattern of coated cylinder : TM_z case	154
5.32	Normalized bistatic scattering pattern of coated cylinder : TE_z case	154
5.33	Normalized bistatic scattering pattern of coated cylinder : TM_z case	155
5.34	Normalized bistatic scattering pattern of coated cylinder : TE_z case	155
A.1	The contour of the integral	160
A.2	The contour C_z of the integral	162
B.3	Snell's Law	167

LIST OF TABLES

4.1 Comparison of roots 97

CHAPTER I

INTRODUCTION

1.1 Outline

The purpose of this research is to develop an approximate asymptotic high-frequency solution for the electromagnetic scattering from a convex conducting surface with dielectric/ferrite coating. For the bare perfectly conducting case, an efficient uniform GTD solution has been developed and used in many engineering applications. However, no such solution exists for the conductor coated with dielectric/ferrite material.

This research is motivated by the need for understanding the effects of loading on the electromagnetic scattering. In some engineering problems there is a need to control the scattered fields from conducting objects such as the reduction of the radar cross section (RCS) in the design of air-borne vehicles. An efficient method to control the EM scattering can be achieved by coating of a dielectric/ferrite material on the conducting scatterers without having to deform the physical structure of the scatterer. The research in this report is focused on the development of an efficient analytical tool to calculate the scattered field from a coated surface and the effects of various coating materials on the scattered field.

It is desired to ultimately develop the uniform geometrical theory of diffraction (UTD) for an general convex surface with material coating. As a first step, we examine the field scattered by an infinite conducting circular cylinder with dielectric/ferrite coating when it is illuminated by a parallel infinite electric or magnetic

line source. Since both the line source and the cylinder are parallel and have infinite lengths, the scattering from the cylinder is essentially a two-dimensional problem. Once the solution for this canonical problem is obtained, it can be easily extended to calculate the field scattered by a general convex coated surface. The scattering from the cylinder with surface impedance is also treated in this research. This problem is of interest in that it provide the solution of scattering field from a cylinder with finite conductivity.

The organization of this report is as follows. Chapter II gives the angular eigenfunction series solutions for the impedance and the coated cylinder. It is noted that the eigenfunction solution is slowly convergent when the radius of cylinder is large in terms of the wave length. Even though the eigenfunction solution is not the goal of this research, it is important because it provides a means of checking the accuracy of the ray solution which is developed in later Chapters.

In Chapter III, high frequency asymptotic solutions are obtained from the asymptotic evaluation of the field expression in the integral form. The solutions obtained are cast in the format of the geometrical theory of diffraction (GTD) as suggested by Keller [1,2]. In the lit region, geometrical optics fields (i.e. the incident and the reflected field) are obtained via the stationary phase method. In the shadow region, the diffracted field is obtained from the evaluation of the integral via Cauchy's residue theorem. It is noted that the ray picture for the impedance and the coated cylinder remains the same as that for the perfectly conducting cylinder. Thus the Keller's GTD ray format given for the conducting cylinder can be used with necessary modifications due to the boundary conditions on the cylinder surface. Even though the solution obtained is accurate in the deep lit region and in the deep shadow region, it fails in the shadow boundary transition region. The reasons for this failure are also analyzed in this Chapter.

Chapter IV examines some characteristics of the creeping waves which prop-

agate azimuthally on the cylinder surface. The propagation constants and the attenuation constants of the creeping wave modes are determined from the zeros of the transcendental equation which characterizes the impedance or the coated cylinder. For the conducting cylinder, the contribution from the first creeping wave mode to the diffraction is always dominant over other higher modes. However this is not always true for the impedance and the coated cylinder. Change of the dominance of the creeping wave mode according to the change of the relevant parameters is illustrated by the some examples. The behavior of the creeping waves for a very large cylinder is compared with the surface waves of the grounded planar slab with the surface impedance or the dielectric/ferrite coating.

In chapter V, the failure of the GTD solution in the shadow boundary transition region is corrected by the heuristic extension of the UTD solution for the conducting cylinder to the impedance and the coated cylinder. For the impedance and the coated cylinder, the transition function $\hat{P}(z, q)$, which is well tabulated for the conducting case, is not available. Instead of direct numerical evaluation of the integral, a heuristic method is used to obtain the numerical data for the transition function $\hat{P}(z, q)$. The universal feature of this transition function is tested for some examples. Using the transition function obtained, the field patterns are calculated and the results are compared with exact eigenfunction solutions.

Chapter VI contains the conclusion for this research.

1.2 Literature survey

For the perfectly conducting case, the asymptotic evaluation of the field scattered by a cylinder or a general convex surface has received much attention and been studied extensively. Such solutions are usually cast in the format of the geometrical theory of diffraction (GTD) as suggested by Keller [1,2]. One of more

recent works on this problem is that of Pathak [3]. He made a significant contribution to this area by developing an approximate uniform geometrical theory of diffraction (UTD) for a perfectly conducting cylinder and arbitrary convex surface with great success.

The problem of scattering by the impedance or the coated cylinder has also received attention for decades. Scattered field by the impedance cylinder has been studied by Wait [17], Streifer [18] and Logan [14]. The main concern of their work was in ground wave propagation excited a dipole on the earth which has been modeled by a cylinder with surface impedance. In their work, the propagation constants for the creeping wave of the impedance cylinder has been obtained with the assumption that the Hankel functions in the formal solution may be approximated by their Fock type Airy functions. It is noted that this assumption is not valid for arbitrary orders and arguments of the Hankel functions. Recently, Wang [4] obtained more accurate numerical data for the propagation constant of the creeping wave, the Regge poles, and the natural frequencies of an impedance cylinder by using both the Debye and the Watson's approximation of Hankel functions. The creeping wave interpretation for the resonance and the correlations between the resonance, the Regge poles, and the natural frequencies are also discussed. Most recent work on the scattering from the impedance cylinder has been done by Wang and Kim [5] who has developed uniform GTD solution for this problem. The accuracy of his results has been confirmed by excellent agreement with exact eigenfunction solutions.

For the coated cylinder, Tang (1957) has found an angular eigenfunction series solution for the back scattered field and has presented numerical and experimental results when the incident wave length λ_0 is comparable with radius of the cylinder. The propagation constant for the first creeping wave mode on the surface of cylinder with lossless dielectric coating was first obtained by Elliott [19] by using

some asymptotic representations of the various necessary Bessel and Hankel function. Based upon Poisson's sum formula, Kodis [21] has obtained an asymptotic solution for the scattered field in terms of the difference between the scattered field of the coated cylinder and of a perfectly conducting cylinder. In his solution, the scattered field is expressed in term of several different rays by tracing the complicated internal process of the field propagation in the dielectric coating. Because of difficulty in tracing the optical rays inside the coating material, his solution is too complicated for numerical calculations. Particularly interesting is the work by Helstrom [22], who has obtained a ray optical solution by asymptotic evaluation of the formal solution. A trajectory of the propagation constants of the creeping wave has been sketched. However, he failed to give exact numerical data.

By employing the same optical rays as given by Kodis, Rao and Hamid [23] investigated GTD solution for this problem. No numerical results were presented in their paper. The backscattering width of a dielectric coated cylinder has been obtained via a high frequency ray solution by the recent work of Wang [6]. Most recently, Paknys and Wang [7,8] have developed an approximate solution for the surface fields induced on a coated cylinder by a magnetic or electric line source on the same surface. Even though the final goal of this work is different from theirs, some of their results associated the propagation constants of the creeping waves are utilized in this work.

CHAPTER II

EIGENFUNCTION SERIES SOLUTION

In this Chapter, the eigenfunction series solutions for the field scattered by the infinite circular conducting cylinder with an impedance boundary surface or a dielectric/ferrite coating will be presented. In the eigenfunction solution, the field expression is given as the sum of each angular eigenfunction mode which satisfies the boundary conditions of a given canonical problem. The angular expansion of eigenfunction modes is an appropriate solution when the radius of the cylinder is small in terms of the wavelength where the asymptotic solution cannot be applied. However, for the cylinder with large radius it is impractical to compute the field from the eigenfunction expansion because it is very slowly convergent.

Even though the eigenfunction solution is not the final goal of this research, it is important because the formulation of a high frequency ray solution begins with the field expression in the eigenfunction series form. Since the eigenfunction solution is based on exact boundary conditions, it is considered to be the exact solution of the given problem. Hence, it can be also used as a means to check the validity of the high frequency ray solution which will be developed in later Chapters. In addition, the eigenfunction solution provides the basis to obtain the numerical data for the transition function $\hat{P}(\xi, q)$ associated with the uniform GTD solution in the vicinity of the shadow boundary.

2.1 The canonical problem

The geometry of the problem for an impedance and a coated cylinder is illustrated in Figure 2.1 (a) and (b) respectively. The impedance cylinder or the coated cylinder is illuminated by a parallel line source located at $O(\rho', \phi')$. The impedance cylinder is an impenetrable cylinder with an impedance boundary surface and the coated cylinder has a material coating on the conducting core cylinder. The coating has a thickness $d = b - a$ and is homogeneous with permittivity ϵ_1 and permeability μ_1 , both of which may be complex. The source is either an electric current filament I (TM_z case) or a magnetic current filament K (TE_z case). The solution to be investigated is the total field at $P(\rho, \phi)$ from the line source which radiates in the presence of a parallel cylinder with an impedance boundary surface or with a material coating. Both the source and the field point are assumed to be located outside cylinder. Since both the line source and the cylinder are assumed to have infinite lengths and to be parallel to the z -axis, the scattering from the cylinder is essentially a two-dimensional problem. The two-dimensional line-source Green's function $G(\vec{\rho}, \vec{\rho}')$ satisfies the equation

$$\left(\nabla_t^2 + k_o^2 \right) G(\vec{\rho}, \vec{\rho}') = -\delta(\vec{\rho} - \vec{\rho}') \quad (2.1)$$

in the domain $b \leq (\rho, \rho') < \infty$; $0 \leq (\phi, \phi') \leq 2\pi$ where ∇_t^2 is two-dimensional Laplacian operator. Thus Equation (2.1) can be rewritten as

$$\left[\frac{1}{\rho} \frac{\partial}{\partial \rho} \rho \frac{\partial}{\partial \rho} + \frac{1}{\rho^2} \frac{\partial^2}{\partial \phi^2} + k_o^2 \right] G(\vec{\rho}, \vec{\rho}') = \frac{-\delta(\rho - \rho') \delta(\phi - \phi')}{\rho} \quad (2.2)$$

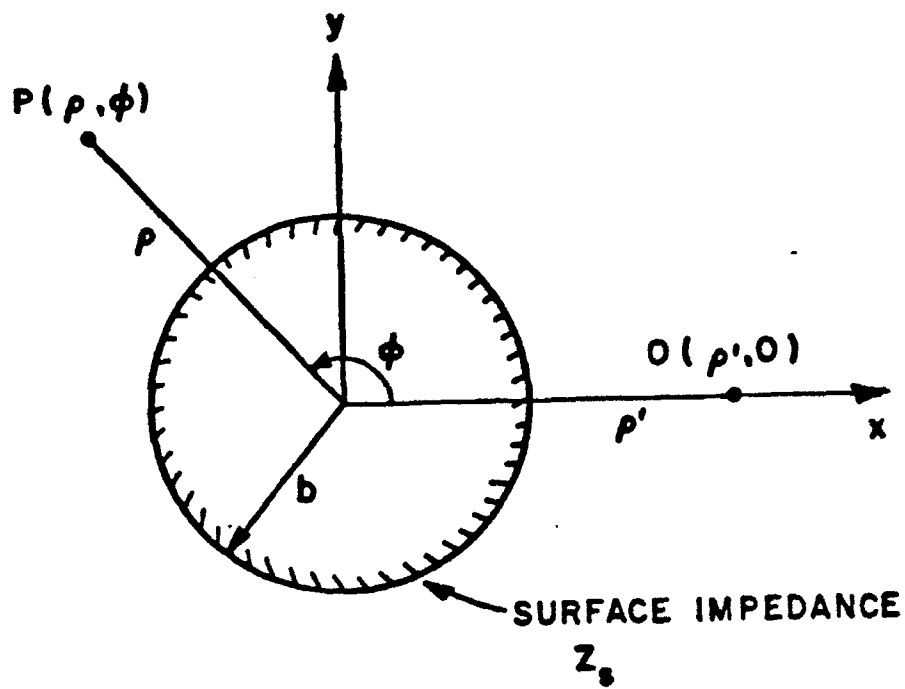
Without loss of generality, we can set $\phi' = 0$ and $0 \leq \phi \leq \pi$ for convenience. Once the solution $G(\vec{\rho}, \vec{\rho}')$ for Equation (2.2) subject to the boundary conditions on the cylinder surfaces and the Sommerfeld radiation condition as $\rho \rightarrow \infty$ is found,

the field components at $P(\rho, \phi)$ can be readily obtained. For excitation by a line source of electric current I (TM_z case), the field components of \vec{E} and \vec{H} outside the cylinder are given as (for $e^{j\omega t}$ time variation)

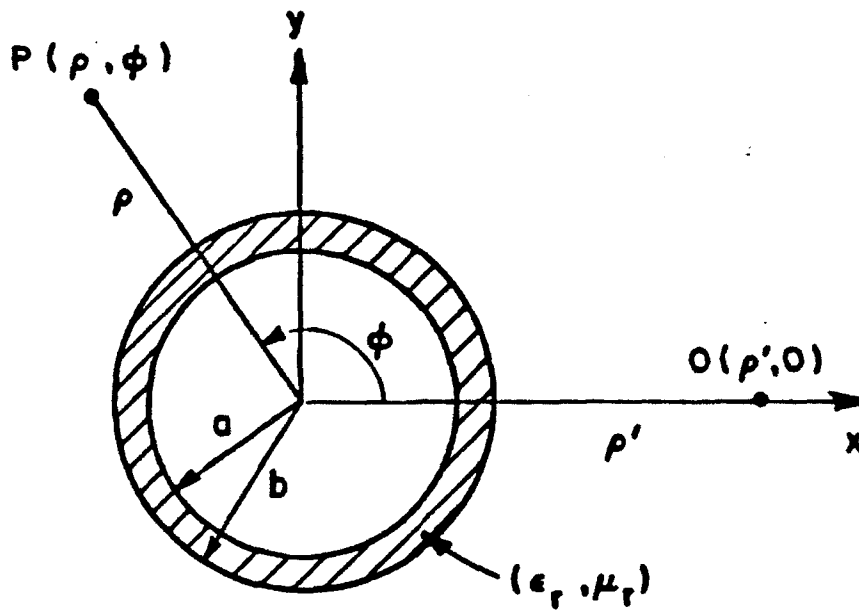
$$\begin{aligned}
 E_z &= -j\omega\mu_o I G, & H_z &= 0 \\
 E_\rho &= 0, & H_\rho &= \frac{I}{\rho} \frac{\partial G}{\partial \phi} \\
 E_\phi &= 0, & H_\phi &= -I \frac{\partial G}{\partial \rho}
 \end{aligned} \tag{2.3}$$

For the magnetic line source case (TE_z case), the field components are given as

$$\begin{aligned}
 H_z &= -j\omega\epsilon_o K G, & E_z &= 0 \\
 H_\rho &= 0, & E_\rho &= \frac{-K}{\rho} \frac{\partial G}{\partial \phi} \\
 H_\phi &= 0, & E_\phi &= K \frac{\partial G}{\partial \rho}
 \end{aligned} \tag{2.4}$$



(a)



(b)

Figure 2.1: The geometry of the problem

2.2 Impedance Cylinder

In this section, the eigenfunction solution for Equation (2.2) subject to the boundary condition of the impedance cylinder will be obtained. On the surface of the impenetrable impedance cylinder, the field $G(\vec{\rho}, \vec{\rho}')$ should satisfy the impedance boundary condition given as

$$\frac{\partial G}{\partial \rho} - jk_0 \bar{C} G = 0 \quad (2.5)$$

where \bar{C} represents either normalized surface impedance (TE_z case) or normalized admittance (TM_z case). \bar{C} is assumed to be constant around the surface of the cylinder.

$$\bar{C} = C_s = \frac{Z_o}{Z_s} \quad \text{for } TM_z \quad ; \quad \bar{C} = C_h = \frac{Z_s}{Z_o} \quad \text{for } TE_z \quad (2.6)$$

where Z_o is the intrinsic impedance of free space (i.e. $Z_o = \sqrt{\frac{\mu_o}{\epsilon_o}}$) and Z_s is the constant impedance on the cylinder surface. The subscript s and h in C denote TM_z (soft) and TE_z (hard) respectively.

2.2.1 TM_z case

At the field point $P(\rho, \phi)$, the total field consists of the two terms; the incident field $G_o(\rho, \phi)$ and the scattered field $G_s(\rho, \phi)$.

$$G(\vec{\rho}, \vec{\rho}') = G(\rho, \phi) = G_o(\rho, \phi) + G_s(\rho, \phi) \quad (2.7)$$

When the line source is an electric current filament I , the incident electric field is parallel to the cylinder axis which is taken as the z -axis. From the free space Green's function for two-dimensional line source, the z -polarized incident electric field $G_o(\rho, \phi)$ is given as

$$G_o(\rho, \phi) = \frac{-j}{4} H_o^{(2)}(k_o|\bar{\rho} - \bar{\rho}'|) \quad (2.8)$$

Using the additional theorem for $H_o^{(2)}(k_o|\bar{\rho} - \bar{\rho}'|)$, $G_o(\rho, \phi)$ can be expanded in a series form given by

$$G_o(\rho, \phi) = \frac{-j}{4} \sum_{n=-\infty}^{\infty} H_n^{(2)}(k_o\rho_>) J_n(k_o\rho_<) e^{-jn\phi} \quad (2.9)$$

where $\rho_> = \rho'$, $\rho_< = \rho$ for $\rho < \rho'$, and $\rho_> = \rho$, $\rho_< = \rho'$ for $\rho > \rho'$. It is pointed out that the scattered field $G_s(\rho, \phi)$ from an infinite parallel cylinder by z-polarized incident field $G_o(\rho, \phi)$ is also z-polarized. Considering the Equation (2.2) and the radiation condition at infinity, we assume that the scattered field from the cylinder can be expressed as

$$G_s(\rho, \phi) = \frac{-j}{4} \sum_{n=-\infty}^{\infty} A_s(n) H_n^{(2)}(k_o\rho_<) H_n^{(2)}(k_o\rho_>) e^{-jn\phi} \quad (2.10)$$

The total field at $P(\rho, \phi)$ is the summation of the incident field and the scattered field. Thus, $G(\rho, \phi)$ is given as

$$G(\rho, \phi) = \frac{-j}{4} \sum_{n=-\infty}^{\infty} H_n^{(2)}(k_o\rho_>)[J_n(k_o\rho_<) + A_s(n)H_n^{(2)}(k_o\rho_<)]e^{-jn\phi} \quad (2.11)$$

The unknown scattering coefficient $A_s(n)$ in Equation (2.11) can be easily determined from the boundary condition given in Equation (2.5). Thus, $A_s(n)$ is given as

$$A_s(n) = -\frac{J_n'(k_ob) - jC_s J_n(k_ob)}{H_n^{(2)'}(k_ob) - jC_s H_n^{(2)}(k_ob)} \quad (2.12)$$

The primes in Equation (2.12) represent derivatives with respect to the arguments. For the unification of notation, all Bessel functions included are replaced by Hankel functions $H_n^{(1)}(x)$ and $H_n^{(2)}(x)$. From the well-known relationships of Bessel

functions and Hankel functions, Equation (2.11) can be rewritten as

$$G(\rho, \phi) = \frac{-j}{8} \sum_{n=-\infty}^{\infty} H_n^{(2)}(k_o \rho >) \left[H_n^{(1)}(k_o \rho <) + F_s(n) H_n^{(2)}(k_o \rho <) \right] e^{-jn\phi} \quad (2.13)$$

where

$$F_s(n) = - \frac{H_n^{(1)'}(k_o b) - j C_s H_n^{(1)}(k_o b)}{H_n^{(2)'}(k_o b) - j C_s H_n^{(2)}(k_o b)} \quad (2.14)$$

A plane wave incident is a limiting case when the source is located at infinity (i.e. $\rho' \rightarrow \infty$). The total field for plane wave incidence can be readily obtained by replacing $H_n^{(2)}(k_o \rho')$ by its large argument form. Thus, $G(\rho, \phi)$ for the plane wave incidence can be expressed as

$$G(\rho, \phi) = \frac{U_o}{2} \sum_{n=-\infty}^{\infty} \left[H_n^{(1)}(k_o \rho) + F_s(n) H_n^{(2)}(k_o \rho) \right] e^{-jn(\phi - \frac{\pi}{2})} \quad (2.15)$$

where U_o is the incident field at reference point which is chosen at center of cylinder.

2.2.2 TE_z case

When the line source is a magnetic current filament K , the source radiates a z-polarized incident magnetic field $G_o(\rho, \phi)$ which is also given as

$$G_o(\rho, \phi) = \frac{-j}{4} H_o^{(2)}(k_o |\vec{\rho} - \vec{\rho}'|) \quad (2.16)$$

Using a similar procedure as for the TM_z case, the total field at $P(\rho, \phi)$ is obtained as

$$G(\rho, \phi) = \frac{-j}{4} \sum_{n=-\infty}^{\infty} H_n^{(2)}(k_o \rho >) \left[J_n(k_o \rho <) + A_h(n) H_n^{(2)}(k_o \rho <) \right] e^{-jn\phi} \quad (2.17)$$

The scattering coefficient $A_h(n)$ subject to the boundary condition in Equation (2.5) is given as

$$A_h(n) = - \frac{J_n'(k_0 b) - jC_h J_n(k_0 b)}{H_n^{(2)'}(k_0 b) - jC_h H_n^{(2)}(k_0 b)} \quad (2.18)$$

If we replace $J_n(x)$ and $N_n(x)$ with $H_n^{(1)}(x)$ and $H_n^{(2)}(x)$, Equation (2.17) can be rewritten as

$$G(\rho, \phi) = \frac{-j}{8} \sum_{n=-\infty}^{\infty} H_n^{(2)}(k_0 \rho >) \left[H_n^{(1)}(k_0 \rho <) + F_h(n) H_n^{(2)}(k_0 \rho <) \right] e^{-jn\phi} \quad (2.19)$$

where

$$F_h(n) = - \frac{H_n^{(1)'}(k_0 b) - jC_h H_n^{(1)}(k_0 b)}{H_n^{(2)'}(k_0 b) - jC_h H_n^{(2)}(k_0 b)} \quad (2.20)$$

For the case of plane wave incidence, the total field $G(\rho, \phi)$ is given as

$$G(\rho, \phi) = \frac{U_0}{2} \sum_{n=-\infty}^{\infty} \left[H_n^{(1)}(k_0 \rho) + F_h(n) H_n^{(2)}(k_0 \rho) \right] e^{-jn(\phi - \frac{\pi}{2})} \quad (2.21)$$

2.3 Coated Cylinder

Following the same procedure as for the impedance cylinder, the eigenfunction solution for the field scattered by the infinity conducting cylinder with dielectric/ferrite coating for both TE_z and TM_z cases is obtained in this section. For the coated cylinder, it should be noted that fields can penetrate into the air/coating interface ($\rho = b$) on the given boundary condition that tangential components of both the electric and magnetic fields should be continuous at the interface.

At the surface of the core conducting cylinder, fields should satisfy the soft or hard boundary conditions according to the polarization of the incident fields.

$$G(a, \phi) = 0 \quad ; \text{for soft boundary } (TM_z \text{ case}) \quad (2.22)$$

$$\left. \frac{\partial G(\rho, \phi)}{\partial \rho} \right|_{\rho=a} = 0 \quad ; \text{for hard boundary } (TE_z \text{ case}) \quad (2.23)$$

The above boundary conditions simply mean that on the surface of the conducting core cylinder, the tangential component of the electric field vanishes for both the TM_z and the TE_z cases.

2.3.1 TM_z case

Since the incident field from the source is independent of the scatterer, the expression for the incident field $G_o(\rho, \phi)$ remains unchanged.

$$G_o(\rho, \phi) = \frac{-j}{4} \sum_{n=-\infty}^{\infty} H_n^{(2)}(k_o \rho >) J_n(k_o \rho <) e^{-jn\phi} \quad (2.24)$$

The scattered field $G_s(\rho, \phi)$ outside the cylinder (i.e. $\rho \geq b$) can be expressed as

$$G_s(\rho, \phi) = \frac{-j}{4} \sum_{n=-\infty}^{\infty} A_s(n) H_n^{(2)}(k_0 \rho_>) H_n^{(2)}(k_0 \rho_<) e^{-jn\phi} \quad (2.25)$$

Thus the total field outside the cylinder is given as

$$G(\rho, \phi) = \frac{-j}{4} \sum_{n=-\infty}^{\infty} H_n^{(2)}(k_0 \rho_>) \left[J_n(k_0 \rho_<) + A_s(n) H_n^{(2)}(k_0 \rho_<) \right] e^{-jn\phi} \quad (2.26)$$

The field inside the coating material is not of interest in this research. However, in order to find the unknown coefficient $A_s(n)$, it is necessary to find the field inside the coating material also. Inside the coating material (i.e. $a \leq \rho < b$), $G(\rho, \phi)$ should satisfy

$$\left[\frac{1}{\rho} \frac{\partial}{\partial \rho} \rho \frac{\partial}{\partial \rho} + \frac{1}{\rho^2} \frac{\partial^2}{\partial \phi^2} + k_1^2 \right] G(\rho, \phi) = 0 \quad (2.27)$$

It is assumed that the source is located outside the cylinder (i.e. $\rho' > b$). Thus, the total field $G(\rho, \phi)$ inside the coating material (i.e. $a \leq \rho < b$) can be expressed as

$$G(\rho, \phi) = \frac{-j}{4} \sum_{n=-\infty}^{\infty} H_n^{(2)}(k_0 \rho') \left[B_s(n) J_n(k_1 \rho) + D_s(n) H_n^{(2)}(k_1 \rho) \right] e^{-jn\phi} \quad (2.28)$$

The unknown coefficients $A_s(n)$, $B_s(n)$ and $D_s(n)$ can be determined from the boundary conditions given as follows;

$$E_z(\rho, \phi) = 0 \quad \text{at} \quad \rho = a \quad (2.29)$$

$$E_z(\rho, \phi) \quad \text{is continuous at} \quad \rho = b \quad (2.30)$$

$$H_\phi(\rho, \phi) \quad \text{is continuous at } \rho = b \quad (2.31)$$

Thus, the scattering coefficient $A_s(n)$ is given as

$$A_s(n) = -\frac{J_n'(k_0 b) - jC_s(n)J_n(k_0 b)}{H_n^{(2)'}(k_0 b) - jC_s(n)H_n^{(2)}(k_0 b)} \quad (2.32)$$

where $C_s(n)$ for the coated cylinder is defined as

$$C_s(n) \equiv -j \frac{Z_0}{Z_1} \cdot \frac{J_n(k_1 a)N_n'(k_1 b) - N_n(k_1 a)J_n'(k_1 b)}{J_n(k_1 a)N_n(k_1 b) - N_n(k_1 a)J_n(k_1 b)} \quad (2.33)$$

Z_1 and k_1 denote the characteristic impedance and the wave number of the coating material respectively (i.e. $Z_1 = \sqrt{\frac{\mu_1}{\epsilon_1}}$, $k_1 = \omega \sqrt{\epsilon_1 \mu_1}$).

It is interesting to note that

$$\lim_{a \rightarrow b} C_s(n) = \infty \quad (2.34)$$

Equation (2.34) can be easily proved using the Wronskian of the Bessel functions. Thus, when the thickness of the coating is very small in terms of the wavelength, the behavior of the field is essentially the same as for the TM_z case of the conducting cylinder.

By replacing $J_n(x)$ and $N_n(x)$ with $H_n^{(1)}(x)$ and $H_n^{(2)}(x)$, the Equation (2.26) can be rewritten as

$$G(\rho, \phi) = \frac{-j}{8} \sum_{n=-\infty}^{\infty} H_n^{(2)}(k_0 \rho >) \left[H_n^{(1)}(k_0 \rho <) + F_s(n) H_n^{(2)}(k_0 \rho <) \right] e^{-jn\phi} \quad (2.35)$$

where

$$F_s(n) = -\frac{H_n^{(1)'}(k_0 b) - jC_s(n)H_n^{(1)}(k_0 b)}{H_n^{(2)'}(k_0 b) - jC_s(n)H_n^{(2)}(k_0 b)} \quad (2.36)$$

$C_s(n)$ in Equation (2.33) can also be rewritten as

$$C_s(n) = -j \frac{Z_0}{Z_1} \cdot \frac{H_n^{(1)'}(k_1 b) H_n^{(2)}(k_1 a) - H_n^{(2)'}(k_1 b) H_n^{(1)}(k_1 a)}{H_n^{(1)}(k_1 b) H_n^{(2)}(k_1 a) - H_n^{(2)}(k_1 b) H_n^{(1)}(k_1 a)} \quad (2.37)$$

The total field at $P(\rho > b, \phi)$ for an incident plane wave can also be obtained from Equation (2.35).

$$G(\rho, \phi) = \frac{U_0}{2} \sum_{n=-\infty}^{\infty} \left[H_n^{(1)}(k_0 \rho) + F_s(n) H_n^{(2)}(k_0 \rho) \right] e^{-jn(\phi - \frac{\pi}{2})} \quad (2.38)$$

2.3.2 TE_z case

The boundary conditions of the coated cylinder for the TE_z case are given as follows;

$$E_\phi(\rho, \phi) = 0 \quad \text{at } \rho = a \quad (2.39)$$

$$H_z(\rho, \phi) \quad \text{is continuous at } \rho = b \quad (2.40)$$

$$E_\phi(\rho, \phi) \quad \text{is continuous at } \rho = b \quad (2.41)$$

By using the same procedure as for the TM_z case with the above boundary conditions, total field $G(\rho, \phi)$ is given as

$$G(\rho, \phi) = \frac{-j}{4} \sum_{n=-\infty}^{\infty} H_n^{(2)}(k_0 \rho >) \left[J_n(k_0 \rho <) + A_h(n) H_n^{(2)}(k_0 \rho <) \right] e^{-jn(\phi - \frac{\pi}{2})} \quad (2.42)$$

where

$$A_h(n) = - \frac{J_n'(k_{ob}) - jC_h(n)J_n(k_{ob})}{H_n^{(2)'}(k_{ob}) - jC_h(n)H_n^{(2)}(k_{ob})} \quad (2.43)$$

where $C_h(n)$ for the coated cylinder is defined as

$$C_h(n) \equiv -j \frac{Z_1}{Z_0} \cdot \frac{J_n'(k_1a)N_n'(k_1b) - N_n'(k_1a)J_n'(k_1b)}{J_n'(k_1a)N_n(k_1b) - N_n'(k_1a)J_n(k_1b)} \quad (2.44)$$

It can be easily proved that

$$\lim_{a \rightarrow b} C_h(n) = 0. \quad (2.45)$$

Thus, for very thin coatings, the behavior of the field is essentially the same as for the TE_z case of the conducting cylinder.

In terms of the Hankel functions only, the Equation (2.42), (2.43), and (2.44) are rewritten as

$$G(\rho, \phi) = \frac{-j}{8} \sum_{n=-\infty}^{\infty} H_n^{(2)}(k_0\rho >) \left[H_n^{(1)}(k_0\rho <) + F_h(n)H_n^{(2)}(k_0\rho <) \right] e^{-jn\phi} \quad (2.46)$$

where

$$F_h(n) = - \frac{H_n^{(1)'}(k_{ob}) - jC_h(n)H_n^{(1)}(k_{ob})}{H_n^{(2)'}(k_{ob}) - jC_h(n)H_n^{(2)}(k_{ob})} \quad (2.47)$$

and

$$C_h(n) = -j \frac{Z_1}{Z_0} \cdot \frac{H_n^{(1)'}(k_1b)H_n^{(2)'}(k_1a) - H_n^{(2)'}(k_1b)H_n^{(1)'}(k_1a)}{H_n^{(1)}(k_1b)H_n^{(2)'}(k_1a) - H_n^{(2)}(k_1b)H_n^{(1)'}(k_1a)} \quad (2.48)$$

The total field at $P(\rho > b, \phi)$ for an incident plane wave is given as

$$G(\rho, \phi) = \frac{U_0}{2} \sum_{n=-\infty}^{\infty} \left[H_n^{(1)}(k_0\rho) + F_h(n)H_n^{(2)}(k_0\rho) \right] e^{-jn(\phi - \frac{\pi}{2})} \quad (2.49)$$

2.4 Examples and the discussion

Some examples of the eigenfunction solution¹ for plane wave incidence are given in Figure 2.1 ~ 2.21. The geometry of the problem is shown in Figure 2.1. Figure 2.2 ~ 2.9 illustrates how the normalized field pattern of the impedance cylinder changes as the surface impedance increases from zero (i.e. TE_z case) to infinity (i.e. TM_z case). In these examples, surface impedances are taken to be purely imaginary (i.e. pure capacitive for TM_z and pure inductive for TE_z). The cases of complex impedance will be given in later Chapters in the comparison with the ray solution. Figure 2.10 ~ 2.15 and Figure 2.16 ~ 2.21 illustrate the change of the scattering pattern as the thickness of coating increases for TM_z and TE_z respectively. In these examples, $\epsilon_r=4$ and $\mu_r=1$. The cases of complex ϵ_r and μ_r are given in later Chapters.

It can be observed that manifest effects due to the changing values of the impedance or the thickness are shown for the field pattern in the shadow region. From these examples, we can observe that the scattered field in the shadow region does not simply increase or decrease as the surface impedance or the thickness of the coating increases. However, it is not possible to give any physical interpretation for the change of the scattering pattern from the eigenfunction solutions before we introduce the ray concept which will be given in later Chapters. Thus, detailed discussion of the scattering mechanism is deferred to later Chapters.

¹The FORTRAN subroutine for the Bessel functions provided by Prof. J.H. Richmond have been essential for obtaining these results.

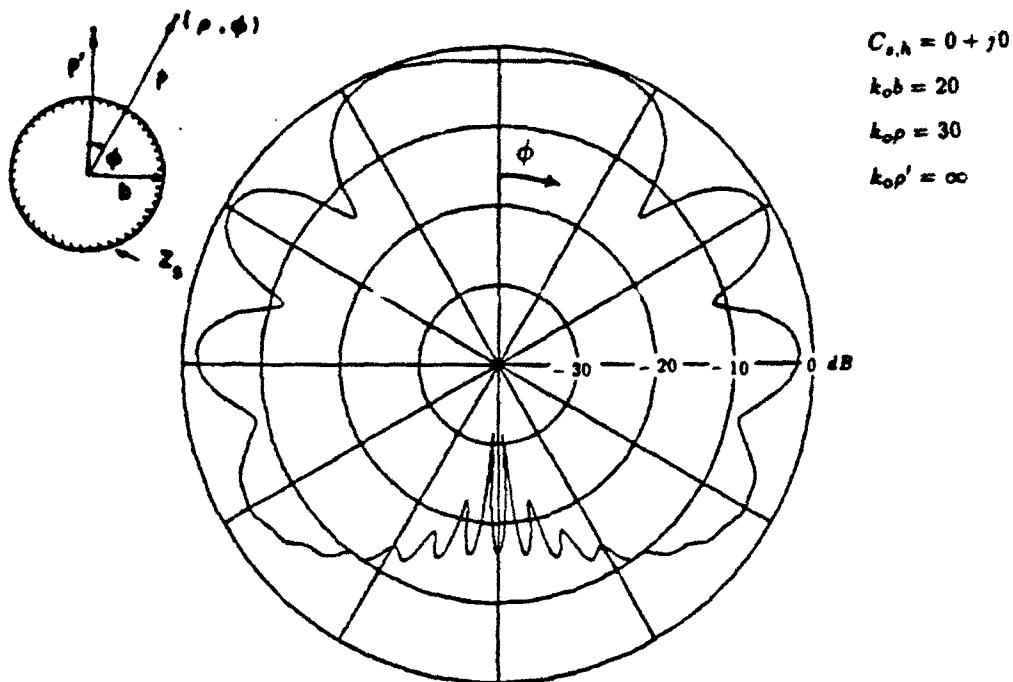


Figure 2.2: Normalized bistatic scattering pattern of impedance cylinder

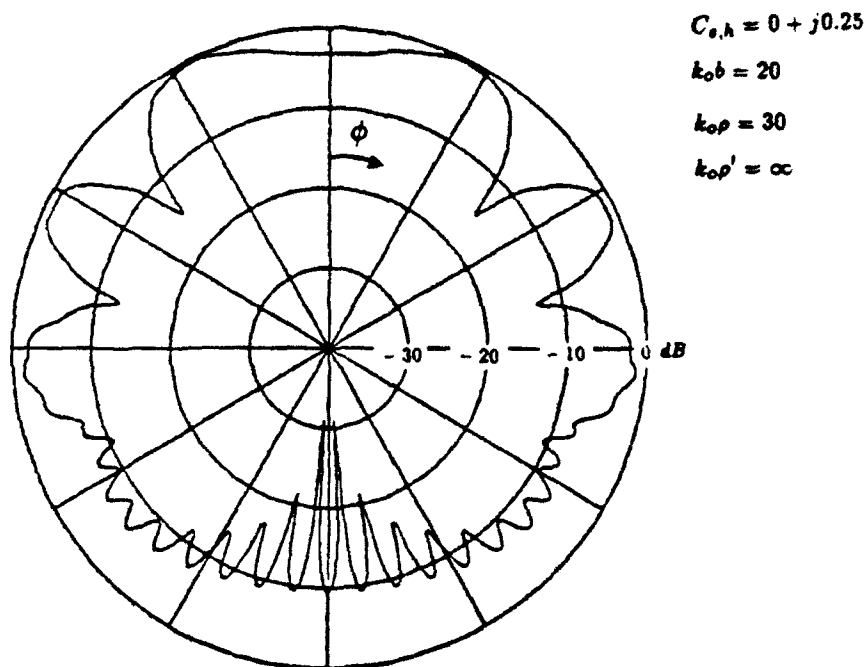


Figure 2.3: Normalized bistatic scattering pattern of impedance cylinder

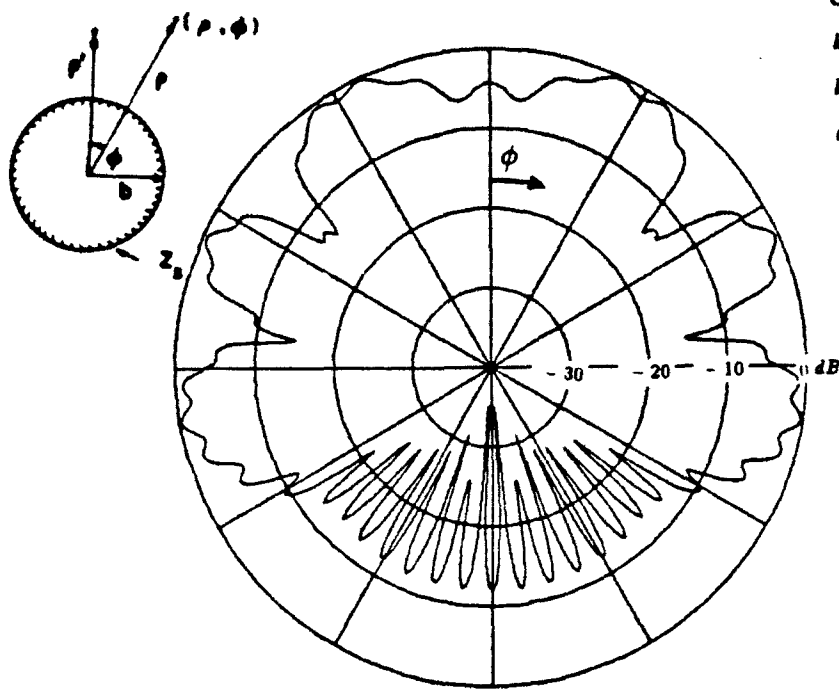


Figure 2.4: Normalized bistatic scattering pattern of impedance cylinder

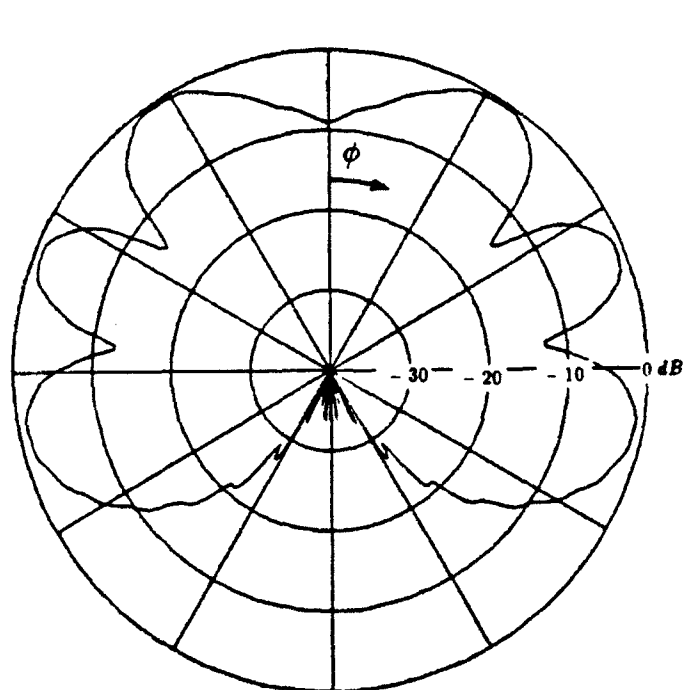


Figure 2.5: Normalized bistatic scattering pattern of impedance cylinder

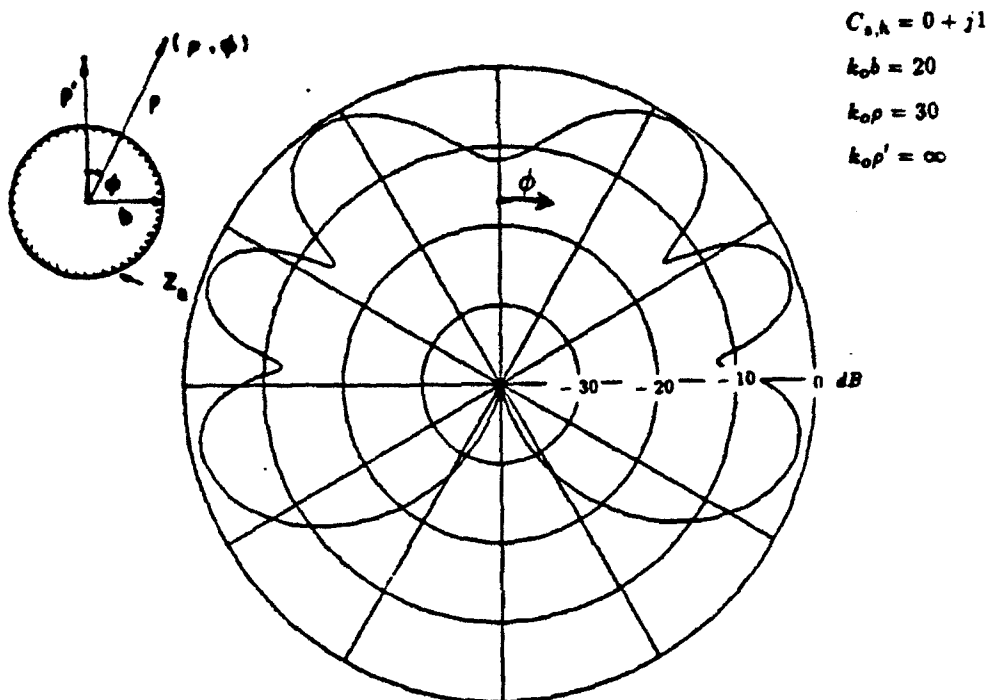


Figure 2.6: Normalized bistatic scattering pattern of impedance cylinder

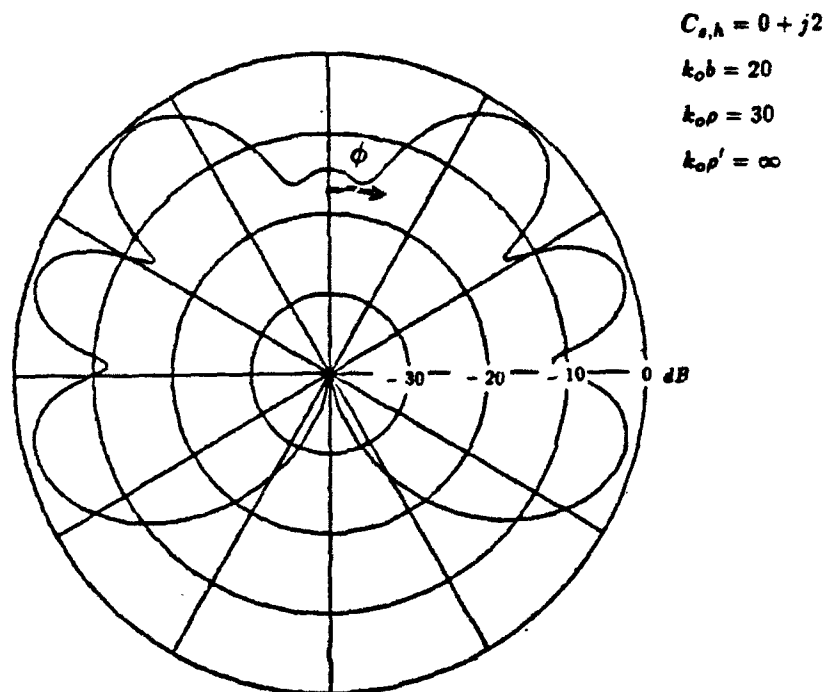
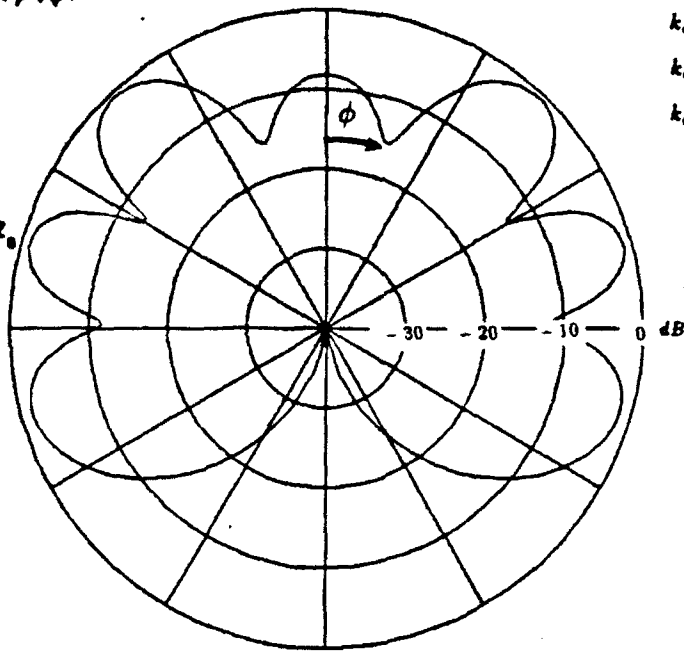
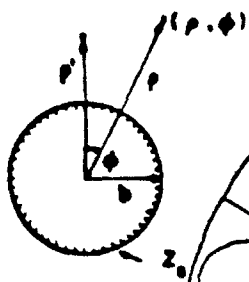


Figure 2.7: Normalized bistatic scattering pattern of impedance cylinder



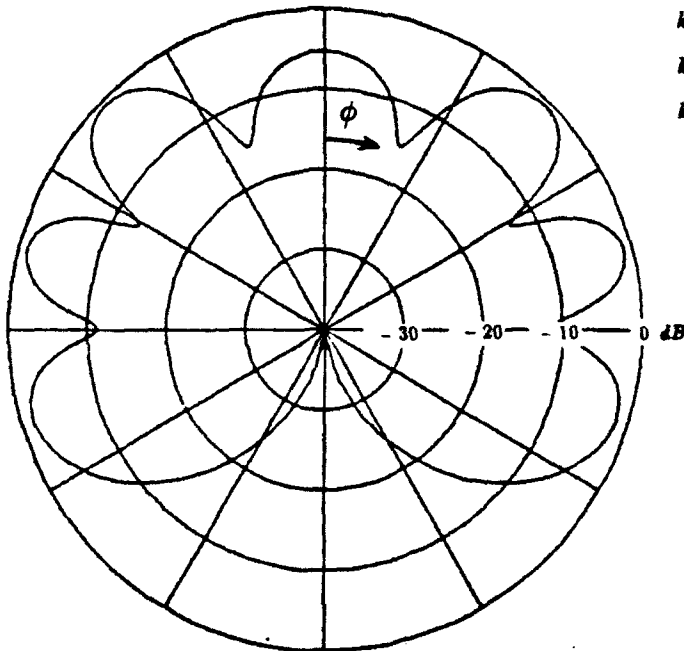
$$C_{s,h} = 0 + j5$$

$$k_{ob} = 20$$

$$k_{o\rho} = 30$$

$$k_{o\rho'} = \infty$$

Figure 2.8: Normalized bistatic scattering pattern of impedance cylinder



$$C_{s,h} = 0 + j\infty$$

$$k_{ob} = 20$$

$$k_{o\rho} = 30$$

$$k_{o\rho'} = \infty$$

Figure 2.9: Normalized bistatic scattering pattern of impedance cylinder

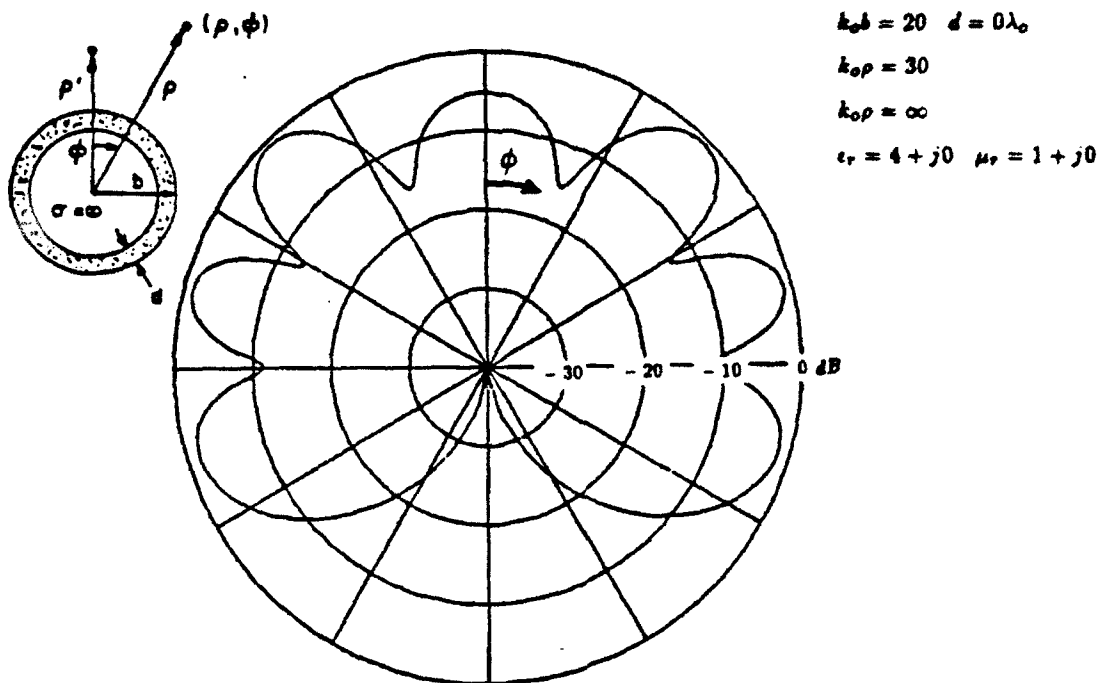


Figure 2.10: Normalized bistatic scattering pattern of coated cylinder : TM_2 case

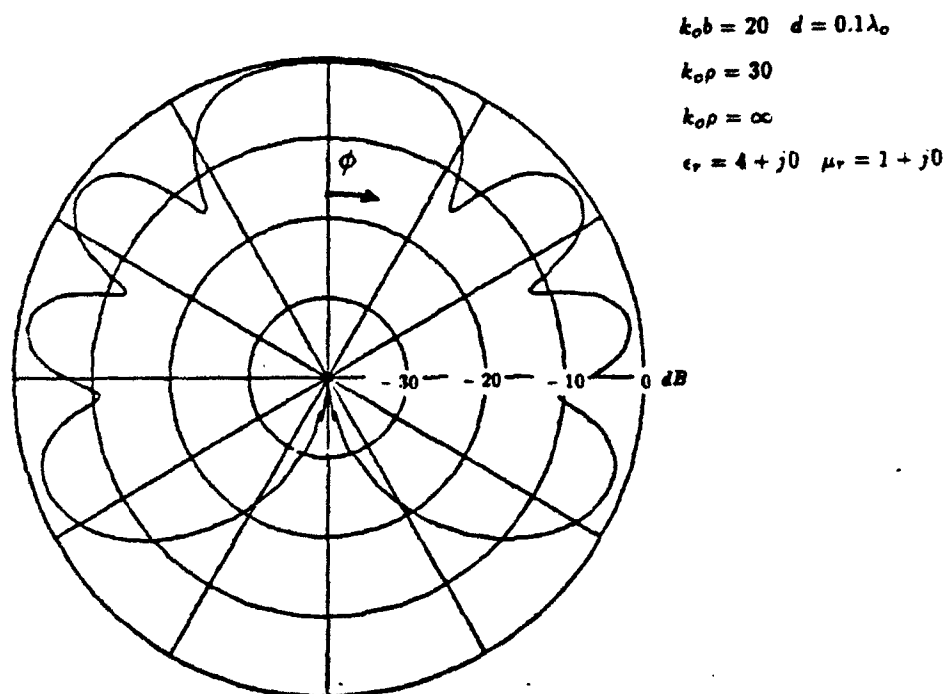
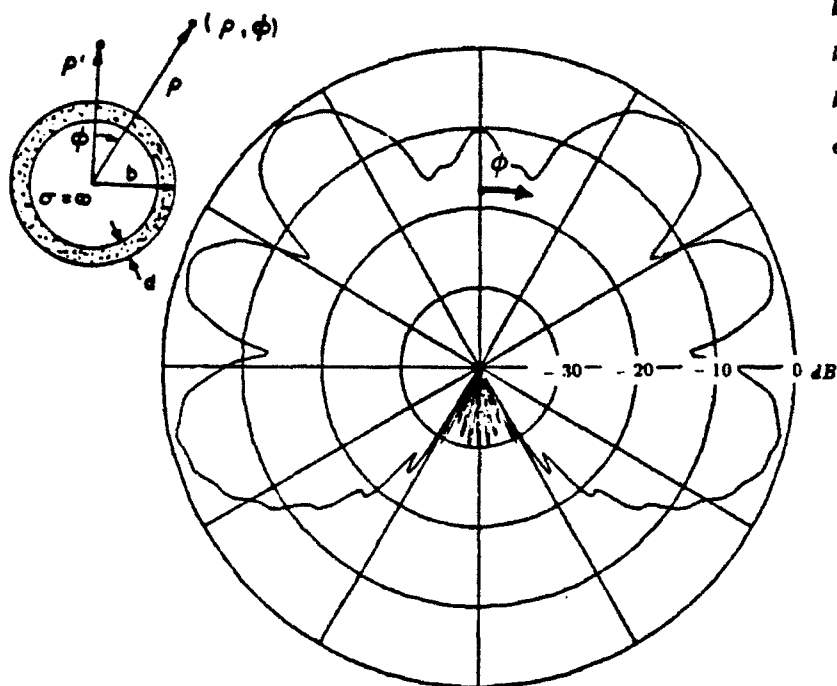


Figure 2.11: Normalized bistatic scattering pattern of coated cylinder : TM_2 case



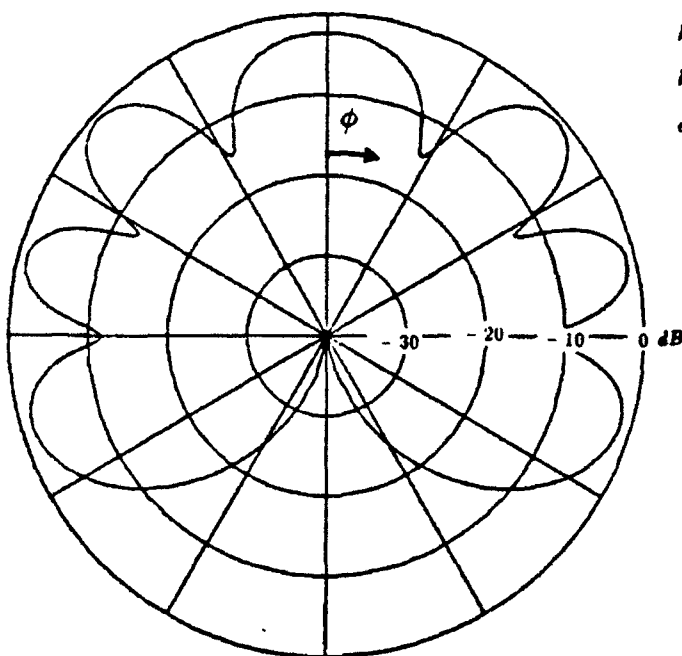
$$k_0 b = 20 \quad d = 0.2 \lambda_0$$

$$k_0 \rho = 30$$

$$k_0 \rho = \infty$$

$$\epsilon_r = 4 + j0 \quad \mu_r = 1 + j0$$

Figure 2.12: Normalized bistatic scattering pattern of coated cylinder : TM_2 case



$$k_0 b = 20 \quad d = 0.3 \lambda_0$$

$$k_0 \rho = 30$$

$$k_0 \rho = \infty$$

$$\epsilon_r = 4 + j0 \quad \mu_r = 1 + j0$$

Figure 2.13: Normalized bistatic scattering pattern of coated cylinder : TM_2 case

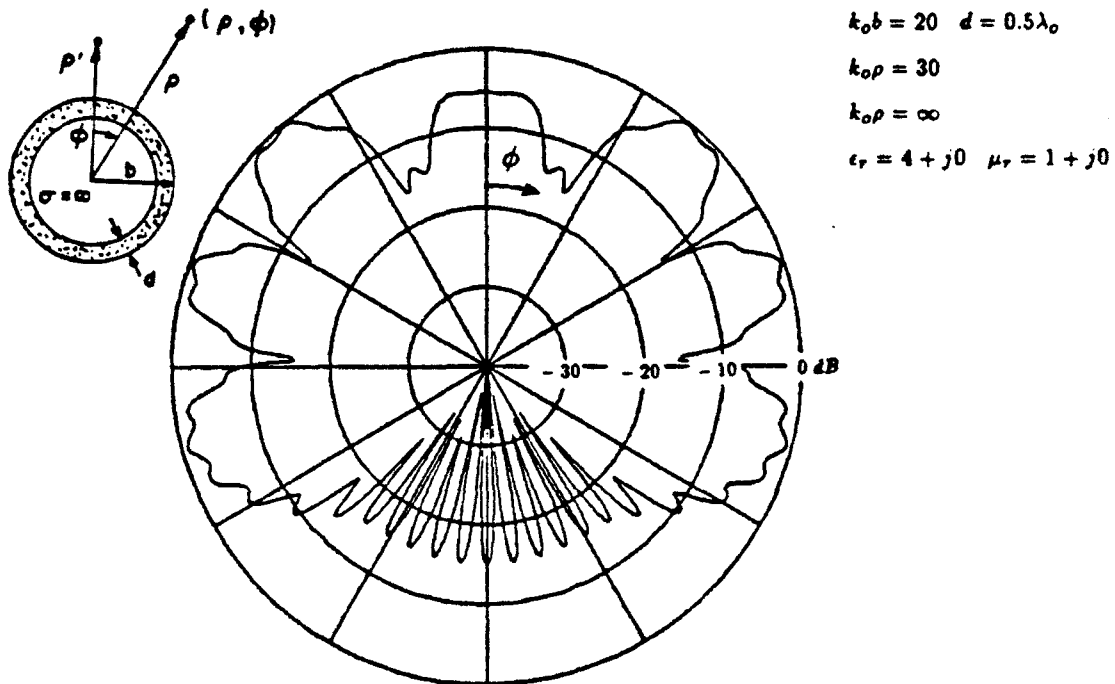


Figure 2.14: Normalized bistatic scattering pattern of coated cylinder : TM_2 case

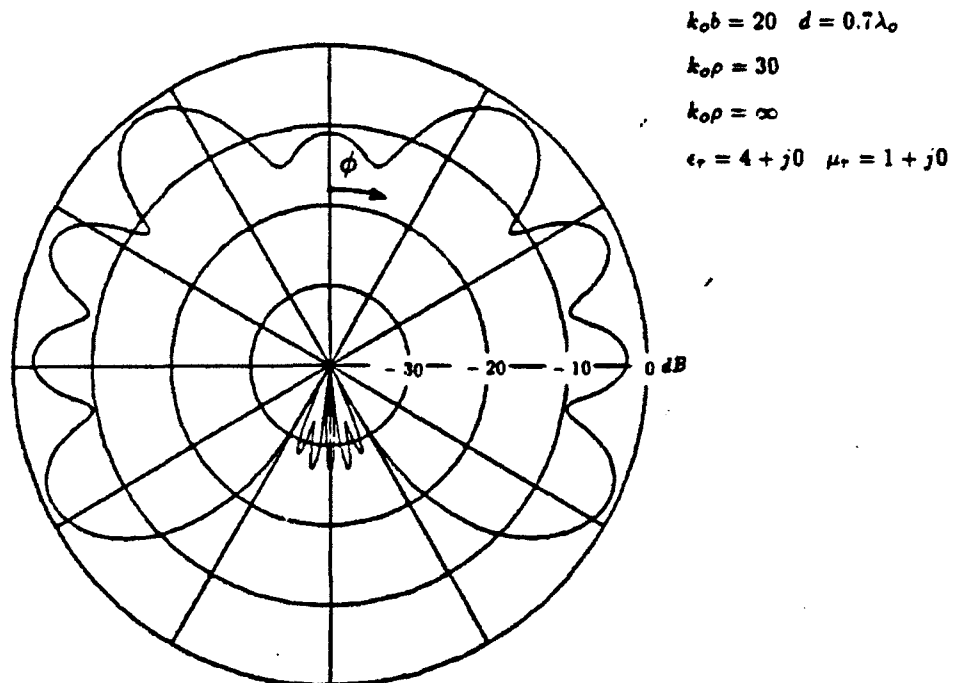
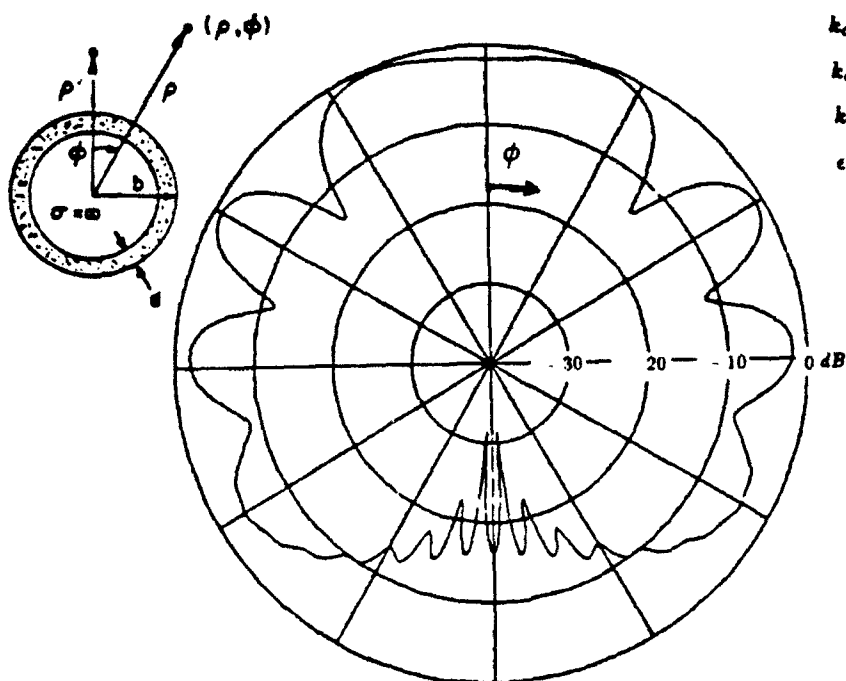


Figure 2.15: Normalized bistatic scattering pattern of coated cylinder : TM_2 case



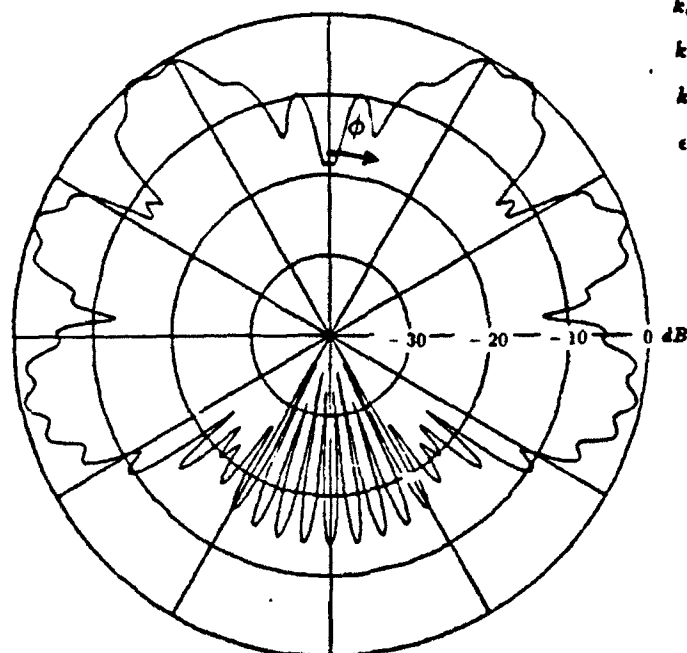
$$k_0 b = 20 \quad d = 0 \lambda_0$$

$$k_0 \rho = 30$$

$$k_0 \rho = \infty$$

$$\epsilon_r = 4 + j0 \quad \mu_r = 1 + j0$$

Figure 2.16: Normalized bistatic scattering pattern of coated cylinder : TE_2 case



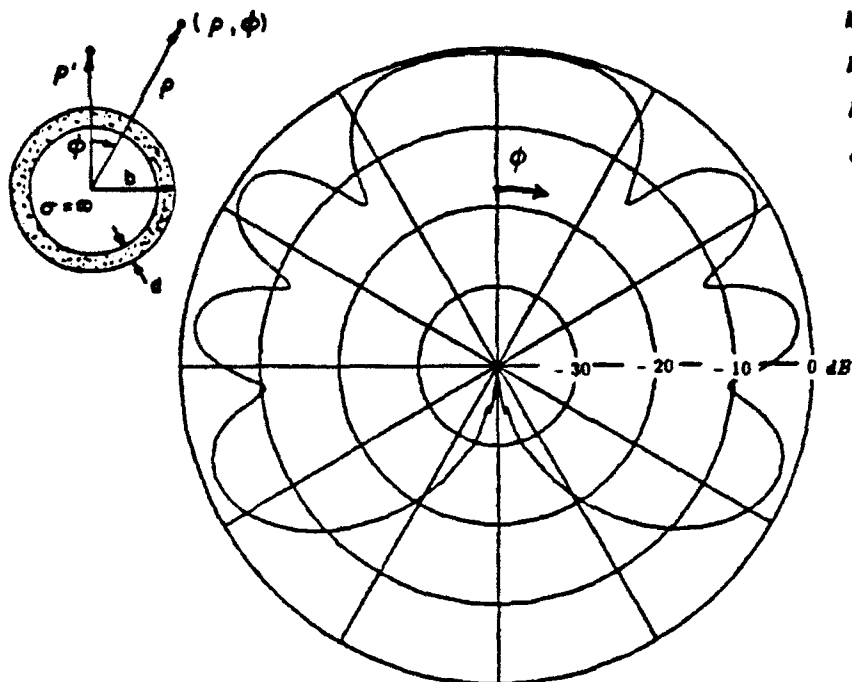
$$k_0 b = 20 \quad d = 0.1 \lambda_0$$

$$k_0 \rho = 30$$

$$k_0 \rho = \infty$$

$$\epsilon_r = 4 + j0 \quad \mu_r = 1 + j0$$

Figure 2.17: Normalized bistatic scattering pattern of coated cylinder : TE_2 case



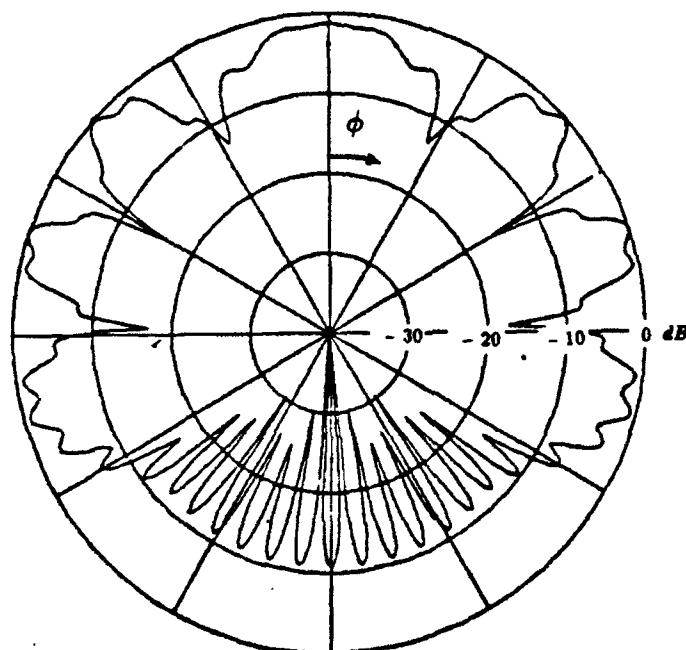
$$k_0 b = 20 \quad d = 0.2 \lambda_0$$

$$k_0 \rho = 30$$

$$k_0 \rho = \infty$$

$$\epsilon_r = 4 + j0 \quad \mu_r = 1 + j0$$

Figure 2.18: Normalized bistatic scattering pattern of coated cylinder : TE_2 case



$$k_0 b = 20 \quad d = 0.4 \lambda_0$$

$$k_0 \rho = 30$$

$$k_0 \rho = \infty$$

$$\epsilon_r = 4 + j0 \quad \mu_r = 1 + j0$$

Figure 2.19: Normalized bistatic scattering pattern of coated cylinder : TE_2 case

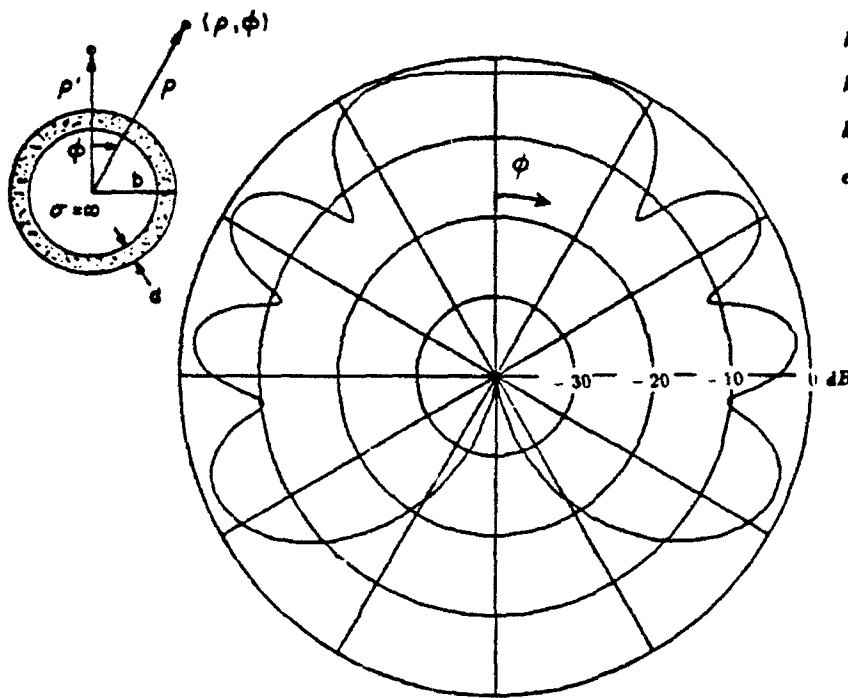


Figure 2.20: Normalized bistatic scattering pattern of coated cylinder : TE_2 case

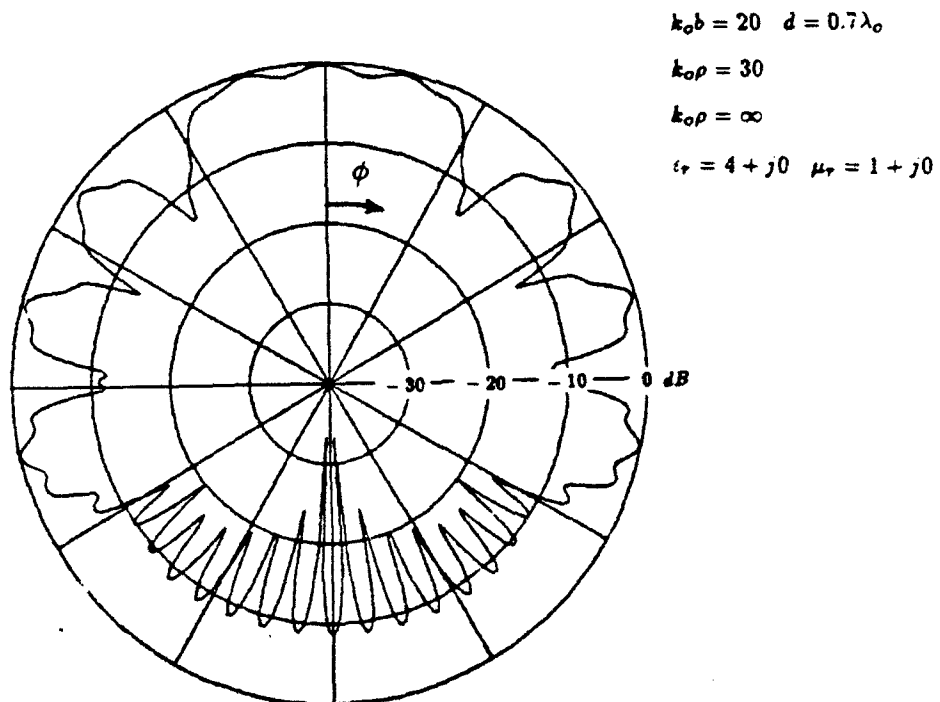


Figure 2.21: Normalized bistatic scattering pattern of coated cylinder : TE_2 case

CHAPTER III

GTD SOLUTION

Ray-optical solutions for the field scattered by the impedance and the coated cylinder are obtained in this Chapter. For the perfectly conducting cylinder, Keller [1] developed an asymptotic solution to this problem and interpreted it in the ray-optical terms within the framework of his geometrical theory of diffraction (GTD). Even though the boundary conditions to be considered are different, the same procedure as that for the derivation of GTD solution for the conducting cylinders can be taken to deduce the GTD solutions for the impedance and the coated cylinder. First, the field representation in the angular eigenfunction series as given in Chapter II is transformed into the integral form. Then, the integral is evaluated asymptotically via the stationary phase method or the residue theorem.

It is noted that the behavior of high-frequency field is characterized by various geometric optical domains as illustrated in Figure 3.1. Separate analysis is given for each geometric optical domain as the field representation has different format according to the region where the field point is located. Lit region(I) and shadow region(III) are separated by the shadow boundaries (SB) according to the illumination from the source. Small angular ranges adjacent to the shadow boundaries which are indicated as shaded region(II) are the penumbral or transition region. The solution obtained in this Chapter is not valid in this region. The analysis for the field in transition region will be given in Chapter V. In this analysis, we also exclude the surface or caustic boundary layer region(IV) which is in the immediate

vicinity of the cylinder surface.

As mentioned, Keller's pure ray-optical solution fails within the transition region adjacent to the shadow boundaries. The failure of Keller's GTD solution has been overcome by the development of a uniform version of GTD by Pathak [3]. Hence, it may seem to be obsolete to develop the pure ray-optical solution for our problem which will inevitably fail in the transition region. Nevertheless, it appears that the ordinary GTD solution is a necessary step to be taken for the development of the uniform GTD which will be discussed in Chapter V. This is because the ray format to be used in the uniform GTD solution comes from the ordinary GTD solution.

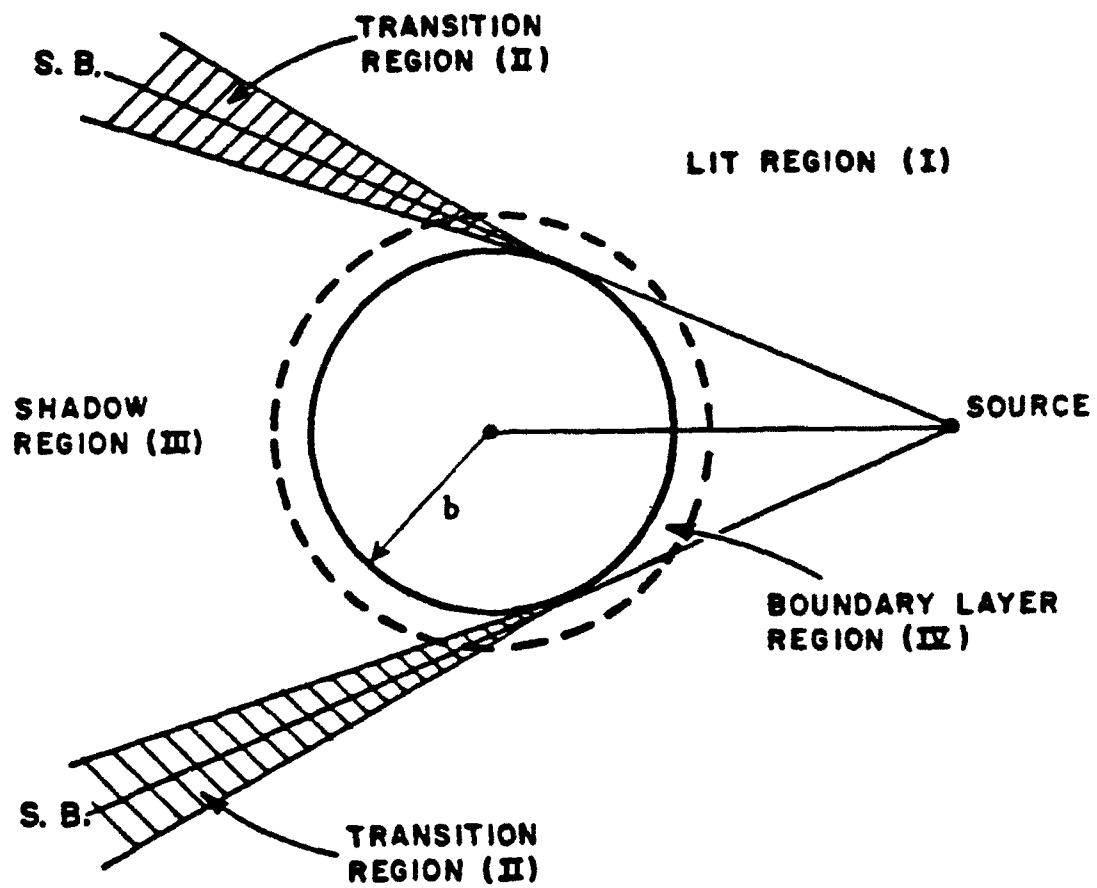


Figure 3.1: The geometric optical domains

3.1 Integral Representation of the Field

As discussed in Appendix A, the field representation in the eigenfunction series form given in Chapter II can be transformed into an integral form. The eigenfunction series solution of interest has the form given by

$$G(\rho, \phi) \equiv u = \sum_{n=-\infty}^{\infty} B_{s,h}(n) \exp(-jn\phi) \quad (3.1)$$

where $B_{s,h}(n)$ depends on the polarization of the incident field and the subscripts s and h correspond to the TM_z and TE_z cases respectively.

From Equations (2.13), (2.19), (2.35) and (2.46), $B_{s,h}(n)$ is given as

$$B_{s,h}(n) = \frac{-j}{8} H_n^{(2)}(k_o\rho>) \left[H_n^{(1)}(k_o\rho<) + F_{s,h}(n) H_n^{(2)}(k_o\rho<) \right] \quad (3.2)$$

From Equation (A.3) in Appendix A, the eigenfunction series can be transformed into the integral representation.

$$\sum_{n=-\infty}^{\infty} B_{s,h}(n) \exp(-jn\phi) = \frac{-j}{2} \oint_{C_x} B_{s,h}(\nu) \frac{\exp[-j\nu(\phi - \pi)]}{\sin \nu\pi} d\nu \quad (3.3)$$

where C_x is the contour which encloses the lower half of complex ν -plane with a large semicircle. From Equation (3.2), $B_{s,h}(\nu)$ is given by

$$B_{s,h}(\nu) = \frac{-j}{8} H_\nu^{(2)}(k_o\rho>) \left[H_\nu^{(1)}(k_o\rho<) + F_{s,h}(\nu) H_\nu^{(2)}(k_o\rho<) \right] \quad (3.4)$$

and

$$F_{s,h}(\nu) = - \frac{H_\nu^{(1)'}(k_ob) - jC_{s,h}(\nu)H_\nu^{(1)}(k_ob)}{H_\nu^{(2)'}(k_ob) - jC_{s,h}(\nu)H_\nu^{(2)}(k_ob)} \quad (3.5)$$

For the impedance cylinder,

$$C_s(\nu) = C_s = \frac{Z_o}{Z_s} \quad \text{for } TM_z \quad (3.6)$$

and

$$C_h(\nu) = C_h = \frac{Z_s}{Z_o} \quad \text{for } TE_z \quad (3.7)$$

For the coated cylinder, $C_s(\nu)$ and $C_h(\nu)$ are given as

$$C_s(\nu) = -j \frac{Z_o}{Z_1} \cdot \frac{H_\nu^{(1)'}(k_1 b) H_\nu^{(2)}(k_1 a) - H_\nu^{(2)'}(k_1 b) H_\nu^{(1)}(k_1 a)}{H_\nu^{(1)}(k_1 b) H_\nu^{(2)'}(k_1 a) - H_\nu^{(2)}(k_1 b) H_\nu^{(1)'}(k_1 a)} \quad \text{for } TM_z \quad (3.8)$$

and

$$C_h(\nu) = -j \frac{Z_1}{Z_o} \cdot \frac{H_\nu^{(1)'}(k_1 b) H_\nu^{(2)'}(k_1 a) - H_\nu^{(2)'}(k_1 b) H_\nu^{(1)'}(k_1 a)}{H_\nu^{(1)}(k_1 b) H_\nu^{(2)'}(k_1 a) - H_\nu^{(2)}(k_1 b) H_\nu^{(1)'}(k_1 a)} \quad \text{for } TE_z \quad (3.9)$$

It is noted that $H_{-\nu}^{(1)}(x) = e^{j\nu\pi} H_\nu^{(1)}(x)$ and $H_{-\nu}^{(2)}(x) = e^{-j\nu\pi} H_\nu^{(2)}(x)$, therefore, it can be easily seen that B_ν is an even function of ν (i.e. $B_{s,h}(-\nu) = B_{s,h}(\nu)$).

From the Equation (A.5) in Appendix A,

$$u = -j \int_{-\infty-j\epsilon}^{\infty-j\epsilon} B_{s,h}(\nu) \frac{\cos \nu(\phi - \pi)}{\sin \nu\pi} d\nu \quad (3.10)$$

i.e.,

$$u = \frac{-1}{8} \int_{-\infty-j\epsilon}^{\infty-j\epsilon} H_\nu^{(2)}(k_o \rho >) \left[H_\nu^{(1)}(k_o \rho <) + F_{s,h}(\nu) H_\nu^{(2)}(k_o \rho <) \right] \frac{\cos \nu(\phi - \pi)}{\sin \nu\pi} d\nu$$

(3.11)

It is noted that

$$\frac{\cos \nu(\phi - \pi)}{\sin \nu\pi} = je^{-j\nu\phi} + j \frac{e^{-j\nu(2\pi+\phi)} + e^{-j\nu(2\pi-\phi)}}{1 - e^{-j2\nu\pi}} \quad (3.12)$$

Thus, the integral representation of the field can be decomposed into two terms as

$$u = u^o + u^{cw} \quad (3.13)$$

where

$$u^o = \frac{-j}{8} \int_{-\infty-j\epsilon}^{\infty-j\epsilon} H_\nu^{(2)}(k_o\rho_>) \left[H_\nu^{(1)}(k_o\rho_<) + F_{s,h}(\nu) H_\nu^{(2)}(k_o\rho_<) \right] e^{-j\nu\phi} d\nu \quad (3.14)$$

and

$$u^{cw} = \frac{-j}{8} \int_{-\infty-j\epsilon}^{\infty-j\epsilon} H_\nu^{(2)}(k_o\rho_>) \left[H_\nu^{(1)}(k_o\rho_<) + F_{s,h}(\nu) H_\nu^{(2)}(k_o\rho_<) \right] \\ \times \frac{e^{-j\nu(2\pi+\phi)} + e^{-j\nu(2\pi-\phi)}}{1 - e^{-j2\nu\pi}} d\nu \quad (3.15)$$

It has been pointed out [13] that u^o in Equation (3.14) contains all the geometric-optical, transition and the dominant diffraction effects. In the following sections, the integral in Equation (3.14) will be evaluated asymptotically via the stationary phase method to yield the geometric-optical fields in the lit region. A residue series solution for the integral gives the creeping-wave representation in the shadow region. The lit and the shadow region separated by the shadow boundary (S.B.) are indicated in Figure 3.1. The term u^{cw} represents multiply encircling creeping waves, which will be discussed later in this Chapter.

3.2 Field in the deep lit region - G.O. field

Lit region is in the angular range of $0 \leq |\phi| < \phi_{sb}$, where the field point is in the line of sight from the source. In this region, the asymptotic evaluation of u^o given in Equation (3.14) leads to geometric-optical fields: incident field u^i and reflected field u^r . It should be noted that this solution is valid in the deep lit region excluding the transition region in the vicinity of the shadow boundary. For simplicity of calculation, we assume that $\rho < \rho'$. For the case of $\rho > \rho'$, the same procedure can be taken to obtain the same result.

Equation (3.14) is decomposed into two terms as

$$u^o \equiv u_1^o + u_2^o \quad (3.16)$$

where

$$u_1^o = \frac{-j}{8} \int_{-\infty-j\epsilon}^{\infty-j\epsilon} H_\nu^{(2)}(k_o\rho') H_\nu^{(1)}(k_o\rho) e^{-j\nu\phi} d\nu \quad (3.17)$$

and

$$u_2^o = \frac{-j}{8} \int_{-\infty-j\epsilon}^{\infty-j\epsilon} F_{s,h}(\nu) H_\nu^{(2)}(k_o\rho') H_\nu^{(2)}(k_o\rho) e^{-j\nu\phi} d\nu \quad (3.18)$$

3.2.1 Evaluation of u_1^o

Equation (3.17) can be asymptotically evaluated via the stationary phase method after $H_\nu^{(2)}(k_o\rho')$ and $H_\nu^{(1)}(k_o\rho)$ are replaced by their asymptotic approximations. The problem with this method is that the Hankel functions have different asymptotic approximations in the different regions along the path of the integral where ν changes from $-\infty$ to $+\infty$. Therefore, strictly speaking, it is necessary to divide the integral path into several sections according to the valid regions of the approximation, which makes the evaluation cumbersome. To circumvent

this difficulty, an alternative method will be employed to obtain the same result. First, we represent $H_\nu^{(2)}(k_o\rho')$ and $H_\nu^{(1)}(k_o\rho)$ by their integral form.

$$H_\nu^{(2)}(k_o\rho') = \frac{1}{\pi} \int_{C_2} \exp(-jk\rho' \sin \alpha + j\nu\alpha) d\alpha \quad (3.19)$$

and

$$H_\nu^{(1)}(k_o\rho) = \frac{1}{\pi} \int_{C_1} \exp(-jk\rho \sin \beta + j\nu\beta) d\beta \quad (3.20)$$

The contour C_1 and C_2 are depicted in Figure 3.2. After replacing $H_\nu^{(2)}(k_o\rho')$ and $H_\nu^{(1)}(k_o\rho)$ in Equation (3.17) by their integral forms and rearranging the integral, we obtain

$$u_1^o = \frac{-j}{8\pi^2} \int_{C_2} \int_{C_1} \exp(-jk_o\rho \sin \beta - jk_o\rho' \sin \alpha) \\ \times \left\{ \int_{-\infty-j\epsilon}^{\infty-j\epsilon} \exp[j\nu(\alpha + \beta - \phi)] d\nu \right\} d\beta d\alpha \quad (3.21)$$

Assuming that α and β are real variables, it can be seen from the well-known relationship of the inverse Laplace transformation that

$$\int_{-\infty-j\epsilon}^{\infty-j\epsilon} \exp[j\nu(\alpha + \beta - \phi)] d\nu = -j \int_{\epsilon-j\infty}^{\epsilon+j\infty} \exp[s(\alpha + \beta - \phi)] ds \\ = 2\pi\delta(\alpha + \beta - \phi) \quad (3.22)$$

Incorporating Equation (3.22) into Equation (3.21), we obtain

$$u_1^o = \frac{-j}{4\pi} \int_{C_2} \exp[-jk_o\rho' \sin \alpha - jk_o\rho \sin(\phi - \alpha)] d\alpha \quad (3.23)$$

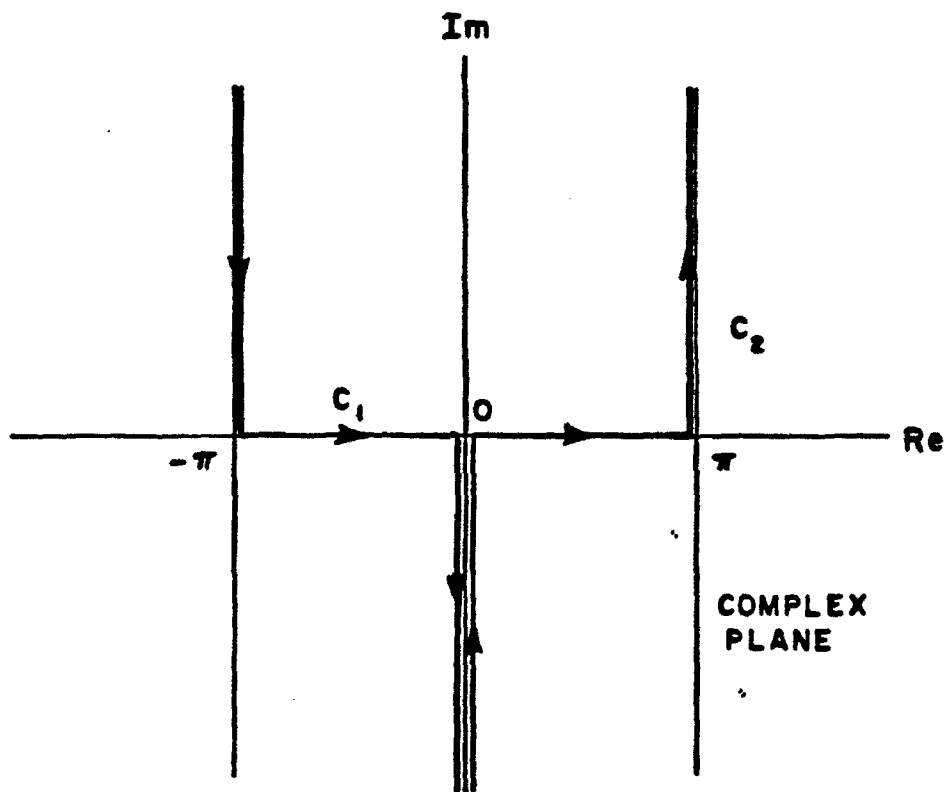


Figure 3.2: The contours C_1 and C_2

In obtaining Equation (3.23), we assumed that $\phi - \alpha$ lies on the contour C_1 .

Thus,

$$-\pi \leq \phi - \alpha \leq 0 \quad (3.24)$$

Asymptotic evaluation of the integral in Equation (3.23) can be easily obtained via the stationary phase method. Equation (3.23) can be rewritten as

$$u_1^o = \frac{-j}{4\pi} \int_{C_2} \exp[jk_o \rho' \Phi(\alpha)] d\alpha \quad (3.25)$$

where

$$\Phi(\alpha) = -\sin \alpha - \frac{\rho}{\rho'} \sin(\phi - \alpha) \quad (3.26)$$

At the stationary point, $\Phi'(\alpha_s) = 0$, therefore, the stationary point α_s is determined by the relationship

$$\Phi'(\alpha_s) = \left. \frac{\partial \Phi(\alpha)}{\partial \alpha} \right|_{\alpha=\alpha_s} = -\cos \alpha_s + \frac{\rho}{\rho'} \cos(\phi - \alpha_s) = 0. \quad (3.27)$$

The stationary point should lie on the contour C_2 in order for u_1^o to have nonzero value. Therefore

$$0 \leq \alpha_s \leq \pi \quad (3.28)$$

From Equations (3.24) and (3.28)

$$\phi \leq \alpha_s \leq \pi \quad (3.29)$$

It was assumed $\rho' > \rho$ and $0 \leq \phi \leq \pi$. Thus, it can be shown that in order for α_s to satisfy the given condition in Equation (3.29)

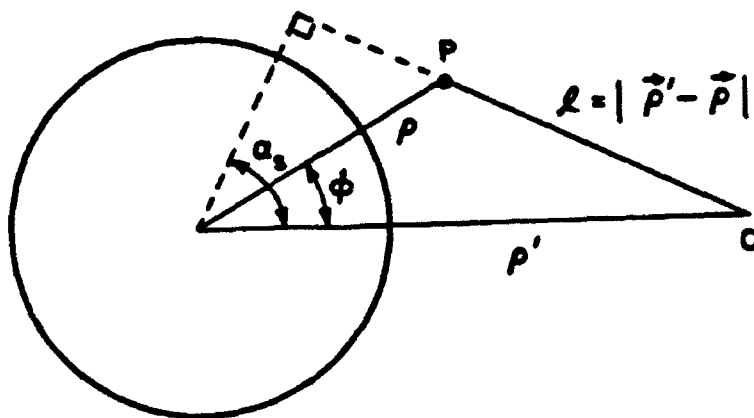


Figure 3.3: Physical meaning of the stationary point

$$\phi \leq \cos^{-1} \left(\frac{\rho}{\rho'} \right) \quad (3.30)$$

Thus, u_1^o contributes only when the above condition is satisfied.

Final result of the asymptotic evaluation of the integral yields

$$u_1^o \approx \frac{-j}{4} \sqrt{\frac{2}{\pi}} \frac{\exp[jk_o(\rho \sin \beta_s - \rho' \sin \alpha_s) + j\frac{\pi}{4}]}{\sqrt{k_o \rho' \sin \alpha_s - k_o \rho \sin \beta_s}} \quad (3.31)$$

The physical meaning of the stationary point is illustrated in Figure 3.3. From the Figure 3.3, we observe that the distance from the source to field point is given as

$$l = |\vec{\rho}' - \vec{\rho}| = \rho' \sin \alpha_s - \rho \sin(\alpha_s - \phi) \quad (3.32)$$

Therefore, u_1^o can be expressed as

$$u_1^o \approx \frac{e^{-j\frac{\pi}{4}}}{2\sqrt{2\pi}} \frac{e^{-jk_o l}}{\sqrt{k_o l}} \quad \text{for } 0 \leq \phi \leq \cos^{-1} \left(\frac{\rho}{\rho'} \right) \quad (3.33)$$

From the above result, we conclude that u_1^o is the direct incident field from the source to the field point for $0 \leq \phi \leq \cos^{-1}(\rho/\rho')$. In obtaining above result, the integral representations for the Hankel functions are used instead of the Debye approximations. Even though the same result can be obtained by using the Debye approximations, this method is mathematically more rigorous.

Note that u_1^o is independent of the boundary conditions of the cylinder. Thus the result obtained here can be applied to both the impedance and the coated cylinder.

3.2.2 Evaluation of u_2^o

In this section, u_2^o in Equation (3.18) is evaluated asymptotically via the stationary phase method. The alternative method used for the evaluation of u_1^o can not be easily applied here because $F_{s,h}(\nu)$ in the integrand is a function of ν . Therefore, we replace the Hankel functions in the integrand by their asymptotic approximations. It is noted that the Hankel functions in the integrand have different asymptotic approximations according to the changing values of ν along the contour path. In order to take a mathematically rigorous procedure it is necessary to divide the integral path into many sections because the integrand of Equation (3.18) has Hankel functions with 3 different arguments ($k_o\rho$, $k_o\rho'$, k_ob) for the impedance cylinder and the 5 different arguments ($k_o\rho$, $k_o\rho'$, k_ob , k_1a , k_1b) for the coated cylinder. To simplify the procedure we first divide the integral into two terms as

$$u_2^o \equiv I_1 + I_2 \quad (3.34)$$

where

$$I_1 = \frac{-j}{8} \int_{k_ob-j\epsilon}^{\infty-j\epsilon} F_{s,h}(\nu) H_\nu^{(2)}(k_o\rho') H_\nu^{(2)}(k_o\rho) e^{-j\nu\phi} d\nu \quad (3.35)$$

and

$$I_2 = \frac{-j}{8} \int_{-\infty-j\epsilon}^{k_ob-j\epsilon} F_{s,h}(\nu) H_\nu^{(2)}(k_o\rho') H_\nu^{(2)}(k_o\rho) e^{-j\nu\phi} d\nu \quad (3.36)$$

Evaluation of I_1

First, we assume that the asymptotic evaluation of the integral depends only on the stationary phase point and therefore the contribution from the end point at $\nu = k_ob$ can be ignored. This assumption is valid when the stationary phase

point ν_s is not close to $k_0 b$. When the field point is in the deep lit region, it can be shown that the stationary phase point is located far enough from $k_0 b$. However, as the field point approaches the shadow boundary, this assumption is no longer valid. The case when the ν_s approaches $k_0 b$ will be discussed in Chapter V in the treatment of the field in transition region.

Assuming that ν is not close to $k_0 b$ in the given integral path of Equation (3.35) where $k_0 b < \text{Re}[\nu] < \infty$, it can be observed that

$$H_\nu^{(1)}(k_0 b) \approx -H_\nu^{(2)}(k_0 b) \quad (3.37)$$

Thus, from Equation (3.5),

$$F_{s,h}(\nu) \approx 1 \quad (3.38)$$

Therefore, I_1 can be simplified as

$$I_1 \approx \frac{-j}{8} \int_{k_0 b - j\epsilon}^{\infty - j\epsilon} H_\nu^{(2)}(k_0 \rho') H_\nu^{(2)}(k_0 \rho) e^{-j\nu\phi} d\nu \quad (3.39)$$

The integrand in above Equation (3.39) includes two Hankel functions, $H_\nu^{(2)}(k_0 \rho')$ and $H_\nu^{(2)}(k_0 \rho)$. As remarked before, they have different asymptotic approximations along the path of the integral. Here, we make another assumption that both ρ' and ρ are large enough that the stationary phase point ν_s is always located such that;

$$\left| \frac{\nu}{k_0 \rho} \right| \ll 1 \quad \text{and} \quad \left| \frac{\nu}{k_0 \rho'} \right| \ll 1 \quad (3.40)$$

This is a reasonable assumption because the field in the surface boundary layer region(IV) of Figure 3.1 is not of interest in this analysis. From the Debye approximations of the Hankel functions for this range of ν

$$H_\nu^{(2)}(k_o\rho')H_\nu^{(2)}(k_o\rho) \approx \frac{2j}{\pi k_o} \frac{\exp[-jk_o\rho' \sin \alpha - jk_o\rho \sin \beta + j\nu(\alpha + \beta)]}{\sqrt{\rho'\rho \sin \alpha \sin \beta}} \quad (3.41)$$

where $\alpha \equiv \cos^{-1}(\nu/k_o\rho')$ and $\beta \equiv \cos^{-1}(\nu/k_o\rho)$.

Therefore, I_1 can be approximated as

$$I_1 \approx \frac{1}{4\pi k_o} \int_{C_\nu} \frac{\exp[jk_o\rho'\Phi(\nu)]}{\sqrt{\rho'\rho \sin \alpha \sin \beta}} d\nu \quad (3.42)$$

where $\Phi(\nu)$ is defined as

$$\Phi(\nu) \equiv -\sin \alpha - \frac{\rho}{\rho'} \sin \beta + \frac{\nu}{\rho'}(\alpha + \beta - \phi) \quad (3.43)$$

and C_ν denotes the integral path of ν subject to Equation (3.40) and the condition that $|\nu/k_o\rho| \gg 1$. At the stationary phase point, $\Phi'(\nu_s) = 0$. Therefore, it can be easily shown that

$$\alpha_s + \beta_s = \phi \quad (3.44)$$

where $\alpha_s = \cos^{-1}(\nu_s/k_o\rho')$ and $\beta_s = \cos^{-1}(\nu_s/k_o\rho)$. Physical meaning of the α_s and β_s is depicted in Figure 3.4. It is important to note that both α_s and β_s should satisfy the condition;

$$0 \leq \text{Re}[\alpha_s] \leq \pi \quad \text{and} \quad 0 \leq \text{Re}[\beta_s] \leq \pi \quad (3.45)$$

It can be verified that in order for α_s and β_s to lie on the integral path C_ν subject to the above condition, the following condition on ϕ should be satisfied

$$\cos^{-1}\left(\frac{\rho}{\rho'}\right) \leq \phi < \phi_{sb} \quad (3.46)$$

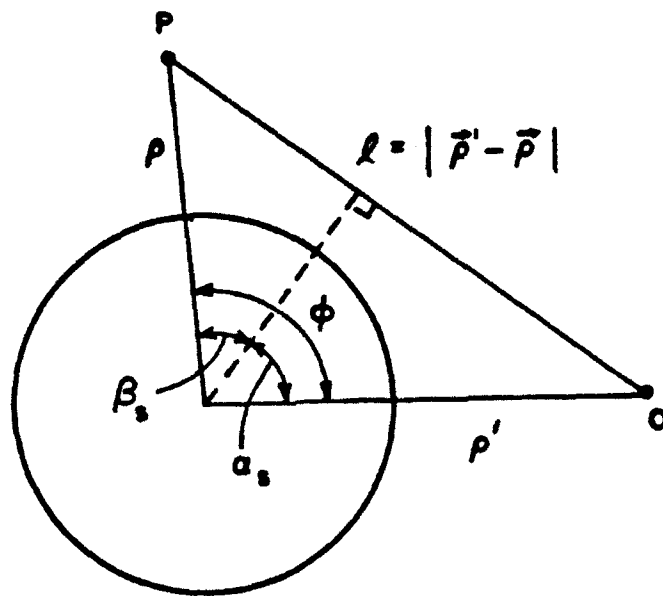


Figure 3.4: Physical meaning of the stationary point

where

$$\phi_{sb} = \cos^{-1} \left(\frac{b}{\rho'} \right) + \cos^{-1} \left(\frac{b}{\rho} \right) \quad (3.47)$$

For the region where ϕ satisfies the above condition, the asymptotic evaluation of the integral in Equation (3.42) can be obtained via the stationary phase method. The result is given by

$$I_1 \approx \frac{-j}{4} \sqrt{\frac{2}{\pi}} e^{j\frac{\pi}{4}} \frac{\exp[-j(k_0 \rho' \sin \alpha_s + k_0 \rho \sin \beta_s)]}{\sqrt{k_0 \rho' \sin \alpha_s + k_0 \rho \sin \beta_s}} \quad (3.48)$$

From the Figure 3.4, it can be seen that

$$l = |\rho' - \rho| = \rho' \sin \alpha_s + \rho \sin \beta_s \quad (3.49)$$

Therefore,

$$I_1 \approx \frac{e^{-j\frac{\pi}{4}}}{2\sqrt{2\pi}} \frac{e^{-jk_0 l}}{\sqrt{k_0 l}} \quad \text{for } \cos^{-1} \left(\frac{\rho}{\rho'} \right) \leq \phi < \phi_{sb} \quad (3.50)$$

Thus, it is shown that I_1 gives the same result as the evaluation of u_1^0 for $0 \leq \phi \leq \cos^{-1}(\rho/\rho')$.

3.2.3 Incident field

We conclude from the results we obtained so far that the incident field u^i consists of two terms. For $0 \leq \phi \leq \cos^{-1}(\rho/\rho')$, u^i comes from the asymptotic evaluation of u_0^1 given in Equation (3.33) and for $\cos^{-1}(\rho/\rho') \leq \phi < \phi_{sb}$, u^i comes from the evaluation of I_1 in Equation (3.48). Consequently, we obtain the incident field u_i for the lit region ($0 \leq \phi < \phi_{sb}$) as

$$u^i \approx \frac{e^{-j\frac{\pi}{4}}}{2\sqrt{2\pi}} \frac{e^{-jk_0 l}}{\sqrt{k_0 l}} \quad \text{for } 0 \leq \phi < \phi_{sb} \quad (3.51)$$

This result is valid for both the impedance and the coated cylinder. In fact, the direct incident from the source is independent of the boundary conditions of the scatterer. It should be emphasized again that these results are not valid when the field point is close to either the shadow boundary (S.B.) or the surface of the cylinder where the Debye approximations of the Hankel functions cannot be applied.

3.2.4 Evaluation of I_2

A similar procedure as used for the evaluation of I_1 can be applied to obtain the asymptotic solution for I_2 . First the Hankel functions in the integrand are replaced by their appropriate asymptotic approximations and then the stationary phase method is used to obtain the final result.

$$I_2 = \frac{-j}{8} \int_{-\infty-j\epsilon}^{k_0 b-j\epsilon} F_{s,h}(\nu) H_\nu^{(2)}(k_0 \rho') H_\nu^{(2)}(k_0 \rho) e^{-j\nu\phi} d\nu \quad (3.52)$$

$F_{s,h}(\nu)$ in Equation (3.5) can be rearranged as

$$F_{s,h}(\nu) = \left(\frac{H_\nu^{(1)}(k_0 b)}{H_\nu^{(2)}(k_0 b)} \right) \cdot \left(- \frac{H_\nu^{(1)'}(k_0 b)/H_\nu^{(1)}(k_0 b) - jC_{s,h}(\nu)}{H_\nu^{(2)'}(k_0 b)/H_\nu^{(2)}(k_0 b) - jC_{s,h}(\nu)} \right) \quad (3.53)$$

We define $S_{s,h}(\nu)$ as

$$S_{s,h}(\nu) \equiv - \frac{H_\nu^{(1)'}(k_0 b)/H_\nu^{(1)}(k_0 b) - jC_{s,h}(\nu)}{H_\nu^{(2)'}(k_0 b)/H_\nu^{(2)}(k_0 b) - jC_{s,h}(\nu)} \quad (3.54)$$

From the Debye approximations of the Hankel functions, it can be shown that for $-\infty < \nu < k_0 b$,

$$H_\nu^{(1)}(k_0 b) \approx \sqrt{\frac{2}{\pi k_0 b \sin \gamma}} \exp \left[j \left(k_0 b \sin \gamma - \gamma \nu - \frac{\pi}{4} \right) \right] \quad (3.55)$$

$$H_\nu^{(2)}(k_0b) \approx \sqrt{\frac{2}{\pi k_0b \sin \gamma}} \exp \left[-j \left(k_0b \sin \gamma - \gamma\nu - \frac{\pi}{4} \right) \right] \quad (3.56)$$

$$\frac{H_\nu^{(1)}(k_0b)}{H_\nu^{(2)}(k_0b)} \approx -j \exp[2j(k_0b \sin \gamma - \gamma\nu)] \quad (3.57)$$

$$\frac{H_\nu^{(1)'}(k_0b)}{H_\nu^{(1)}(k_0b)} \approx j \sin \gamma \quad (3.58)$$

and

$$\frac{H_\nu^{(2)'}(k_0b)}{H_\nu^{(2)}(k_0b)} \approx -j \sin \gamma \quad (3.59)$$

where $\gamma \equiv \cos^{-1}(\nu/k_0b)$.

Thus, $F_{s,h}(\nu)$ and $S_{s,h}(\nu)$ can be simplified as

$$F_{s,h}(\nu) \approx -j \exp[2j(k_0b \sin \gamma - \gamma\nu)] \cdot S_{s,h}(\nu) \quad (3.60)$$

where

$$S_{s,h}(\nu) \approx \frac{\sin \gamma - C_{s,h}(\nu)}{\sin \gamma + C_{s,h}(\nu)} \quad (3.61)$$

Substituting Equation (3.60) into Equation (3.52), we obtain

$$I_2 \approx \frac{-1}{8} \int_{-\infty-j\epsilon}^{k_0b-j\epsilon} S_{s,h}(\nu) H_\nu^{(2)}(k_0\rho') H_\nu^{(2)}(k_0\rho) \exp[2j(k_0b \sin \gamma - \gamma\nu) - j\nu\phi] d\nu \quad (3.62)$$

By using the Debye approximations for $H_\nu^{(2)}(k_0\rho')$ and $H_\nu^{(2)}(k_0\rho)$, I_2 can be expressed as

$$I_2 = \frac{-j}{4\pi k_o} \int_{-\infty-j\epsilon}^{k_o b-j\epsilon} \frac{S_{s,h}(\nu)}{\sqrt{\rho' \rho \sin \alpha \sin \beta}} \exp[jk_o \rho' \Phi(\nu)] d\nu \quad (3.63)$$

where

$$\Phi(\nu) \equiv -\sin \alpha - \frac{\rho}{\rho'} \sin \beta + \frac{2b}{\rho'} \sin \gamma + \frac{\nu}{k_o \rho} (\alpha + \beta - 2\gamma - \phi) \quad (3.64)$$

The derivatives of $\Phi(\nu)$ with respect to ν , are given as

$$\Phi'(\nu) = \frac{d\Phi(\nu)}{d\nu} = \frac{1}{k_o \rho'} (2\gamma - \alpha - \beta + \phi) \quad (3.65)$$

and

$$\Phi''(\nu) = \frac{d^2\Phi(\nu)}{d\nu^2} = \frac{1}{k_o \rho'} \left(\frac{2}{k_o b \sin \gamma} - \frac{1}{k_o \rho' \sin \alpha} - \frac{1}{k_o \rho \sin \beta} \right) \quad (3.66)$$

In order to obtain the derivatives, we used the relationship

$$\nu = k_o \rho' \cos \alpha = k_o \rho \cos \beta = k_o b \cos \gamma \quad (3.67)$$

therefore

$$\frac{d\alpha}{d\nu} = \frac{-1}{k_o \rho' \sin \alpha} \quad \frac{d\beta}{d\nu} = \frac{-1}{k_o \rho \sin \beta} \quad \frac{d\gamma}{d\nu} = \frac{-1}{k_o b \sin \gamma} \quad (3.68)$$

The stationary phase point ν_s is determined by the relationship given by

$$\alpha_s + \beta_s - 2\gamma_s = \phi \quad (3.69)$$

where $\alpha_s = \cos^{-1}(\nu_s/k_o \rho')$, $\beta_s = \cos^{-1}(\nu_s/k_o \rho)$ and $\gamma_s = \cos^{-1}(\nu_s/k_o b)$.

At the stationary point ν_s

$$\Phi(\nu_s) = \frac{2b}{\rho'} \sin \gamma_s - \sin \alpha_s - \frac{\rho}{\rho'} \sin \beta_s \quad (3.70)$$

and

$$\Phi''(\nu_s) = \frac{1}{k_0 \rho'} \left(\frac{2}{k_0 b \sin \gamma_s} - \frac{1}{k_0 \rho' \sin \alpha_s} - \frac{1}{k_0 \rho \sin \beta_s} \right) \quad (3.71)$$

The physical meaning of the stationary phase point is depicted in Figure 3.5. It should be noted that

$$0 \leq \text{Re}[\alpha_s] \leq \pi, \quad 0 \leq \text{Re}[\beta_s] \leq \pi, \quad 0 \leq \text{Re}[\gamma_s] \leq \pi \quad (3.72)$$

From the Figure 3.5, it can be seen that

$$\rho' \sin \alpha_s > b \sin \gamma_s$$

$$\rho \sin \beta_s > b \sin \gamma_s \quad (3.73)$$

Therefore

$$\Phi''(\nu_s) = \frac{\rho' \sin \alpha_s - b \sin \gamma_s}{k_0 \rho' b \sin \alpha_s \sin \gamma_s} + \frac{\rho \sin \beta_s - b \sin \gamma_s}{k_0 \rho b \sin \beta_s \sin \gamma_s} > 0 \quad (3.74)$$

The asymptotic evaluation of the integral using the stationary phase method leads to the result

$$I_2 \approx \frac{-j}{4} S_{s,h}(\nu_s) \sqrt{\frac{2}{\pi}} e^{j\frac{\pi}{4}} \exp[j(2k_0 b \sin \gamma_s - k_0 \rho \sin \beta_s - k_0 \rho' \sin \alpha_s)] \\ \times \sqrt{\frac{b \sin \gamma_s}{2k_0 \rho' \rho \sin \alpha_s \sin \beta_s - k_0 \rho b \sin \beta_s \sin \gamma_s - k_0 \rho' b \sin \alpha_s \sin \gamma_s}} \quad (3.75)$$

After the rearrangement of the above equation, we obtain

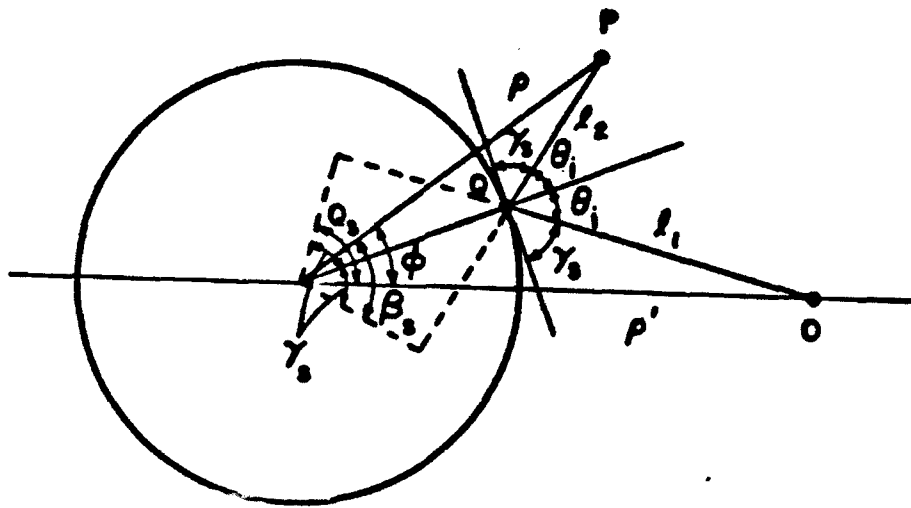


Figure 3.5: Physical meaning of the stationary point

$$I_2 \approx \frac{-j}{4} S_{s,h}(\nu_s) \sqrt{\frac{2}{\pi}} e^{j\frac{\pi}{4}} \frac{\exp[-j(k_0 \rho' \sin \alpha_s - k_0 b \sin \gamma_s)]}{\sqrt{k_0 \rho' \sin \alpha_s - k_0 b \sin \gamma_s}} \times$$

$$\sqrt{\frac{b \sin \gamma_s (\rho' \sin \alpha_s - b \sin \gamma_s)}{2(\rho' \sin \alpha_s - b \sin \gamma_s)(\rho \sin \beta_s - b \sin \gamma_s) + b \sin \gamma_s (\rho' \sin \alpha_s + \rho \sin \beta_s - 2b \sin \gamma_s)}} \times \exp[-j(k_0 \rho \sin \beta_s - k_0 b \sin \gamma_s)] \quad (3.76)$$

From the Figure 3.5, we observe that

$$l_1 = \rho' \sin \alpha_s - b \sin \gamma_s \quad (3.77)$$

and

$$l_2 = \rho \sin \beta_s - b \sin \gamma_s \quad (3.78)$$

Thus, I_2 can be expressed as

$$I_2 \approx \frac{e^{-j\frac{\pi}{4}}}{2\sqrt{2\pi}} \frac{e^{-jk_0 l_1}}{\sqrt{k_0 l_1}} \cdot S_{s,h}(\nu_s) \sqrt{\frac{l_2 b \sin \gamma_s}{2l_1 l_2 + (l_1 + l_2) b \sin \gamma_s}} e^{-jk_0 l_2} \quad (3.79)$$

3.2.5 Reflected Field

The result of the asymptotic evaluation of I_2 as given in Equation (3.79) represents the field reflected on the surface of the cylinder. From the result obtained in the previous section, it is clear that

$$\frac{e^{-j\frac{\pi}{4}}}{2\sqrt{2\pi}} \frac{e^{-jk_0 l_1}}{\sqrt{k_0 l_1}} = u^i(Q) \quad (3.80)$$

where $u^i(Q)$ represents the incident field at the specular reflection point Q as shown in Figure 3.6. From the comparison of this result with the ray format of the perfectly conducting cylinder it is apparent that $S_{s,h}(\nu_s)$ represents the reflection coefficient $R_{s,h}$.

Thus Equation (3.79) can be rewritten as

$$u^r = \frac{e^{-j\frac{\pi}{4}}}{2\sqrt{2\pi}} \frac{e^{-jk_0 l_1}}{\sqrt{k_0 l_1}} \cdot R_{s,h}(\nu_s) \sqrt{\frac{l_1 b \cos \theta_i}{2l_1 l_2 + (l_1 + l_2)b \cos \theta_i}} e^{-jk_0 l_2} \quad (3.81)$$

We define S_p as

$$S_p \equiv \sqrt{\frac{l_1 b \cos \theta_i}{2l_1 l_2 + (l_1 + l_2)b \cos \theta_i}} \quad (3.82)$$

It can be easily identified that S_p is the usual spreading factor associated with the reflection field from a curved surface, which is given as

$$S_p = \sqrt{\frac{\bar{\rho}^r}{\bar{\rho}^r + l_2}} \quad (3.83)$$

where the reflected ray caustic distance $\bar{\rho}^r$ can be calculated from the relationship,

$$\frac{1}{\bar{\rho}^r} = \frac{1}{l_1} + \frac{2}{b \cos \theta_i} \quad (3.84)$$

The spreading factor S_p accounts for the spreading of electromagnetic energy after the reflection occurs.

Thus, the ray format for the reflected field can be expressed as

$$u^r = u^i(Q) \cdot R_{s,h} \cdot S_p e^{-jk_o l_2} \quad (3.85)$$

It is interesting to observe that the ray format for the reflected field associated with the impedance or the coated cylinder remains the same as that associated with the perfectly conducting cylinder.

Reflection coefficient $R_{s,h}$

Since the reflected ray should satisfy Snell's law of reflection, the incident angle θ_i must be equal to the reflection angle θ_r at the point Q in the Figure 3.6. From the physical meaning of the stationary point γ_s , it is noted that $\gamma_s = \frac{\pi}{2} - \theta_i$ (i.e. $\sin \gamma_s = \cos \theta_i$). Thus, the reflection coefficient for the impedance cylinder is

$$R_{s,h} = S_{s,h}(\nu_s) \approx \frac{\cos \theta_i - C_{s,h}}{\cos \theta_i + C_{s,h}} \quad (3.86)$$

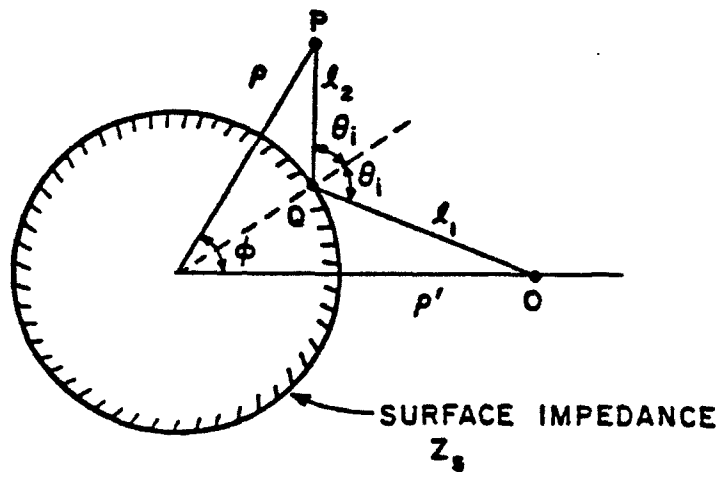
Substituting the Equations (3.6) and (3.7) into Equation (3.86), the reflection coefficients for the impedance cylinder are given as

$$R_s \approx - \frac{Z_o - Z_s \cos \theta_i}{Z_o + Z_s \cos \theta_i} \quad \text{for } TM_z \quad (3.87)$$

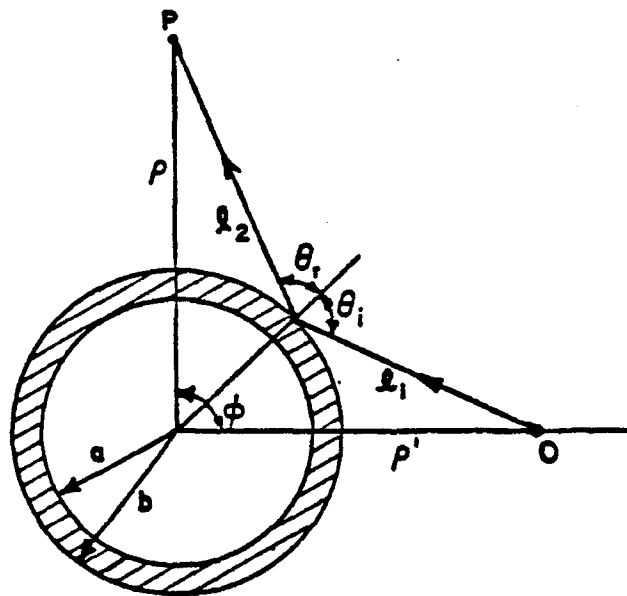
and

$$R_h \approx \frac{Z_o - Z_s / \cos \theta_i}{Z_o + Z_s / \cos \theta_i} \quad \text{for } TE_z \quad (3.88)$$

Note that the reflection coefficients of the impedance cylinder are the same as the well-known reflection coefficients for a plane wave incidence on a infinite ground



(a) Impedance Cylinder



(b) Coated Cylinder

Figure 3.6: Reflection field

plane with surface impedance Z_s .

As given in the Appendix B, the reflection coefficients for the coated cylinder can be obtained by the asymptotic approximation for $S_{s,h}(\nu_s)$ using the Debye approximations of the Hankel functions. The results are summarized as follows

$$R_s = - \frac{Z_o - jZ_1 \cos \theta_i / \cos \theta_t \tan\{\Psi(a, b, k_1)\}}{Z_o + jZ_1 \cos \theta_i / \cos \theta_t \tan\{\Psi(a, b, k_1)\}} \quad \text{for } TM \quad (3.89)$$

and

$$R_h = \frac{Z_o - jZ_1 \cos \theta_t / \cos \theta_i \tan\{\Psi(a, b, k_1)\}}{Z_o + jZ_1 \cos \theta_t / \cos \theta_i \tan\{\Psi(a, b, k_1)\}} \quad \text{for } TE \quad (3.90)$$

where Z_1 represents the characteristic impedance of the coating material (i.e. $Z_1 = \sqrt{\frac{\mu_1}{\epsilon_1}}$) and θ_i and θ_t are the incident and the transmission angle of the wave at the air/coating interface. $\Psi(a, b, k_1)$ is defined as

$$\Psi(a, b, k_1) \equiv k_1(b \sin \beta_b - a \sin \beta_a) - k_o b(\beta_b - \beta_a) \sin \theta_i \quad (3.91)$$

where

$$\sin \beta_b \equiv \cos \theta_t = \sqrt{1 - \left(\frac{k_o}{k_1} \sin \theta_i\right)^2} \quad (3.92)$$

and

$$\sin \beta_a = \sqrt{1 - \left(\frac{b}{a} \sin \theta_t\right)^2} = \sqrt{1 - \left(\frac{k_1 b}{k_o a} \sin \theta_i\right)^2} \quad (3.93)$$

Comparing the reflection coefficients for the coated cylinder with those for the impedance cylinder it can be observed that the equivalent impedance of the coated cylinder associated with the reflected field is

$$Z_s^{eq}(\phi) = jZ_1 \cdot \frac{\tan\{\Psi(a, b, k_1)\}}{\cos \theta_t} \quad \text{for } TM_z \quad (3.94)$$

and

$$Z_s^{eq}(\phi) = jZ_1 \cos \theta_t \tan\{\Psi(a, b, k_1)\} \quad \text{for } TE_z \quad (3.95)$$

This result shows that the equivalent impedance is not only dependent on the polarization of the incident field but also on the incident angle at the reflection point. Therefore, it is apparent that the constant surface impedance cylinder can not be appropriately used for the equivalent model of the coated cylinder. However, it will be shown later in this Chapter that the equivalent impedance in association with the diffracted field is constant along the cylinder surface. For the thin coating, it can be seen that $\beta_a \approx \beta_b$ and therefore $\Psi(a, b, k_1)$ can be approximated as

$$\Psi(a, b, k_1) \approx k_1(b - a) \sin \beta_a = k_1 d \cos \theta_t \quad (3.96)$$

Thus, for a thin coating, R_s and R_h can be approximated as

$$R_s = - \frac{Z_o - jZ_1 \cos \theta_i / \cos \theta_t \tan(k_1 d \cos \theta_t)}{Z_o + jZ_1 \cos \theta_i / \cos \theta_t \tan(k_1 d \cos \theta_t)} \quad \text{for } TM \quad (3.97)$$

and

$$R_h = \frac{Z_o - jZ_1 \cos \theta_i / \cos \theta_t \tan(k_1 d \cos \theta_t)}{Z_o + jZ_1 \cos \theta_i / \cos \theta_t \tan(k_1 d \cos \theta_t)} \quad \text{for } TE \quad (3.98)$$

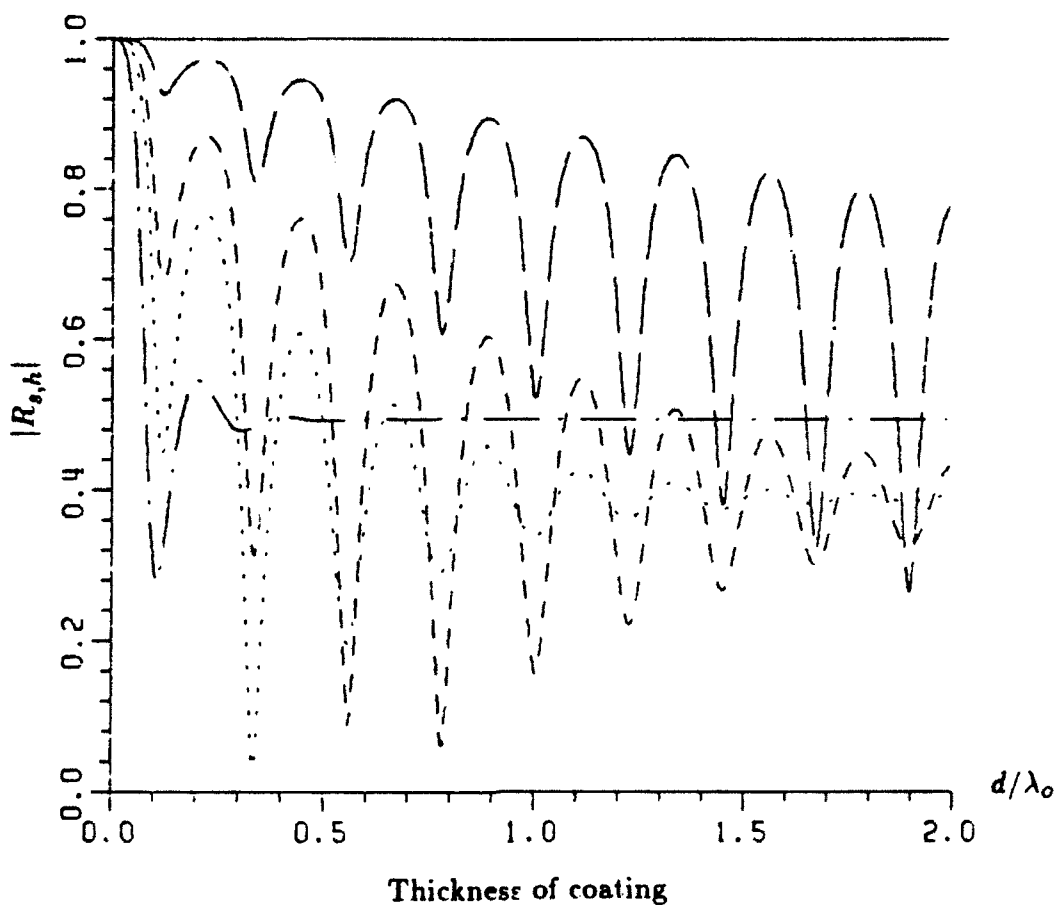
and

$$Z_s^{eq}(\phi) = jZ_1 \cdot \frac{\tan(k_1 d \cos \theta_t)}{\cos \theta_t} \quad \text{for } TM_z \quad (3.99)$$

$$Z_s^{eq}(\phi) = jZ_1 \cos \theta_i \tan(k_1 d \cos \theta_i) \quad \text{for } TE_z \quad (3.100)$$

It can be noticed from Equation (3.97), (3.98), (3.99) and (3.100) that the reflection coefficients and the equivalent surface impedances of the coated cylinder coincide with those of the grounded planar dielectric/ferrite slab with plane-wave incidence [7]. This result is consistent with the postulate of the GTD solution that the reflection is a local phenomenon at high frequency.

It is well-known that the reflection coefficients for the conducting surface are fixed to ± 1 regardless of the incident angle θ_i at the reflection point Q_r . However for the impedance cylinder, the reflection coefficients are dependent on the incident angle θ_i and the surface impedance Z_s . For the coated cylinder, the reflection coefficients are dependent on the incident angle θ_i as well as on ϵ_r , μ_r and thickness d of the material coating. Figure 3.7 and 3.8 illustrate the change of $R_{s,h}$ of the coated cylinder as ϵ_r , μ_r and d changes for the normal incidence (i.e. $\theta_i = 0$). For the lossless material coating where both ϵ_r and μ_r have real values, it can be easily seen that the phase of $R_{s,h}$ changes as d changes but $|R_{s,h}| = 1$ regardless of coating thickness. Physically, the phase of $R_{s,h}$ accounts for the lagging of the reflected field. If there exists a loss factor in ϵ_r or μ_r of the coating material, $|R_{s,h}|$ can be smaller than 1. Consequently, the magnitude and the phase of the reflected field can be controlled by proper choice of the relevant parameters (i.e. ϵ_r , μ_r , and coating thickness d).



$$\mu_r = 1.$$

$$\epsilon_r = 5. - j0$$

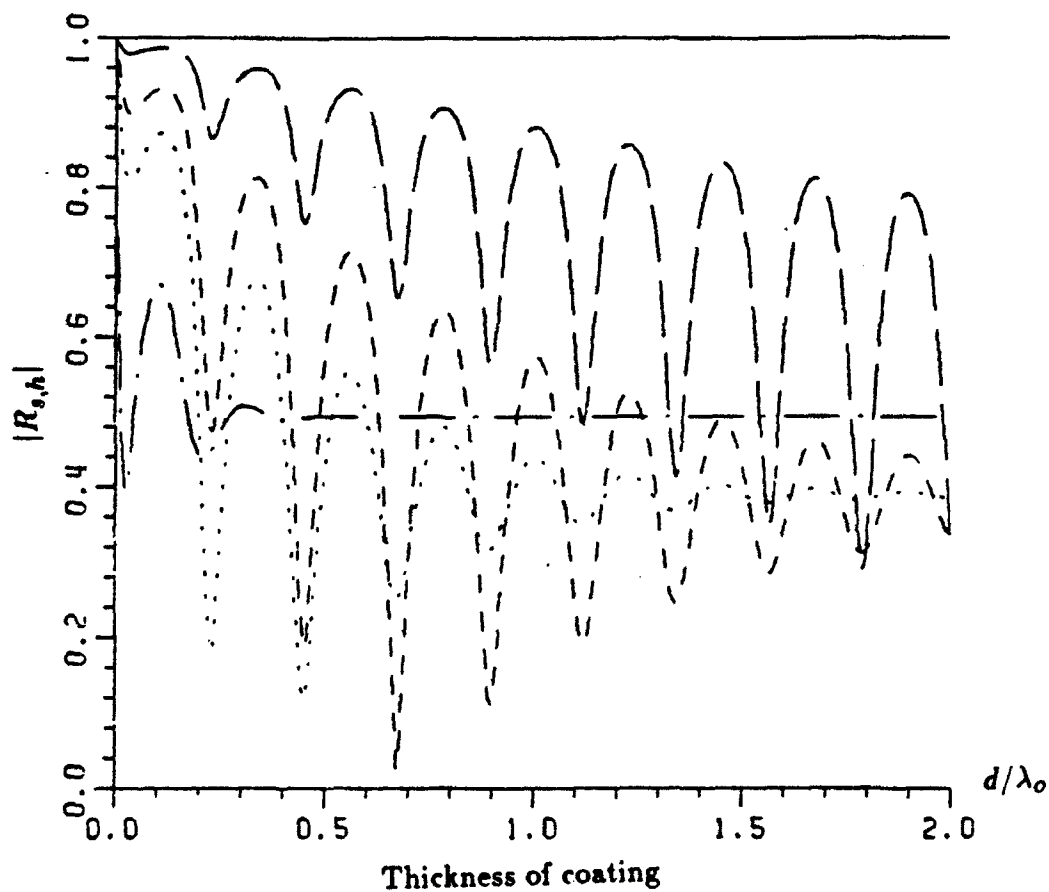
$$\epsilon_r = 5. - j0.1$$

$$\epsilon_r = 5. - j0.5$$

$$\epsilon_r = 5. - j1.$$

$$\epsilon_r = 5. - j5.$$

Figure 3.7: Reflection Coefficient



$\epsilon_r = 1.$

$\mu_r = 5. - j0$ —————

$\mu_r = 5. - j0.1$ - - - - -

$\mu_r = 5. - j0.5$ - - - - -

$\mu_r = 5. - j1.$

$\mu_r = 5. - j5.$ - . - . - .

Figure 3.8: Reflection Coefficient

3.3 Field in the deep shadow region

In this section a ray format for the field in the shadow region is obtained for both the impedance and the coated cylinder. As discussed in the previous section, the behavior of the geometric-optical field (i.e. incident field and reflected field) for the impedance and the coated cylinder are almost the same as for the perfectly conducting cylinder except for the difference in the reflection coefficients. Manifest effects of the surface impedance and the coating of the dielectric/ferrite materials can be observed in the diffracted field in the shadow region.

The diffracted field is entirely associated with the creeping wave on the curved surface of the cylinder. The creeping wave which propagates azimuthally on the cylinder surface carries the electromagnetic energy into the shadow region. A detailed discussion of the characteristics of creeping wave will be given in the next Chapter.

3.3.1 Residue series solution

The diffracted field can be obtained by a residue series solution for the integral representation of the field given in Equation (3.14). As discussed in Appendix A, the residue series representation of the field is the result of a Watson transformation of the field given in eigenfunction series form. As illustrated in Figure 3.9, the integral path of the Equation (3.14) is deformed such that the contour C_z encloses the lower half of complex ν -plane with a large semicircle. It can be shown that the contribution from the arc of the large semicircle vanishes as its radius approaches infinity. Thus, one obtains

$$u^o = \frac{-j}{8} \oint_{C_z} H_\nu^{(2)}(k_o\rho_>) \left[H_\nu^{(1)}(k_o\rho_<) + F_{s,h}(\nu) H_\nu^{(2)}(k_o\rho_<) \right] e^{-j\nu\phi} d\nu \quad (3.101)$$

The integral in Equation (3.101) is now evaluated using the residue theorem. Before we use the residue theorem, the poles of the integrand must be found. The poles of the integrand come only from the poles of $F_{s,h}(\nu)$. From the Equation (3.5), the poles of $F_{s,h}(\nu)$ are obtained by finding the roots of

$$H_{\nu_n}^{(2)'}(k_{ob}) - jC_{s,h}(\nu_n)H_{\nu_n}^{(2)}(k_{ob}) = 0 \quad (3.102)$$

Equation (3.102) is referred to as *transcendental* equation. A detailed discussion of the roots of the transcendental equation is given in Chapter IV. The residue series solution subject to Equation (3.102) is

$$u^o = \frac{\pi}{4} \sum_{n=1}^{\infty} H_{\nu_n}^{(2)}(k_{o\rho'}) H_{\nu_n}^{(2)}(k_{o\rho}) \frac{H_{\nu_n}^{(1)'}(k_{ob}) - jC_{s,h}(\nu_n)H_{\nu_n}^{(1)}(k_{ob})}{\frac{\partial}{\partial \nu} [H_{\nu}^{(2)'}(k_{ob}) - jC_{s,h}(\nu)H_{\nu}^{(2)}(k_{ob})]_{\nu=\nu_n}} e^{-j\nu_n \phi} \quad (3.103)$$

This equation can be further simplified by using the Wronskian of the Hankel functions. From the relationship of the Wronskian,

$$W [H_{\nu_n}^{(1)}(k_{ob}), H_{\nu_n}^{(2)}(k_{ob})] = H_{\nu_n}^{(1)}(k_{ob})H_{\nu_n}^{(2)'}(k_{ob}) - H_{\nu_n}^{(1)'}(k_{ob})H_{\nu_n}^{(2)}(k_{ob}) = \frac{-4j}{\pi k_{ob}} \quad (3.104)$$

From Equations (3.102) and (3.104), it can be easily verified that

$$H_{\nu_n}^{(1)'}(k_{ob}) - jC_{s,h}(\nu_n)H_{\nu_n}^{(1)}(k_{ob}) = \frac{4j}{\pi k_{ob} H_{\nu_n}^{(2)}(k_{ob})} \quad (3.105)$$

Hence Equation (3.103) can be rewritten as

$$u^o = \frac{j}{k_{ob}} \sum_{n=1}^{\infty} \frac{H_{\nu_n}^{(2)}(k_{o\rho'}) H_{\nu_n}^{(2)}(k_{o\rho})}{H_{\nu_n}^{(2)}(k_{ob}) \frac{\partial}{\partial \nu} [H_{\nu}^{(2)'}(k_{ob}) - jC_{s,h}(\nu)H_{\nu}^{(2)}(k_{ob})]_{\nu=\nu_n}} e^{-j\nu_n \phi} \quad (3.106)$$

Due to the attenuation of the creeping wave, the residue series solution is fast convergent in the deep shadow region. The symbol "∞" is used to emphasize that only a few dominant modes are enough to obtain the accurate result. It is found that, for most applications, the dominant n_{th} mode in Equation (3.106) is adequate for the calculation of the field in the deep shadow region. It should be noted that the dominant n_{th} mode is not necessarily the first mode as for the conducting cylinder. A detailed discussion on the dominance of the residue series mode for the impedance and the coated cylinder will be given in Chapter IV.

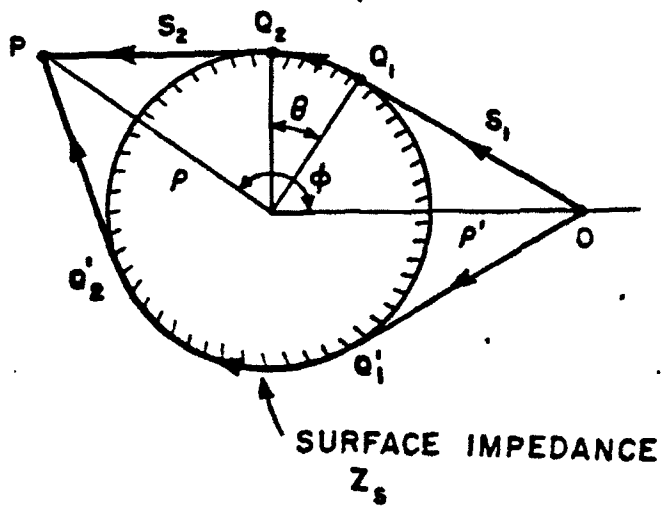
As the field point approaches the shadow boundary transition region, the residue series solution becomes slowly convergent. This is because the arc length of the creeping wave propagation is short in the transition region and therefore even the modes with high attenuation can no longer be ignored.

The multiply encircling wave u^{cw} can also be obtained from the residue series solution for the integral representation given in Equation (3.15). Thus,

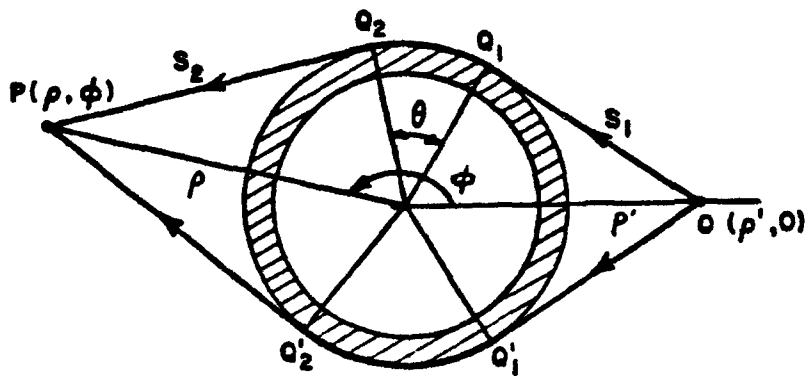
$$u^{cw} = \frac{j}{k_{ob}} \sum_{n=1}^{\infty} \frac{H_{\nu_n}^{(2)}(k_{o\rho'}) H_{\nu_n}^{(2)}(k_{o\rho})}{H_{\nu_n}^{(2)}(k_{ob}) \frac{\partial}{\partial \nu} \left[H_{\nu}^{(2)'}(k_{ob}) - jC_{s,h}(\nu) H_{\nu}^{(2)}(k_{ob}) \right]_{\nu=\nu_n}} \times \frac{e^{-j\nu_n(2\pi+\phi)} + e^{-j\nu_n(2\pi-\phi)}}{1 - e^{-j2\nu_n\pi}} \quad (3.107)$$

3.3.2 Diffracted field

Physically, the residue series representation of u^o as given in Equation (3.106) can be interpreted as the diffracted field which explains the transmission of the wave into the shadow region. However, the ray-picture interpretation can not be obtained from the rigorous residue series solutions given in Equation (3.106). The Keller type GTD ray format which gives the residue series solution a creeping-wave



(a) Impedance Cylinder



(b) Coated Cylinder

Figure 3.10: Field in the shadow region

diffraction interpretation as illustrated in Figure 3.10 can be obtained by following procedures. From the Debye approximation of the Hankel functions are

$$H_{\nu_n}^{(2)}(k_o \rho') \approx \sqrt{\frac{2}{\pi k_o \rho' \sin \alpha_n}} \exp \left[-j \left(k_o \rho' \sin \alpha_n - \alpha_n \nu_n - \frac{\pi}{4} \right) \right] \quad (3.108)$$

and

$$H_{\nu_n}^{(2)}(k_o \rho) \approx \sqrt{\frac{2}{\pi k_o \rho \sin \beta_n}} \exp \left[-j \left(k_o \rho \sin \beta_n - \beta_n \nu_n - \frac{\pi}{4} \right) \right] \quad (3.109)$$

where

$$\alpha_n \equiv \cos^{-1} \left(\frac{\nu_n}{k_o \rho'} \right) \quad (3.110)$$

and

$$\beta_n \equiv \cos^{-1} \left(\frac{\nu_n}{k_o \rho} \right) \quad (3.111)$$

Here, we make assumptions that α_n and β_n can be approximated by

$$\alpha_n = \cos^{-1} \left(\frac{\nu_n}{k_o \rho'} \right) \approx \cos^{-1} \left(\frac{b}{\rho'} \right) \quad (3.112)$$

and

$$\beta_n = \cos^{-1} \left(\frac{\nu_n}{k_o \rho} \right) \approx \cos^{-1} \left(\frac{b}{\rho} \right) \quad (3.113)$$

Based on the assumptions given in Equations (3.112) and (3.113)

$$k_o \rho' \sin \alpha_n = \sqrt{(k_o \rho')^2 - \nu_n^2} \approx k_o \sqrt{\rho'^2 - b^2} = k_o s_1 \quad (3.114)$$

and

$$k_o \rho \sin \beta_n = \sqrt{(k_o \rho)^2 - \nu_n^2} \approx k_o \sqrt{\rho^2 - b^2} = k_o s_2 \quad (3.115)$$

As shown in Figure 3.10, s_1 and s_2 are the distance from the source to the tangential point Q_1 and the distance from the tangential point Q_2 to the field point respectively. Therefore,

$$H_{\nu_n}^{(2)}(k_o \rho') \approx \sqrt{\frac{2}{\pi k_o s_1}} \exp \left\{ -j \left[k_o s_1 - \nu_n \cos^{-1} \left(\frac{b}{\rho'} \right) - \frac{\pi}{4} \right] \right\} \quad (3.116)$$

and

$$H_{\nu_n}^{(2)}(k_o \rho) \approx \sqrt{\frac{2}{\pi k_o s_2}} \exp \left\{ -j \left[k_o s_2 - \nu_n \cos^{-1} \left(\frac{b}{\rho} \right) - \frac{\pi}{4} \right] \right\} \quad (3.117)$$

Substituting Equations (3.116) and (3.117) into Equation (3.106), u^d can be expressed as

$$u^d \approx \frac{-2j}{\pi} \cdot \frac{1}{k_o b} \cdot \frac{e^{-jk_o s_1}}{\sqrt{k_o s_1}} \cdot \frac{e^{-jk_o s_2}}{\sqrt{k_o s_2}} \cdot e^{-j\frac{\pi}{2}} \times \sum_{n=1}^{\infty} \frac{e^{-j\nu_n \theta}}{H_{\nu_n}^{(2)}(k_o b) \frac{\partial}{\partial \nu} \left[H_{\nu}^{(2)'}(k_o b) - j C_{s,h}(\nu) H_{\nu}^{(2)}(k_o b) \right]_{\nu=\nu_n}} \quad (3.118)$$

As shown in Figure 3.10, θ is defined as

$$\theta \equiv \phi - \cos^{-1} \left(\frac{b}{\rho'} \right) - \cos^{-1} \left(\frac{b}{\rho} \right) \quad (3.119)$$

Rearrangement of Equation (3.118) leads to Keller's surface diffracted ray format for 2-dimensional case.

$$u^d \approx u^i(Q_1) \cdot \sum_{n=1}^{\infty} \left\{ \mathcal{D}_n^{s,h}(Q_1) \cdot e^{-j\nu_n \theta} \cdot \mathcal{D}_n^{s,h}(Q_2) \right\} \frac{e^{-jk_o s_2}}{\sqrt{k_o s_2}} \quad (3.120)$$

Thus

$$u^d \approx u^i(Q_1) \cdot \sum_{n=1}^{\infty} \left\{ \mathcal{D}_n^{s,h}(Q_1) \cdot \exp[-(\alpha'_n + j\beta'_n)t] \cdot \mathcal{D}_n^{s,h}(Q_2) \right\} \frac{e^{-jk_0s_2}}{\sqrt{k_0s_2}} \quad (3.121)$$

where α'_n and β'_n represent the attenuation constant and the propagation constant of the creeping wave respectively. It can be easily shown that

$$\alpha'_n = -Im \left[\frac{\nu_n}{b} \right] \quad (3.122)$$

$$\beta'_n = Re \left[\frac{\nu_n}{b} \right] \quad (3.123)$$

$\mathcal{D}_n^{s,h}(Q)$ is referred to as the surface diffraction coefficients. For the circular cylinder, $\mathcal{D}_n^{s,h}(Q_1)$ is equal to $\mathcal{D}_n^{s,h}(Q_2)$. From a comparison of Equation (3.118) and Equation (3.120), the diffraction coefficient $\mathcal{D}_n^{s,h}(Q)$ can be expressed as

$$\mathcal{D}_n^{s,h}(Q) = \left[\sqrt{\frac{2}{\pi}} \cdot \frac{4}{k_0b} \cdot \frac{e^{-j\frac{3\pi}{4}}}{H_{\nu_n}^{(2)}(k_0b) \frac{\partial}{\partial \nu} \left[H_{\nu}^{(2)'}(k_0b) - jC_{s,h}(\nu)H_{\nu}^{(2)}(k_0b) \right]_{\nu=\nu_n}} \right]^{\frac{1}{2}} \quad (3.124)$$

Now it is clear, from the Equation (3.120), that the residue series solution can be interpreted as a creeping-wave diffraction as illustrated in the Figure 3.10. It should be noted that the ray path associated with the perfectly conducting cylinder remains unchanged for both the impedance and the coated cylinder. As shown in Figure 3.10, the incident rays which strike the cylinder at the tangential points(Q_1 and Q_2) with grazing angle launch creeping waves which travel along the arc of geodesic path on the cylinder surface following *Fermat's principle*. As

these creeping waves propagate, they decrease exponentially and continuously shed diffracted rays.

However, in using the ray solution given in Equation (3.120), one has to be aware of the approximations given by the Equation (3.112) and (3.113). For the conducting cylinder, the dominant pole is determined such that $\nu_n \approx k_0 b$. Therefore, the above assumption is always reasonable if the source or the field point is not very close to cylinder surface, where GTD ray solution fails. However, for the impedance or the coated cylinder, the dominant poles are not always close to $k_0 b$. Therefore, the approximation given in Equation (3.112) and (3.113) are valid only when both ρ' and ρ are large compared with the radius of the cylinder (i.e. $\rho' \gg b$ and $\rho \gg b$). Unless both ρ' and ρ are large, a non-ray format as given in Equations (3.106) should be used. This imposes an additional restriction on the validity of the GTD ray solution of the impedance and the coated cylinder.

For the perfectly conducting cylinder, the expression for $\mathcal{D}_n^{s,h}(Q)$ can be further simplified by using the approximation of the Hankel function in terms of the Miller type Airy function. However, for the impedance and the coated cylinder where the dominant ν_n is not necessarily close to $k_0 b$, Airy functions can not properly approximate the Hankel functions involved in the expression of $\mathcal{D}_n^{s,h}(Q)$.

Ray format for the multiply encircling wave u^{cw} can also be obtained by taking the same procedure as for the u^o . It is interesting to note that

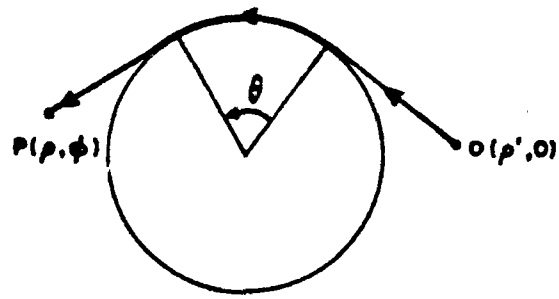
$$\frac{e^{-j\nu_n(2\pi+\phi)} + e^{-j\nu_n(2\pi-\phi)}}{1 - e^{-j2\nu_n\pi}} = \sum_{p=1}^{\infty} e^{-j\nu_n(2\pi p+\phi)} + \sum_{p=-1}^{-\infty} e^{j\nu_n(2\pi p+\phi)} \quad (3.125)$$

Thus,

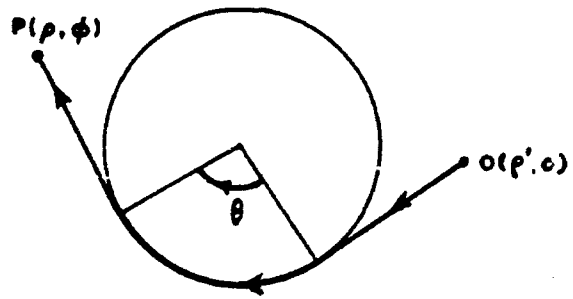
$$u^{cw} \approx u^i(Q_1) \cdot \sum_{p=1}^{\infty} \sum_{n=1}^{\infty} \left\{ \mathcal{D}_n^{s,h}(Q_1) \cdot e^{-j\nu_n(2\pi p+\theta)} \cdot \mathcal{D}_n^{s,h}(Q_2) \right\} \frac{e^{-jk_0 s_2}}{\sqrt{k_0 s_2}}$$

$$+ u^i(Q_1) \cdot \sum_{p=-1}^{-\infty} \sum_{n=1}^{\infty} \{ \mathcal{D}_n^{s,h}(Q_1) \cdot e^{-j\nu_n(2\pi p + \theta)} \cdot \mathcal{D}_n^{s,h}(Q_2) \} \frac{e^{-jk_0 s_2}}{\sqrt{k_0 s_2}} \quad (3.126)$$

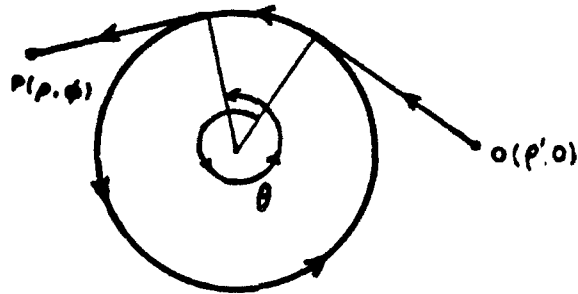
Thus u^{cw} consists of two terms. The first term represents multiple encirclements in the counterclockwise sense, and the other term represents those in the opposite direction. As illustrated in Figure 3.11-(a), u^o in Equation (3.106) represents the diffraction field which travels the shortest arc length on the cylinder surface in a counterclockwise direction (i.e. $p = 0$). Recall that ϕ is assumed to be positive and less than π .



(a) $p = 0$



(b) $p = -1$



(c) $p = 1$

Figure 3.11: Ray encirclements associated with the summation index p

3.3.3 Equivalent impedance associated with the creeping wave of the coated cylinder

In this section the equivalent impedance associated with the creeping wave of the coated cylinder will be obtained.

It is noted C_s and C_h for the impedance cylinder are given as

$$C_s = \frac{Z_o}{Z_s} \quad \text{for TM} \quad ; \quad C_h = \frac{Z_s}{Z_o} \quad \text{for TE} \quad (3.127)$$

Equivalently, $C_s(\nu_n)$ and $C_h(\nu_n)$ for the coated cylinder may be expressed as

$$C_s(\nu_n) = \frac{Z_o}{Z_s^{eq}(\nu_n)} \quad \text{for TM} \quad ; \quad C_h(\nu_n) = \frac{Z_s^{eq}(\nu_n)}{Z_o} \quad \text{for TE} \quad (3.128)$$

where $Z_s^{eq}(\nu_n)$ represents the equivalent modal surface impedance associated with the diffraction field of the coated cylinder. From Equations (3.128) with (3.8) and (3.9) we obtain

$$Z_s^{eq}(\nu_n) = jZ_1 \cdot \frac{H_{\nu_n}^{(1)}(k_1 b)H_{\nu_n}^{(2)}(k_1 a) - H_{\nu_n}^{(2)}(k_1 b)H_{\nu_n}^{(1)}(k_1 a)}{H_{\nu_n}^{(1)'}(k_1 b)H_{\nu_n}^{(2)'}(k_1 a) - H_{\nu_n}^{(2)'}(k_1 b)H_{\nu_n}^{(1)'}(k_1 a)} \quad \text{for } TM_z \quad (3.129)$$

and

$$Z_s^{eq}(\nu_n) = -jZ_1 \cdot \frac{H_{\nu_n}^{(1)'}(k_1 b)H_{\nu_n}^{(2)'}(k_1 a) - H_{\nu_n}^{(2)'}(k_1 b)H_{\nu_n}^{(1)'}(k_1 a)}{H_{\nu_n}^{(1)}(k_1 b)H_{\nu_n}^{(2)}(k_1 a) - H_{\nu_n}^{(2)}(k_1 b)H_{\nu_n}^{(1)}(k_1 a)} \quad \text{for } TE_z \quad (3.130)$$

As mentioned in the previous section, the equivalent impedance associated with the reflected field of the coated cylinder is dependent on ϕ . However, these equivalent modal impedances associated with the diffracted field as given by Equation (3.129) and (3.130) are constant along the cylinder surface.

3.4 Numerical results and discussion

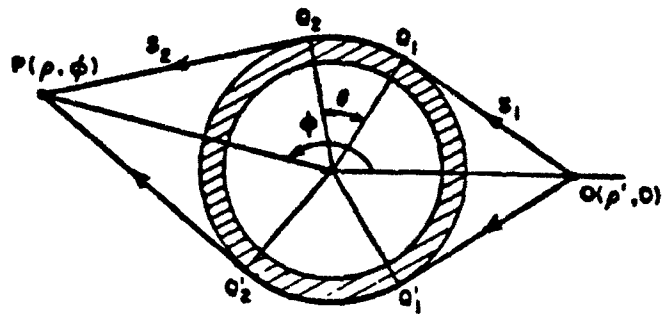
3.4.1 Numerical results

In this section, the GTD solution derived in this Chapter is employed to calculate the electromagnetic field scattered from the impedance and the coated cylinder. The geometry of the problem is illustrated in Figure 1.1. The two-dimensional line source is located at $O(\rho', \phi' = 0)$, and the receiver is located at $P(\rho, \phi)$. Plane wave incidence is the case when $\rho' = \infty$. For the electric line source excitation (TM_z case), the pattern is plotted for the total electric field intensity E_z , and for the magnetic line source excitation (TE_z case), the pattern is shown for the total magnetic field intensity H_z . When the field point is in the shadow region as shown in Figure 3.12-(a), the asymptotic solutions employ two ray paths, one is $\overline{OQ_1Q_2P}$ and the other is $\overline{OQ'_1Q'_2P}$. For the field point P located in the lit region as shown in Figure 3.12-(b), the ray path $\overline{OQ_1Q_2P}$ is replaced by the path $\overline{OQ_RP}$, where Q_R is the specular reflection point defined by $\theta_i = \theta_r$.

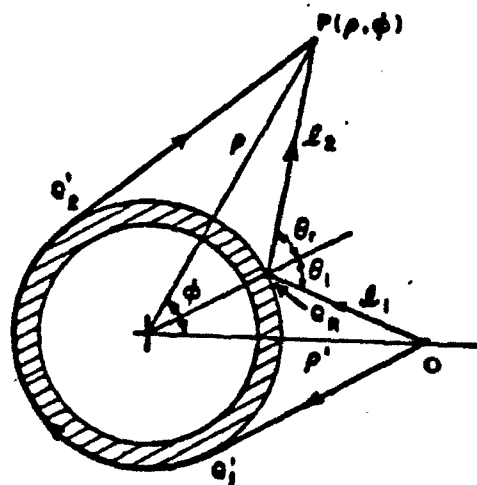
Typical results for the field patterns due to a line source radiating in the presence of a impedance cylinder are shown in Figure 3.13 ~ 3.16. For the cylinders with lossless dielectric coatings, the numerical results are shown in Figure 3.17 ~ 3.26. The field patterns due to a plane-wave incidence on the cylinder with lossy dielectric coatings and the lossy composite coating are shown in Figure 3.27 ~ 3.36. The results in each case are compared with eigenfunction series solutions. The surface impedances of the impedance cylinders were chosen such that $q = \pm 1$ where q is defined as

$$q \equiv -jmC_{s,h} \quad \text{where} \quad m \equiv \left(\frac{k_0 b}{2}\right)^{\frac{1}{2}} \quad (3.131)$$

i.e.



(a) Shadow region



(b) Lit region

Figure 3.12: Ray paths employed for the GTD solution

$$q = -jm \frac{Z_o}{Z_s} \quad \text{for } TM_z \quad (3.132)$$

$$q = -jm \frac{Z_s}{Z_o} \quad \text{for } TE_z \quad (3.133)$$

Thus the surface impedances chosen in the examples are pure imaginary (Positive q represents capacitive impedance for TM_z and inductive impedance for TE_z and negative q represents inductive impedance for TM_z and capacitive impedance for TE_z .)

3.4.2 Discussion

The numerical results of GTD solution as illustrated in Figure 3.13 ~ 3.36 show excellent agreement with the eigenfunction results in the deep lit region and in the deep shadow region. However, as expected, the GTD solution fails within the shadow boundary (SB) transition region. Neither Geometrical Optics solution for the lit region nor the residue series solution for the shadow region are accurate in the vicinity of the shadow boundary. These two solutions have a discontinuity at the shadow boundary. The failure of the ordinary GTD solution in the transition region can be explained as follows. In the formulation of the G.O. field (i.e., the incident field u^i and the reflected field u^r), an assumption is made that the Bessel functions in the integrand can be approximated by their Debye approximations. It is well known that the Debye approximation of $H_\nu^{(1,2)}(z)$ is appropriate on the condition that

$$|\nu - z| > |\nu^{\frac{1}{2}}| \quad (3.134)$$

As the field point approaches the shadow boundary, the stationary phase point ν_s on which the evaluation of the integral via the stationary phase method is based is close enough to the argument z that the condition in Equation (3.134) is not satisfied. In fact, in the transition region the Bessel functions are appropriately approximated by their Watson's approximation formula where the Bessel functions are expressed in terms of the Airy functions. Another cause for the failure of the ordinary GTD solution in the transition region comes from the fact that the contribution from the end point at $\nu = k_0 b$ is not included in the evaluation of the integral via the stationary phase method. In the transition region the stationary phase point is located near the end point and, therefore, the contribution from the end point can no longer be ignored. The residue series solution which is fast convergent in the deep shadow region becomes slowly convergent as the field point approaches the shadow boundary. This can be explained by the attenuation of the creeping wave mode. In the deep shadow region, the creeping waves attenuate as they travel a large distance in terms of the wave length along the surface of the cylinder. Therefore only a few creeping wave modes with low attenuation constants contribute to the field in the deep shadow region. However in the transition region, the arc distance of attenuation of the creeping wave on the cylinder surface is so small that even the creeping wave modes with high attenuation constant cannot be ignored. Slow convergence of the creeping wave in the transition region makes it difficult, if not impossible, to obtain the result with acceptable accuracy.

The failure of the ordinary GTD solution for the field in the transition region necessitates the development of Uniform Geometrical Theory of Diffraction (UTD) which will be discussed in the Chapter V.

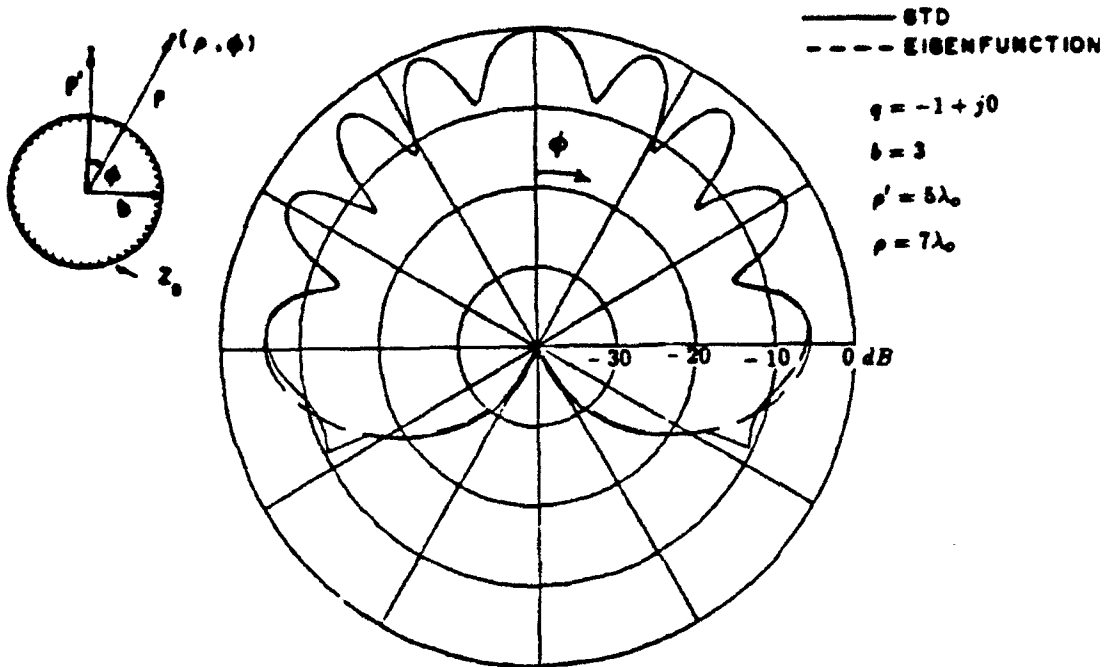


Figure 3.13: Normalized bistatic scattering pattern of impedance cylinder

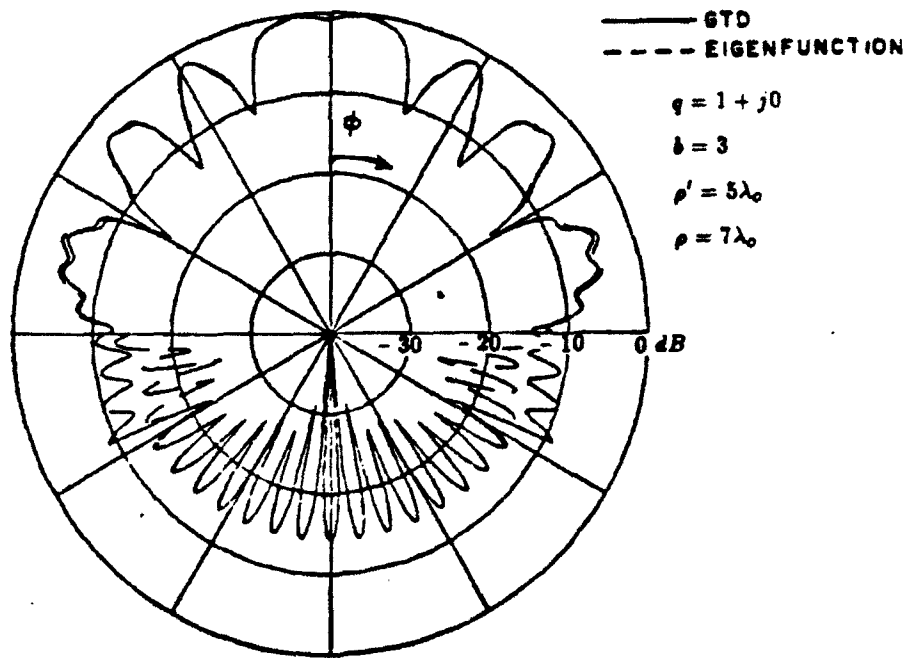


Figure 3.14: Normalized bistatic scattering pattern of impedance cylinder

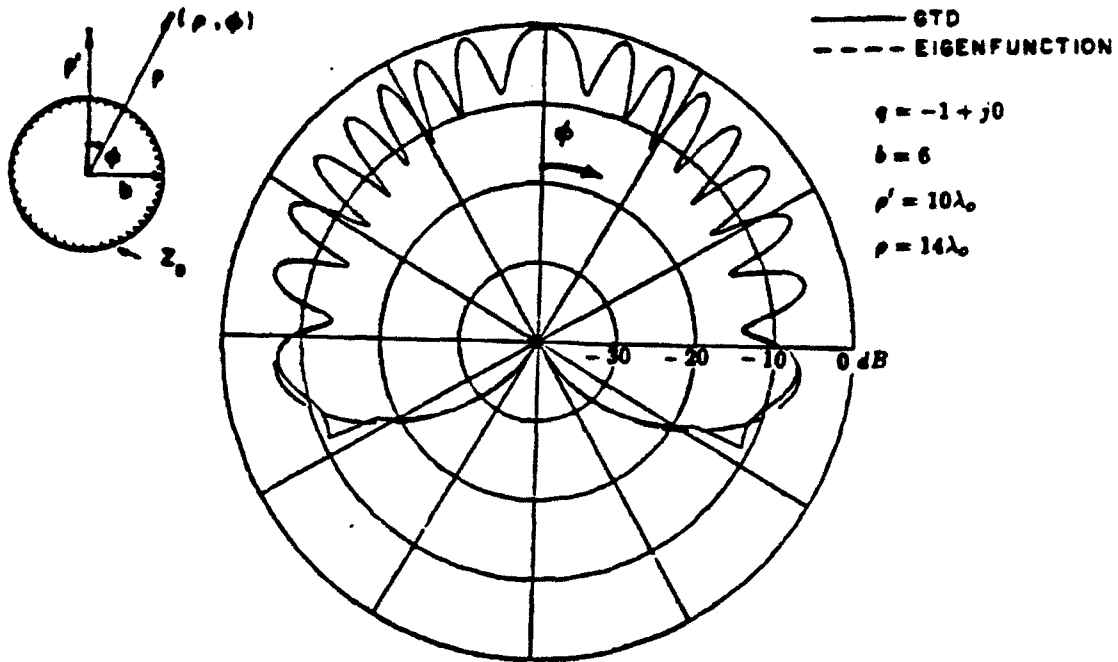


Figure 3.15: Normalized bistatic scattering pattern of impedance cylinder

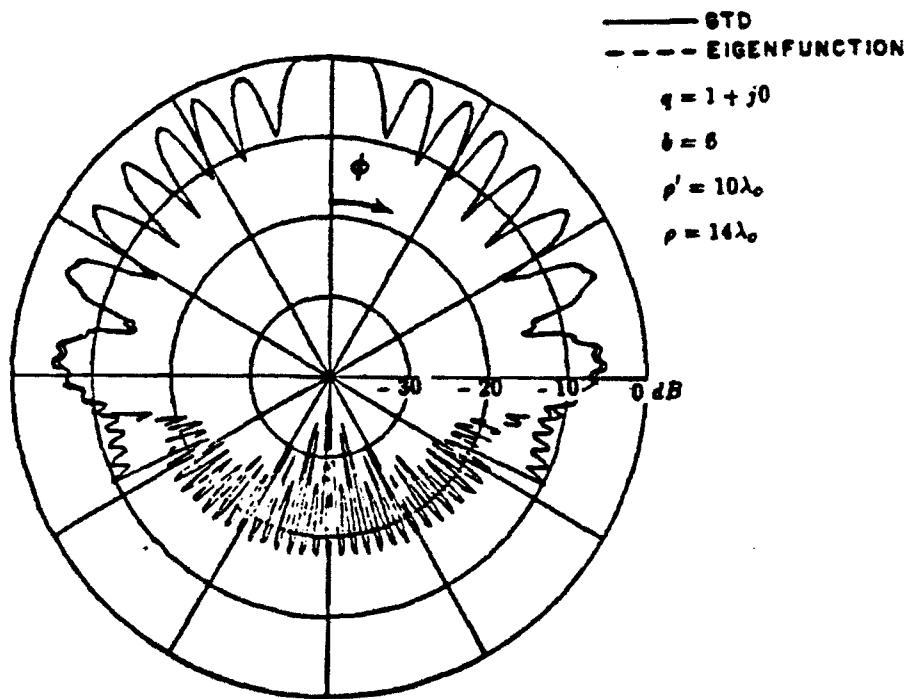


Figure 3.16: Normalized bistatic scattering pattern of impedance cylinder

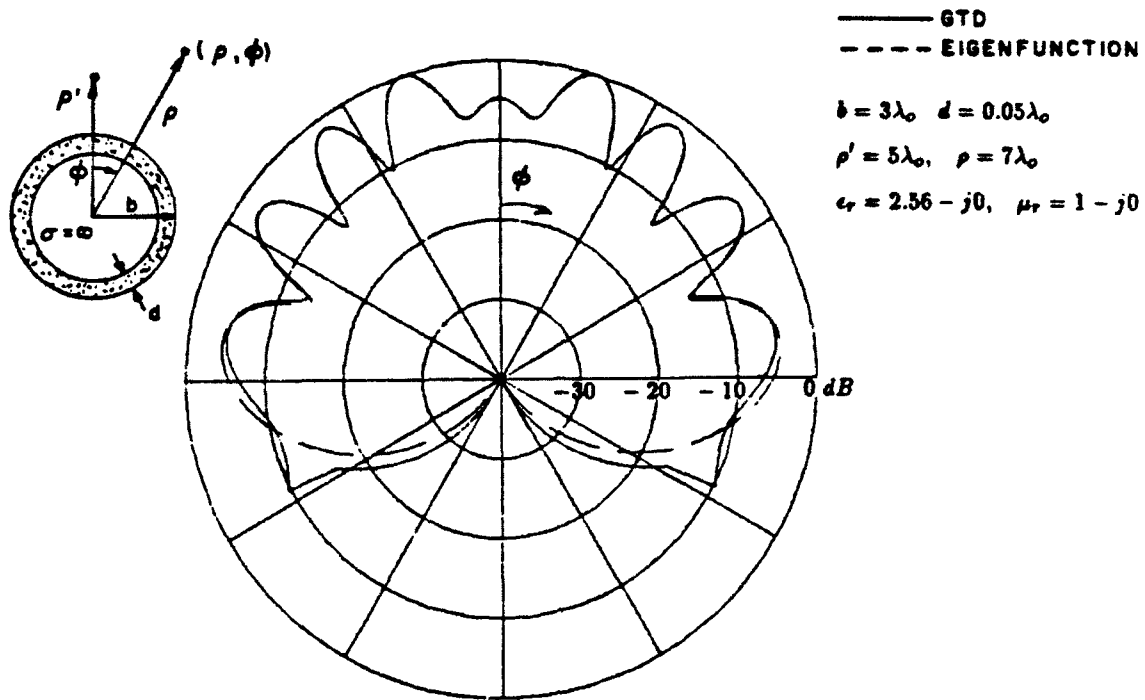


Figure 3.17: Normalized bistatic scattering pattern of coated cylinder : TM_2 case

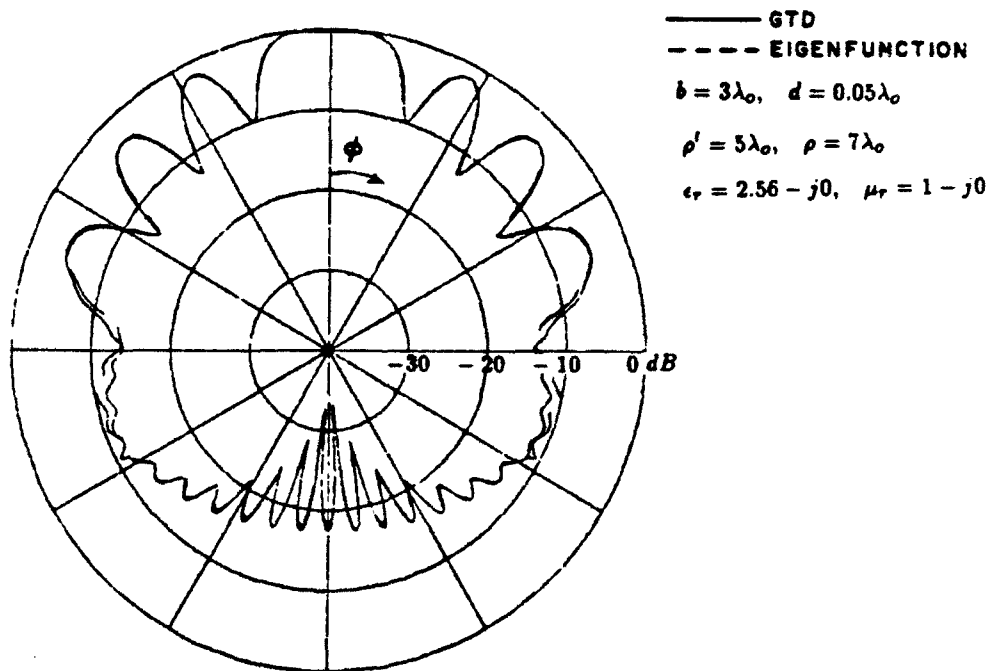


Figure 3.18: Normalized bistatic scattering pattern of coated cylinder : TE_2 case

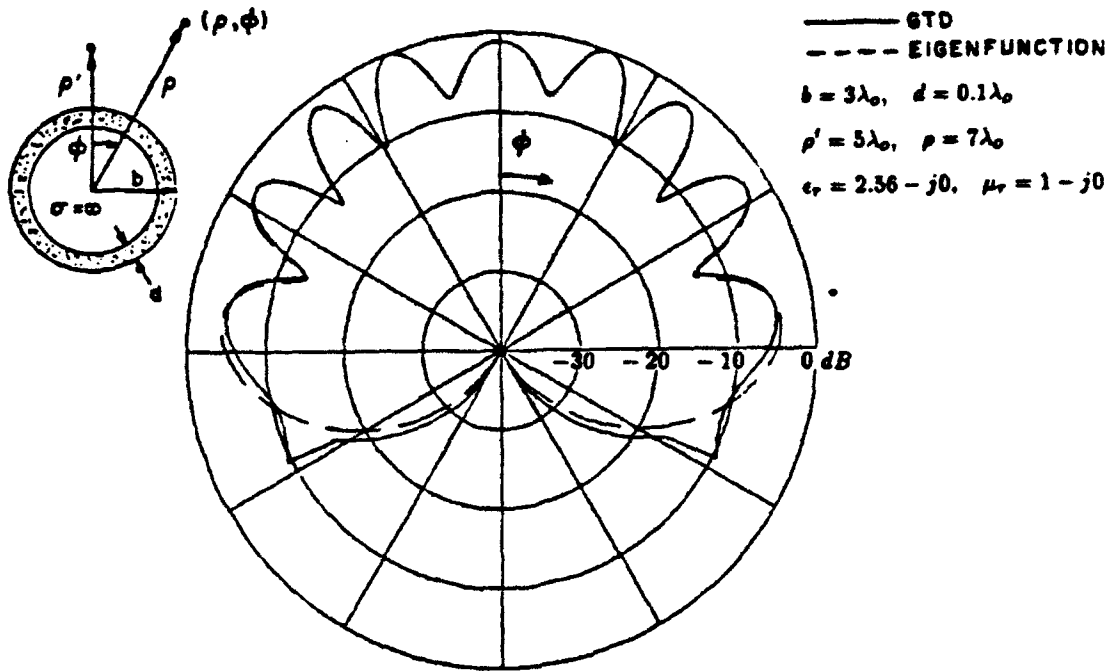


Figure 3.19: Normalized bistatic scattering pattern of coated cylinder : TM_2 case

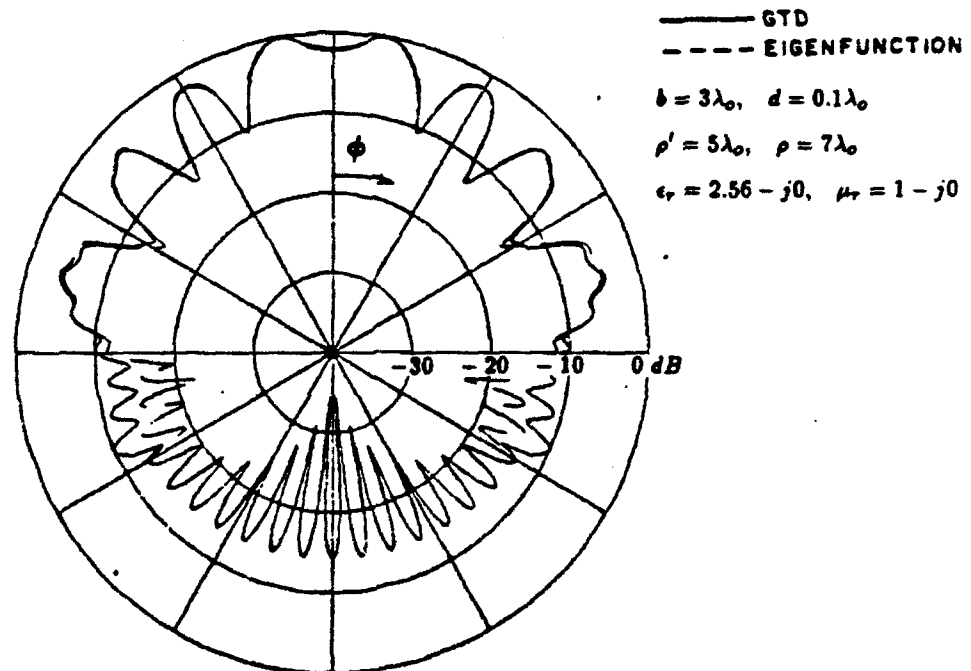


Figure 3.20: Normalized bistatic scattering pattern of coated cylinder : TE_2 case

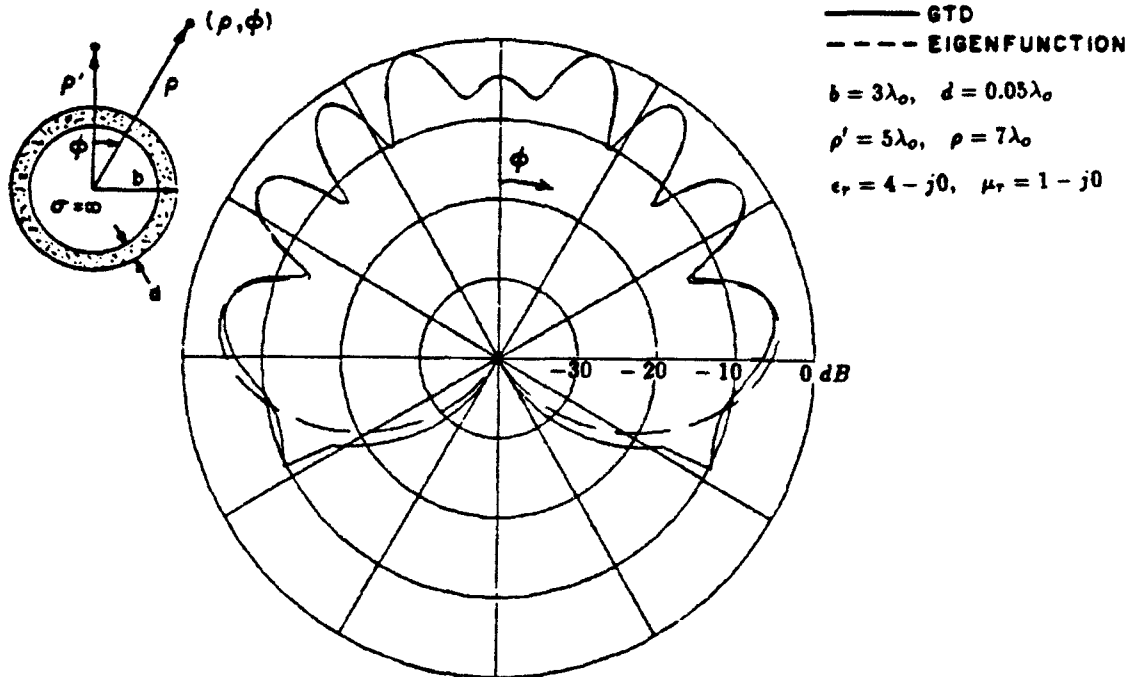


Figure 3.21: Normalized bistatic scattering pattern of coated cylinder : TM_2 case

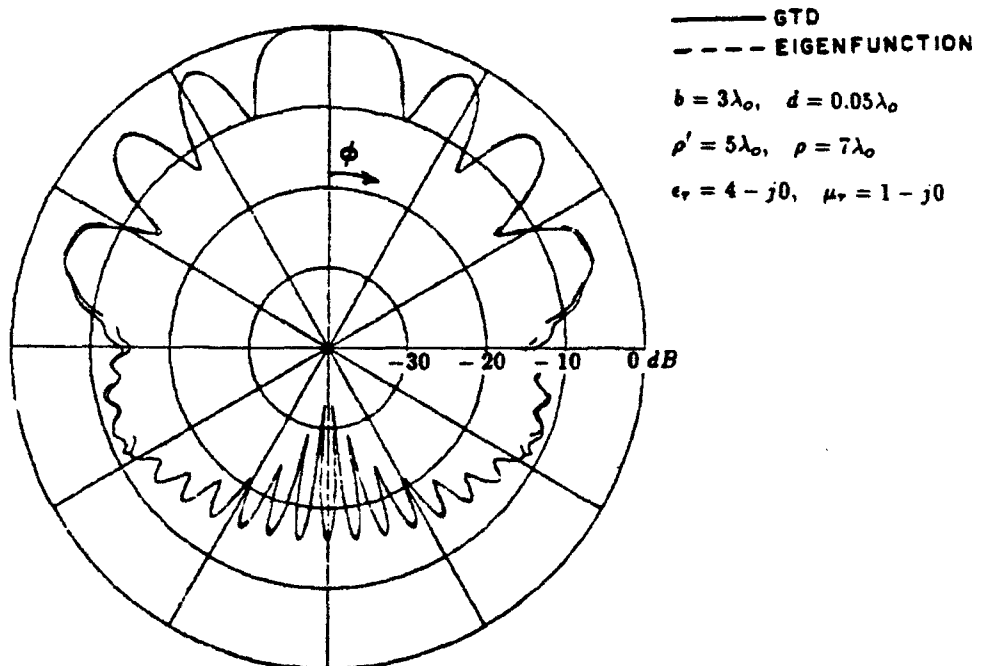


Figure 3.22: Normalized bistatic scattering pattern of coated cylinder : TE_2 case

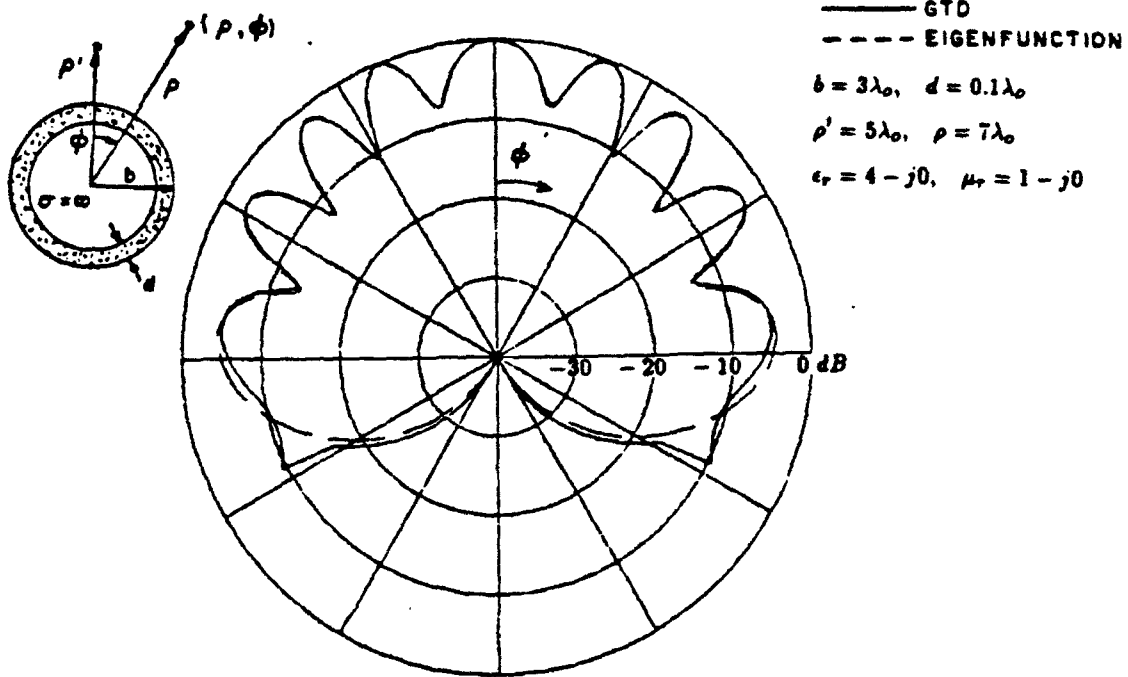


Figure 3.23: Normalized bistatic scattering pattern of coated cylinder : TM_2 case

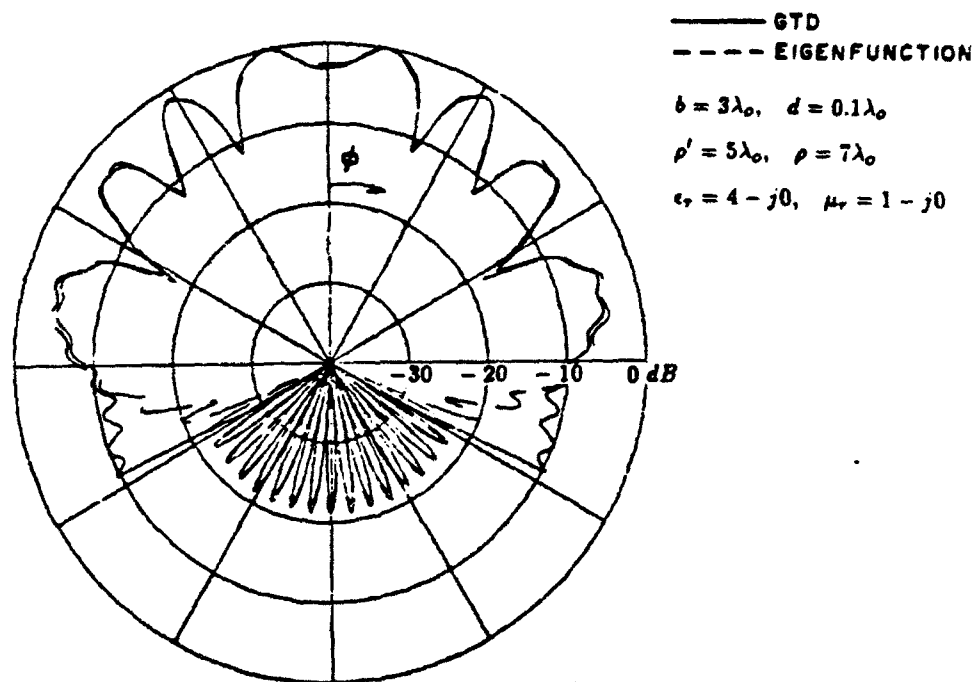


Figure 3.24: Normalized bistatic scattering pattern of coated cylinder : TE_2 case

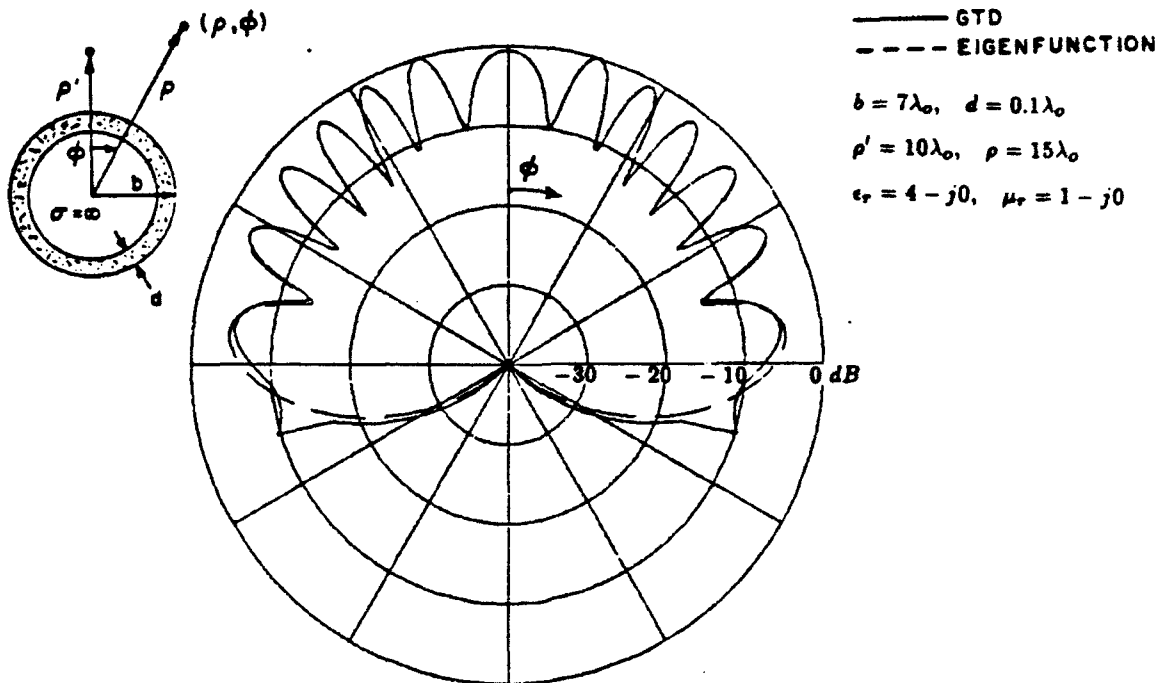


Figure 3.25: Normalized bistatic scattering pattern of coated cylinder : TM_2 case

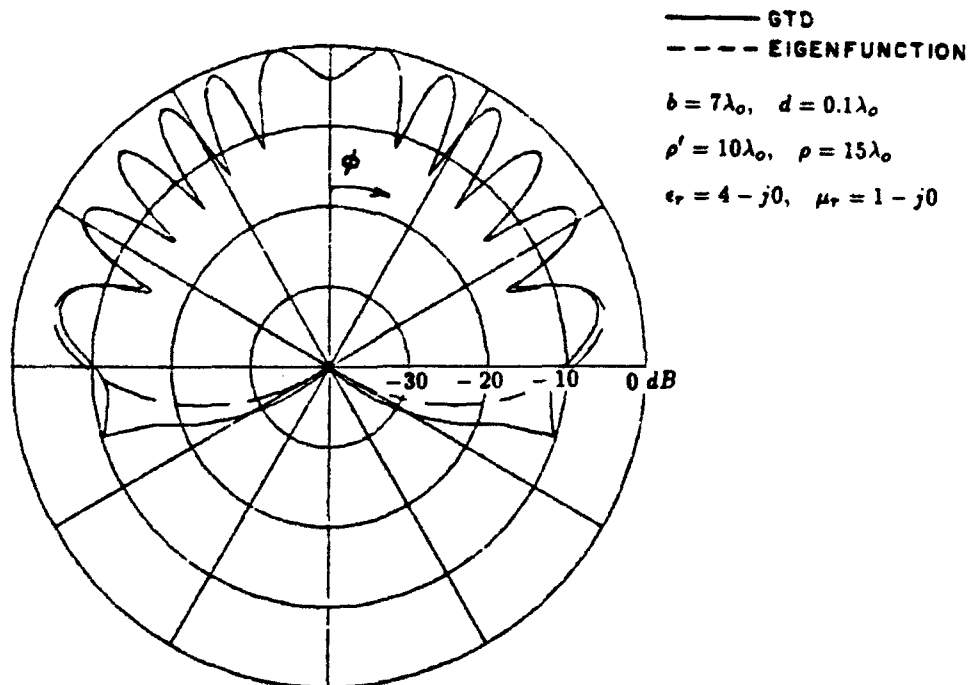


Figure 3.26: Normalized bistatic scattering pattern of coated cylinder : TE_2 case

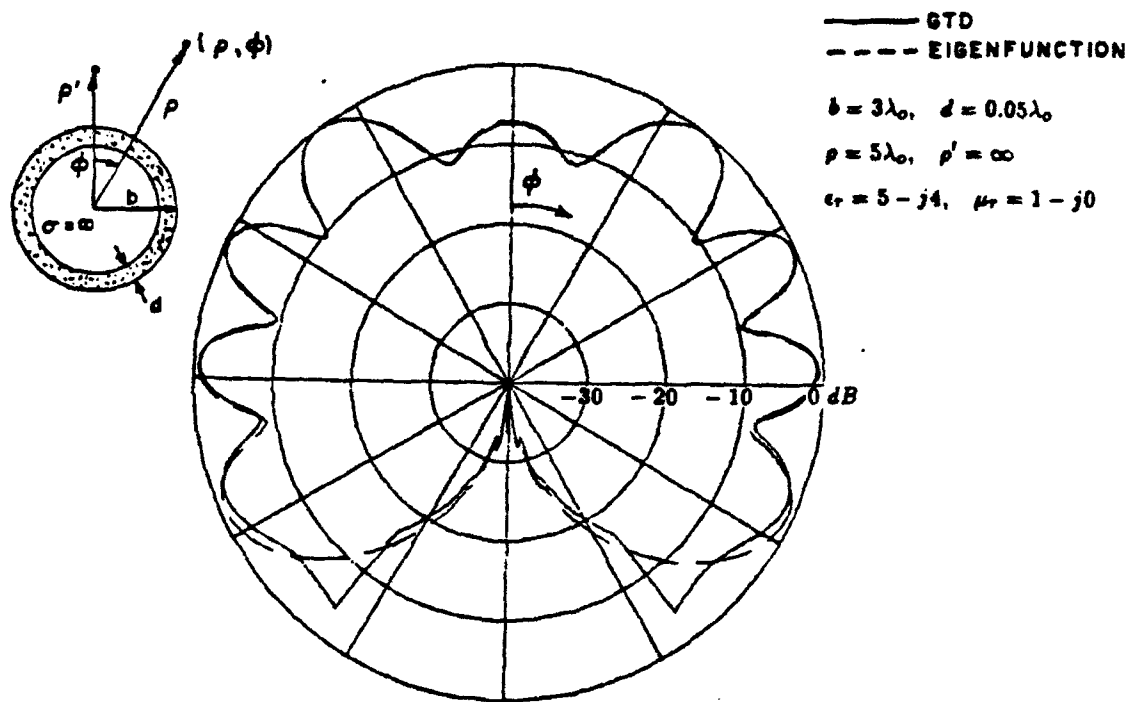


Figure 3.27: Normalized bistatic scattering pattern of coated cylinder : TM_z case

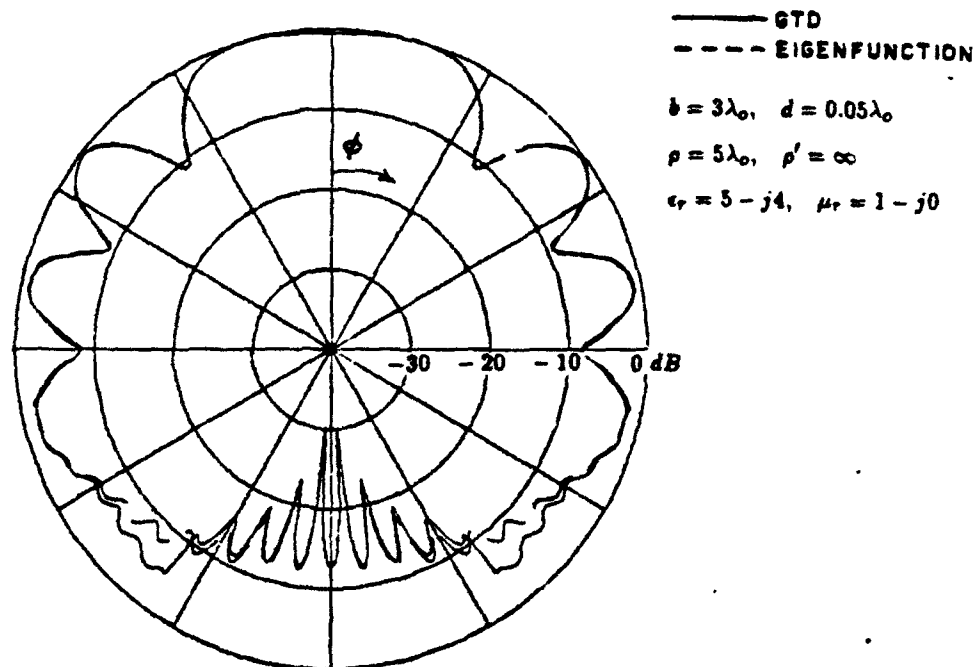


Figure 3.28: Normalized bistatic scattering pattern of coated cylinder : TE_z case

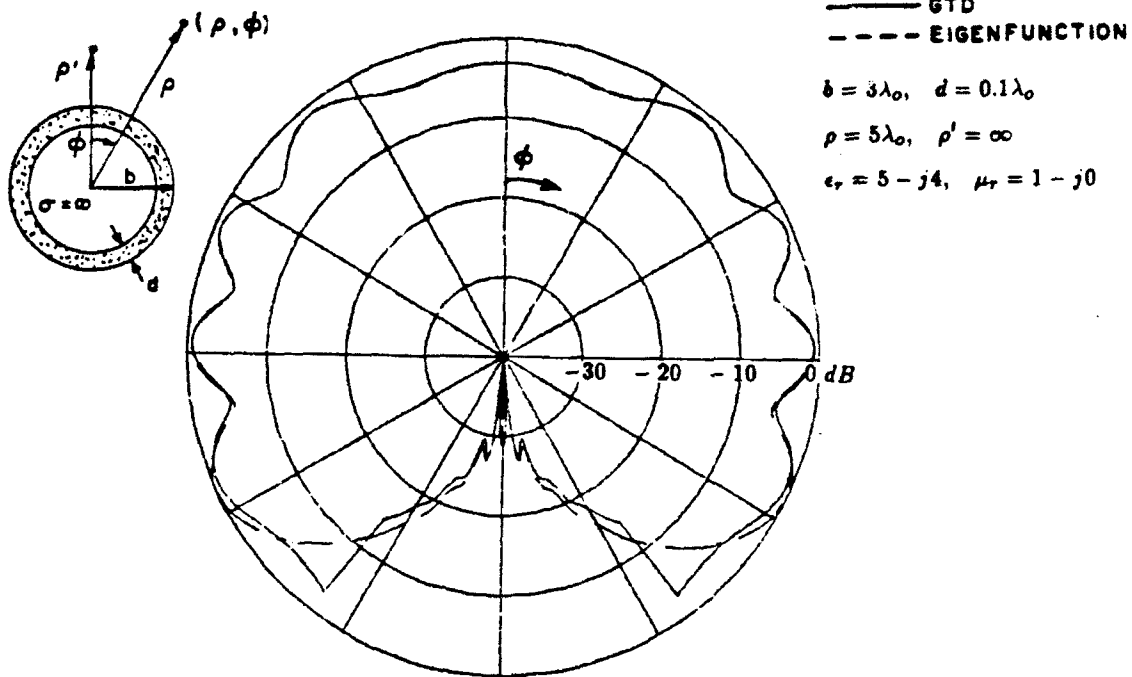


Figure 3.29: Normalized bistatic scattering pattern of coated cylinder : TM_2 case

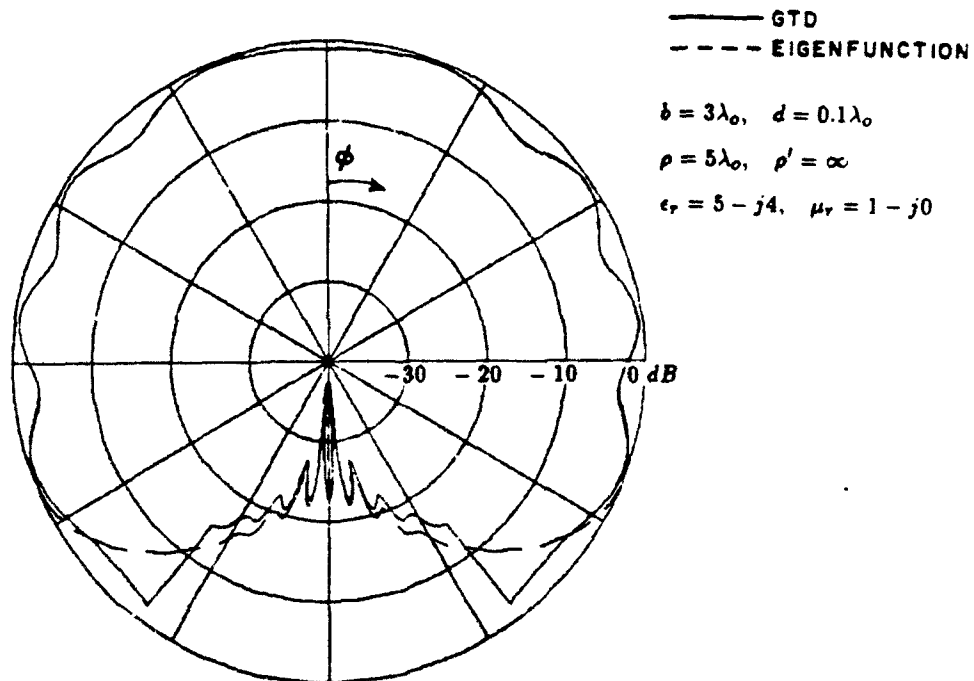


Figure 3.30: Normalized bistatic scattering pattern of coated cylinder : TE_2 case

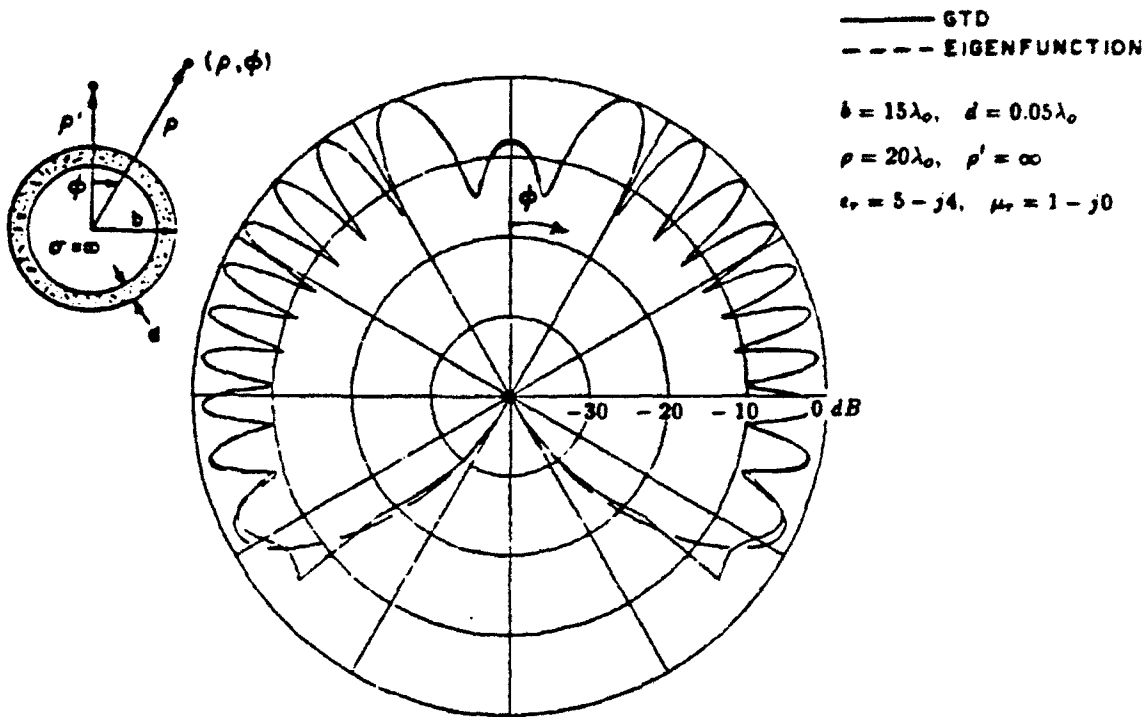


Figure 3.31: Normalized bistatic scattering pattern of coated cylinder : TM_2 case

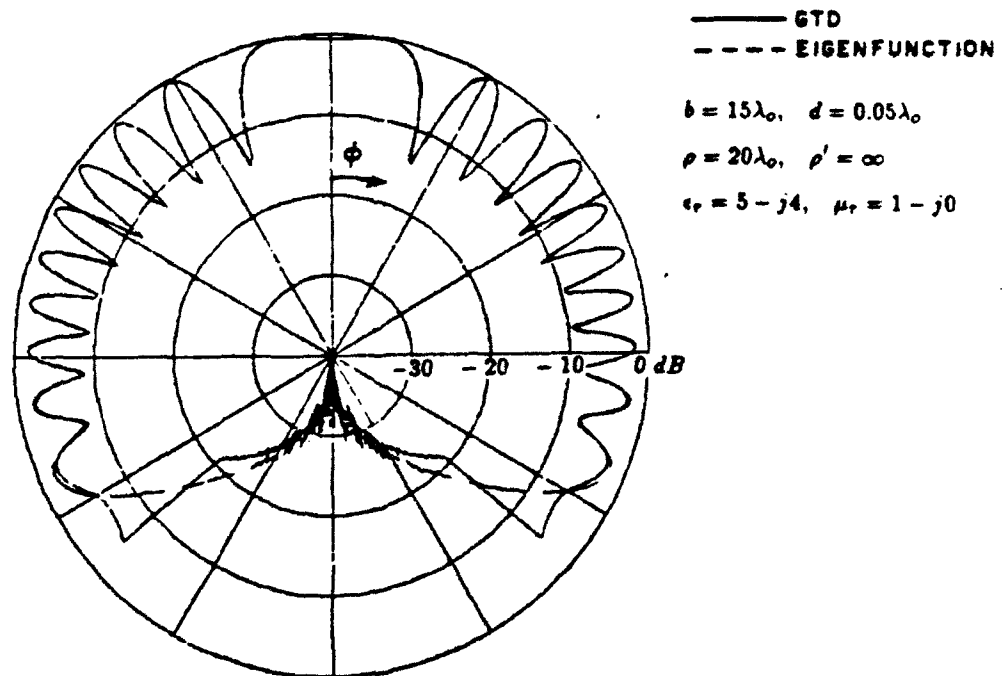


Figure 3.32: Normalized bistatic scattering pattern of coated cylinder : TE_2 case

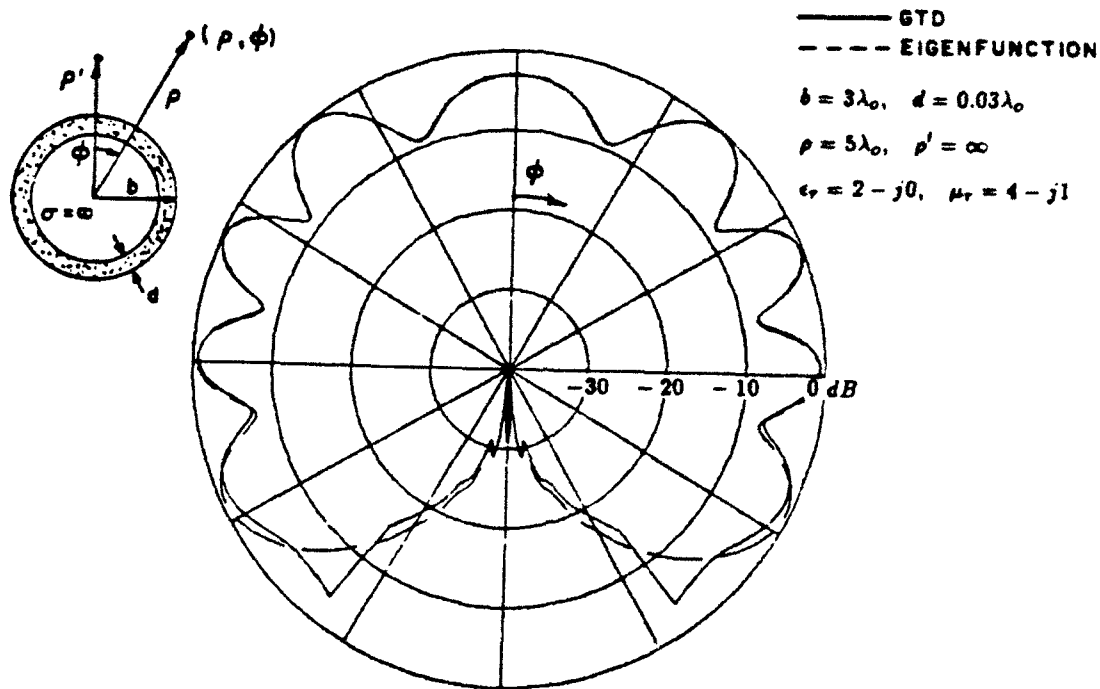


Figure 3.33: Normalized bistatic scattering pattern of coated cylinder : TM_2 case

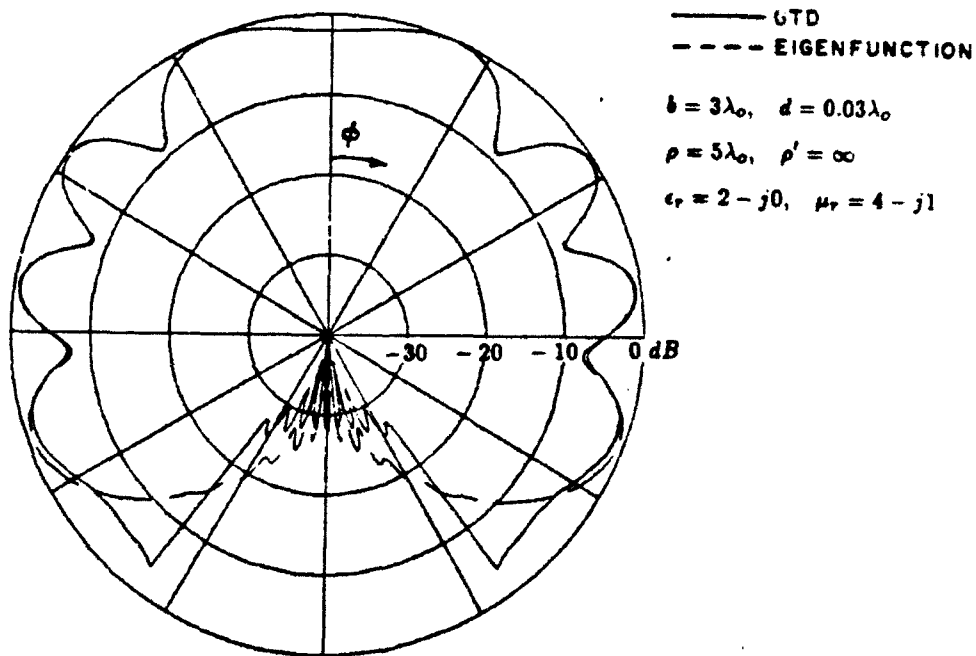


Figure 3.34: Normalized bistatic scattering pattern of coated cylinder : TE_2 case

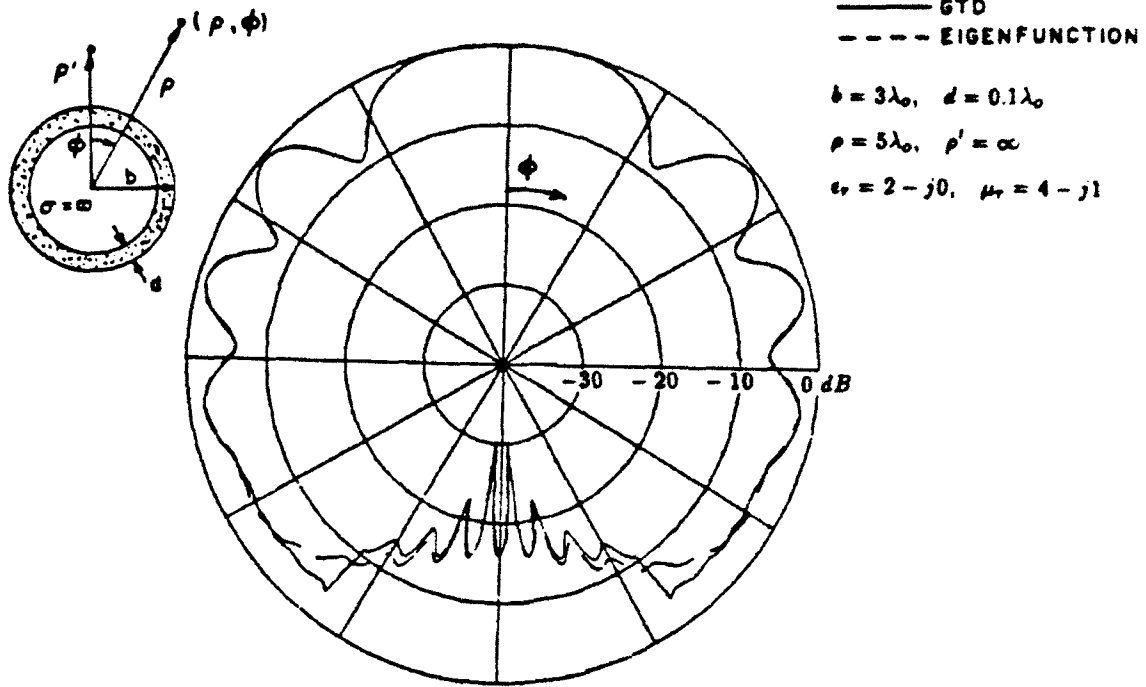


Figure 3.35: Normalized bistatic scattering pattern of coated cylinder : TM_2 case

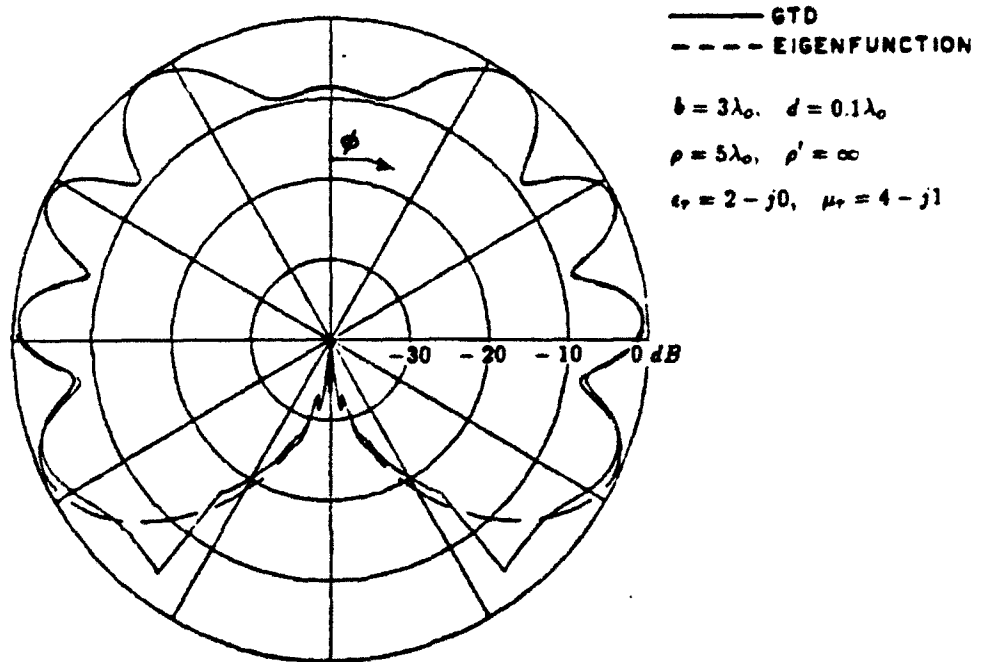


Figure 3.36: Normalized bistatic scattering pattern of coated cylinder : TE_2 case

CHAPTER IV

CHARACTERISTICS OF THE CREEPING WAVES

In the previous Chapter, the ray format for the diffracted field in the deep shadow region was obtained. It is well known that the geodesic ray path of the diffracted field includes part of the arc along the cylinder surface. The field which propagates along the arc of cylinder surface is commonly called the *creeping wave*. It is the purpose of this Chapter to further investigate the behavior of the creeping wave on the cylinder surface. As mentioned, the effect of the surface impedance or the coating of dielectric/ferrite material is more obviously illustrated in the diffracted field than in the geometrical optics field (incident and reflected field). This can be explained by the fact that the diffracted field is launched by the creeping wave which propagates on the cylinder surface under direct influence of the surface impedance or the coating material. Thus it is important to investigate and understand the fundamental characteristics of the creeping wave before we attempt to control the diffraction field from an object with the surface impedance or the dielectric/ferrite coating.

For the perfectly conducting case, the behaviors of the creeping wave on the curved surface has been extensively studied, and they are well understood now.

For the impedance cylinder, this problem has been also studied by Wait [17], Streifer [18] and Logan[20]. They obtained propagation constants for the creeping wave based on the Watson's approximation where the Hankel functions are expressed in terms of the Fock-type Airy functions. In this Chapter, their results are

reproduced for the comparison with our results. Recently, Wang [4] has obtained more accurate numerical data for the propagation constant of the creeping wave, the Regge poles, and the natural frequencies of an impedance cylinder by using both the Debye and the Watson's approximations of the Hankel functions. The creeping wave interpretation for the resonance and the correlation between the resonance, the Regge poles, and the natural frequencies of the impedance cylinder has been also discussed. The propagation constants for the first creeping wave mode on the cylinder with lossless coating has been obtained by Elliott[19]. The most recent work on this problem has been made by Paknys and Wang [7,8]. They made an important contribution by giving some accurate numerical results for this problem. In the following sections of this Chapter, some part of their work is further expanded by using basically the same numerical approximations for the calculation of Hankel functions involved in the formal solution. Some aspects pertaining to the creeping wave which were not treated in their work are also discussed in this Chapter.

4.1 Propagation and Attenuation Constants

In Chapter III, it was shown that the ray format for the diffracted field is given as

$$\begin{aligned}
 u^d &\approx u^i(Q_1) \cdot D_n^{s,h}(Q_1) \cdot e^{-j\nu_n \theta} \cdot D_n^{s,h}(Q_2) \\
 &= u^i(Q_1) \cdot D_n^{s,h}(Q_1) \cdot e^{-(\alpha'_n + j\beta'_n)l} \cdot D_n^{s,h}(Q_2)
 \end{aligned} \tag{4.1}$$

From the above Equation (4.1), it can be easily seen that

$$\alpha'_n = -Im \left[\frac{\nu_n}{b} \right] \quad ; \quad \beta'_n = Re \left[\frac{\nu_n}{b} \right] \tag{4.2}$$

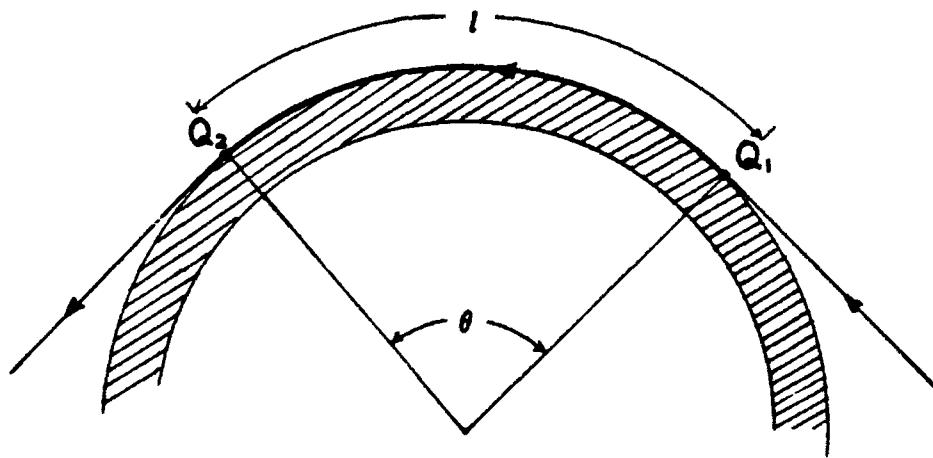


Figure 4.1: Creeping wave

α'_n and β'_n denote the attenuation constant and the propagation constant of the creeping wave mode respectively. The propagation constant determines the phase velocity of the creeping wave and the attenuation constant represents the loss of the electromagnetic energy due to shedding of the diffraction field and the loss due to the surface impedance or the lossy coating material. The relative phase velocity of the creeping wave v_p/c is given by

$$\frac{v_p}{c} = \frac{k_o}{\beta'_n} = \frac{k_o b}{\text{Re}[\nu_n]} \quad (4.3)$$

where c denotes the velocity of the light.

The propagation constant and the attenuation constant are determined from the roots of the transcendental equation which characterizes the impedance or the coated cylinder as given by

$$H_\nu^{(2)'}(k_o b) - j C_{s,h}(\nu) H_\nu^{(2)}(k_o b) \Big|_{\nu=\nu_n} = 0 \quad (4.4)$$

The complex root of the transcendental equation denoted as ν_n is sometimes called as *Regge pole*. It is well known that there exists an infinite number of roots for the Equation (4.4). The subscript n denotes the mode number of the root.

4.1.1 Impedance cylinder

For the impedance cylinder, $C_{s,h}(\nu_n)$ in the Equation (4.4) is given by

$$C_s(\nu) = C_s = \frac{Z_o}{Z_s} \quad \text{for } TM_z \quad (4.5)$$

and

$$C_h(\nu) = C_h = \frac{Z_s}{Z_o} \quad \text{for } TE_z \quad (4.6)$$

Recent work by Paknys and Wang [7,8] shows a trajectory of the Regge poles for purely imaginary impedances. In their work, the Hankel functions are evaluated exactly as well as asymptotically by using both the Debye approximations and the Watson's approximation according to the ranges of validity. The accuracy of their results is fully confirmed by the excellent agreement between the field pattern of the eigenfunction series solution and the field pattern obtained by using their propagation constant. Following the same approximations for the Hankel functions, the trajectories of the Regge poles for various complex impedances are obtained as shown in Figure 4.2 for $k_0b=20$. Newton-Raphson's method has been used for the numerical search for the roots of the transcendental equation.

It can be easily seen that for $C_{s,h}=0$, the roots of transcendental equation are determined from the well known zeros of $H_\nu^{(2)'}(k_0b)$ which are commonly called *hard poles* of the conducting cylinder. These hard poles are given as

$$\nu_n = \eta_n \approx k_0b + \left(\frac{k_0b}{2}\right)^{1/3} \beta_n e^{-j\frac{\pi}{3}} \quad (4.7)$$

where $\beta_n=1.0188, 3.2482, 4.8201, \dots$

For the small value of $|C_{s,h}|$, the hard pole of the conducting cylinder can be used as initial guessing of the root in the numerical search via Newton-Raphson's method.

For $C_{s,h} = \infty$, the roots of transcendental equation are determined from the zeros of $H_\nu^{(2)}(k_0b)$ which are the *soft poles* of the conducting cylinder. They are given by

$$\nu_n = \xi_n \approx k_0b + \left(\frac{k_0b}{2}\right)^{1/3} \alpha_n e^{-j\frac{\pi}{3}} \quad (4.8)$$

where $\alpha_n=2.3381, 4.0879, 5.5205, \dots$

Figure 4.2 illustrates trajectories of ν_n as the magnitude of $C_{s,h}$ increases where

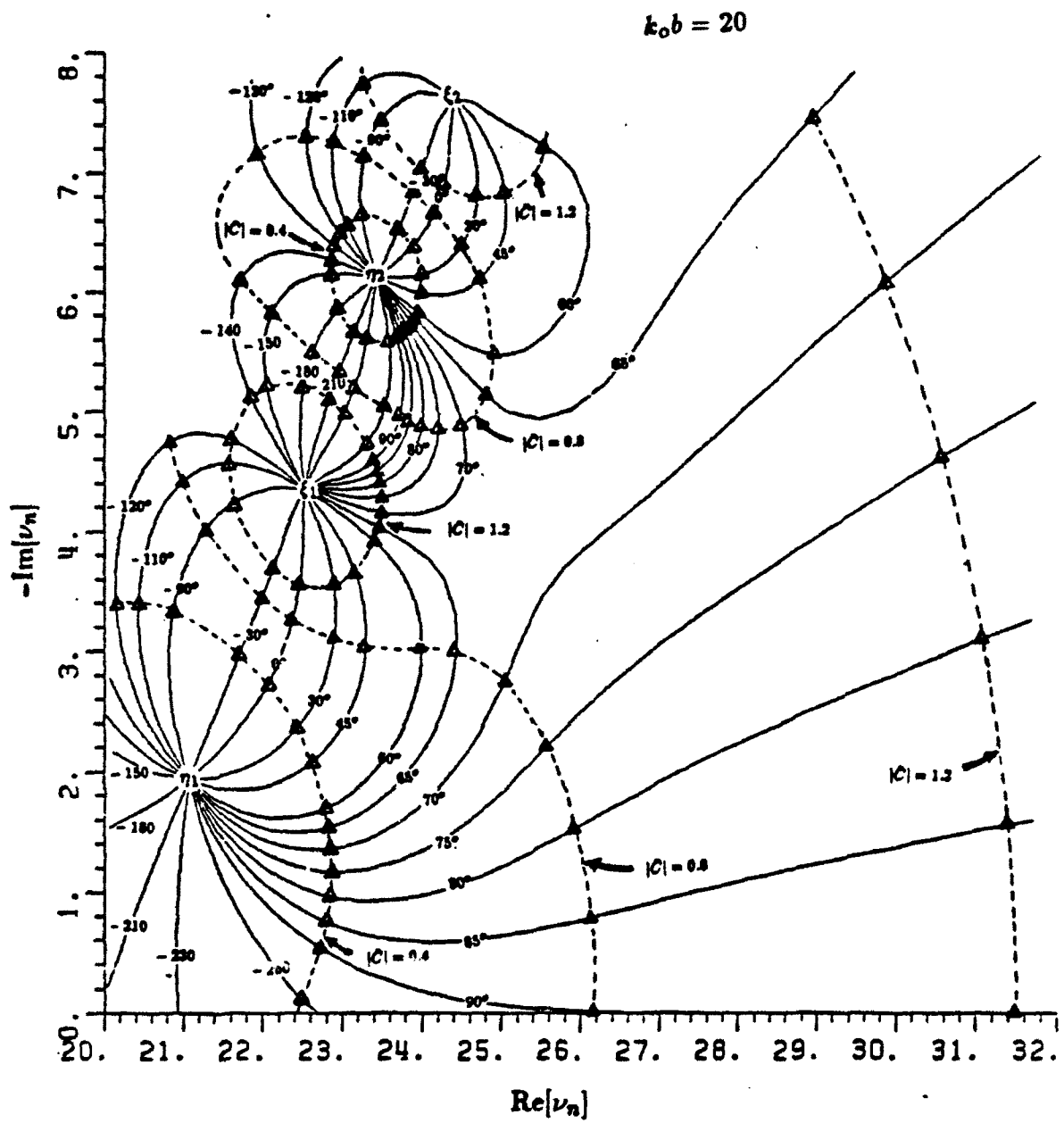


Figure 4.2: The roots of the transcendental equation for the impedance cylinder

the phase of the $C_{s,h}$ is fixed. The trajectories of the ν_n can be obtained by starting from the hard poles η_n and slowly increasing the magnitude of $C_{s,h}$.

When the phase of $C_{s,h}$ is between $-270^\circ \sim -90^\circ$, the impedance has a negative real value and therefore, such a $C_{s,h}$ is nonphysical. Our interests are the cases where the phase is between $-90^\circ \sim 90^\circ$.

From Figure 4.2, we can observe two different type of behavior of the equiphase trajectories for the first mode roots. All trajectories of roots of the first mode start from the first hard pole which is denoted as η_1 . For the case where the phase of $C_{s,h}$ is between $70^\circ \sim 90^\circ$ in Figure 4.2, the real part of first mode root ν_1 keeps increasing as the magnitude of $C_{s,h}$ increases. This means that the phase velocity of the creeping wave becomes slower as the magnitude of $C_{s,h}$ increases. It can be also noted that ν_1 does not approach the first soft pole ξ_1 . We define such a root as *Elliott-type* root.

For the case where the phase of $C_{s,h}$ lies between $-90^\circ \sim 65^\circ$ in Figure 4.2, the roots approaches the soft pole denoted as ξ_1 as the magnitude of the $C_{s,h}$ increases. We define such a root as *Watson-type* root. The boundary of the two different types is somewhere between 65° and 70° .

For the second creeping wave mode, all the roots start from the second hard pole η_2 . As the magnitude of $C_{s,h}$ increases, the equiphase trajectories exhibit three different types of behavior. When the phase of $C_{s,h}$ equals $90^\circ \sim 70^\circ$, the root approaches the first soft pole ξ_1 . When the phase equals 65° , the real part of ν_2 keep increasing as the magnitude of $C_{s,h}$ increases. For the phase of $C_{s,h}$ between $60^\circ \sim -90^\circ$, the roots approach the second soft pole ξ_2 . Thus, except at 65° where the equiphase trajectory exhibits Elliott-type roots, all other equiphase trajectories of the second mode roots belong to the Watson-type.

Wait [17], Streifer [18] and Logan [20] also examined the roots of the tran-

scendental equation for the impedance cylinder. Their results are based on the assumption that the Hankel functions can be properly approximated in terms of the Fock-type Airy functions.

$$H_\nu^{(1),(2)}(k_0 b) \approx \mp \frac{j}{m\sqrt{\pi}} w_{1,2}(\tau) \quad (4.9)$$

where

$$m = \left(\frac{k_0 b}{2} \right)^{\frac{1}{3}} \quad (4.10)$$

and

$$w_{1,2} = \frac{1}{\sqrt{\pi}} \int_{\Gamma_{1,2}} e^{\tau t - t^3/3} dt \quad (4.11)$$

The contour Γ_1 runs from $\infty \cdot e^{-j2\pi/3}$ to $\infty - j\epsilon$, and Γ_2 is the complex conjugate of Γ_1 . Based upon this approximation, the roots of transcendental equation are determined from the roots of the equation given as

$$w_2'(\tau) - q w_2(\tau) \Big|_{\tau=\tau_n} = 0 \quad (4.12)$$

where

$$q \equiv -jmC_{s,h} \quad (4.13)$$

The root ν_n is given by

$$\nu_n = k_0 b + m\tau_n \quad (4.14)$$

Trajectories of the roots obtained by using this approximation is shown in Figure 4.3 for comparison with our results obtained by using both the Debye and the

$q = -jmC_{s,h}$	ν_n from Figure 4.2	ν_n from Figure 4.3
$q=1 - j0$	21.919 - j0.38098	22.121 - j0.32760
$q=1.1 - j0$	22.246 - j0.28736	22.496 - j0.23492
$q=1.2 - j0$	22.598 - j0.20862	22.905 - j0.15897
$q=1.3 - j0$	22.975 - j0.14478	23.355 - j0.10006
$q=1.4 - j0$	23.380 - j0.09529	23.849 - j0.05769
$q=1.5 - j0$	23.812 - j0.05899	24.390 - j0.02987

Table 4.1: Comparison of roots

Watson's approximation. Sampled data of ν_1 for $q = 1 - j0 \sim q = 1.5 - j0$ obtained by above method are compared with our results in Table 4.1. It can be observed from the Table 4.1 that there are significant discrepancies between these two results. As shown in Figure 4.4, the accuracy of these propagation constants are also tested by the comparison of the field pattern obtained by data in Table 1 with that of the eigenfunction solution for $q = 1 - j0$, $q = 1.2 - j0$ and $q = 1.3 - j0$. It can be observed from the comparison in Figure 4.4 ~ 4.9 that the approximation of the Hankel functions as given in Equation (4.9) is not appropriate when q is larger than 1. This is due to the fact that for $|\nu_n - k_0 b| > (\nu_n)^{1/3}$, the Debye approximation of the Hankel function should be used instead of the approximation given by Equation (4.9).

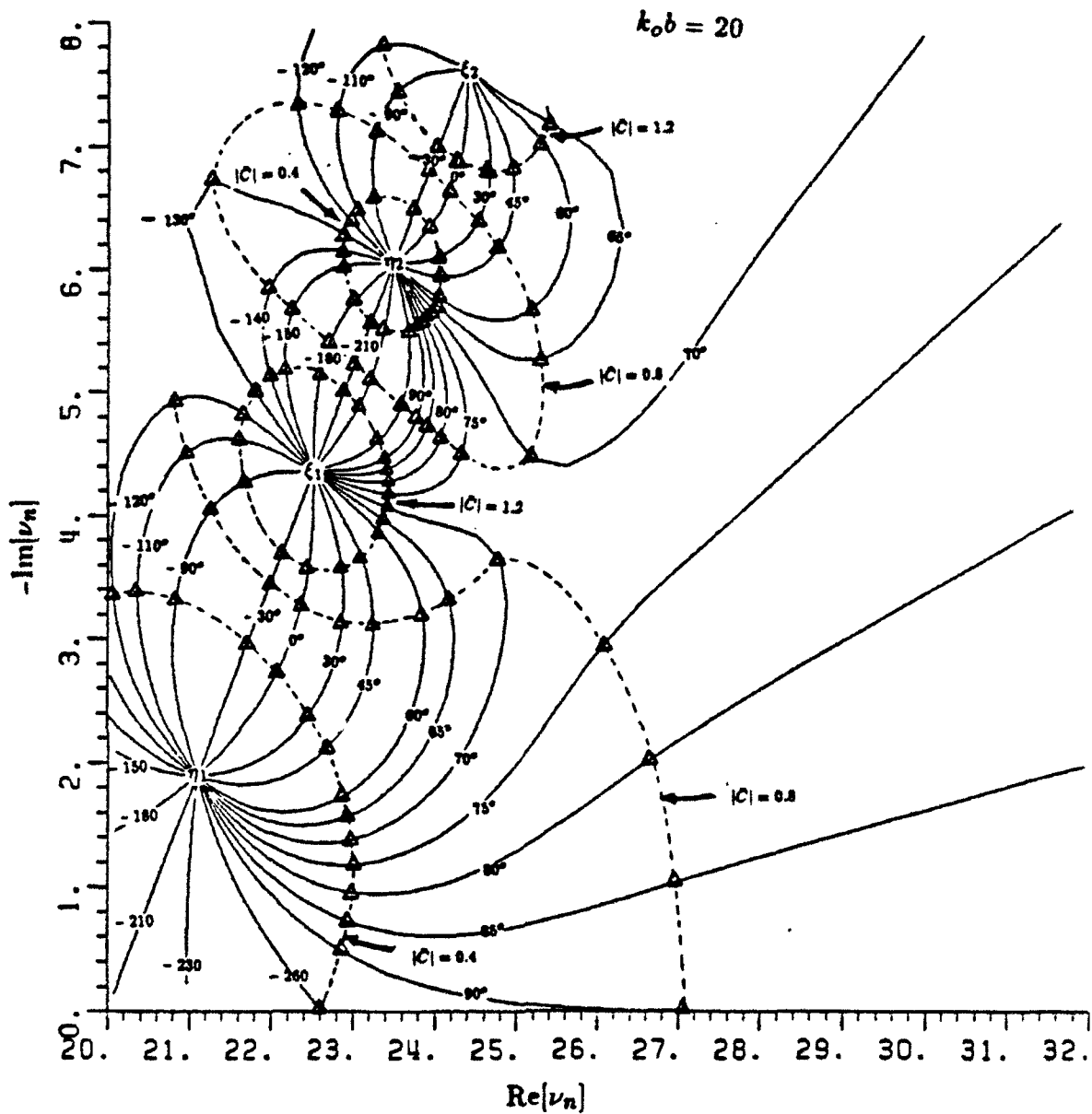


Figure 4.3: The roots of the transcendental equation for the impedance cylinder using Equation (4.12)

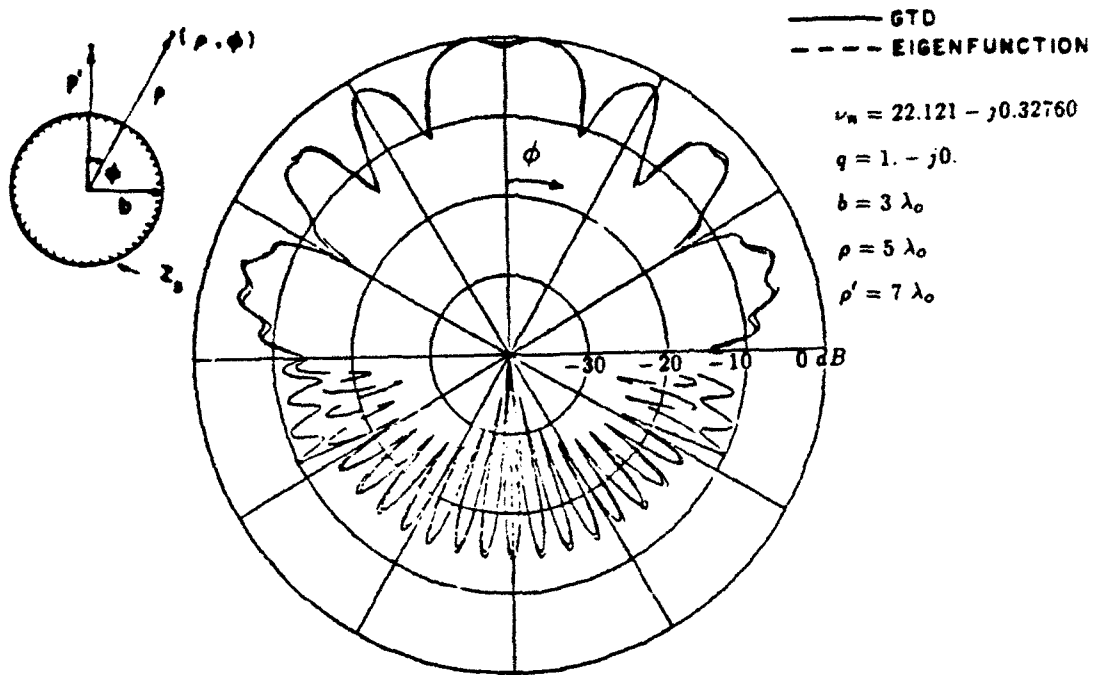


Figure 4.4: Field pattern obtained using the ν_n in Figure 4.3

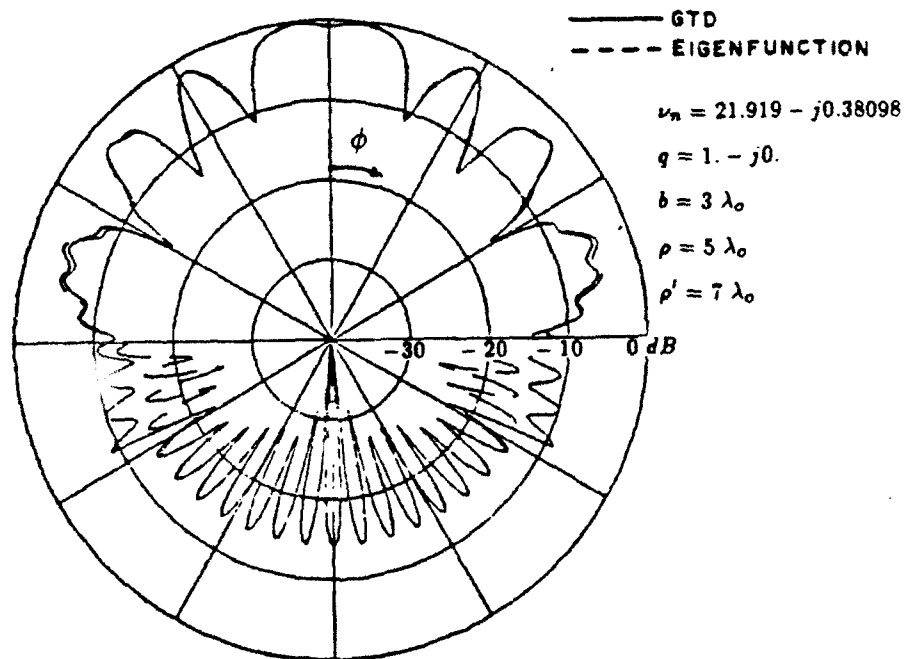


Figure 4.5: Field pattern obtained using the ν_n in Figure 4.2

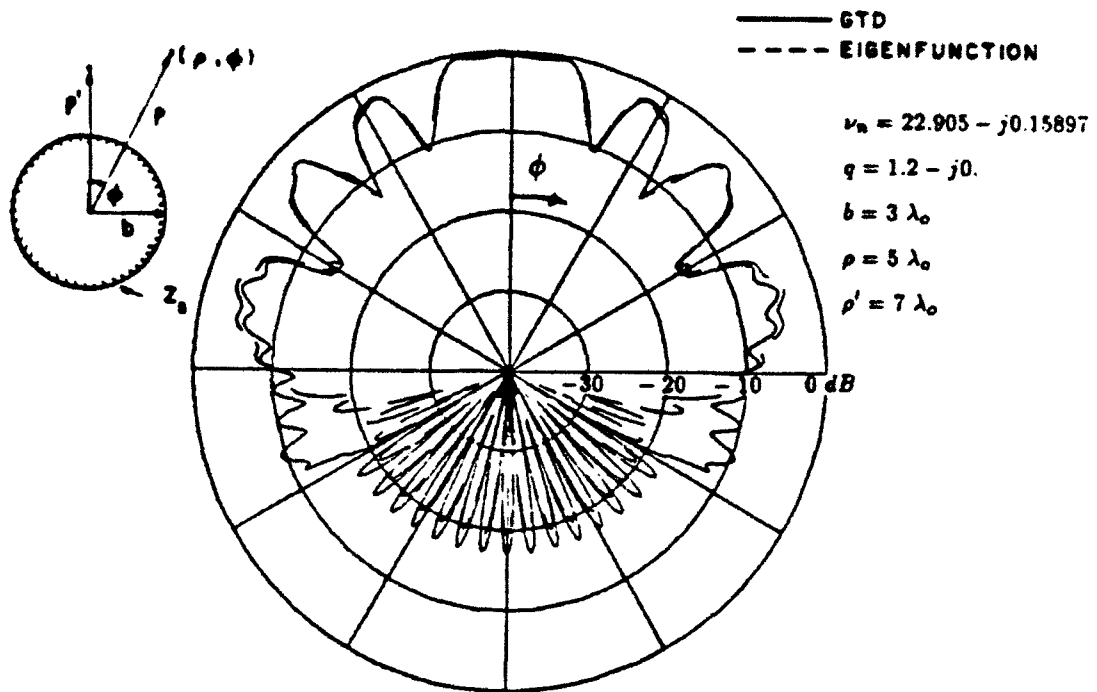


Figure 4.6: Field pattern obtained using the ν_n in Figure 4.3

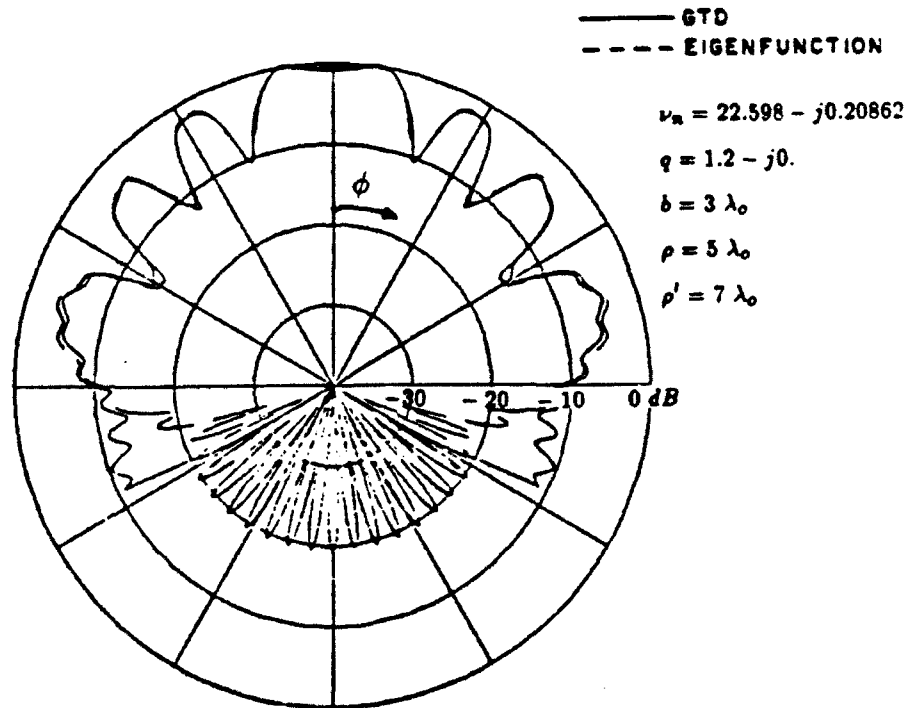


Figure 4.7: Field pattern obtained using the ν_n in Figure 4.2

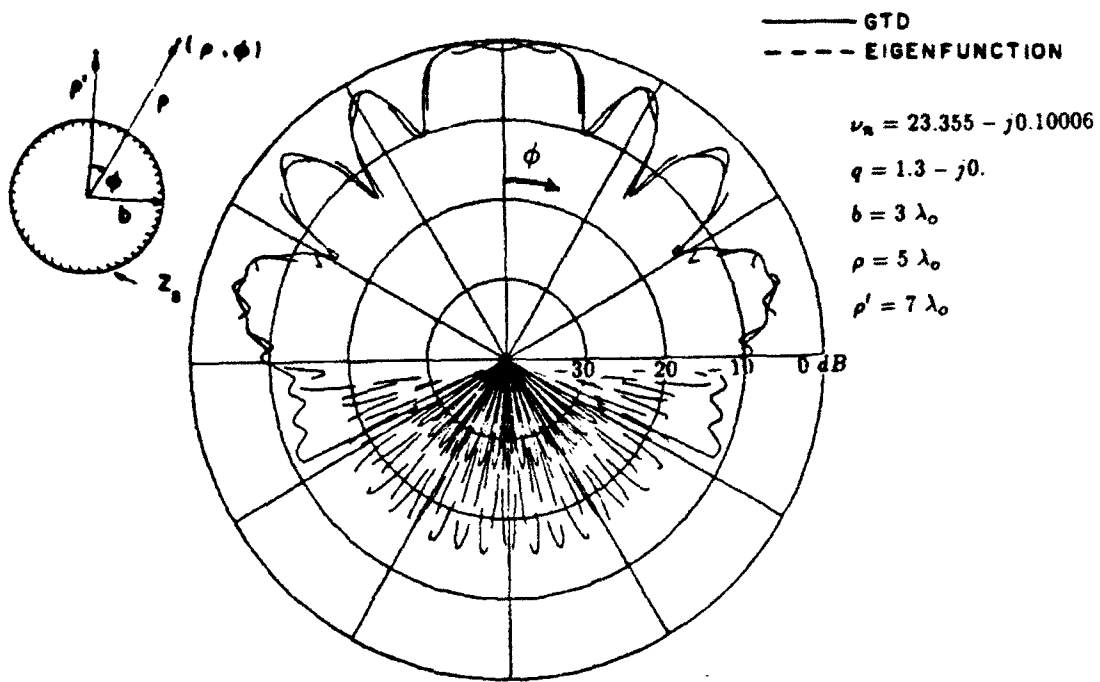


Figure 4.8: Field pattern obtained using the ν_n in Figure 4.3

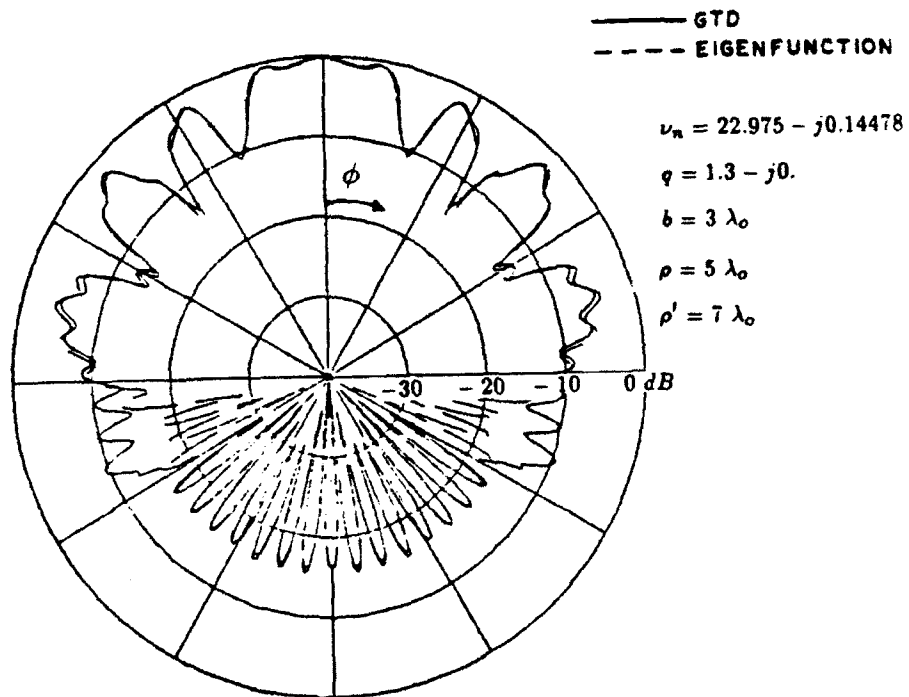


Figure 4.9: Field pattern obtained using the ν_n in Figure 4.2

4.1.2 Coated cylinder

For the coated cylinder, $C_{s,h}(\nu)$ in Equation (4.4) is given as

$$C_s(\nu) = -j \frac{Z_0}{Z_1} \cdot \frac{H_\nu^{(1)'}(k_1 b) H_\nu^{(2)}(k_1 a) - H_\nu^{(2)'}(k_1 b) H_\nu^{(1)}(k_1 a)}{H_\nu^{(1)}(k_1 b) H_\nu^{(2)}(k_1 a) - H_\nu^{(2)}(k_1 b) H_\nu^{(1)}(k_1 a)} \quad \text{for } TM_z \quad (4.15)$$

and

$$C_h(\nu) = -j \frac{Z_1}{Z_0} \cdot \frac{H_\nu^{(1)'}(k_1 b) H_\nu^{(2)'}(k_1 a) - H_\nu^{(2)'}(k_1 b) H_\nu^{(1)'}(k_1 a)}{H_\nu^{(1)}(k_1 b) H_\nu^{(2)'}(k_1 a) - H_\nu^{(2)}(k_1 b) H_\nu^{(1)'}(k_1 a)} \quad \text{for } TE_z \quad (4.16)$$

The propagation constants of the creeping wave mode for the cylinder with lossless dielectric coating was first obtained by Elliott [19]. Recent work by Paknys and Wang [7,8] also shows the trajectories of ν_n for the changing values of the thickness of the lossless dielectric coating and the accuracy of their results is also proved by comparison with the eigenfunction results. By using the same approximations for the Hankel functions as employed by Paknys and Wang, the trajectories of ν_n for the general complex ϵ_r and complex μ_r are obtained and shown in Figures 4.10 ~ 4.13.

From the Wronskian of the Hankel function, it can be easily proved that

$$\lim_{a \rightarrow b} C_s(\nu) = \infty \quad \text{for } TM_z \quad (4.17)$$

and

$$\lim_{a \rightarrow b} C_h(\nu) = 0 \quad \text{for } TE_z \quad (4.18)$$

This means that the propagation constant for the coating with zero thickness is the same as for the perfectly conducting cylinder and therefore, the well known

soft and hard poles of conducting cylinder can be used as the initial guess of roots for the thin coating in the numerical search of ν_n via Newton-Raphson's method. From numerical results given in Figure 4.10 ~ 4.13, we can also observe two different types of behavior in the trajectories as the thickness of the coating increases. When the real part of ν_n increases (i.e. the phase velocity decreases) as the coating thickness increases, we refer to this trajectory as Elliott-type. It can be noted that the Elliott-type trajectory is obtained only when the coating material has a low loss tangent. For the material coating with a high loss tangent, the trajectory of ν_n represents the Watson-type. It can be observed that the Watson-type ν_n approaches a limiting point for each creeping wave mode as the thickness of coating increases. If the coating material has a high loss tangent, the field inside the coating material decreases exponentially as the field point approaches the inner conducting cylinder. Thus the field inside the coating material is confined to near the surface of the cylinder. For this case, further increase of the coating thickness does not affect the propagation and the attenuation constant of the creeping wave mode. Figure 4.14 shows the relative phase velocity and the attenuation of the first creeping wave mode versus coating thickness. Curves are shown for four different sizes of the coated cylinder ($k_0b=20, 40, 100, \infty$) with coating material of $\epsilon_r = 5.1513 - j4.253$ and $\mu_r = 1$. The attenuation shown in Figure 4.14 represents the attenuation per meter at a frequency of 10 GHz. The creeping wave on the cylinder with infinite radius (i.e. $k_0b = \infty$) is, in fact, the surface wave on the planar ground slab¹ with the same coating material.

¹The numerical data for the surface wave were obtained by Prof. Richmond of the Ohio State University.

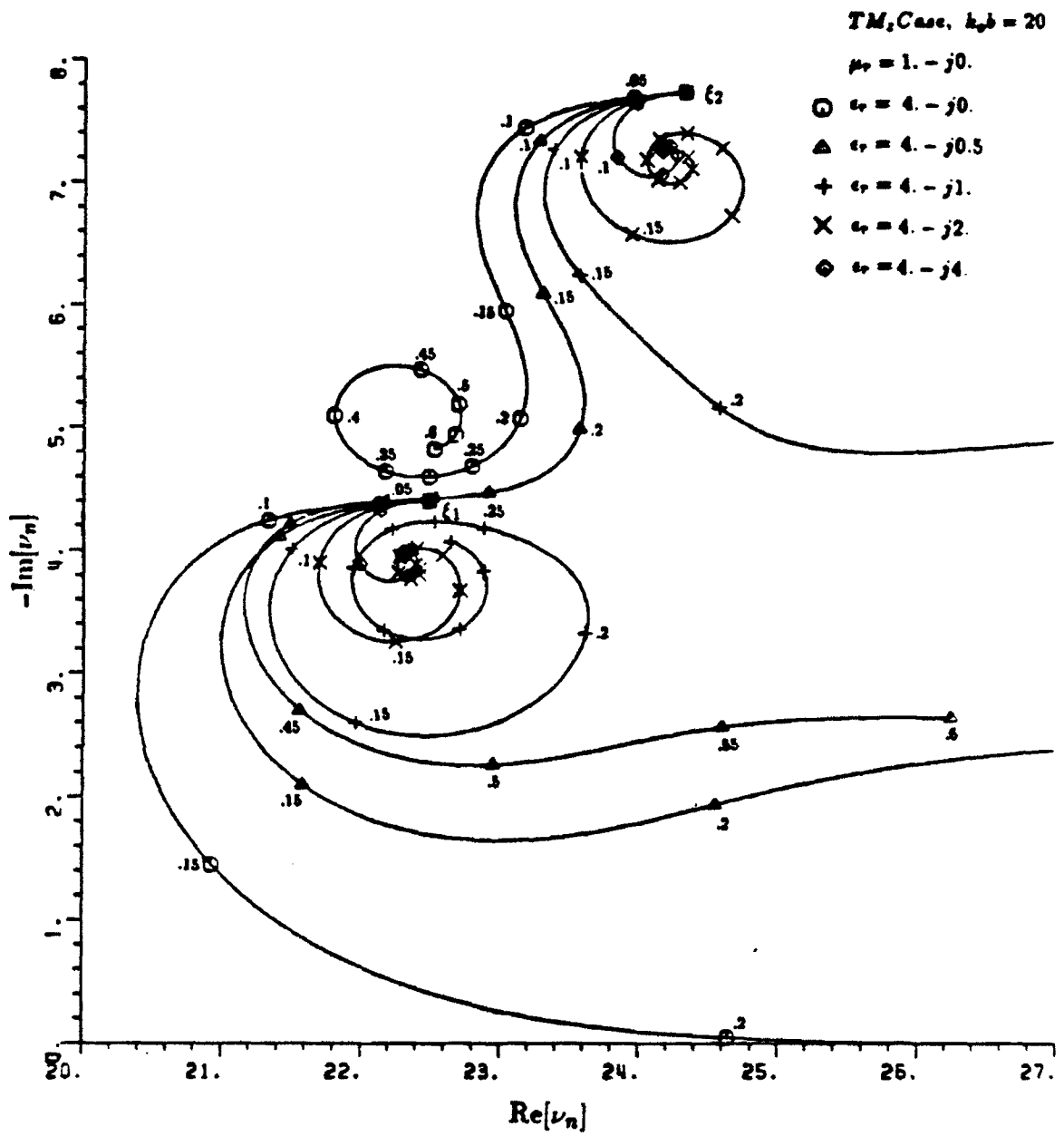


Figure 4.10: The roots of the transcendental equation

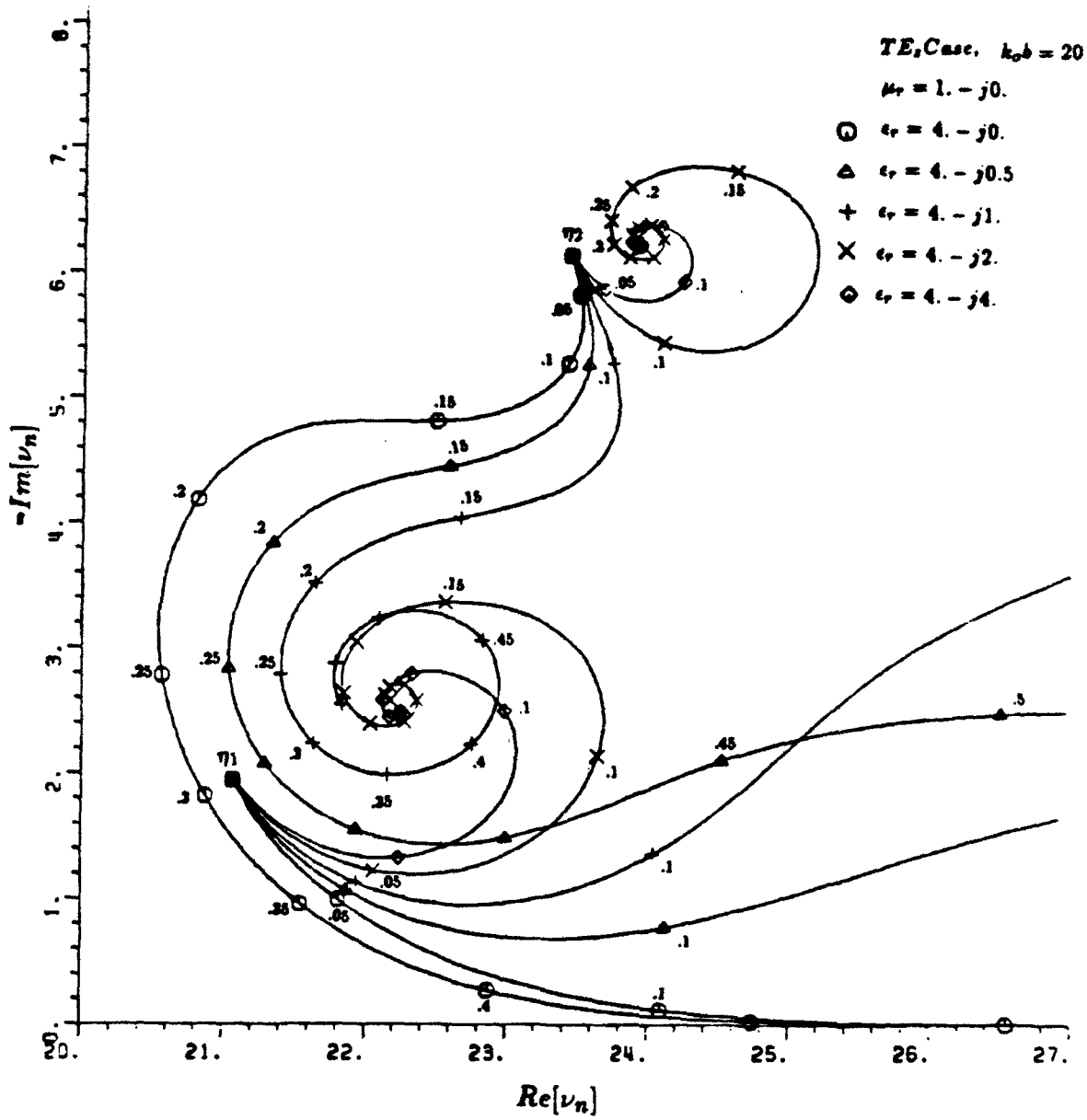


Figure 4.11: The roots of the transcendental equation

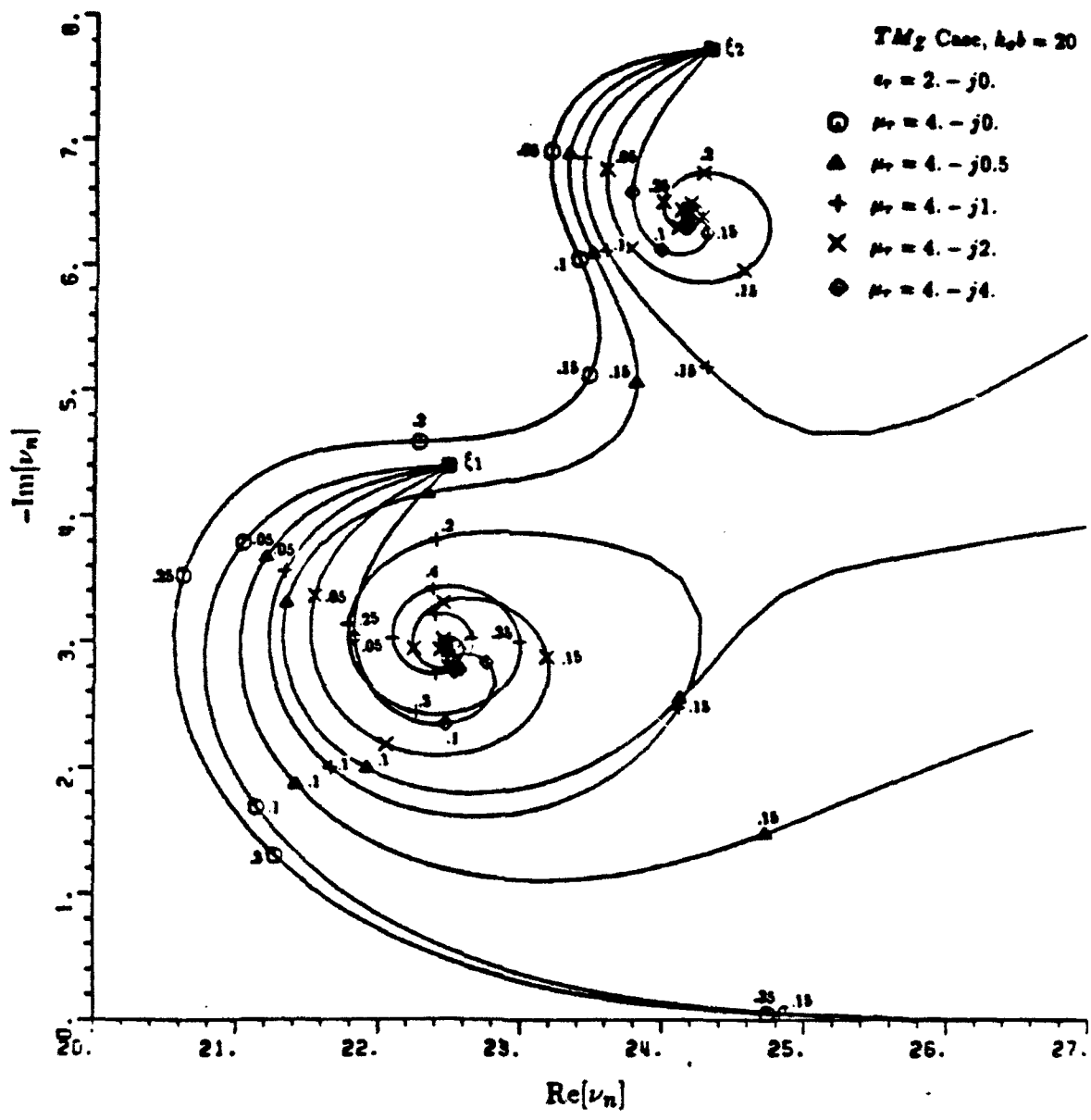


Figure 4.12: The roots of the transcendental equation

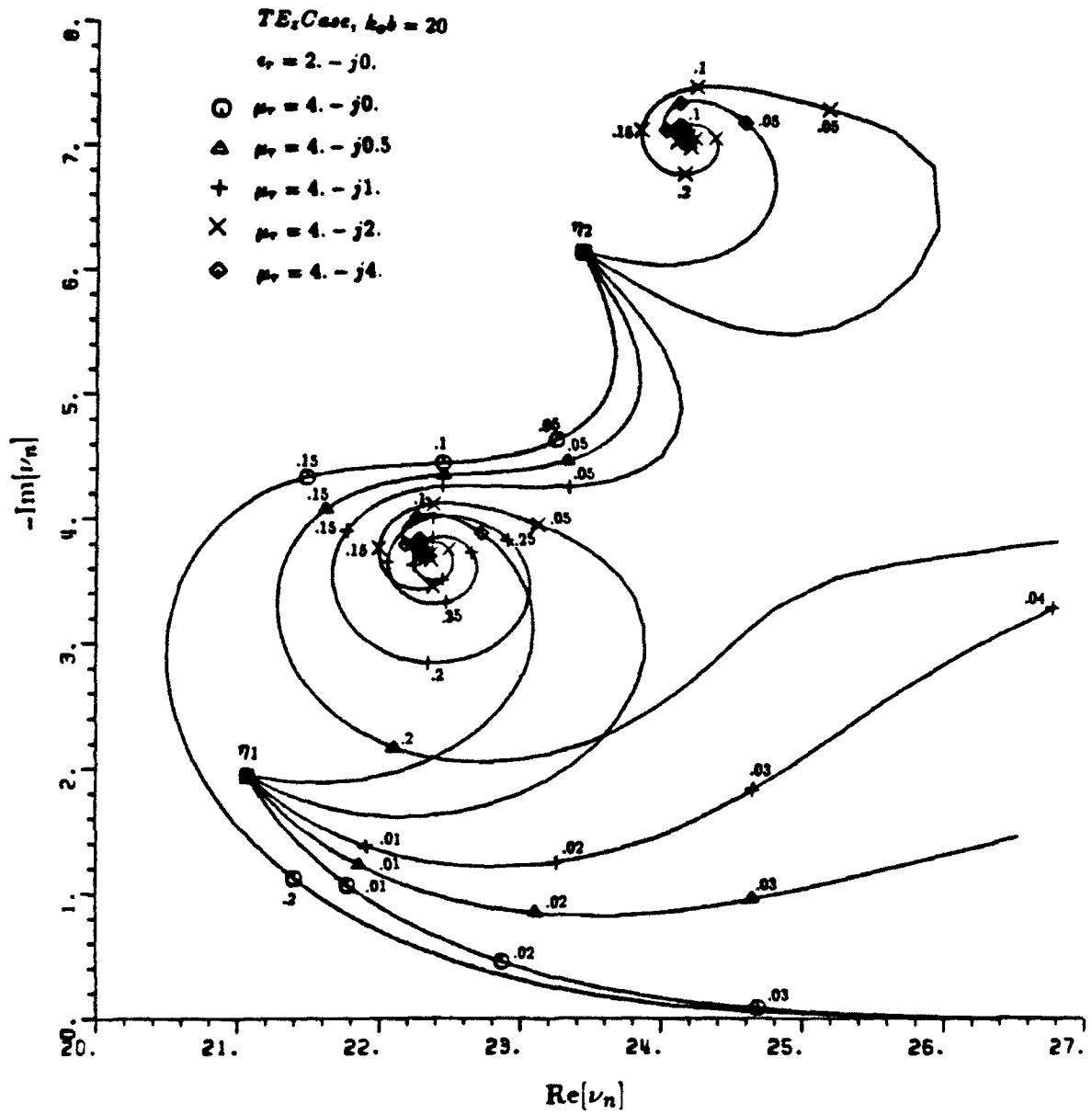


Figure 4.13: The roots of the transcendental equation

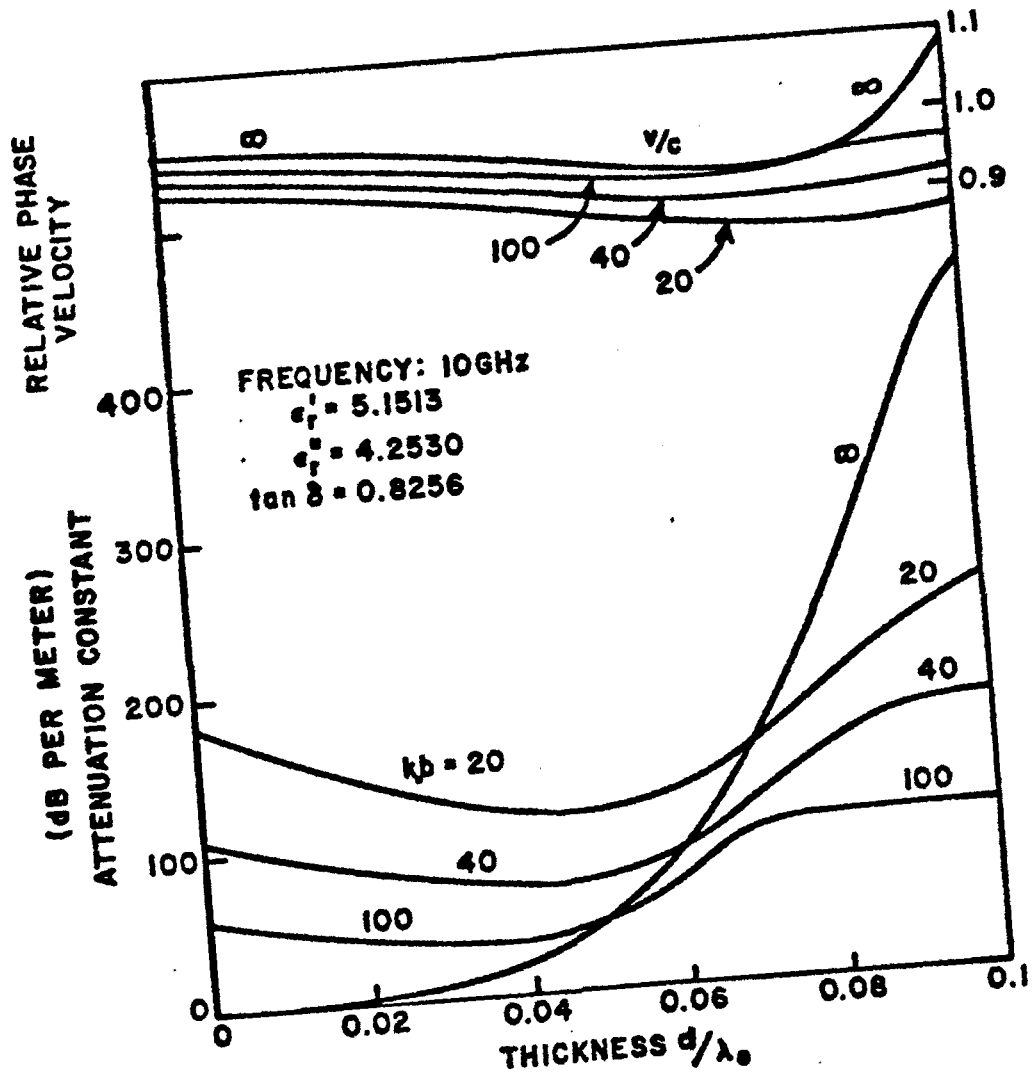


Figure 4.14: The relative phase velocity and the attenuation

4.2 Dominance of Creeping Wave Modes

It is known that the coated cylinder supports an infinite number of creeping wave modes. In this section, the contribution of the different creeping wave modes to the diffraction field is compared. The residue series solution for the diffraction field, which is obtained from the Watson's transformation of slowly convergent angular eigenfunction series solution, is fast convergent in the deep shadow region. Thus in the actual calculation of the diffracted field, one or two dominant modes are enough to obtain a numerically accurate result. It is important therefore to determine which mode is dominant over other modes. One should not conclude that a certain mode is dominant over other modes simply because that it has a smaller attenuation constant. This is because the magnitude of the diffracted field is dependent not only on the attenuation constant but also on the diffraction coefficient given in Equation (3.124). For the perfectly conducting cylinder, the first creeping wave mode is always dominant over all other modes and therefore only the first mode is adequate in practice. This is partly because the first mode has a lower attenuation constant than other higher modes. However, this is not always true for the impedance or the coated cylinder. For the coated cylinder, the dominance of the creeping wave mode changes as the thickness of the coating changes. Thus, for some thickness of coating, the second or even higher mode has a smaller attenuation constant and a larger diffraction coefficient than the first mode and therefore is dominant over the first mode. This fact is well demonstrated by following example.

Figure 4.15 shows the normalized backscattering width of the coated cylinder. The radius of the inner conducting cylinder is $35/2\pi \lambda_0$ (i.e., $k_0 b = 35$). A lossless dielectric material with $\epsilon_r = 2.56$ and $\mu_r = 1$ is coated on the conducting cylinder. The incident plane wave has a magnetic field parallel to the cylinder axis (i.e. TE_z

case). It is known that the distinctive ripples in the backscattered field is due to the creeping wave resonance [4]. Furthermore, the resonances in Figure 4.15 can be traced to the contribution of two creeping wave modes.

For a very thin coating, the diffraction field is small due to high attenuation and therefore normalized backscattering width is mainly determined by the reflection field. As the coating material is lossless, normalized backscattering width is zero dB for very thin coating. The resonance comes from the first creeping wave mode whose trajectory of propagation constant (i.e. ν_1) as a function of coating thickness is shown in Figure 4.17. The resonance from the first creeping wave mode becomes negligible after the thickness of the coating exceeds $0.2 \lambda_0$. For coating thicknesses of $0.2 \lambda_0 \sim 0.45 \lambda_0$, creeping wave is very weak compared with the reflected field and thus has a negligible contribution to the total backscattering field. As the coating thickness increases further, the resonance originated from the second creeping wave begins to appear in the backscattering width between $d = 0.45 \lambda_0$ and $d = 0.7 \lambda_0$. The trajectory of the propagation constants for the second creeping wave mode (i.e. ν_2) is also plotted in Figure 4.17. Thus, the second creeping wave mode plays an important role in the total backscattering field for coating thickness of $0.45 \lambda_0 \sim 0.7 \lambda_0$ and disappears for further increase of the coating thickness. It is also expected that if we further increase the coating thickness, the third or even higher modes can be dominant. This phenomena can be explained as follows.

The magnitude of the diffracted field depends on two factors; the diffraction coefficient and the attenuation constant of the creeping waves. It turns out that, for the range from $d = 0.2 \lambda_0$ to $d = 0.45 \lambda_0$, even the attenuation is small (see Figure 4.17), the diffraction coefficient for the first creeping wave mode as shown in Figure 4.16 is insignificant to contribute to the backscattered field. In the same range, the contribution to the backscattered field due to the second creeping wave mode is

also minimal due to the attenuation. However, when the thickness of the coating is increased beyond $0.45\lambda_o$, the attenuation rate for the second creeping wave mode drops significantly such that its contribution dominates the backscattered field. It is of interest to point out that the thickness of the dielectric coating for the coated cylinder at which the resonances begin to occur corresponds approximately to the cutoff frequencies of the surface waves supported by the planar grounded slab [7]. Similar creeping wave resonances occur in the backscattering width for the TM_z case as shown in the Figure 4.18. The corresponding trajectories of the propagation constants are shown in the Figure 4.20 and the diffraction coefficients for the TM_z modes are shown in Figure 4.19. The explanation for the TE_z resonances also applies to the TM_z case. However, it is found that the second resonance occurring between $d = 0.6\lambda_o$ and $d = 0.75\lambda_o$ as shown in Figure 4.18 comes from a creeping wave with a different origin. Referring to Figure 4.20, it is seen that as the thickness of the coating is decreased, the trajectory of this unusual mode does not lead to the usual second creeping wave mode for the perfectly conducting cylinder (i.e. ξ_2). It appears that there exist an additional set of creeping-wave modes for cylinders with dielectric coating. These 'new' creeping-wave modes yield the dominant contribution to the diffracted field when the coating becomes thick.

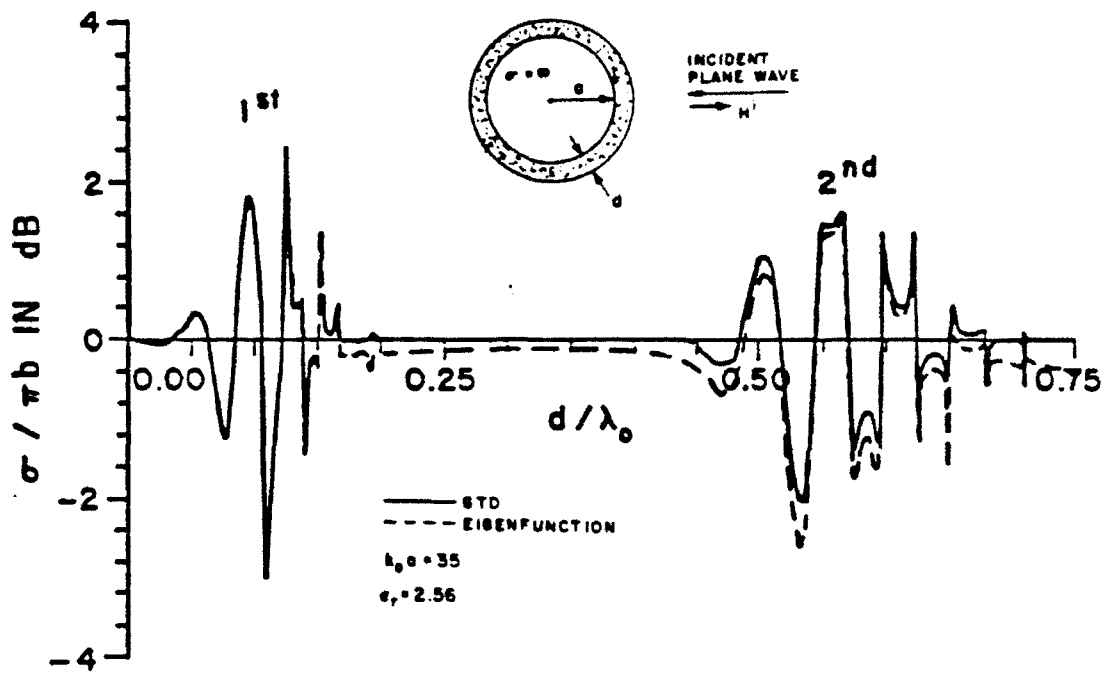


Figure 4.15: Normalized echo width

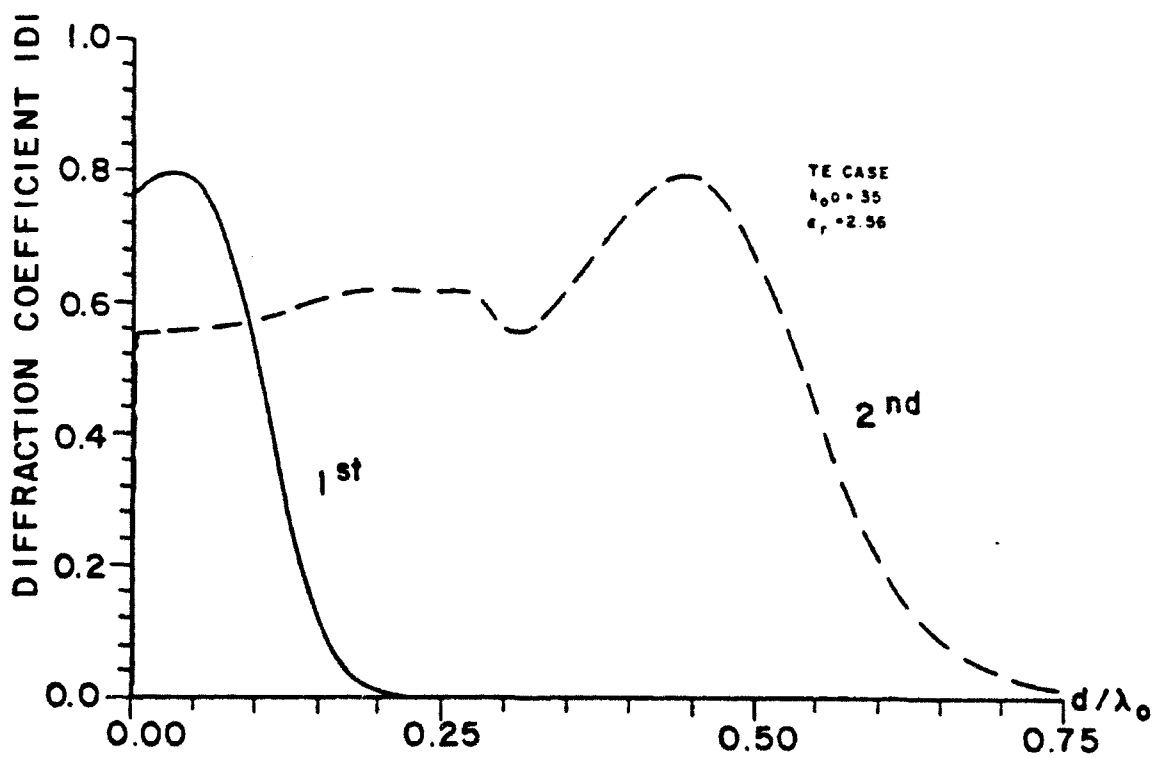


Figure 4.16: Diffraction coefficient

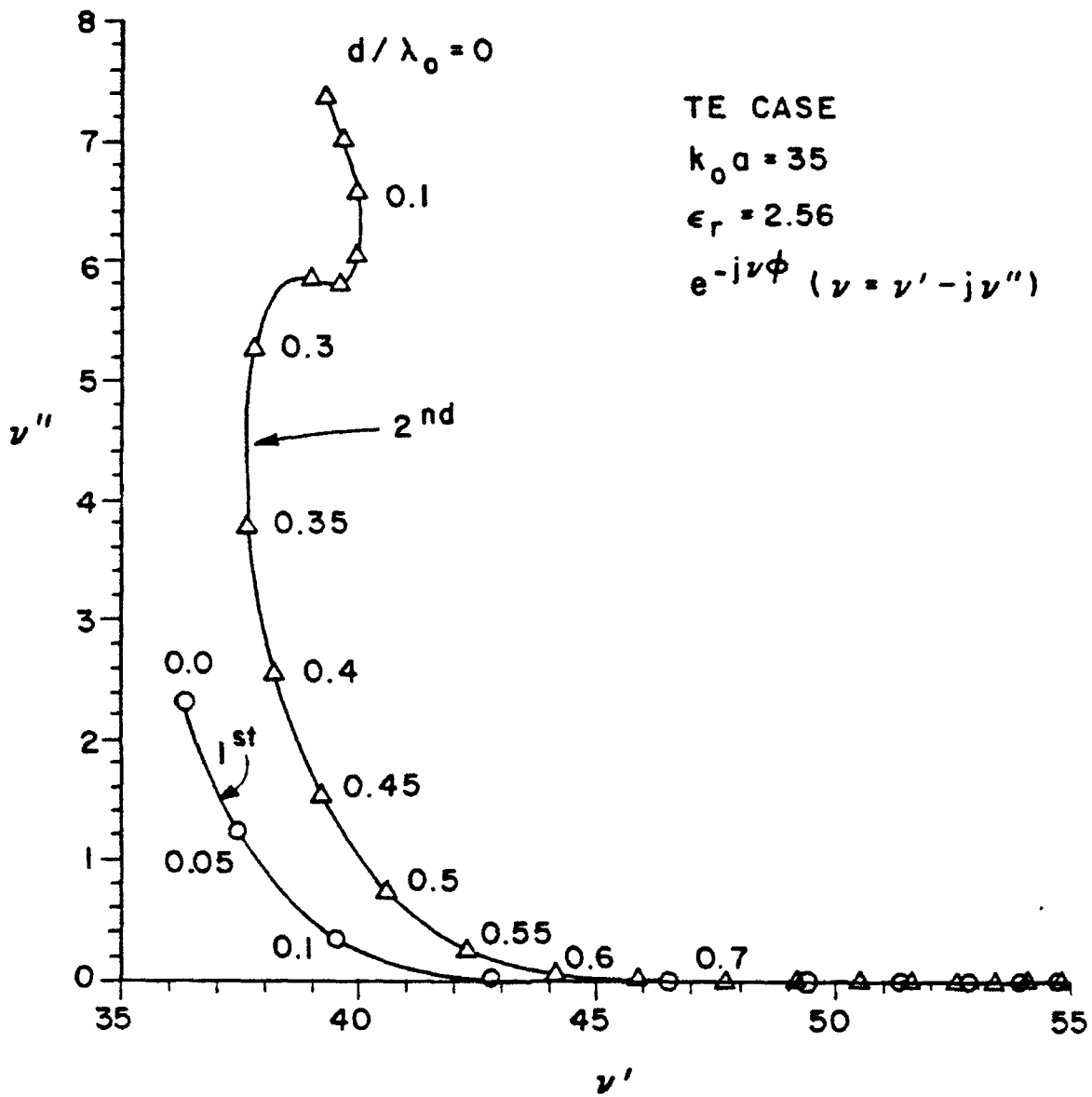


Figure 4.17: Propagation and the attenuation constant

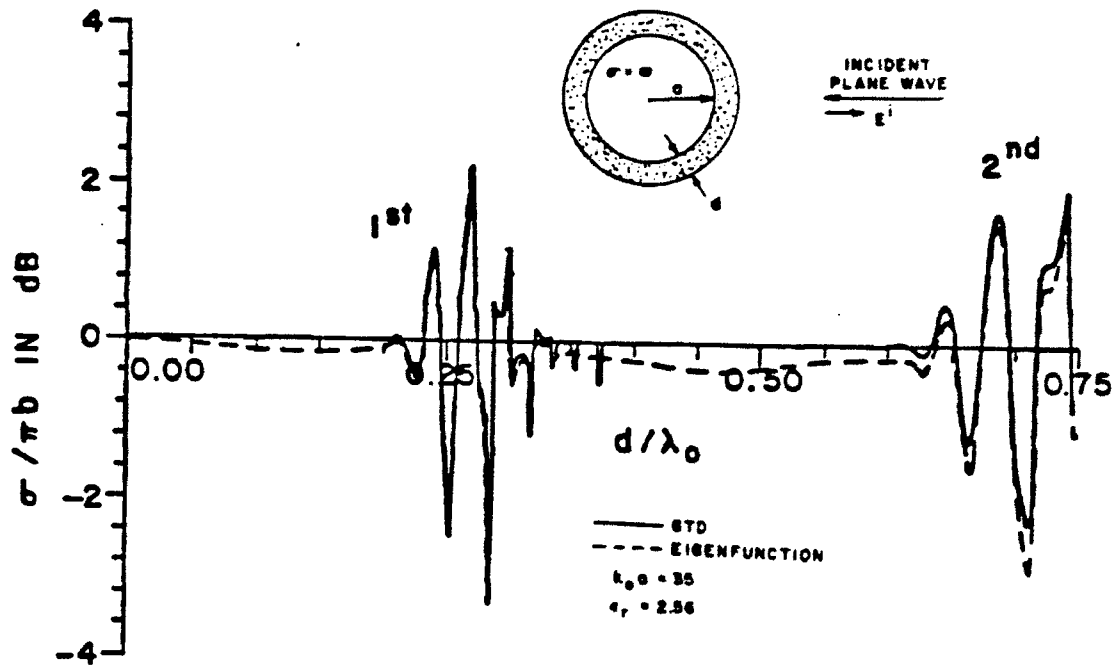


Figure 4.18: Normalized echo width

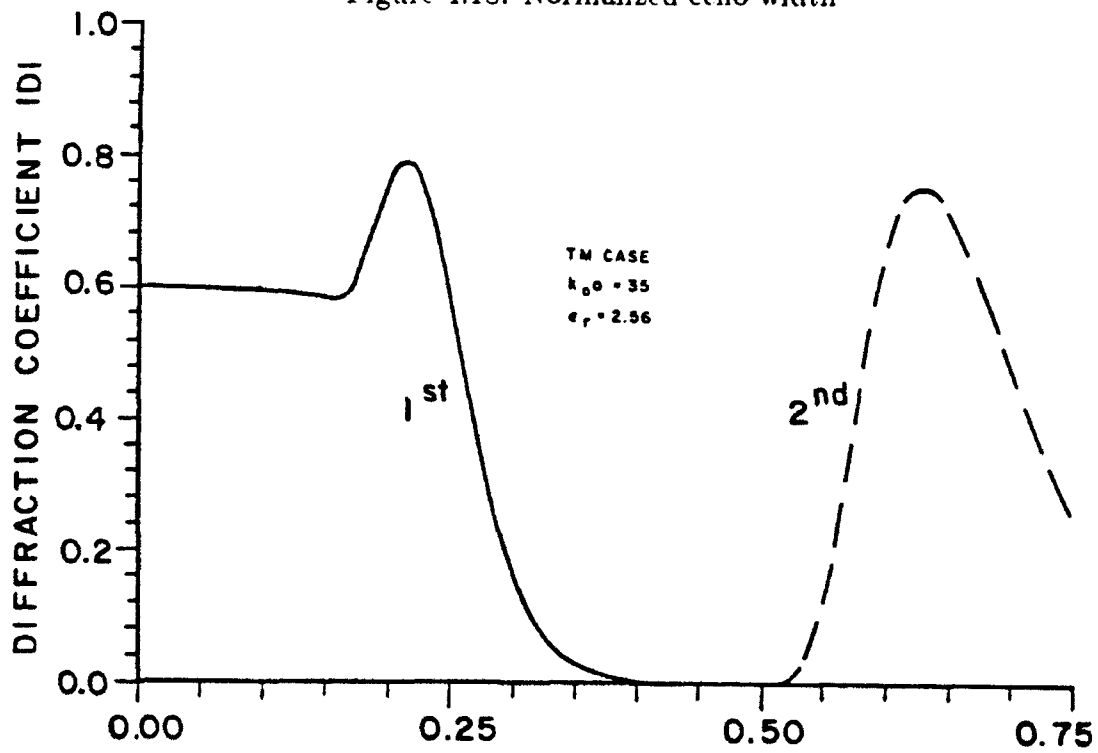


Figure 4.19: Diffraction coefficient

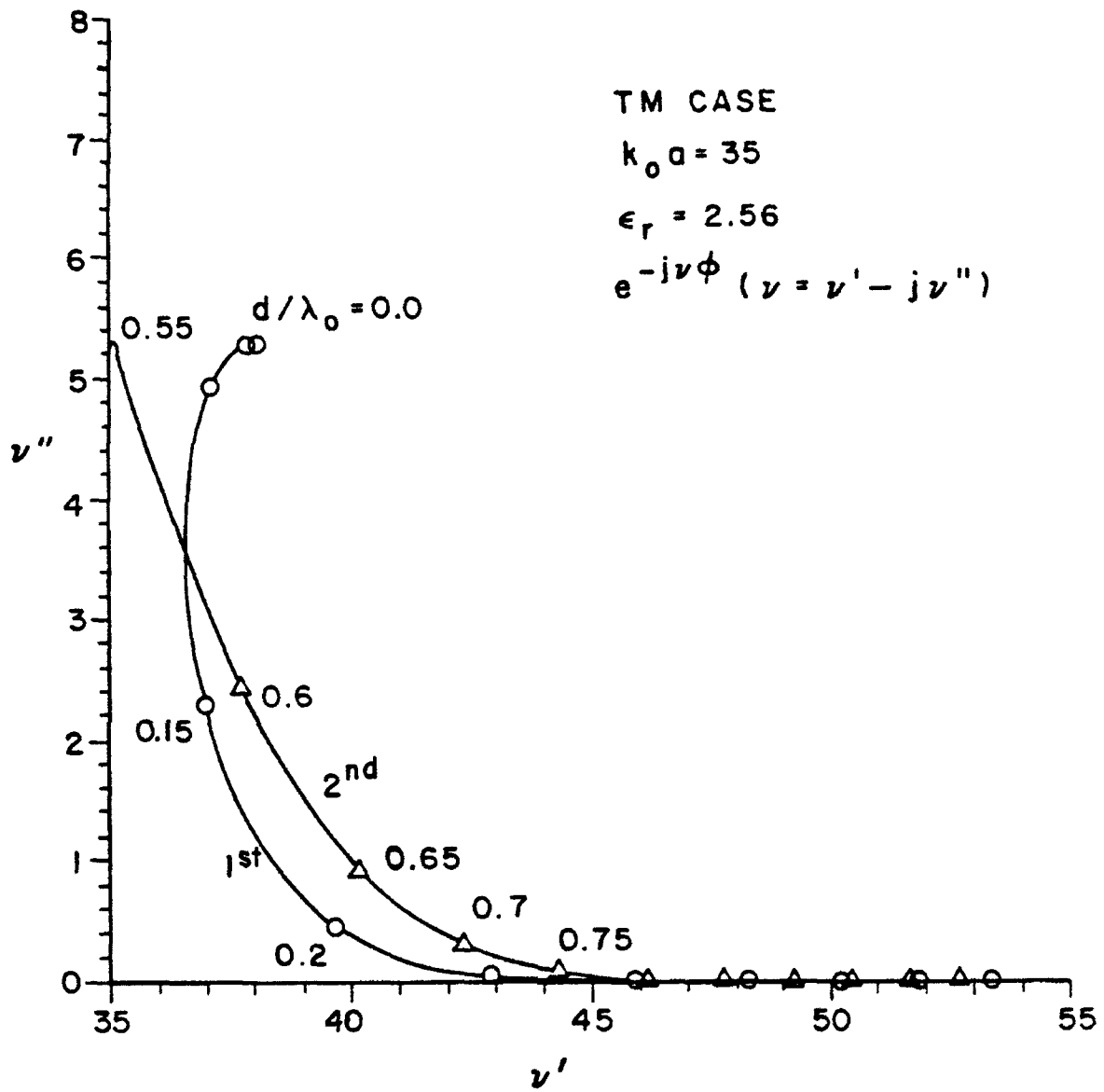


Figure 4.20: Propagation and the attenuation constant

4.3 Creeping waves on a large cylinder

In this section, we investigate the behavior of creeping waves on the coated surface with electrically large radius of curvature. The investigation in this section is prompted by an apparent discrepancy between the attenuation constants for the creeping waves on a coated curved surface and those for the surface wave on a planar grounded slab. Referring to Figure 4.14, as the circumference of the circular cylinder is increased from 20 to 100, the attenuation constants for the creeping waves do not approach the planar-slab limit. This contradicts past experience for the perfectly conducting cylinder with a lossless coating. The radius of the circular cylinder is increased to an even larger value in order to check the limiting case. The attenuation constants were calculated for several cylinders with large radius, and interesting results were obtained. Figure 4.21 presents the roots of the transcendental equation of the circular cylinder ($b = 50\lambda_o$, i.e. $k_o b = 100\pi$) with a high loss material coating ($\epsilon_r = 5.1513 - j4.253$, $\mu_r = 1 - j0$). In Figure 4.21, the trajectories ν_n for the first five of the infinite creeping wave modes are shown as a function of the thickness of coating from zero to a final value of $0.1 \lambda_o$. It is observed from Figure 4.21, that the imaginary part of ν_n of the first creeping wave mode becomes larger than those of mode 2, 3, and 4 as the thickness of the coating is increased. The corresponding attenuation constants are shown in Figure 4.22. It can be seen that the attenuation constant for the first creeping wave mode behaves like that of the surface wave associated with the planar grounded slab as shown in Figure 4.14. The fields associated with the first mode are rapidly attenuated to a negligible value. This phenomena does not occur for the smaller cylinder ($k_o b = 100$ i.e. $b = 100/2\pi \lambda_o$ in Figure 4.14). The diffraction coefficient of each mode is also plotted in Figure 4.23. The dominance of the mode can be determined by comparing both the attenuation and the diffraction coefficient of

each mode.

To further demonstrate the limiting case, numerical results obtained for a cylinder with $b=100 \lambda_0$ are shown in Figure 4.24 and 4.25. It is seen that the attenuation constants of the first creeping wave mode for both cylinders ($b=50 \lambda_0$ and $b=100 \lambda_0$) converge to each other and both approach the planar limit. Finally, the diffraction coefficients for the creeping wave modes of the coated curved surface with a radius of $100 \lambda_0$ are shown in Figure 4.26. Thus, in this section we demonstrated the fact that the first creeping wave mode behaves the same way as the surface wave associated with the planar grounded slab.

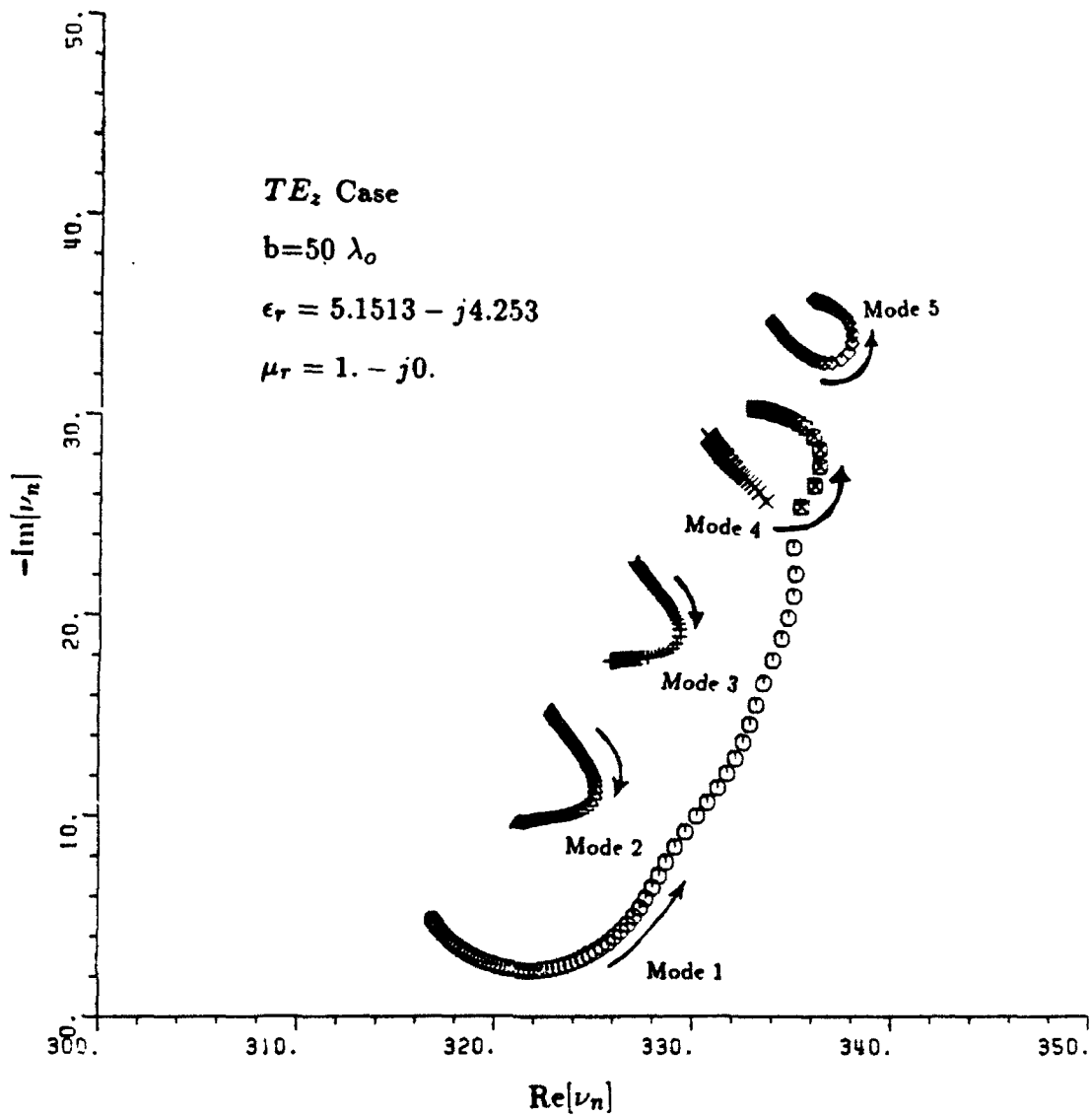


Figure 4.21: Trajectory of roots

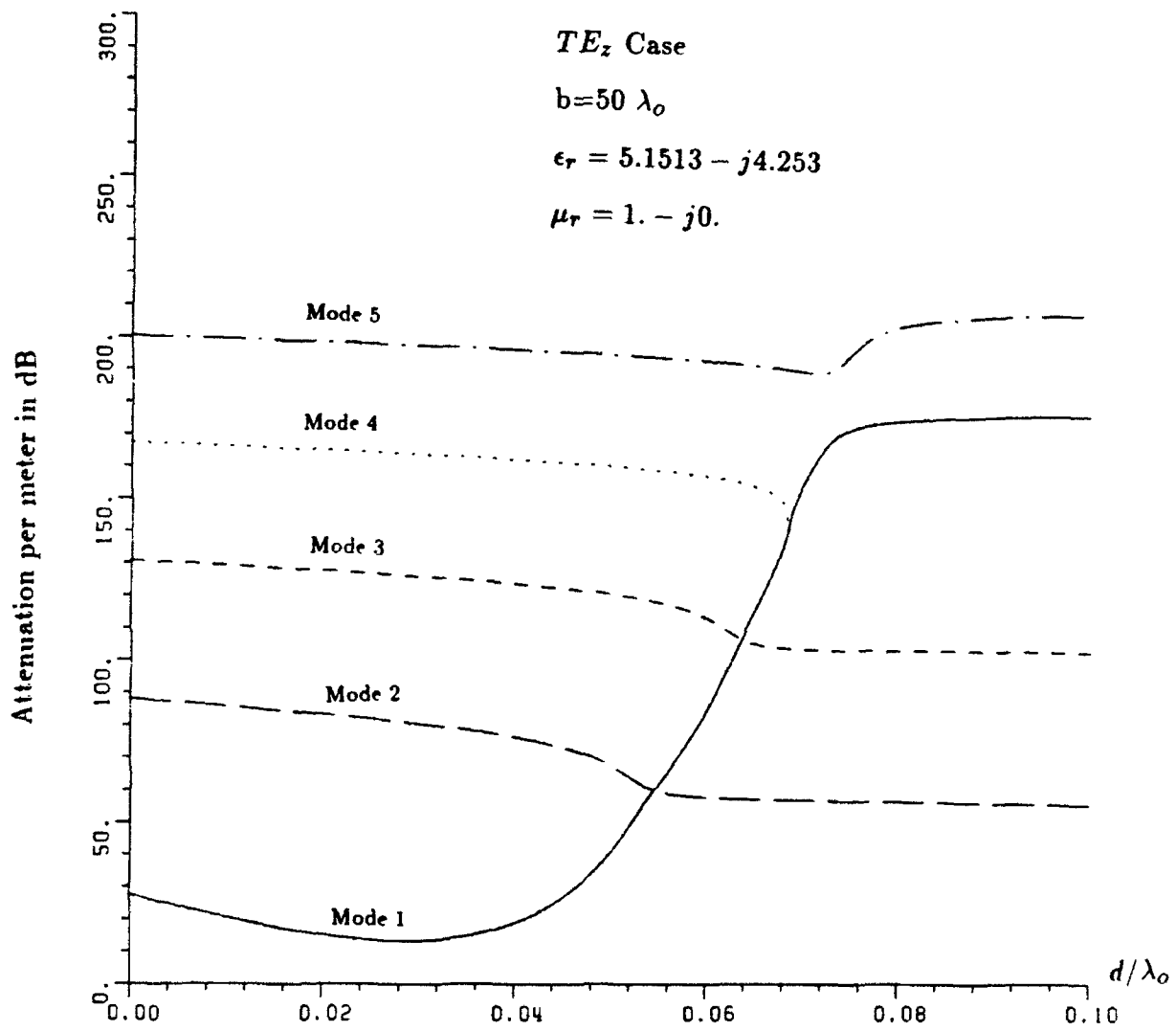


Figure 4.22: Attenuation per meter

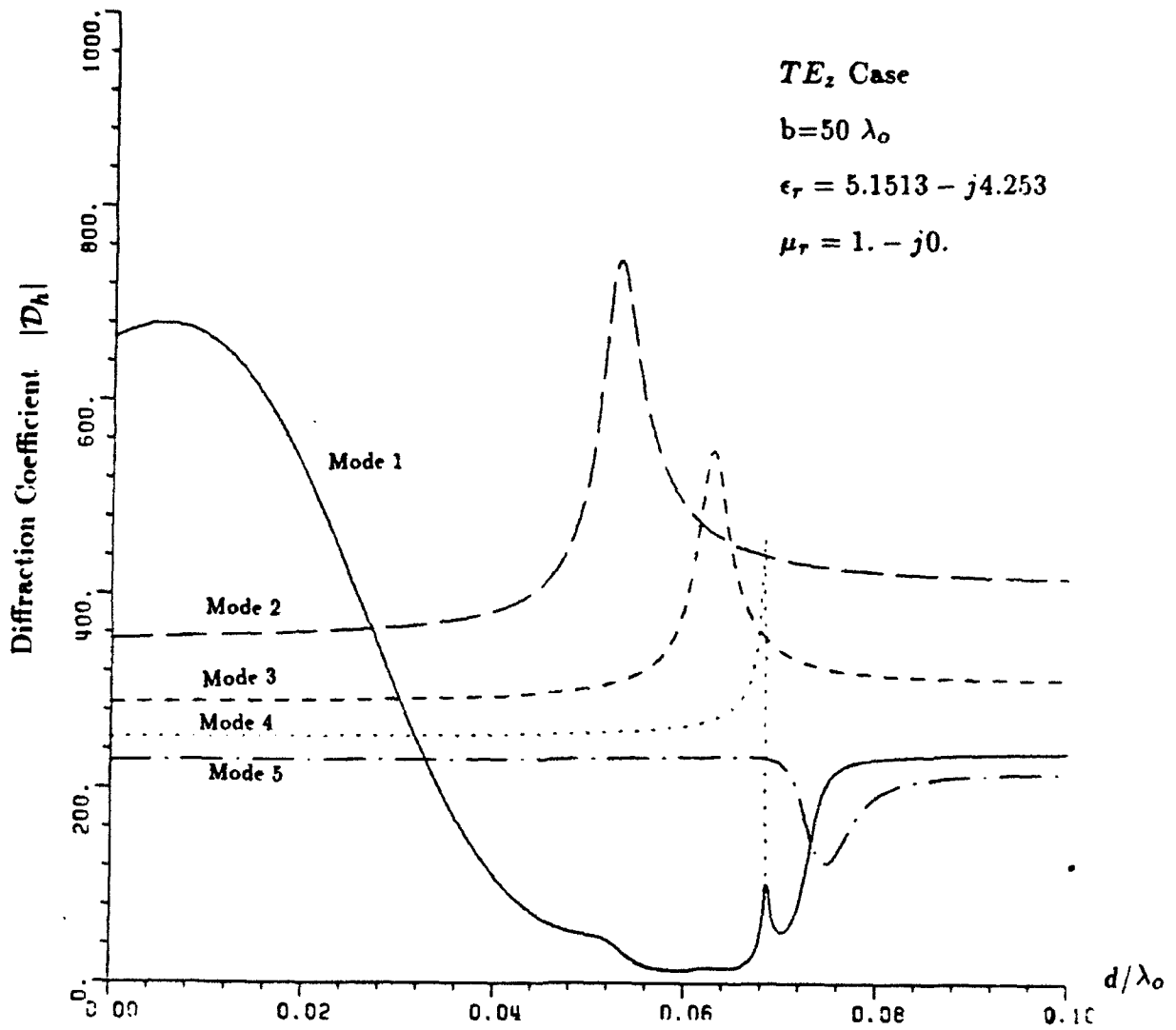


Figure 4.23: Diffraction coefficient

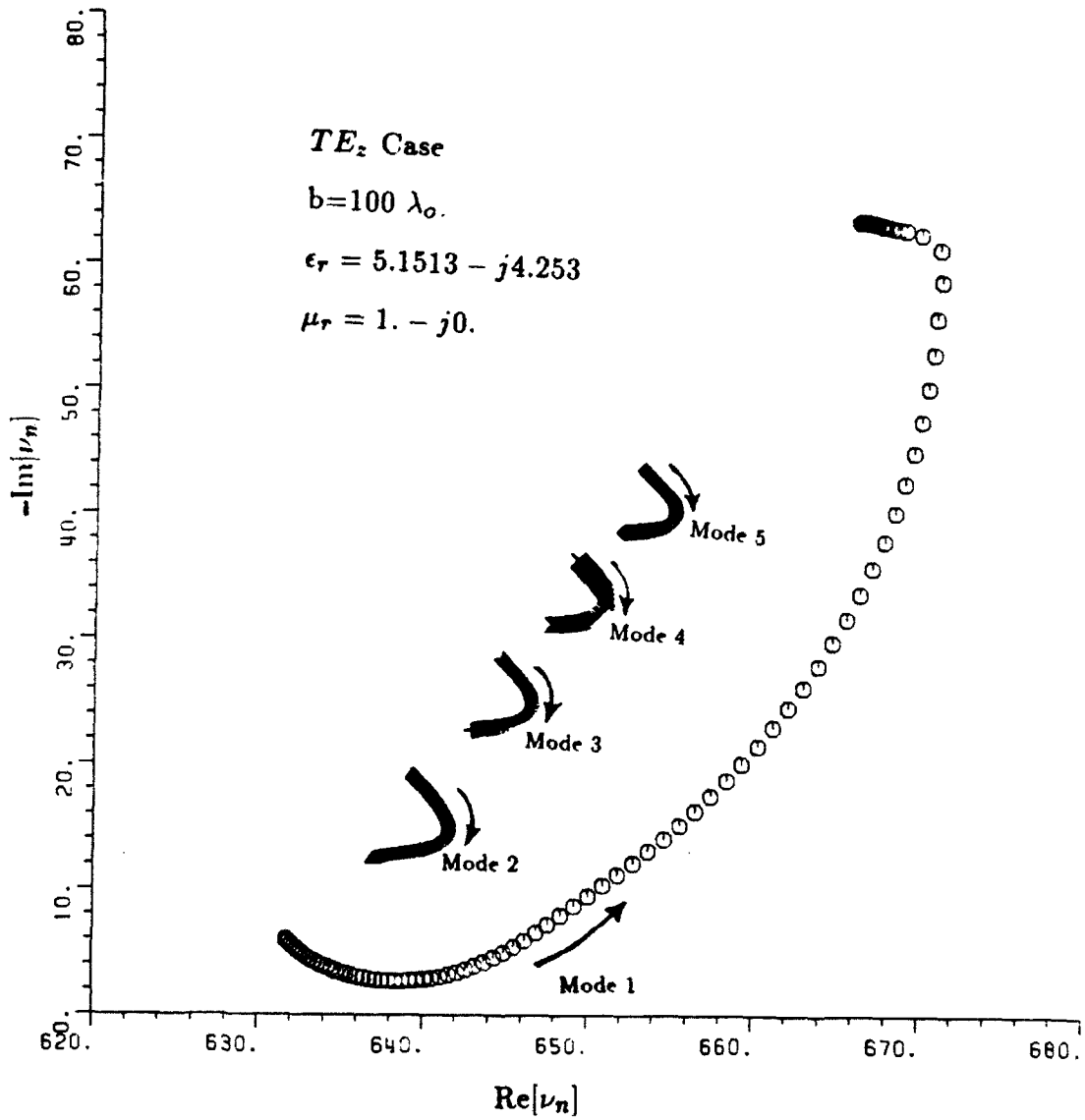


Figure 4.24: Trajectory of roots

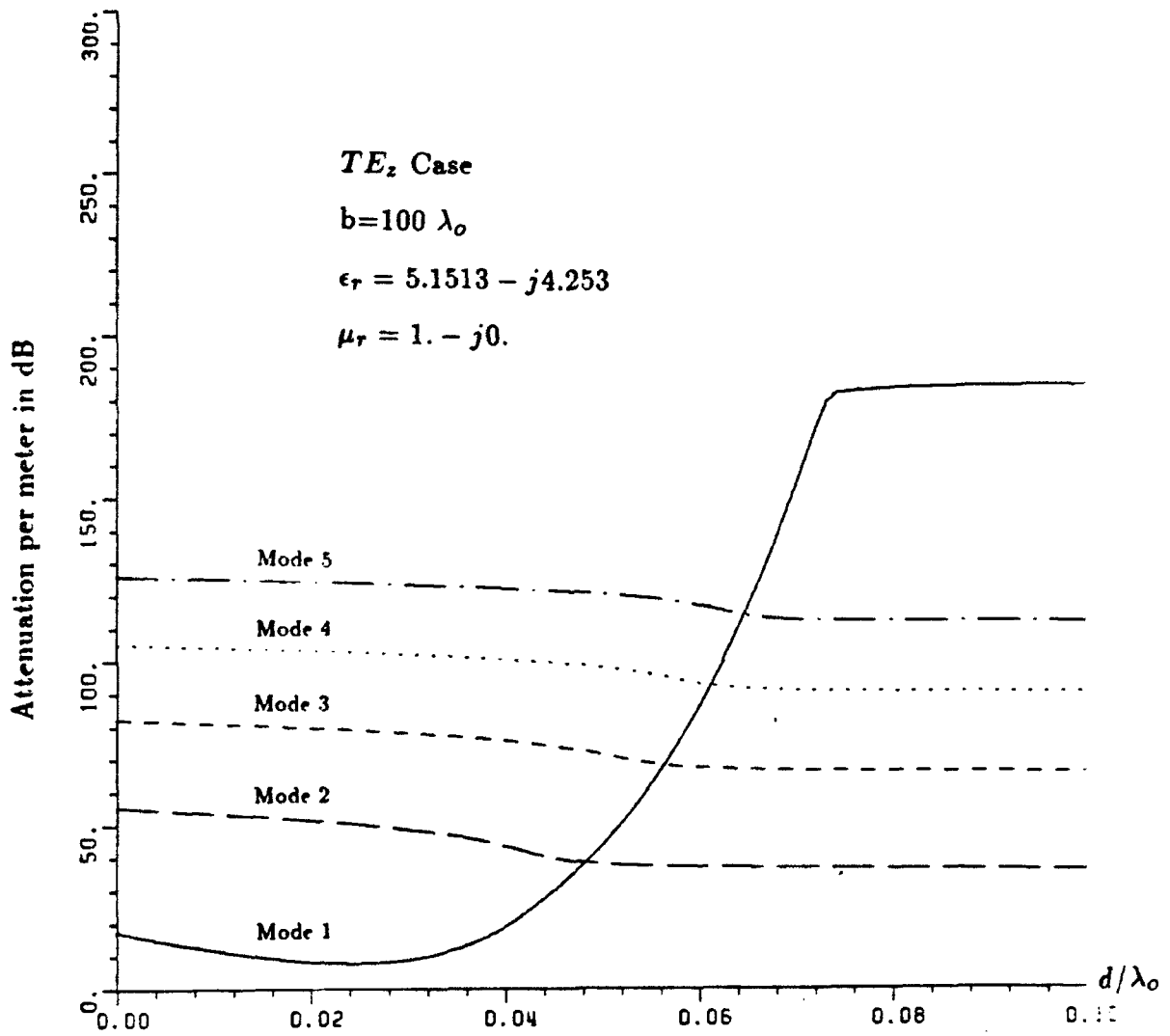


Figure 4.25: Attenuation per meter

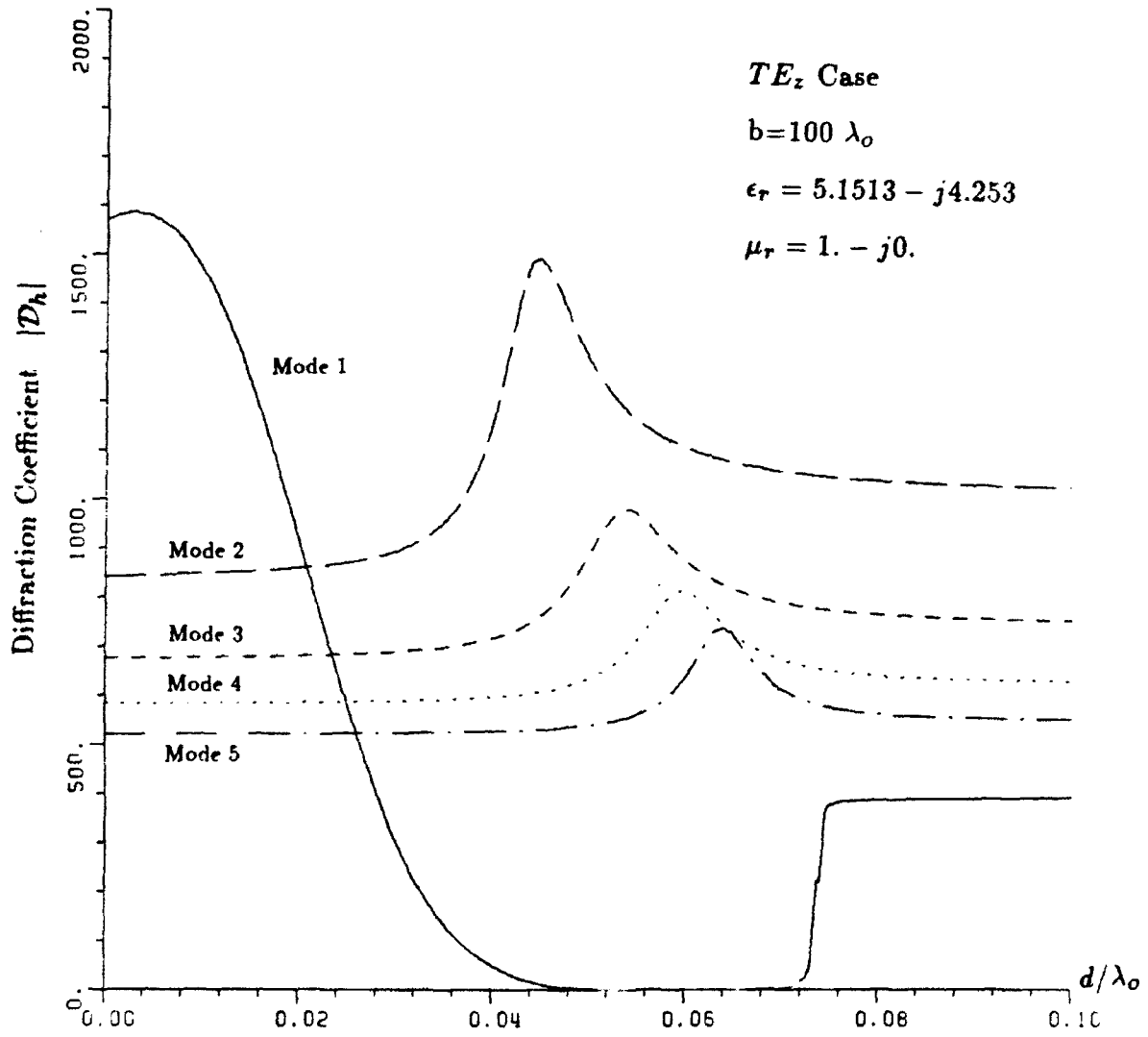


Figure 4.26: Diffraction coefficient

CHAPTER V

FIELD IN THE TRANSITION REGION

As seen from the numerical results of examples given in Chapter III, the GTD solution fails within the shadow boundary (S.B.) transition region. The various causes for this failure are also explained in Chapter III. In this Chapter, we attempt to correct the failure of the ordinary GTD in the transition regions.

For a perfectly conducting cylinder, the uniform GTD solution which is often abbreviated as UTD has already been developed and successfully applied to many engineering problems. UTD solution for the curved surface was first introduced by Pathak [3] for the canonical problem of plane wave scattering by a smooth perfectly conducting circular cylinder. As its name implies, uniform GTD is "uniform" in the sense that it remains valid within the transition regions and it automatically reduces to the ordinary GTD exterior to the transition regions where the ordinary GTD becomes valid and accurate. Both GTD and UTD employ the same ray paths and thus both solutions have the same ray formats.

For the impedance cylinder, UTD solution has already been developed by a heuristic extension of the UTD solution for the conducting cylinder [5]. For the cylinder with dielectric/ferrite coating, the solution which gives a uniform result in the transition region has not yet been developed. However, the fact that both the impedance and the coated cylinder employ the same ray format outside the transition region as for the conducting cylinder suggests the possibility that the same uniform GTD solution developed for the conducting cylinder might also be used

for the coated cylinder within the transition region. Based on this conjecture, we heuristically generalize the UTD solution for the perfectly conducting cylinder to both the impedance and the coated cylinder with necessary modifications in the transition function due to the differences in the boundary conditions. The difficulty in finding the uniform solution for the impedance and the coated cylinder is that the numerical data for the transition function $\hat{P}_{s,h}$, which, is well tabulated for the conducting cylinder is not available. Instead of direct numerical evaluation of the transition function, an exact eigenfunction solution together with the GTD solution is used to obtain the necessary numerical data for $\hat{P}_{s,h}$. The validity and limitation of the heuristic method has also been tested by some examples.

5.1 Uniform GTD solution for the impedance and the coated cylinder

In this section we generalize the uniform GTD solution for the conducting cylinder to the impedance and the coated cylinder based on the conjecture that the ray format given for UTD solution of the conducting cylinder can be retained to both the impedance and the coated cylinder. The lengthy asymptotic analysis and the ray format of UTD solution for the conducting cylinder are given by Pathak [3].

5.1.1 Lit region

From the result given for the conducting cylinder, the ray format for the impedance and the coated cylinder in the lit region can be obtained by replacing $\hat{P}(\xi')$ with $\hat{P}(\xi', q)$. Thus when the field point P_L is in the lit region, u^o is given as

$$u^o(P_L) \approx u^i(P_L) + u^i(Q_R) \mathcal{R}_{s,h} \sqrt{\frac{\bar{\rho}^r}{\bar{\rho}^r + l_2}} e^{-jk_0 l_2} \quad (5.1)$$

where the reflected ray caustic distance $\bar{\rho}^r$ can be calculated from the relationship

$$\frac{1}{\bar{\rho}^r} = \frac{1}{l_1} + \frac{2}{b \cos \theta_i} \quad (5.2)$$

The subscript s and h denotes TM_z (soft) and TE_z (hard) case respectively. In Equation (5.1), the surface reflection coefficient $R_{s,h}$ in the ordinary GTD solution is now replaced by the generalized reflection coefficient $\mathcal{R}_{s,h}$ defined as

$$\mathcal{R}_{s,h} \equiv -\sqrt{\frac{-4}{\xi'}} \exp\left(-j\frac{\xi'^3}{12}\right) \left\{ \frac{e^{-j\pi/4}}{2\xi'\sqrt{\pi}} [1 - F(X^L)] + \hat{P}_{s,h}(\xi', q) \right\} \quad (5.3)$$

where

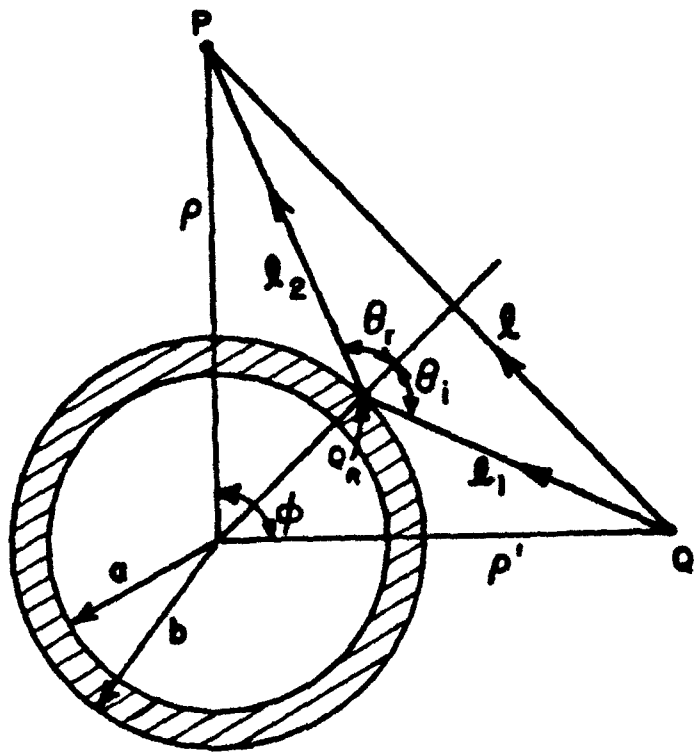


Figure 5.1: Field in the lit part of transition region

$$\xi' = -2m \cos \theta_i \quad ; \quad m = \left(\frac{k_0 b}{2} \right)^{1/3} \quad (5.4)$$

and

$$X^L = 2k_0 \frac{l_1 l_2}{l_1 + l_2} \cos^2 \theta_i \quad (5.5)$$

The relevant parameters θ_i , l_1 , l_2 and the specular reflection point Q_R are shown in Figure 5.1.

The transition function $F(x)$ which involves a Fresnel integral is defined as

$$F(x) \equiv 2j\sqrt{x} e^{jx} \int_{\sqrt{x}}^{\infty} e^{-j\tau^2} d\tau \quad (5.6)$$

The transition function $F(x)$ plays a key role in enforcing the continuity and boundedness of the total field at the shadow boundary.

The transition function $\hat{P}_{s,h}(\xi, q)$, which is generally referred as the *Pekeris caret* function is defined as

$$\hat{P}_{s,h}(\xi, q) \equiv \frac{e^{-j\pi/4}}{\sqrt{\pi}} \int_{-\infty-j\epsilon}^{\infty-j\epsilon} \frac{V'(\tau) - qV(\tau)}{W_2'(\tau) - qW_2(\tau)} e^{-j\xi\tau} d\tau \quad (5.7)$$

where q is defined as

$$q \equiv -jmC_{s,h}(\nu) \quad (5.8)$$

Thus for the impedance cylinder, q is a constant given as

$$q = -jm \frac{Z_o}{Z_s} \quad \text{for } TM_z \quad : \quad q = -jm \frac{Z_s}{Z_o} \quad \text{for } TE_z \quad (5.9)$$

However for the coated cylinder, q is a function of ν . For the simplicity of the calculation, we assume that q can be approximated as

$$q \approx -jmC_{s,h}(\nu_n) \quad (5.10)$$

where ν_n is the dominant n_{th} root of the transcendental equation given in Equation (4.4). The Fock-type Airy functions $V(\tau)$ and $W_2(\tau)$ are defined as

$$2jV(\tau) = W_1(\tau) - W_2(\tau) \quad (5.11)$$

and

$$W_{1,2} = \frac{1}{\sqrt{\pi}} \int_{\Gamma_{1,2}} e^{\tau t - t^3/3} d\tau \quad (5.12)$$

The contour Γ_1 runs from $\infty e^{-j2\pi/3}$ to $\infty - j\epsilon$, and Γ_2 is the complex conjugate of Γ_1 . The transition function $\hat{P}_{s,h}(x, q)$ can also be expressed in terms of the the Fock integrals $p^*(x, q)$ and $q^*(x, q)$.

$$\hat{P}_{s,h}(x, q) = \left[\left\{ \begin{array}{c} p^*(x, q) \\ q^*(x, q) \end{array} \right\} - \frac{1}{2x\sqrt{\pi}} \right] e^{-j\pi/4} \quad (5.13)$$

5.1.2 Shadow region

A ray format for the shadow region can also be obtained from the result given for the conducting cylinder by replacing $\hat{P}(\xi)$ with $\hat{P}(\xi, q)$. When the field point P_d is in the shadow region, the ray format for u^o is given by

$$u^o(P_d) \approx u^i(Q_1) T_{s,h} \frac{e^{-jk_0 s_2}}{\sqrt{s_2}} \quad (5.14)$$

From Equation (3.121), the transfer function $T_{s,h}$ for the ordinary GTD solution is given as

$$T_{s,h} \equiv \frac{1}{\sqrt{k_0}} \sum_n \mathcal{D}_n^{s,h}(Q_1) \exp[-(\alpha'_n + j\beta'_n)t] \mathcal{D}_n^{s,h}(Q_2) \quad (5.15)$$

where the diffraction coefficient $\mathcal{D}_n^{s,h}(Q)$ is given by Equation (3.124). However, in the uniform GTD, the transfer function $T_{s,h}$ is replaced with a generalized transfer function $\mathcal{T}_{s,h}$ defined as

$$\mathcal{T}_{s,h} = -m e^{-jk_0 t} \sqrt{\frac{2}{k_0}} \left\{ \frac{e^{-j\pi/4}}{2\xi\sqrt{\pi}} [1 - F(X^d)] + \hat{P}_{s,h}(\xi, q) \right\} \quad (5.16)$$

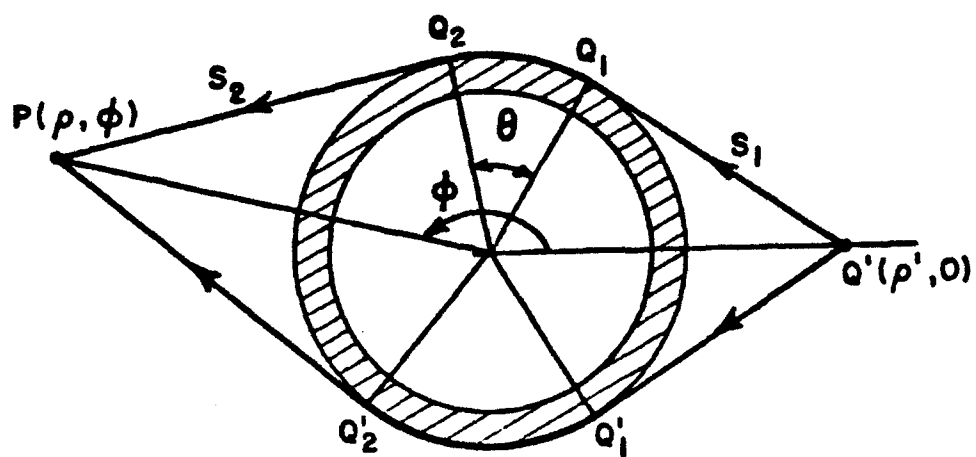


Figure 5.2: Field in the shadow part of transition region

where

$$\xi = m\alpha \quad ; \quad m = \left(\frac{k_0 b}{2} \right)^{1/3} \quad (5.17)$$

$$X^d = k_0 \frac{s_1 s_2}{s_1 + s_2} \frac{\xi^2}{2m^2} \quad (5.18)$$

and

$$t = b \alpha \quad (5.19)$$

The relevant parameters s_1 , s_2 , t , α and two tangent points Q_1 , Q_2 are shown in Figure 5.2. The uniform GTD solution reduces to the ordinary GTD solution in the deep shadow region.

5.2 Transition function

The transition function $\hat{P}_{s,h}(x, q)$ has also been studied by Wait and Conda [17] for a cylinder with finite conductivity. The quantity $e^{-j\frac{\pi}{4}} p^*(\xi, q)$ is, in fact, equivalent to the $G(\xi)$ defined in [17, eq(22)]. For a cylinder with finite conductivity, the function $G(\xi)$ has been evaluated via direct numerical integration and tabulated for the various values of q . However, for a positive real value which occurs for a cylinder with a pure reactive surface impedance or with a lossless coating no numerical data have been given. Under this condition, the direct numerical integration is more involved because the integrand has a singularity close to the integration path. Therefore a heuristic approach [5], rather than the direct integration, is employed in this section to deduce numerical results for the transition integral. This engineering approach is described in following paragraph.

a) Lit part of the transition region

From Equation (5.1) and (5.3) we obtain

$$u^o(P_L) - u^i(P_L) \approx -u^i(Q_R) \sqrt{\frac{-4}{\xi'}} \exp\left(-j\frac{\xi'^3}{12}\right) \times \left[\left\{ \begin{array}{c} p^*(\xi', q) \\ q^*(\xi', q) \end{array} \right\} - \frac{F(X^L)}{2\xi' \sqrt{\pi}} \right] e^{-j\frac{\pi}{4}} \sqrt{\frac{\bar{\rho}^r}{\rho^r + l_2}} e^{-jk_0 l_2} \quad (5.20)$$

Note that

$$u^o(P_L) = u^i(P_L) - u^{cw}(P_L) \quad (5.21)$$

Therefore, the Fock integral can be expressed as

$$\left\{ \begin{array}{c} p^*(\xi', q) \\ q^*(\xi', q) \end{array} \right\} e^{-j\pi/4} \approx \frac{u^i(P_L) - u^{cw}(P_L) - u^i(P_L)}{-u^i(Q_R) \sqrt{\frac{-4}{\xi'}} \exp\left(-j\frac{\xi'^3}{12}\right) \sqrt{\frac{\bar{\rho}^r}{\rho^r + l_2}} e^{-jk_0 l_2}} + \frac{e^{-j\pi/4}}{2\xi' \sqrt{\pi}} F(X^L)$$

(5.22)

For the numerical value of u^t , we use the eigenfunction solution given in Chapter I and for u^{cw} , we use the residue series solution given in Equation (3.126).

a) Shadow part of the transition region

For the shadow part of the transition region, the same procedure employed for the lit part can be used to obtain the numerical data for the $\hat{P}(\xi, q)$. From Equation (5.14) and (5.16)

$$u^o(P_d) \approx -u^i(Q_1) m e^{-jk_0 t} \sqrt{\frac{2}{k_0}} \left[\left\{ \begin{array}{l} p^*(\xi, q) \\ q^*(\xi, q) \end{array} \right\} - \frac{F(X^d)}{2\xi\sqrt{\pi}} \right] e^{-j\frac{\pi}{4}} \frac{e^{-jk_0 s_2}}{\sqrt{s_2}} \quad (5.23)$$

$$u^o(P_d) = u^t(P_d) - u^{cw}(P_d) \quad (5.24)$$

Thus, we obtain

$$\left\{ \begin{array}{l} p^*(\xi, q) \\ q^*(\xi, q) \end{array} \right\} e^{-j\frac{\pi}{4}} \approx \frac{u^t(P_d) - u^{cw}(P_d)}{-u^i(Q_1) m e^{-jk_0 t} \sqrt{\frac{2}{k_0}} \frac{e^{-jk_0 s_2}}{\sqrt{s_2}}} + \frac{e^{-j\pi/4}}{2\xi\sqrt{\pi}} F(X^d) \quad (5.25)$$

As before, we calculate $u^t(P_d)$ from the exact eigenfunction series solution and $u^{cw}(P_d)$ from the residue series solution.

For the impedance cylinder, the numerical data for the Fock integral $e^{-j\pi/4} p^*(\xi, q)$ or $e^{-j\pi/4} q^*(\xi, q)$ obtained from the Equation (5.22) and (5.25) are given in Figure 5.3 and 5.4 for several different q . It can be observed from Figure 5.3 and 5.4 that the numerical results of the Fock integral are weakly dependent on $k_0 b$, $k_0 \rho'$ and $k_0 \rho$. Therefore, curves shown in Figure 5.3 and 5.4 can be used as "universal"

curves. to calculate the scattered field of the impedance cylinder with arbitrary radius.

For the coated cylinder, the numerical data for the Fock integral obtained using the Equation (5.22) and (5.25) are plotted in Figures 5.5, 5.6, 5.8 and 5.9 for various combination of ϵ_1 and $k_0 b$. The Fock integrals obtained for the TM_z coated cylinders are shown in Figures 5.5 and 5.5 and those for the TE_z coated cylinders are shown in Figures 5.8 and 5.9. Note that the Fock integral depends on the q -parameter. The q -parameter which is determined only by the constant surface impedance Z_s for the impedance cylinder is now a function of the radius of coated cylinder, the thickness and the material of the dielectric coating for the coated cylinder. However, it is found that, for the thin coating case, the transition integrals obtained are almost identical providing the q -values are the same. This can be seen from the results presented in Figures Figures 5.5, 5.6, 5.8 and 5.9. It turns out that, providing both have the same q -value, the transition integrals obtained for the coated circular cylinder compare surprisingly well with those obtained for the impedance cylinder. This fact can be established by comparing the results shown in Figures 5.7 and 5.10 with those shown in Figures 5.5, 5.6 and 5.8, 5.9 respectively. As a consequence, the transition integral obtained for the impedance cylinder could be employed in the uniform GTD solution to calculate the scattered fields in the transition region for the coated cylinder. The advantage here is that the procedure involved to deduce the transition integral for the impedance cylinder is much less complicated than that employed for the coated cylinder. Note that the above comments only apply to coated cylinder with a thin coating. At this stage, it is not yet clear whether the concept of uniform GTD solution with 'universal' transition integral is applicable for the case of a cylinder covered with a thick dielectric coating. This needs to be further investigated.

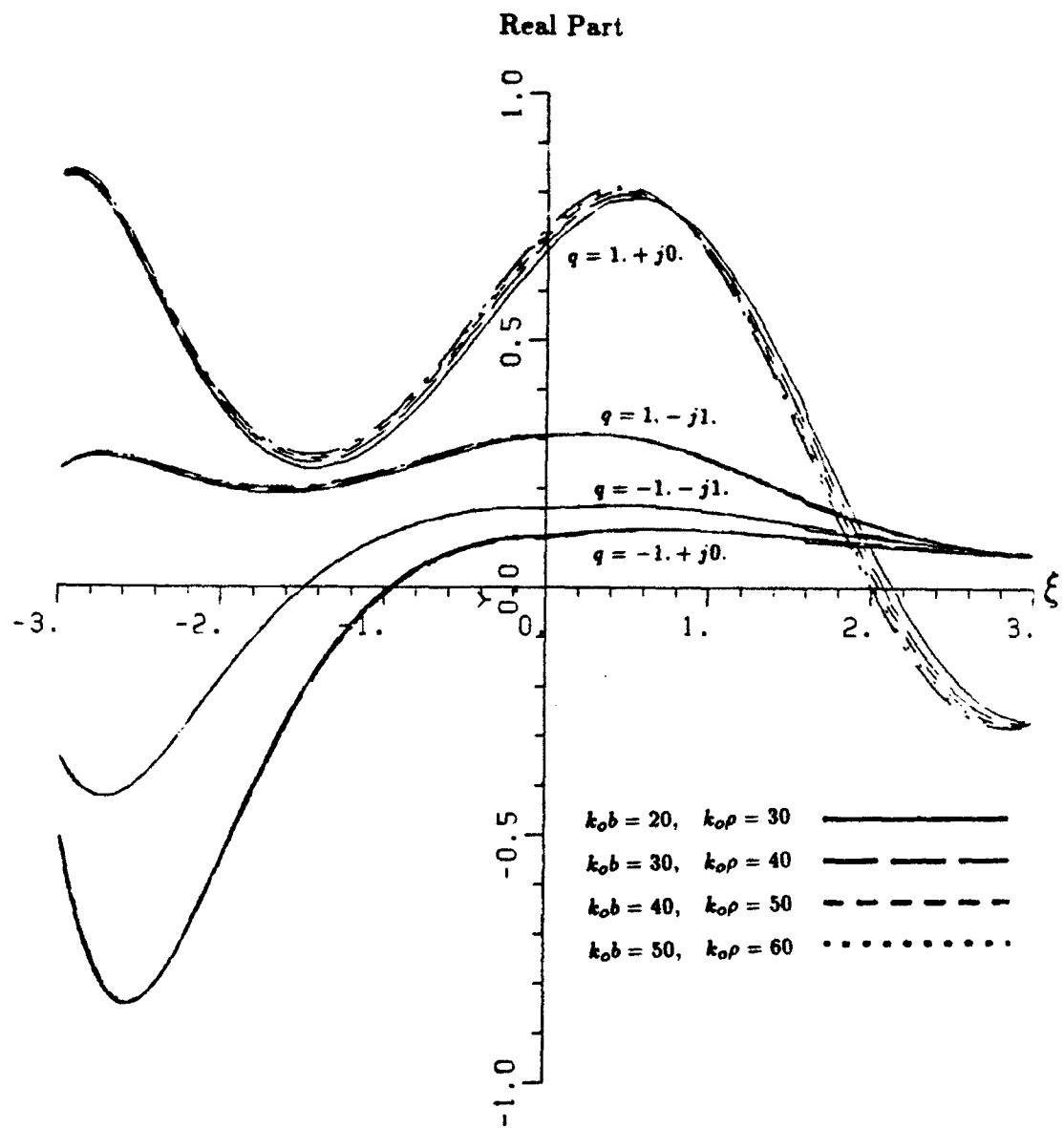


Figure 5.3: The transition integral $p^*(\xi, q)e^{-j\pi/4}$ or $q^*(\xi, q)e^{-j\pi/4}$: Impedance Cylinder

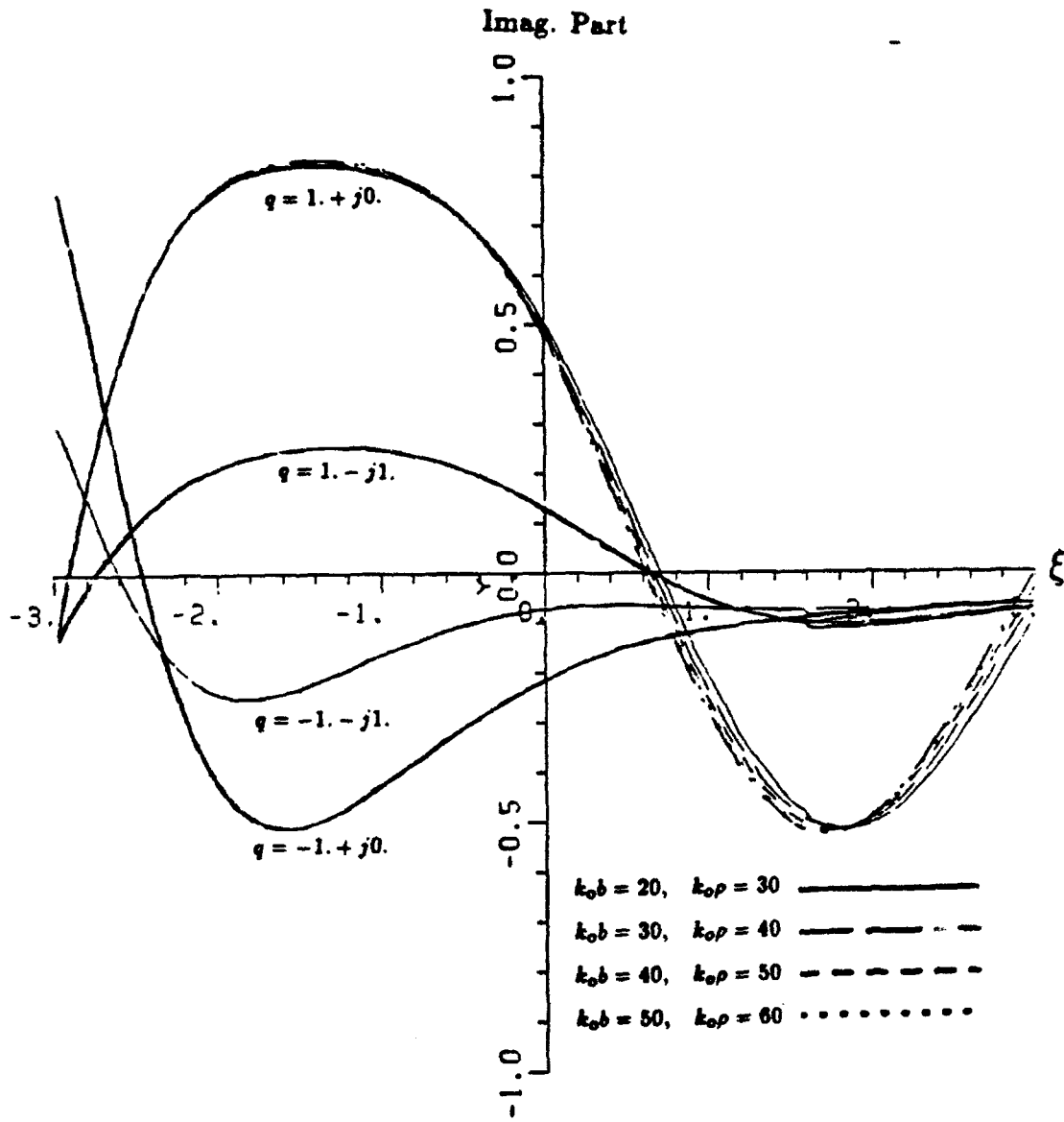
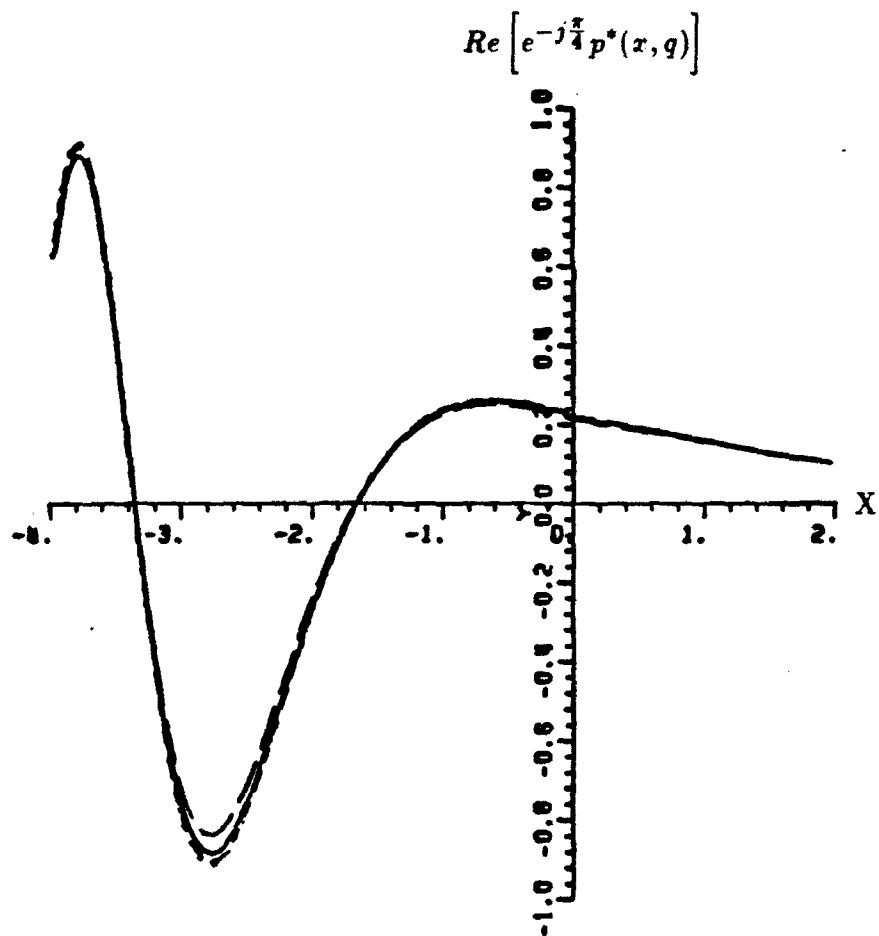


Figure 5.4: The transition integral $p^*(\xi, q)e^{-j\pi/4}$ or $q^*(\xi, q)e^{-j\pi/4}$: Impedance Cylinder



TM₂ case

$$\mu_1 = 1.$$

$$d = 0.1\lambda_0$$

$$q = (-0.19706E + 01, 0.24606E + 00)$$

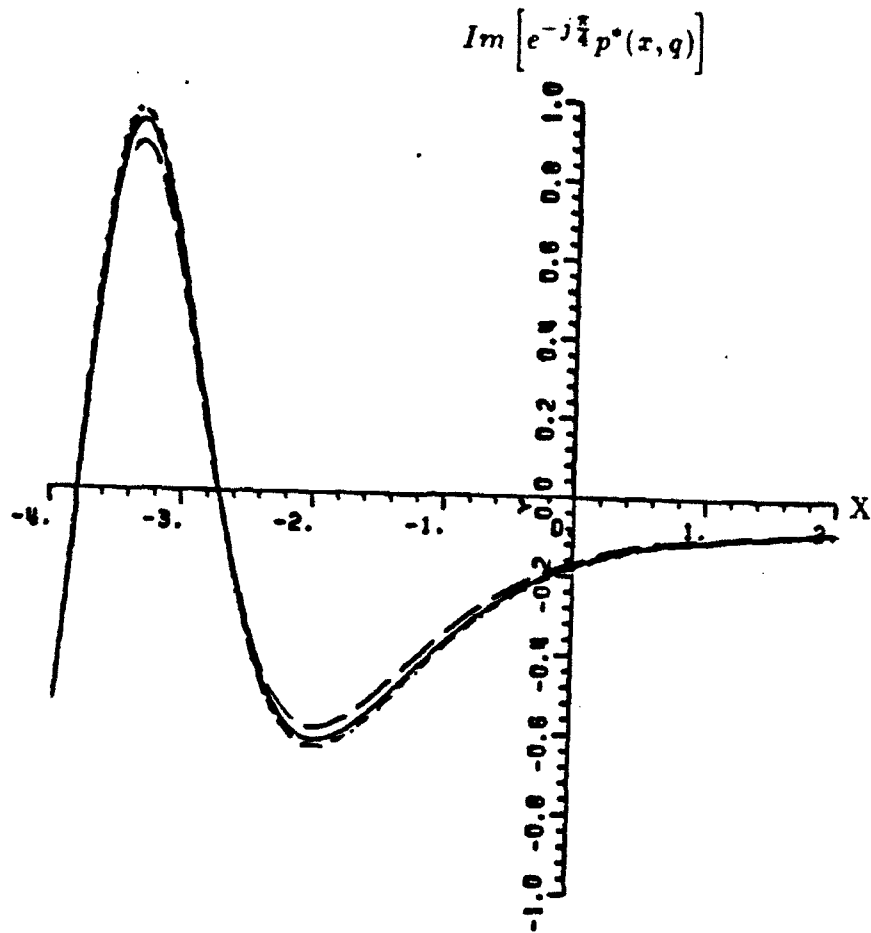
$$k_0 b = 20. \quad \epsilon_1 = (0.40000E + 01, 0.00000E + 00) \quad \text{—————}$$

$$k_0 b = 10. \quad \epsilon_1 = (0.29428E + 01, -0.14608E + 00) \quad \text{-----}$$

$$k_0 b = 30. \quad \epsilon_1 = (0.44707E + 01, 0.44553E - 01) \quad \text{- - - - -}$$

$$k_0 b = 35. \quad \epsilon_1 = (0.46280E + 01, 0.56347E - 01) \quad \text{.....}$$

Figure 5.5: The transition integral $e^{-j\pi/4} p^*(x, q)$: Coated Cylinder



TM_x case

$$\mu_1 = 1.$$

$$d = 0.1\lambda_0$$

$$q = (-0.19706E + 01, 0.24606E + 00)$$

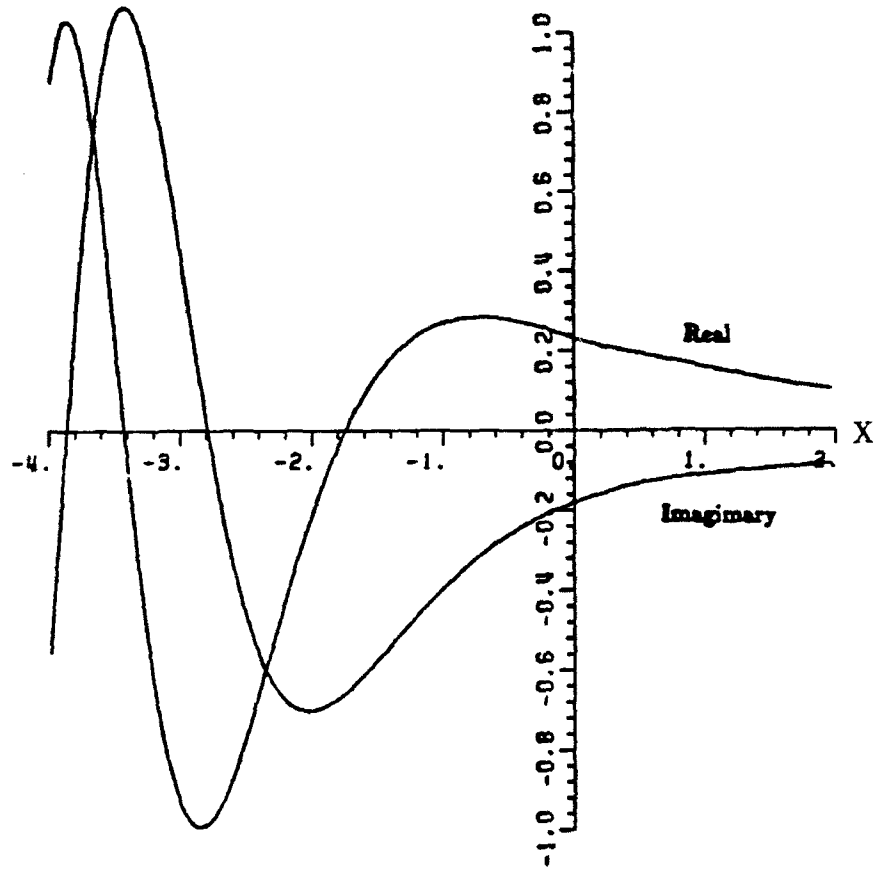
$$k_0 b = 20. \quad \epsilon_1 = (0.40000E + 01, 0.00000E + 00) \quad \text{—————}$$

$$k_0 b = 10. \quad \epsilon_1 = (0.29428E + 01, -0.14608E + 00) \quad \text{- - - - -}$$

$$k_0 b = 30. \quad \epsilon_1 = (0.44707E + 01, 0.44553E - 01) \quad \text{- . - . - .}$$

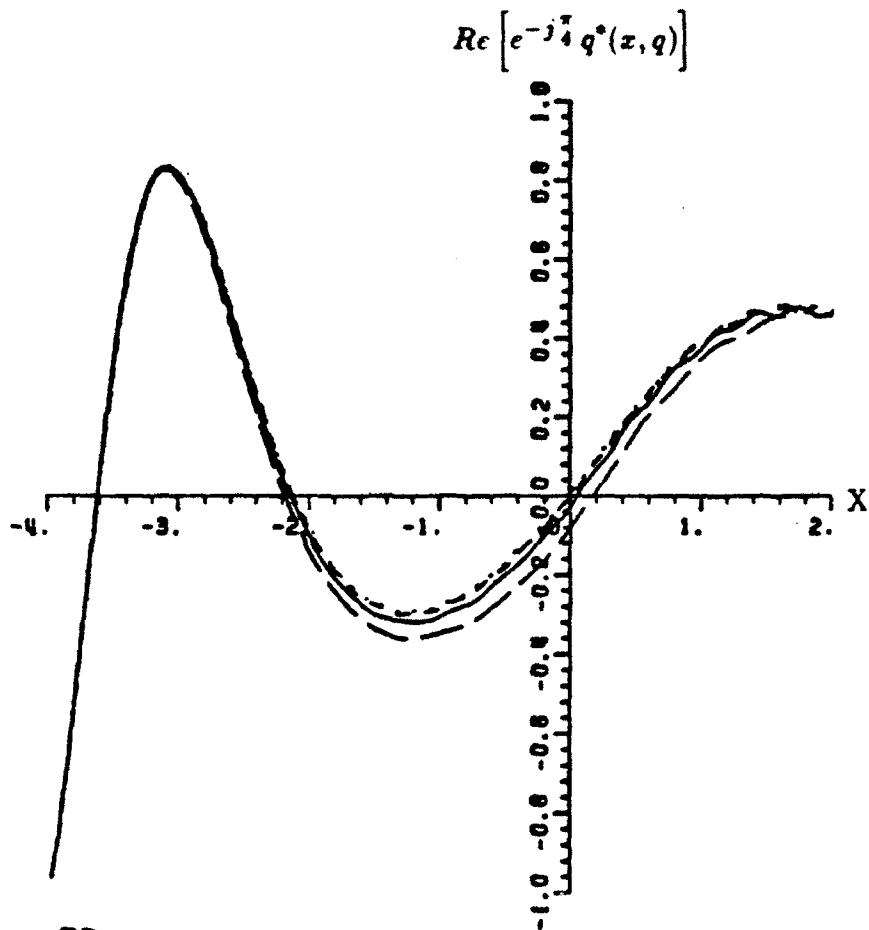
$$k_0 b = 35. \quad \epsilon_1 = (0.46280E + 01, 0.56547E - 01) \quad \text{.....}$$

Figure 5.6: The transition integral $e^{-j\pi/4} p^*(x, q)$: Coated Cylinder.



$$q = (-0.19706E + 01, 0.24606E + 00)$$

Figure 5.7: The transition integral $e^{-j\pi/4}p^*(x, q)$ or $q^*(\xi, q)e^{-j\pi/4}$: Impedance cylinder



TE_z case

$$\mu_1 = 1.$$

$$d = 0.05\lambda_0$$

$$q = (0.51418E + 00, 0.22532E - 01)$$

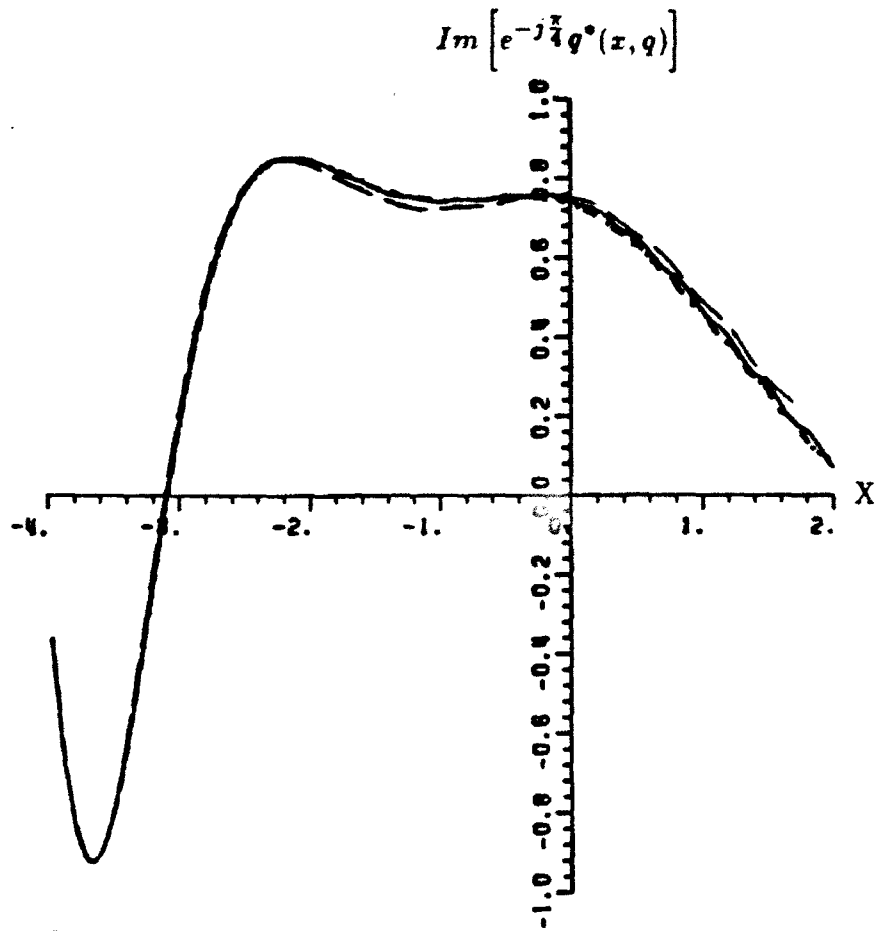
$$k_0 b = 20. \quad \epsilon_1 = (0.40000E + 01, 0.00000E + 00) \quad \text{—————}$$

$$k_0 b = 10. \quad \epsilon_1 = (0.67063E + 01, -0.33697E - 02) \quad \text{-----}$$

$$k_0 b = 30. \quad \epsilon_1 = (0.31092E + 01, -0.37392E - 02) \quad \text{- - - - -}$$

$$k_0 b = 35. \quad \epsilon_1 = (0.28619E + 01, -0.37620E - 02) \quad \text{- - - - -}$$

Figure 5.8: The transition integral $e^{-j\pi/4} q^*(x, q)$: Coated Cylinder



TE_z case

$$\mu_1 = 1.$$

$$d = 0.05\lambda_0$$

$$q = (0.51418E + 00, 0.22532E - 01)$$

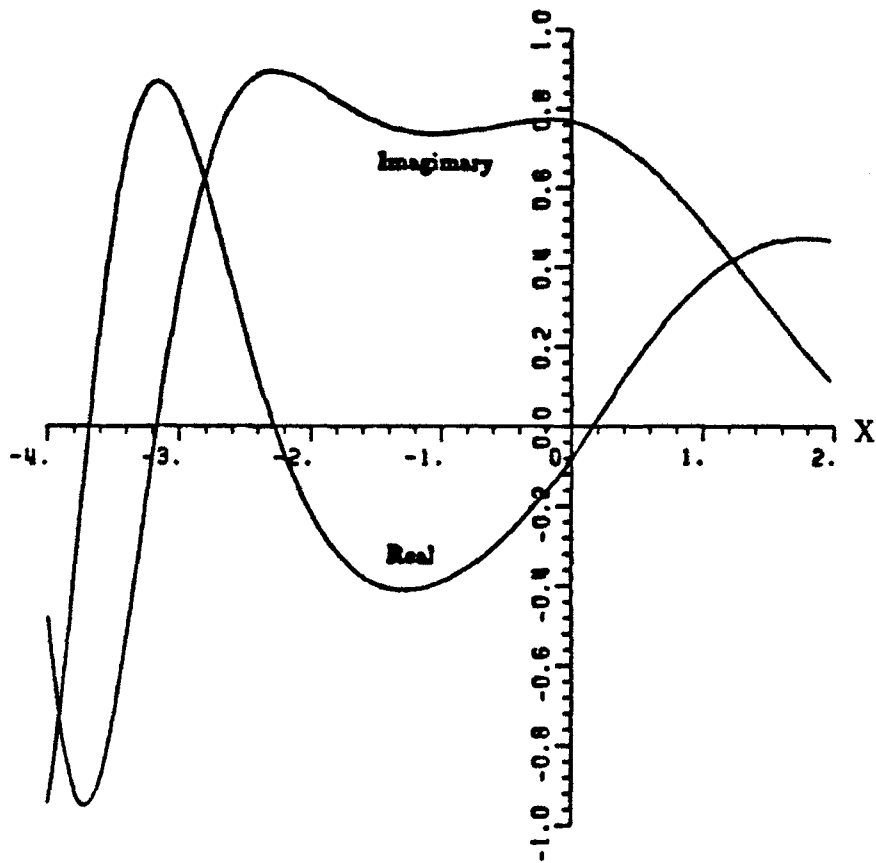
$$k_0 b = 20. \quad \epsilon_1 = (0.40000E + 01, 0.00000E + 00) \quad \text{—————}$$

$$k_0 b = 10. \quad \epsilon_1 = (0.67063E + 01, -0.33697E - 02) \quad \text{- - - - -}$$

$$k_0 b = 30. \quad \epsilon_1 = (0.31092E + 01, -0.37392E - 02) \quad \text{- - - - -}$$

$$k_0 b = 35. \quad \epsilon_1 = (0.28619E + 01, -0.37620E - 02) \quad \text{- - - - -}$$

Figure 5.9: The transition integral $e^{-j\pi/4}q^*(x,q)$: Coated Cylinder



$$q = (0.51418E + 00, 0.22532E - 01)$$

Figure 5.10: The transition integral $e^{-j\pi/4} p^*(x, q)$ or $q^*(\xi, q) e^{-j\pi/4}$: Impedance cylinder

5.3 Numerical results and discussion

In this section, the UTD solution is employed to calculate the electromagnetic field scattered from the impedance and the coated cylinder. The geometry of the problem and the ray paths are the same as those of GTD solution. It is noted that the results obtained with the GTD solution given in Chapter III show excellent agreement with the eigenfunction results in the deep lit and the deep shadow regions. However the GTD solution fails in the transition region adjacent to the shadow boundaries. The angular range of the regions where the pure ray-optical solution fails depends on the range where the approximations involved in the formulation of ordinary GTD solution fails. From the numerical results given in Chapter III, It can be observed that the lit part of the transition region has wider angular range than the shadow part.

It is well known that the uniform GTD reduces to the ordinary GTD in the deep lit and the deep shadow region. Thus, in obtaining the numerical results given in Figure 5.11 ~ 5.34, the uniform GTD solutions given in Equation (5.1) and (5.14) are employed only for the transition region. For the deep lit and the deep shadow region the ordinary GTD solutions given in Chapter III are used. The examples given in Figure 5.11 ~ 5.34 are chosen to have the same configurations as those given in Figure 3.13 ~ 3.36 for the comparison of the GTD and the UTD. It can be observed that the uniform GTD solution provides a continuous pattern across the shadow boundaries and compares well with the eigenfunction-solution results in the transition region. Due to the numerical difficulty in locating the high order dominant root of the transcendental equation, the examples given in Figure 5.11 ~ 5.34 are confined to thin material coatings where the dominant creeping wave mode is either the first or the second mode. At this stage it is not clear whether the solution is applicable to the thick coating case.

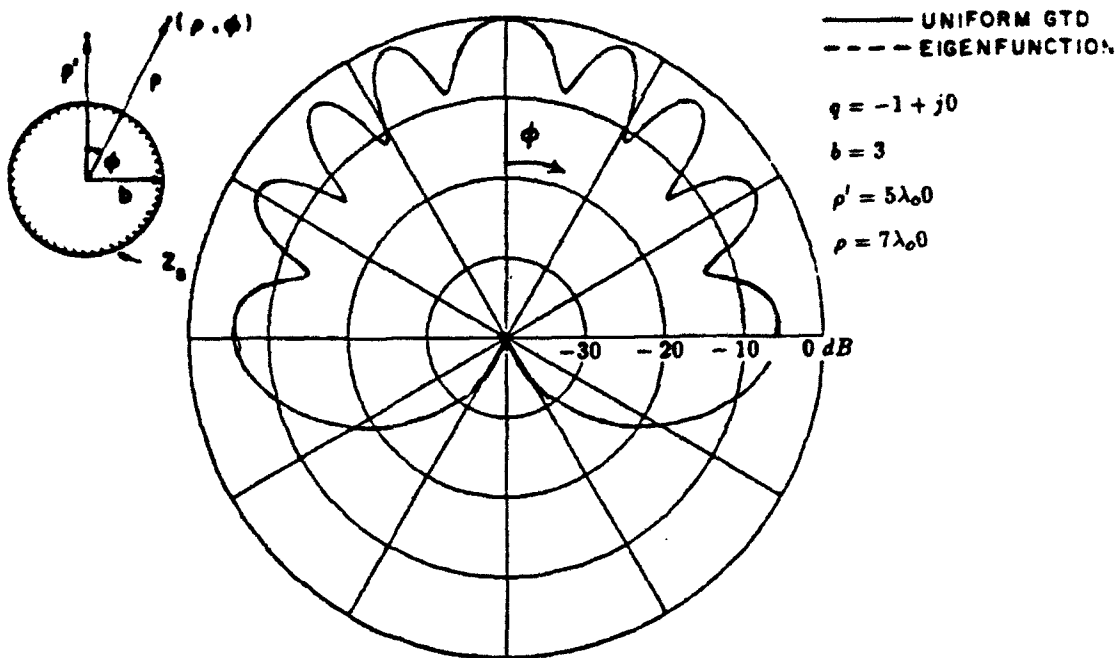


Figure 5.11: Normalized bistatic scattering pattern of impedance cylinder

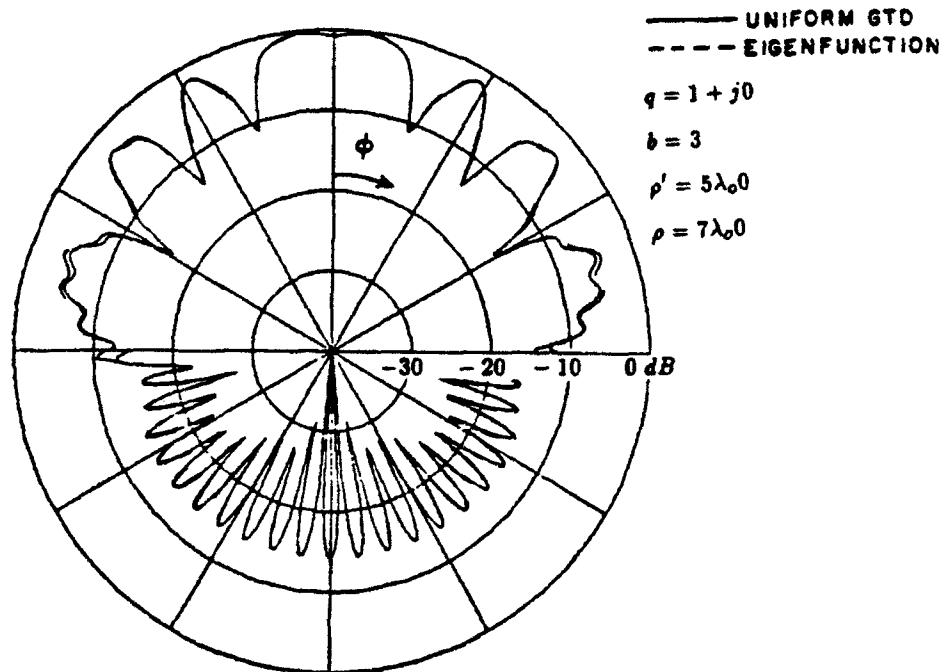


Figure 5.12: Normalized bistatic scattering pattern of impedance cylinder

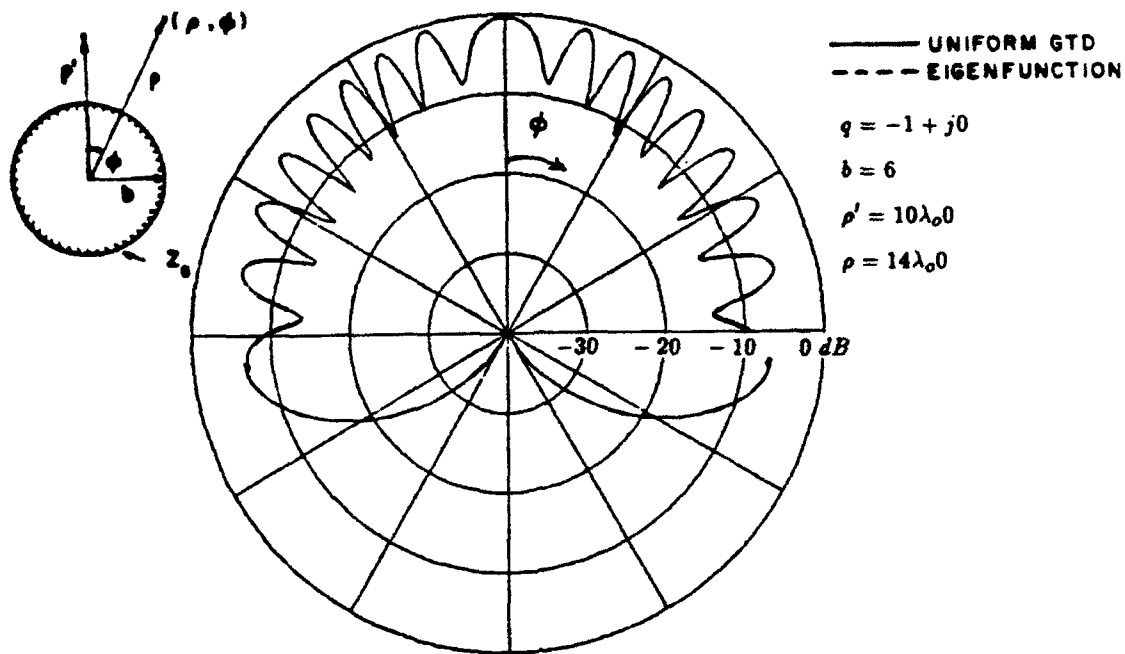


Figure 5.13: Normalized bistatic scattering pattern of impedance cylinder

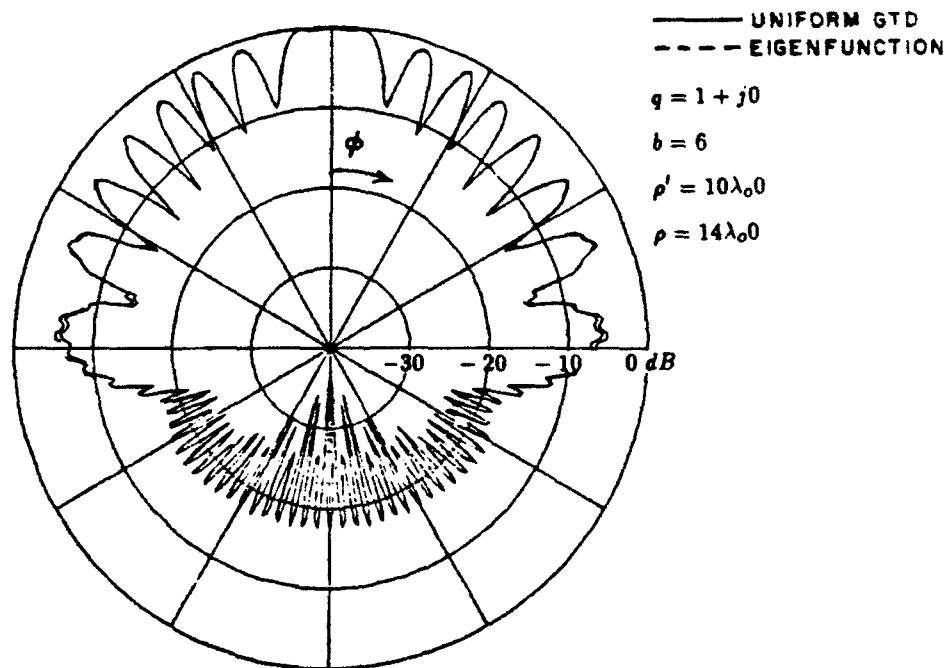


Figure 5.14: Normalized bistatic scattering pattern of impedance cylinder

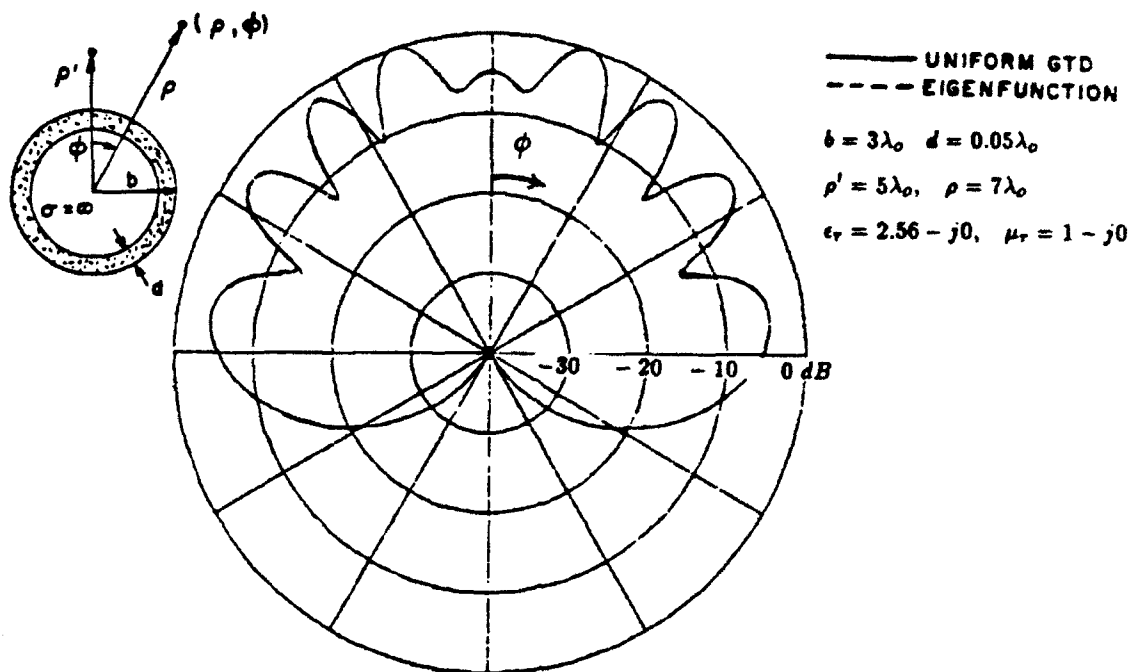


Figure 5.15: Normalized bistatic scattering pattern of coated cylinder : TM_2 case

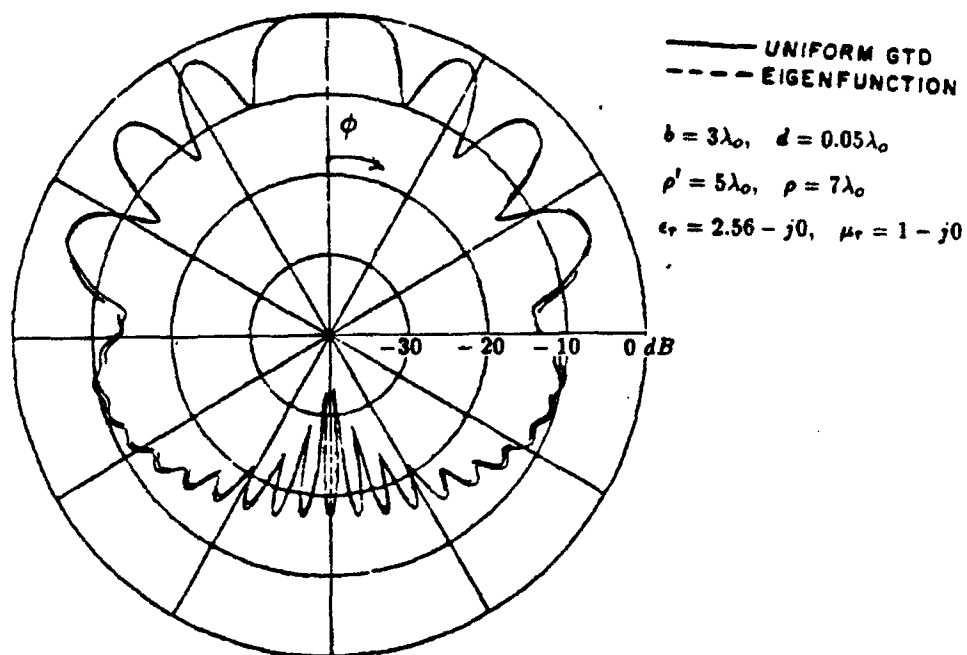


Figure 5.16: Normalized bistatic scattering pattern of coated cylinder : TE_2 case

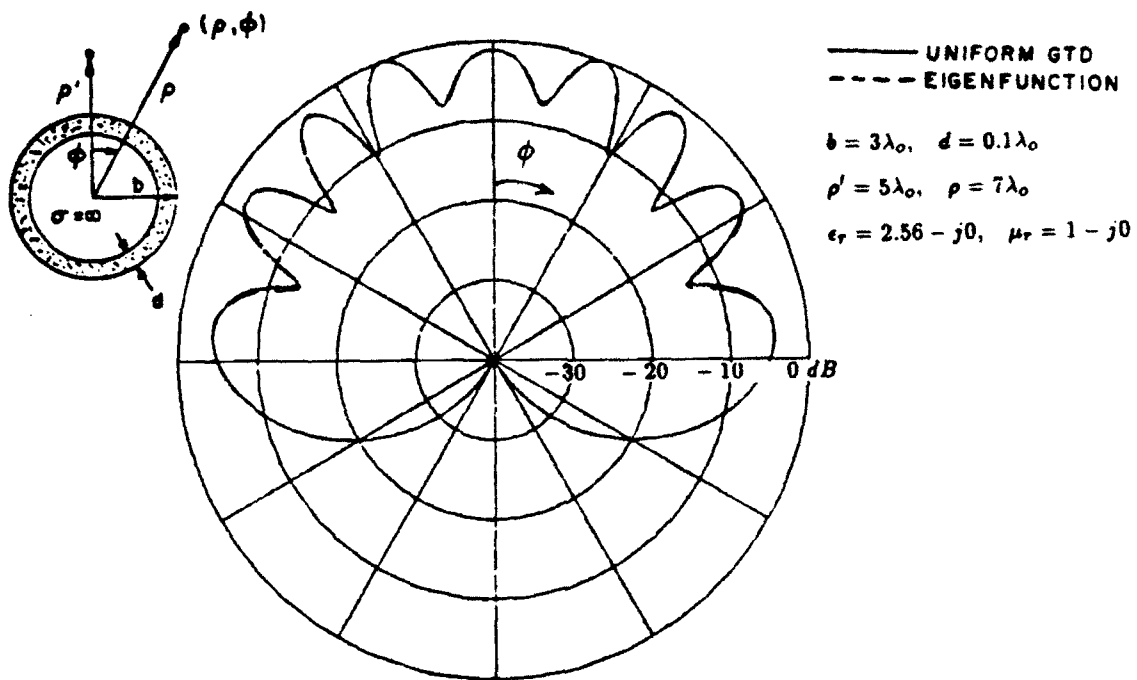


Figure 5.17: Normalized bistatic scattering pattern of coated cylinder : TM_2 case

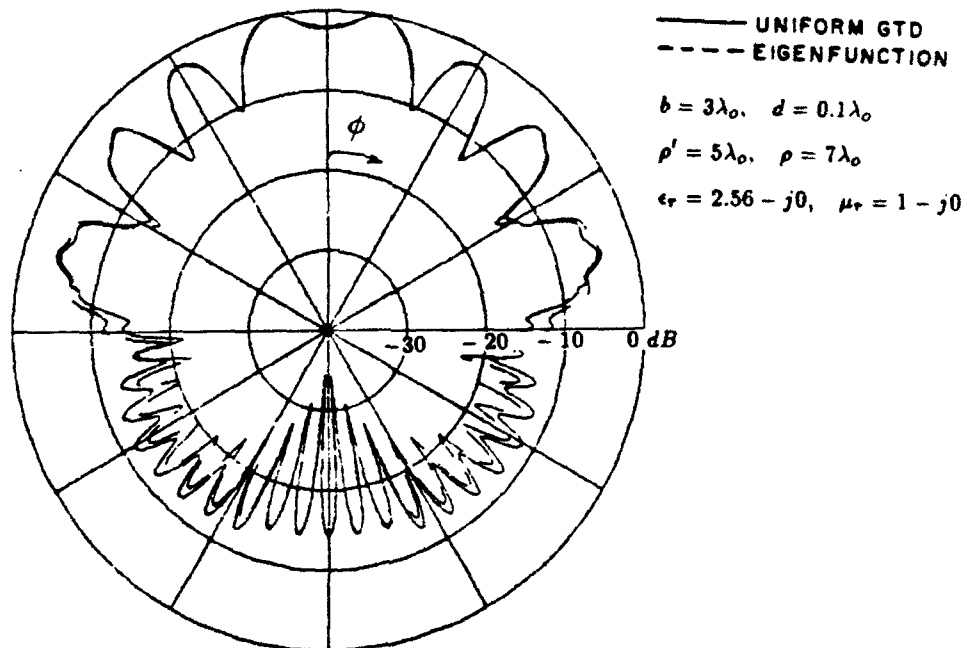


Figure 5.18: Normalized bistatic scattering pattern of coated cylinder : TE_2 case

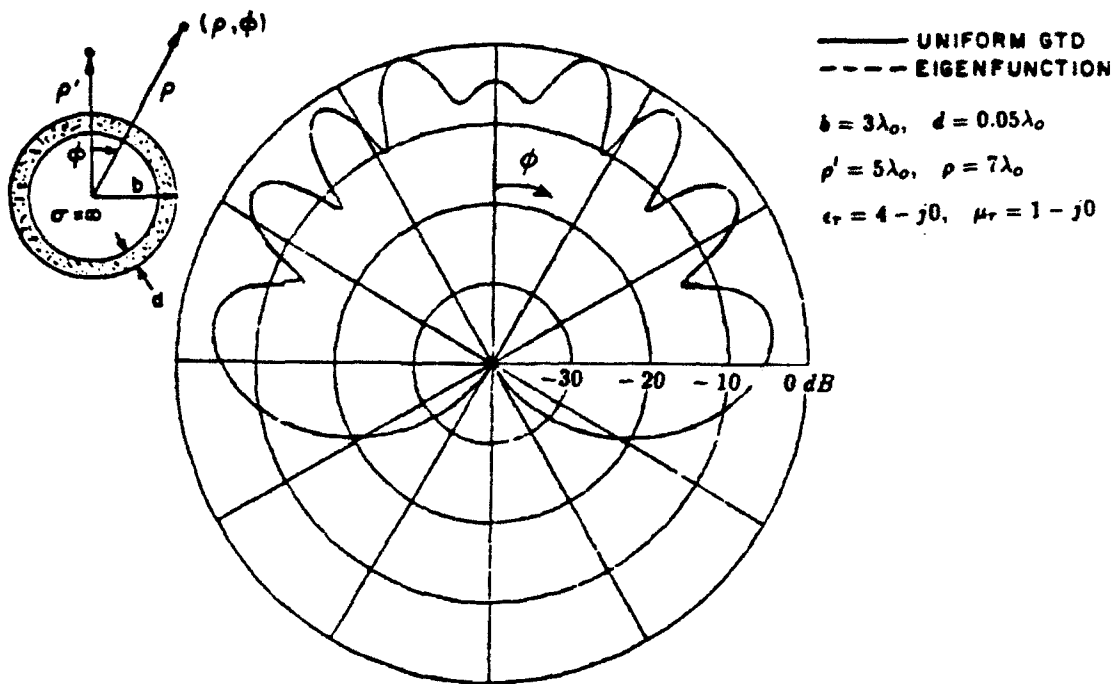


Figure 5.19: Normalized bistatic scattering pattern of coated cylinder : TM_2 case

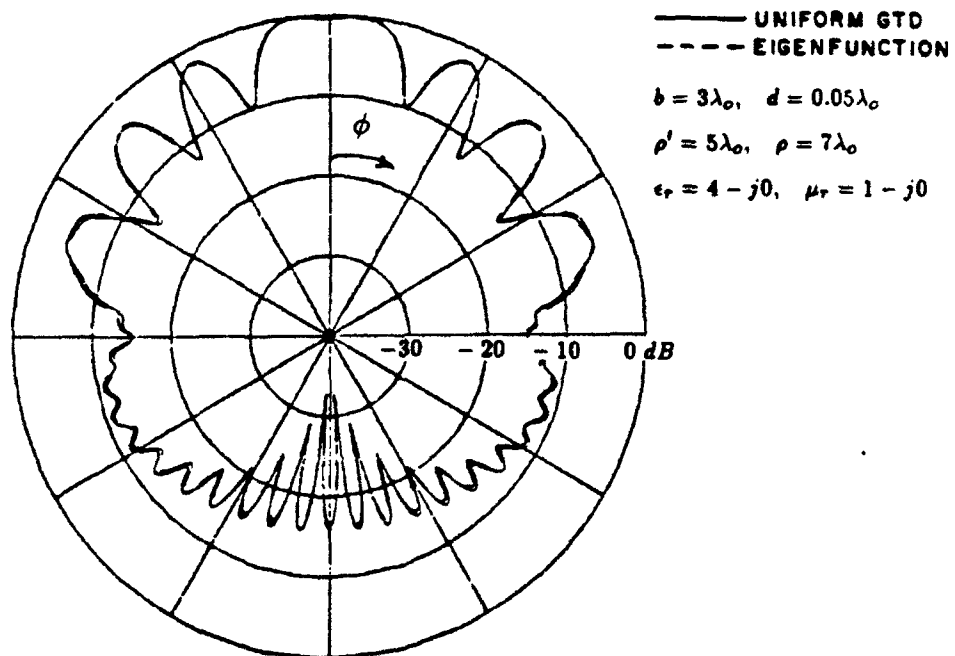


Figure 5.20: Normalized bistatic scattering pattern of coated cylinder : TE_2 case

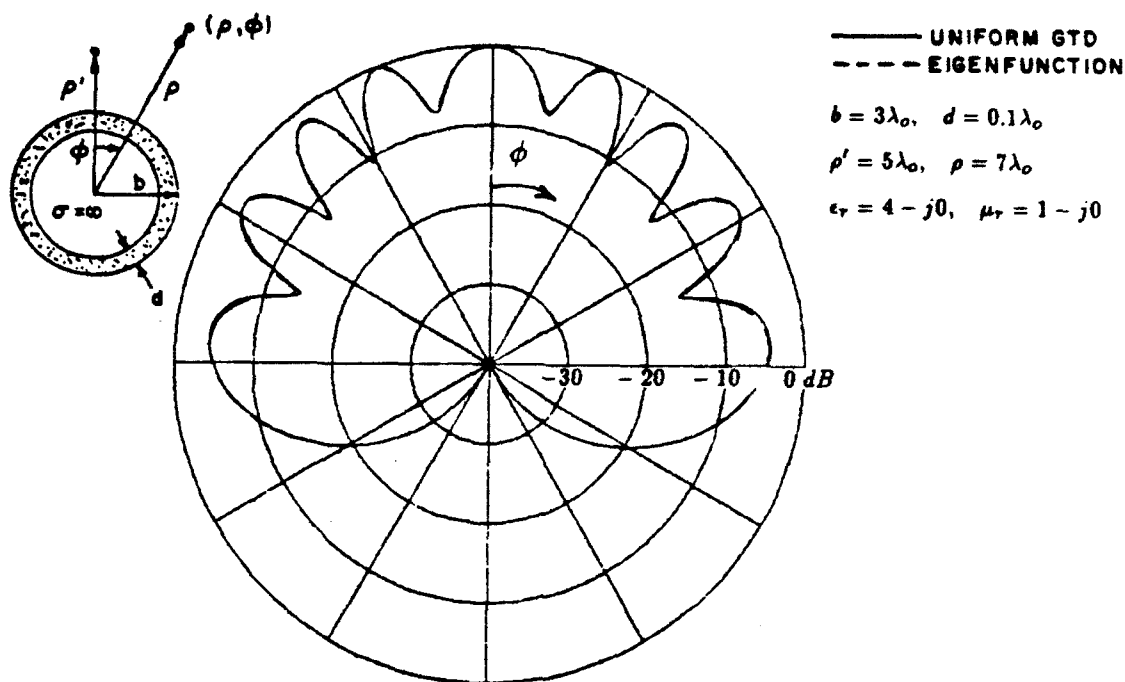


Figure 5.21: Normalized bistatic scattering pattern of coated cylinder : TM_2 case

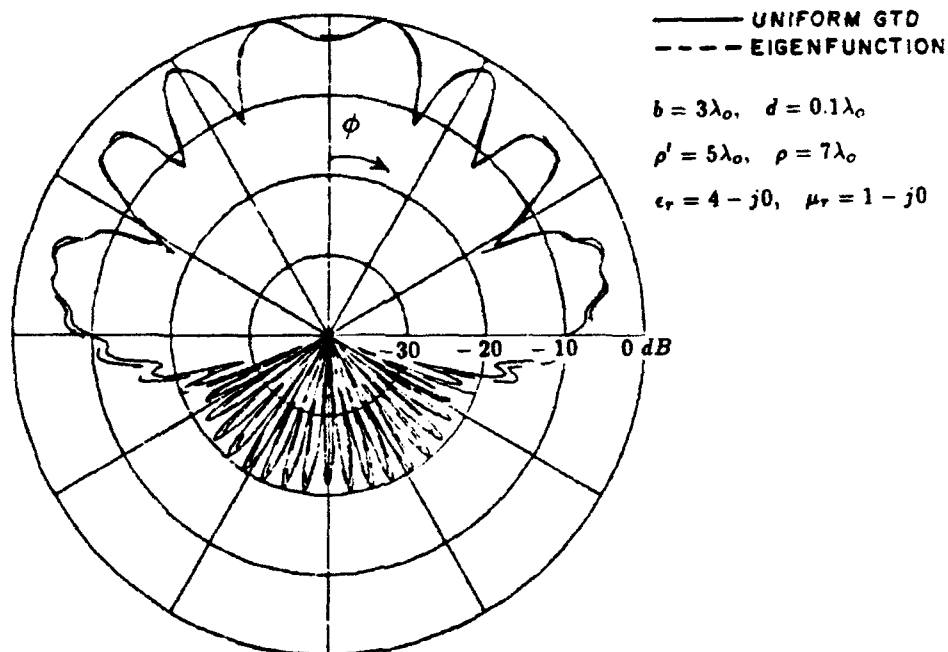


Figure 5.22: Normalized bistatic scattering pattern of coated cylinder : TE_2 case

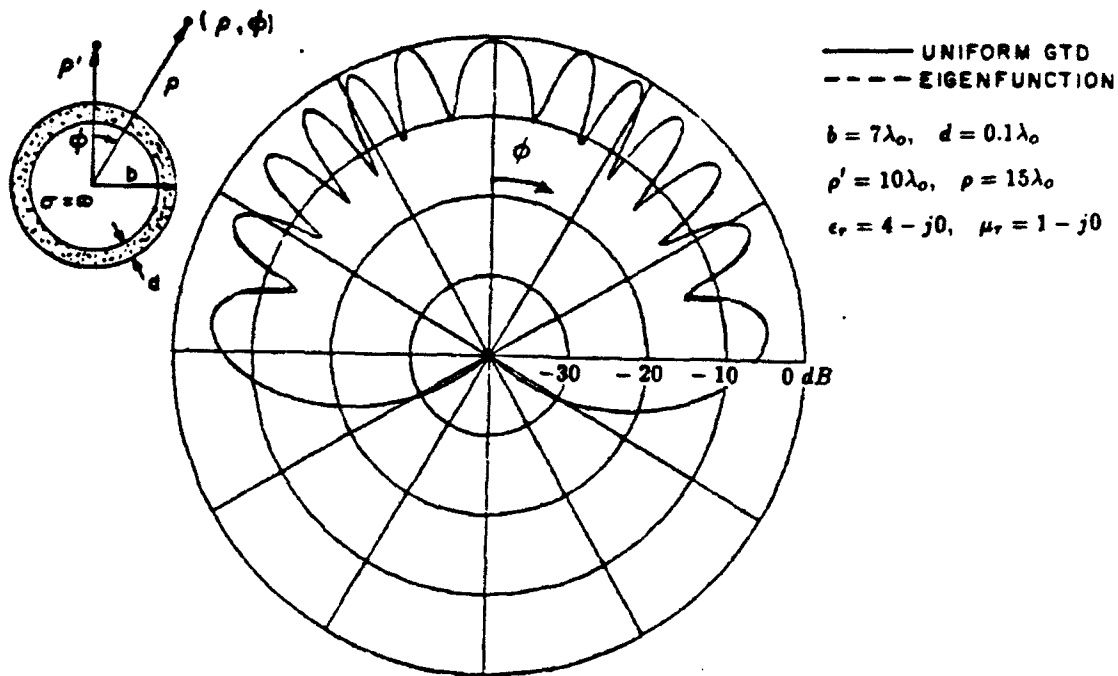


Figure 5.23: Normalized bistatic scattering pattern of coated cylinder : TM_2 case

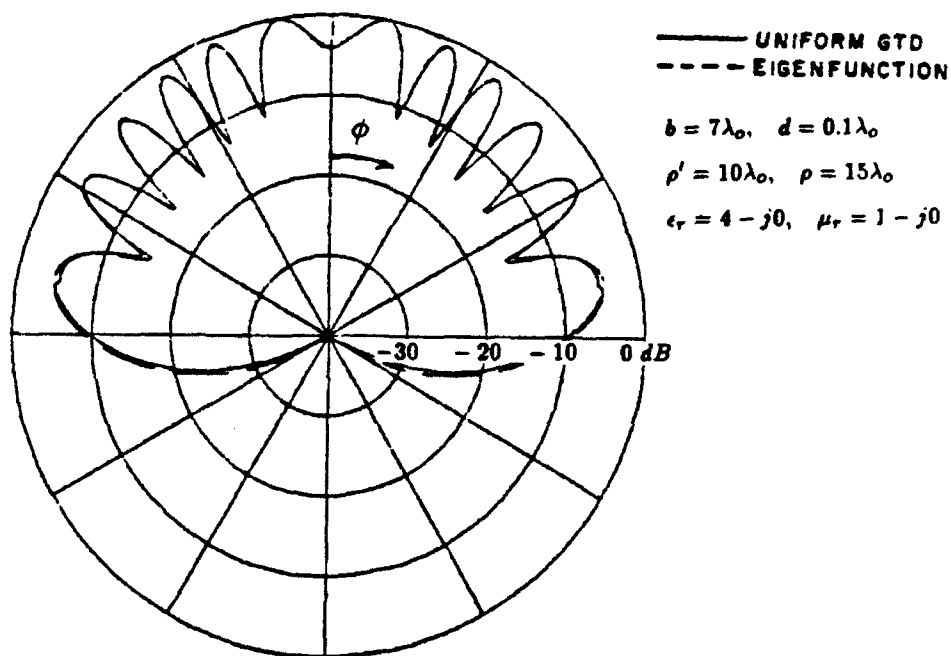


Figure 5.24: Normalized bistatic scattering pattern of coated cylinder : TE_2 case

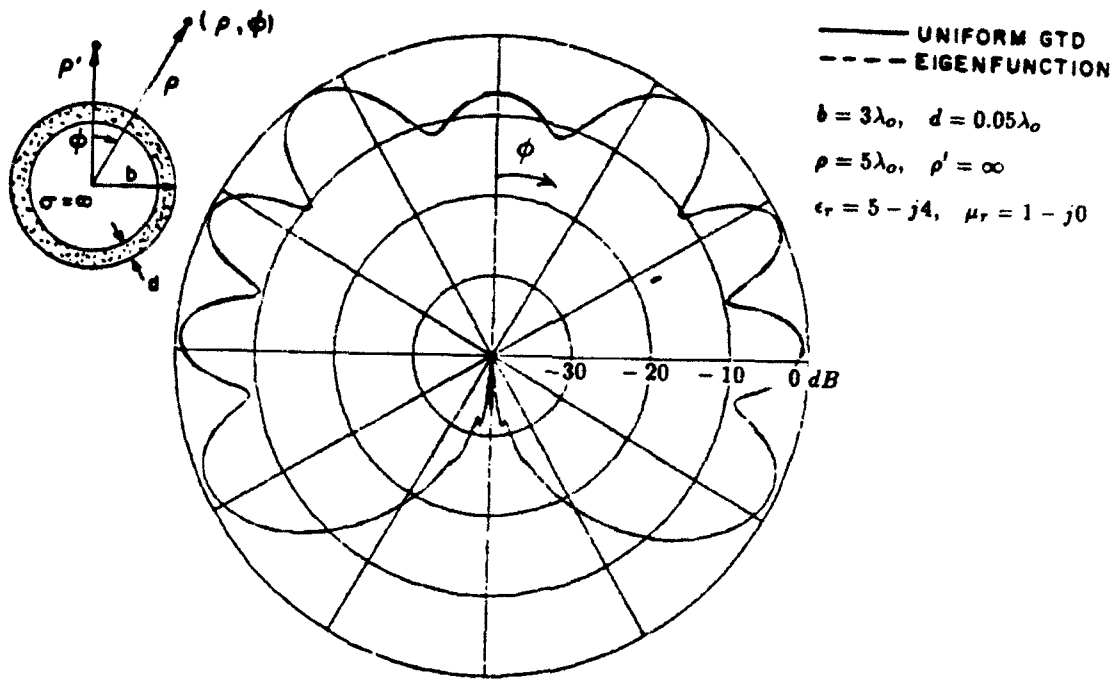


Figure 5.25: Normalized bistatic scattering pattern of coated cylinder : TM_z case

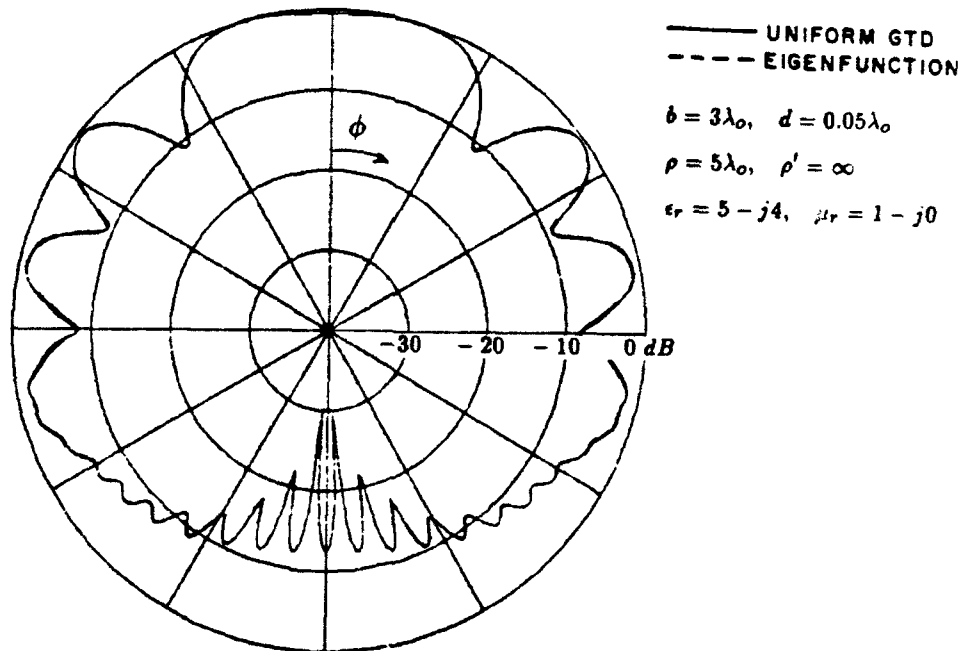


Figure 5.26: Normalized bistatic scattering pattern of coated cylinder : TE_z case

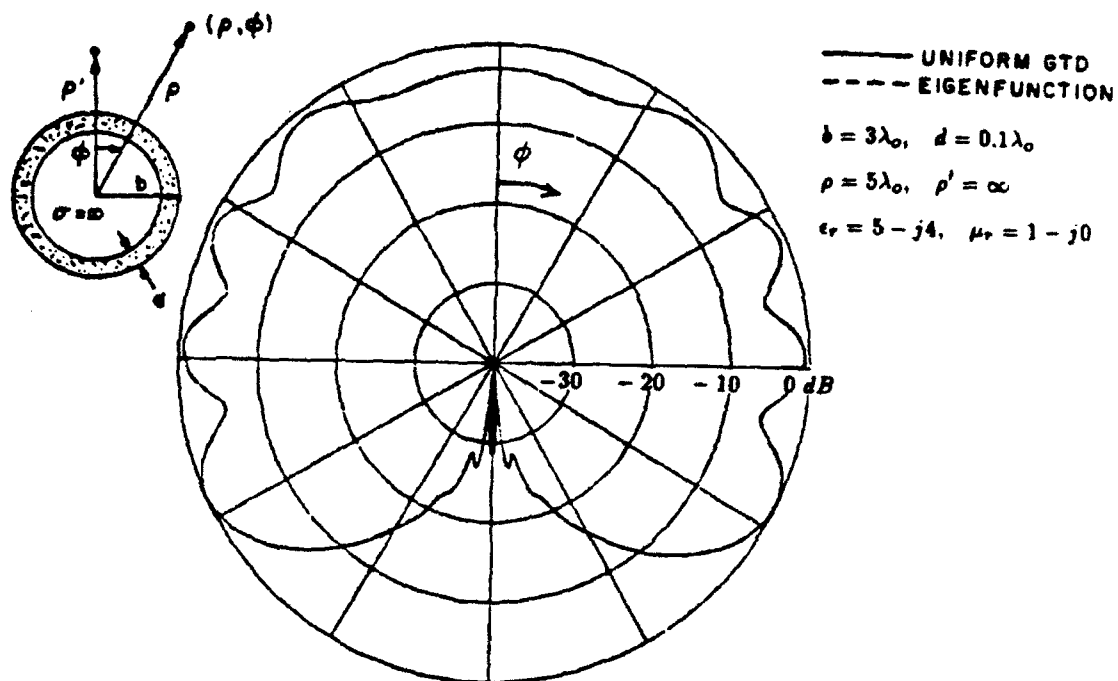


Figure 5.27: Normalized bistatic scattering pattern of coated cylinder : TM_2 case

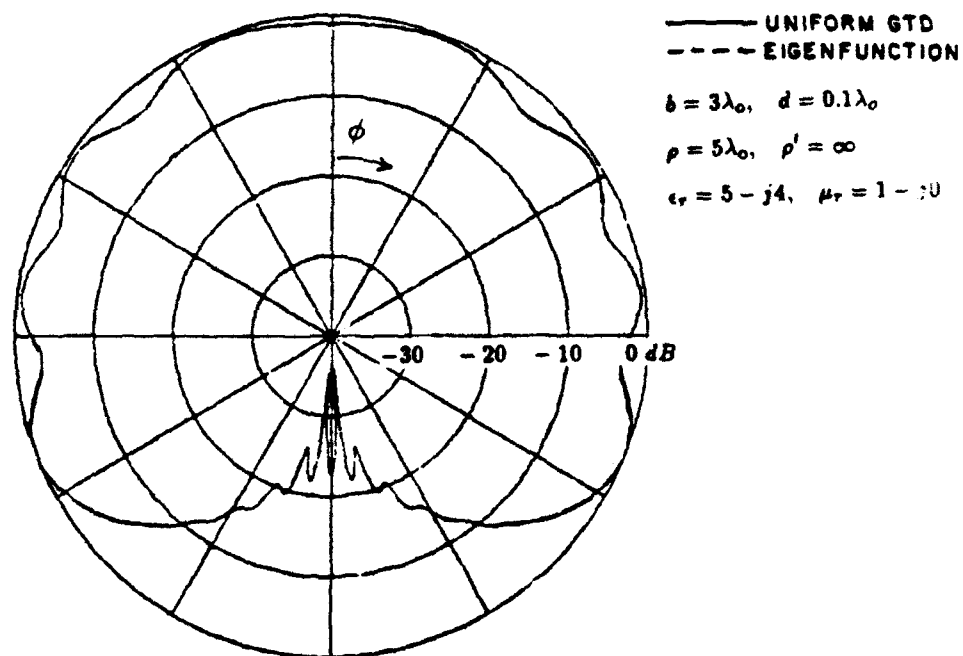


Figure 5.28: Normalized bistatic scattering pattern of coated cylinder : TE_2 case

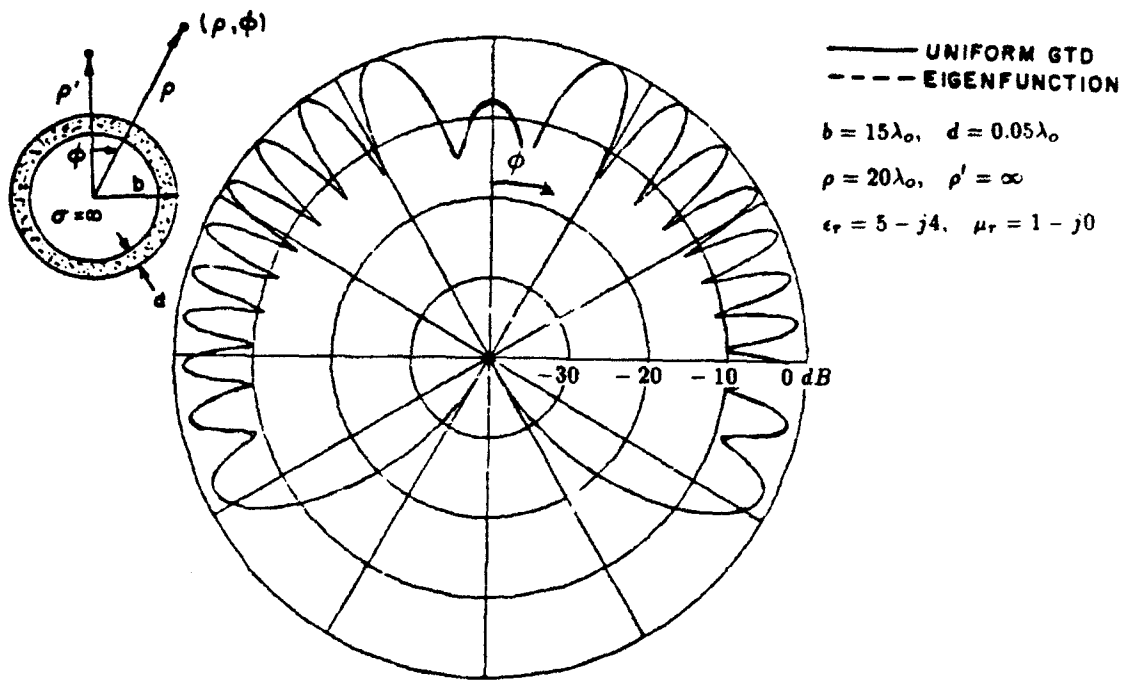


Figure 5.29: Normalized bistatic scattering pattern of coated cylinder : TM_z case

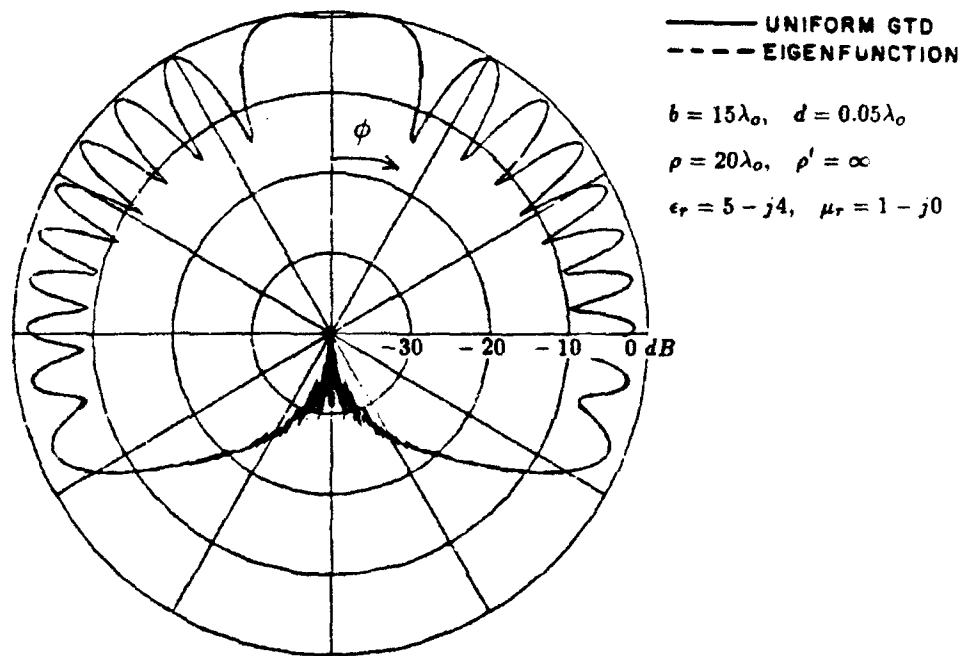


Figure 5.30: Normalized bistatic scattering pattern of coated cylinder : TE_z case

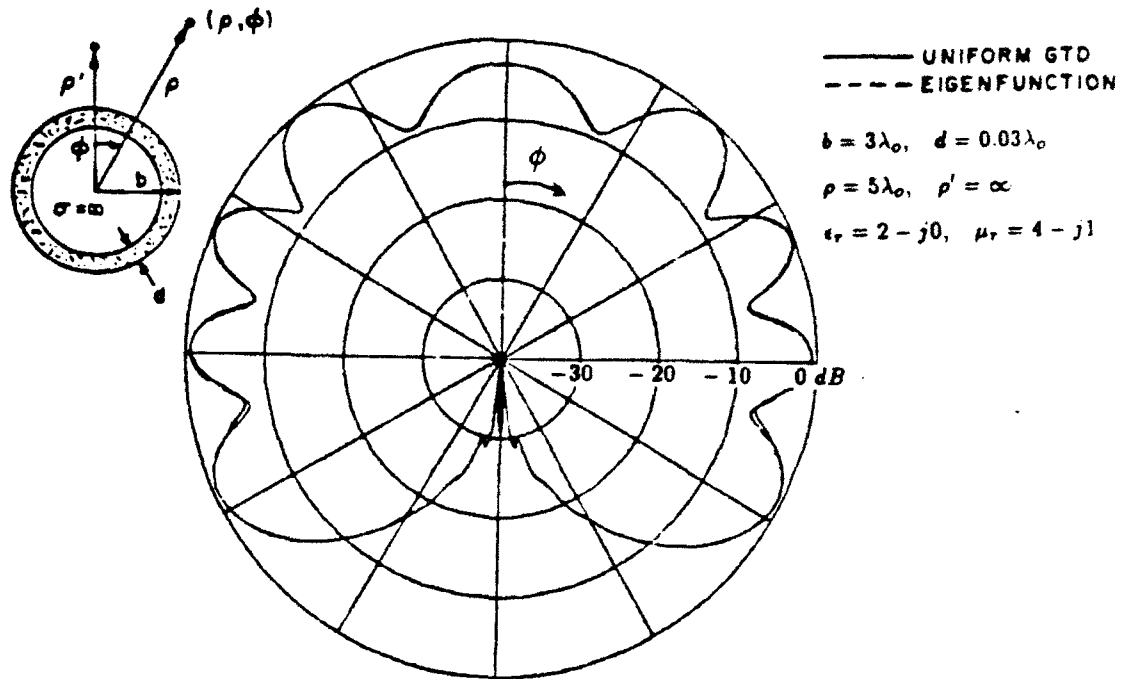


Figure 5.31: Normalized bistatic scattering pattern of coated cylinder : TM_2 case

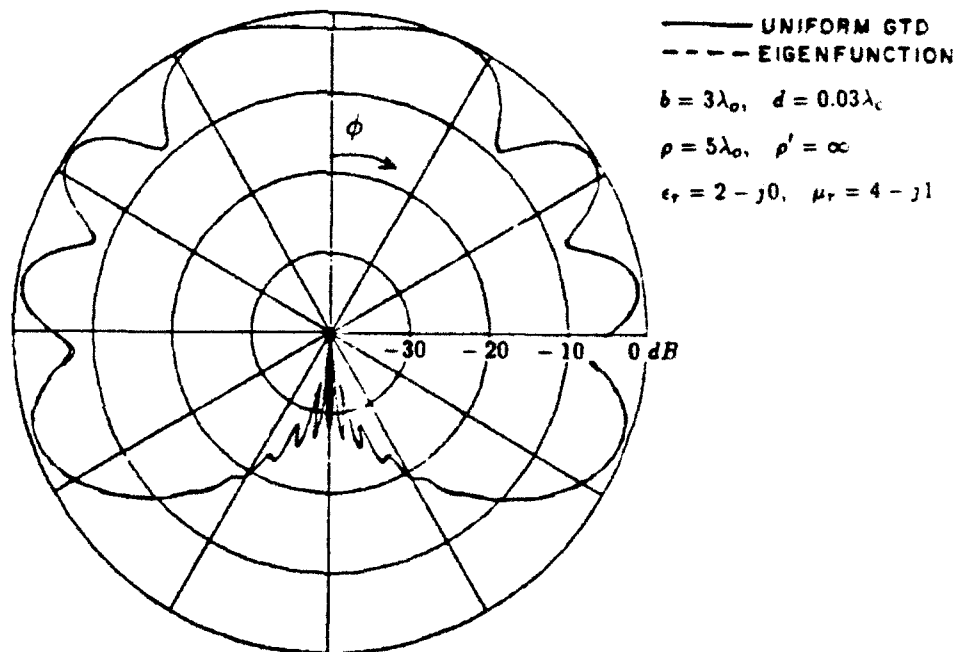


Figure 5.32: Normalized bistatic scattering pattern of coated cylinder : TE_2 case

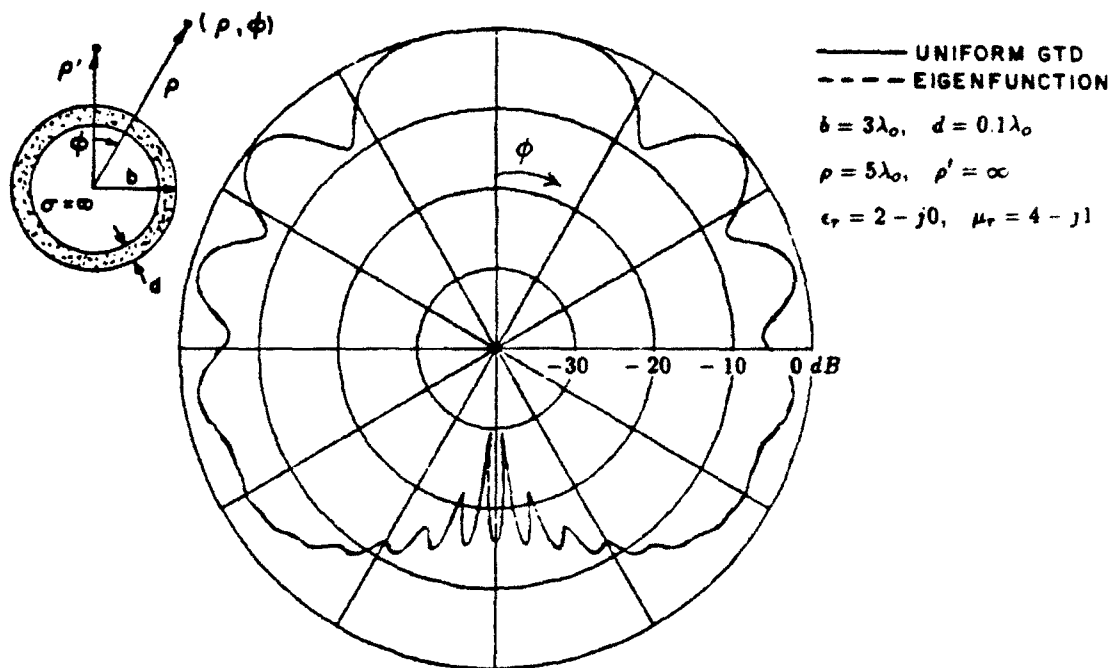


Figure 5.33: Normalized bistatic scattering pattern of coated cylinder : TM_2 case

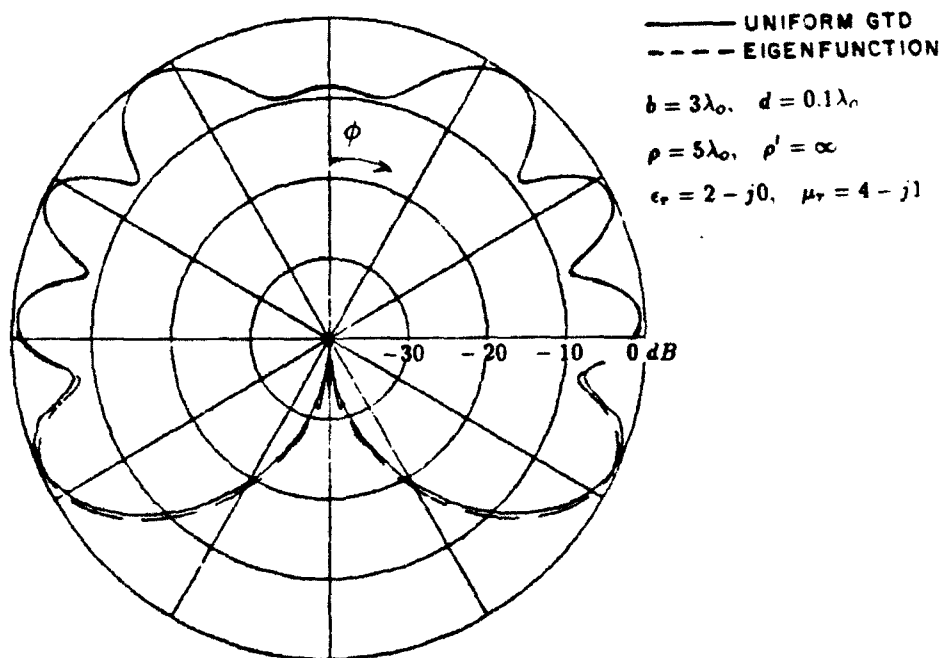


Figure 5.34: Normalized bistatic scattering pattern of coated cylinder : TE_2 case

CHAPTER VI

SUMMARY AND CONCLUSIONS

An approximate asymptotic high-frequency solution is obtained for the field exterior to a two-dimensional circular conducting cylinder with a thin dielectric/ferrite coating. The angular eigenfunction solution of the problem is obtained from the two-dimensional line-source Green's function subject to the boundary conditions on the cylinder surface and the Sommerfeld radiation condition at the infinity. The eigenfunction solution is slowly convergent when the radius of the cylinder is large in term of the wave length. Furthermore, the physical interpretation of the scattering mechanism is not possible from the eigenfunction solution. In order to obtain the ray optical solution of the problem, the angular eigenfunction is transformed into the integral representation and the integral is evaluated asymptotically via the stationary phase method for the field in lit region and via the residue theorem for the field in shadow region. The obtained solution is cast in the format of the geometrical theory of diffraction (GTD).

In the lit region, the geometrical optics (GO) solution consists of the direct incident ray and the reflected ray. The ray picture associated with the reflected ray for the coated cylinder remains the same as that for the conducting cylinder without coating. The only difference is that, for the coated surface, the specular reflection point is located on the coating-air interface. It is shown that for a thin coating case, the reflection coefficient for the field reflected at the specular reflection point on the coated curved surface can be approximated by the reflection coefficient for

a grounded planar dielectric/ferrite slab with a plane wave incidence.

In the shadow region, the residue series solution can be interpreted as the usual creeping wave diffraction of the GTD solution with the same ray path as the diffracted field associated with the conducting cylinder without coating. The propagation constants of the creeping wave mode are obtained from the roots of the transcendental equation which characterizes the coated cylinder. The roots of the transcendental equation are numerically searched via Newton-Raphson's method by using both the Debye and the Watson's approximations of the associated Hankel functions. The trajectories of the roots are plotted for several cases. For the perfectly conducting cylinder, the first creeping wave mode is always dominant over all other higher order modes. However for the coated cylinder, the dominance of the creeping wave mode changes according to the change of the thickness of coating.

In the transition regions adjacent to the shadow boundaries where the pure ray-optical GTD solution fails, a 'universal' transition integral of the uniform GTD (UTD) is employed to obtain the uniform solution. Numerical data for the essential transition integral is deduced, via a heuristic approach, from the exact eigenfunction solution together with the GTD solution for the coated cylinder. The solution is convenient for the engineering applications due to its simple ray format. Numerical results obtained from the UTD solution for the cylinder with thin coating show excellent agreement with the exact eigenfunction results.

This is a first attempt to provide a uniform GTD solution for a conducting surface with material coating. Due to the numerical difficulty in locating the higher order roots of the transcendental equation, the examples given in this research are confined to the thin coating cases where either the first or the second mode of the creeping wave is dominant. At this stage, it is not yet clear whether the solution

is applicable to the thick coating case.

For the future study, the three-dimensional problem, namely, a plane wave incident obliquely upon a coated cylinder should be investigated. It is well known that, unlike the perfectly conducting cylinder, there exists both *TE* and *TM* modes in the scattered fields, even though the incident field may have been either *TE* or *TM*. The electromagnetic characteristics of the creeping waves and their three-dimensional ray interpretations on the coated cylinder should be examined. Also, the scattering from a coated elliptical cylinder should be investigated for the application of the solution to a general convex surface with material coating. This research is important and of interest in that it could eventually lead to an understanding of the creeping waves on the coated bodies with finite extent.

The problem of the radiation from the coated cylinder is the case when the source is mounted on the surface of the cylinder (i.e. $\rho' = b$), and the field point is out of the cylinder surface (i.e. $\rho > b$), A asymptotic high frequency solution for the radiation problem can also be obtained by the similar procedure as that for the scattering problem given in this research.

APPENDIX A

WATSON'S TRANSFORMATION

A.1 Watson's Transformation

For the cylinder with large radius, It is impractical to compute the field from the angular eigenfunction expansion because it is slowly convergent. This difficulty in convergence can be overcome by using the *Watson's transformation*. For the determination of the field in the shadow region by a vertical dipole in the presence of a large metallic sphere, Watson (1918) used a transformation to convert the slowly convergent eigenfunction series into a residue series and hence a contour integral in the complex plane. He then showed that the contour could be deformed so as to enclose a new set of poles and, by evaluating the residue series associated with these new poles, was led to a series which was rapidly convergent. The procedure for converting the original eigenfunction series (convenient for small b/λ_0) to the residue series appropriate for large b/λ_0 is now known as *Watson's transformation*. This method which was originally used for the sphere will be adapted for the cylinder of our interest.

A.2 Integral representation

First, we consider an integral given as

$$I = \frac{-j}{2} \oint_{C_x} B_\nu \frac{\exp[-j\nu(\phi - \pi)]}{\sin \nu\pi} d\nu \quad (A.1)$$

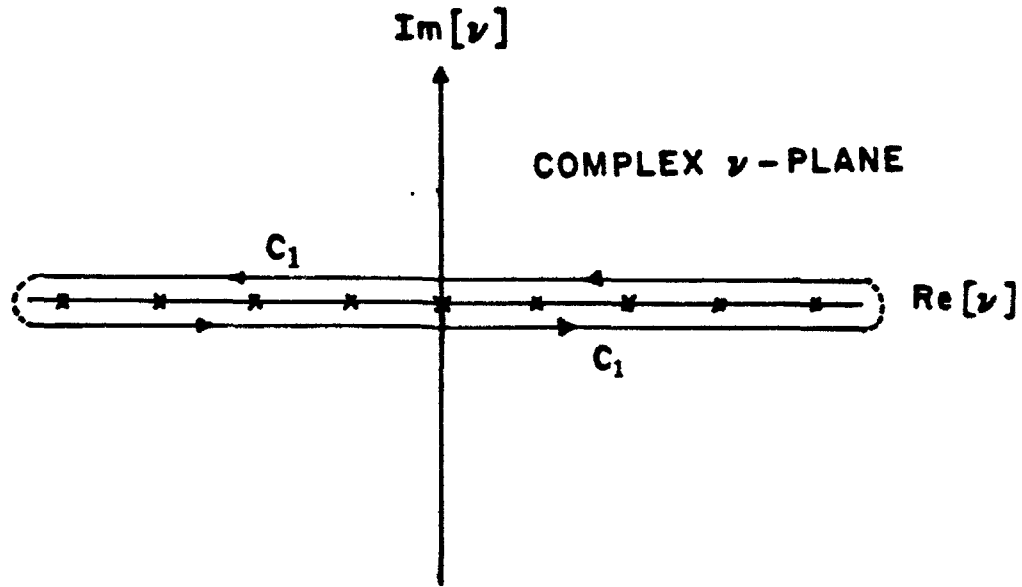


Figure A.1: The contour of the integral

where we assume $|\phi| < \pi$. The contour C_1 encloses counterclockwise all the poles due to the zeros of $\sin \nu\pi$ (i.e. $\nu=m$) as illustrated in Figure A.1. B_ν in Equation (A.1) is assumed to have no poles on real axis. Next, the integral is evaluated via the residue theorem. B

$$\frac{-j}{2} \oint_{C_1} B(\nu) \frac{\exp[-j\nu(\phi - \pi)]}{\sin \nu\pi} d\nu = \pi \sum_{m=-\infty}^{\infty} B(m) \frac{\exp(-jm\phi)e^{jm\pi}}{\frac{\partial}{\partial \nu}[\sin \nu\pi]_{\nu=m}} \quad (A.2)$$

From (1.2), we obtain the relation

$$\frac{-j}{2} \oint_{C_1} B(\nu) \frac{\exp[-j\nu(\phi - \pi)]}{\sin \nu\pi} d\nu = \sum_{m=-\infty}^{\infty} B(m) \exp(-jm\phi) \quad (A.3)$$

assuming that $B(\nu)$ has no poles on the real axis. The integral in Equation (A.3) can be simplified further if $B(\nu)$ is an even function of ν (i.e. $B(-\nu) = B(\nu)$).

First, we decompose the integral into two terms.

$$I = \frac{-j}{2} \int_{-\infty-j\epsilon}^{\infty-j\epsilon} B(\nu) \frac{\exp[-j\nu(\phi - \pi)]}{\sin \nu\pi} d\nu + \frac{-j}{2} \int_{\infty+j\epsilon}^{-\infty+j\epsilon} B(\nu) \frac{\exp[-j\nu(\phi - \pi)]}{\sin \nu\pi} d\nu \quad (A.4)$$

By changing the variable in the second term of Equation (A.4), we obtain the identity

$$\sum_{m=-\infty}^{\infty} B(m) \exp(-jm\phi) = -j \int_{-\infty-j\epsilon}^{\infty-j\epsilon} B(\nu) \frac{\cos \nu(\phi - \pi)}{\sin \nu\pi} d\nu \quad (A.5)$$

where ϵ is a positive number, however small. Above Equation (A.5) represents the transformation of the eigenfunction series into the integral form. In finding the GO field in the lit region, the integral representation of the field will be evaluated via the stationary phase method as given in Chapter III.

A.3 Residue series representation

On the conditions that the poles of $B(\nu)$ are located only in the lower halfplane and the contribution from the semicircle arc can be ignored as its radius approaches infinity, the integral can also be evaluated via the residue theorem by enclosing the contour with a large semicircle in the lower halfplane, as shown in Figure A.2.

$$\sum_{m=-\infty}^{\infty} B(m) \exp(-jm\phi) = -j \int_{C_z} B(\nu) \frac{\cos \nu(\phi - \pi)}{\sin \nu\pi} d\nu \quad (A.6)$$

Hence, the integral given in Equation (A.6) is equal to $-2\pi j$ times the sum of the residues at the poles of $B(\nu)$ (i.e. ν_n) because the contour C_z encloses the poles clockwise.

$$-j \int_{C_z} B(\nu) \frac{\cos \nu(\phi - \pi)}{\sin \nu\pi} d\nu = 2\pi \sum_{n=1}^{\infty} B(\nu_n) \frac{\cos \nu_n(\phi - \pi)}{\sin \nu_n\pi} \quad (A.7)$$

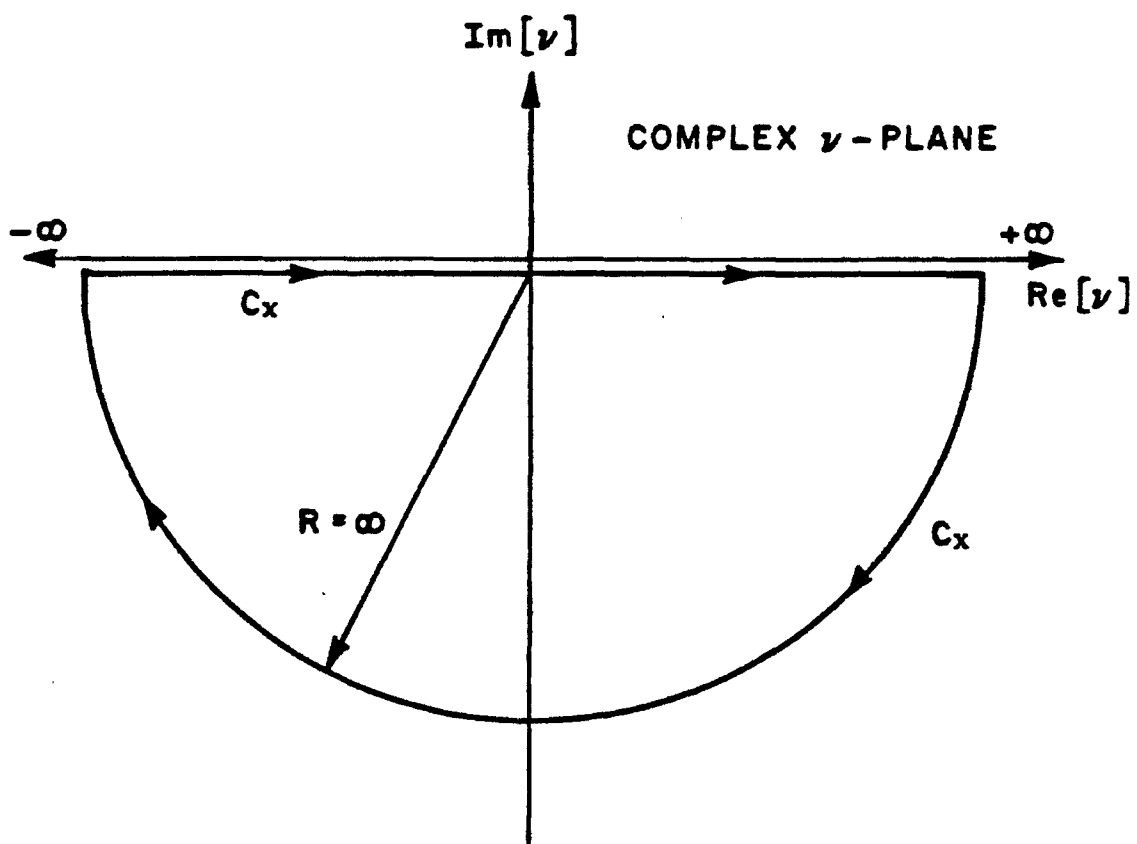


Figure A.2: The contour C_x of the integral

Thus we obtain

$$\sum_{m=-\infty}^{\infty} B(m) \exp(-jm\phi) = 2\pi \sum_{n=1}^{\infty} B(\nu_n) \frac{\cos \nu_n(\phi - \pi)}{\sin \nu_n \pi} \quad (A.8)$$

The above Equation (A.8) represents the transformation of the eigenfunction series into the residue series representation. The notation " ∞ " in above Equation denotes in actual calculation only a few terms are needed to obtain an accurate result. Thus the slowly convergent eigenfunction series is transformed into the fast convergent residue series. Residue series solution will be used for the field representation in the shadow region.

APPENDIX B
REFLECTION COEFFICIENT

The asymptotic approximation of the reflection coefficient for the coated cylinder is developed in this Appendix. From the discussion in Chapter III, the formal expression for the reflection coefficient $R_{s,h}$ is given as

$$R_{s,h} = -S_{s,h}(\nu_s) = \frac{j \sin \alpha_s - j C_{s,h}(\nu_s)}{j \sin \alpha_s + j C_{s,h}(\nu_s)} \quad (B.1)$$

In order to obtain the approximation of $R_{s,h}$, approximation of $C_{s,h}(\nu_s)$ should be found first.

B.1 TM_z case

$$C_s(\nu) = -j \frac{Z_0}{Z_1} \frac{H_\nu^{(1)'}(k_1 b) H_\nu^{(2)}(k_1 a) - H_\nu^{(2)'}(k_1 b) H_\nu^{(1)}(k_1 a)}{H_\nu^{(1)}(k_1 b) H_\nu^{(2)}(k_1 a) - H_\nu^{(2)}(k_1 b) H_\nu^{(1)}(k_1 a)} \quad (B.2)$$

From the Debye approximation of the Hankel function,

$$H_\nu^{(1)}(k_1 a) \approx \sqrt{\frac{2}{\pi k_1 a \sin \beta_a}} \exp \left[j \left(k_1 a \sin \beta_a - \beta_a k_1 a \cos \beta_a - \frac{\pi}{4} \right) \right] \quad (B.3)$$

$$H_\nu^{(2)}(k_1 a) \approx \sqrt{\frac{2}{\pi k_1 a \sin \beta_a}} \exp \left[-j \left(k_1 a \sin \beta_a - \beta_a k_1 a \cos \beta_a - \frac{\pi}{4} \right) \right] \quad (B.4)$$

$$H_{\nu}^{(1)}(k_1 b) \approx \sqrt{\frac{2}{\pi k_1 b \sin \beta_b}} \exp \left[j \left(k_1 b \sin \beta_b - \beta_b k_1 b \cos \beta_b - \frac{\pi}{4} \right) \right] \quad (B.5)$$

$$H_{\nu}^{(2)}(k_1 b) \approx \sqrt{\frac{2}{\pi k_1 b \sin \beta_b}} \exp \left[-j \left(k_1 b \sin \beta_b - \beta_b k_1 b \cos \beta_b - \frac{\pi}{4} \right) \right] \quad (B.6)$$

It should be noted that β_a and β_b in above Equations (B.3) ~ (B.6) are defined by the following relations

$$\nu \equiv k_1 a \cos \beta_a = k_1 b \cos \beta_b \quad (B.7)$$

Thus, we obtain

$$H_{\nu}^{(1)}(k_1 b) H_{\nu}^{(2)}(k_1 a) \approx \frac{2}{\pi k_1 \sqrt{ab \sin \beta_a \sin \beta_b}} e^{j\Psi(a,b,k_1)} \quad (B.8)$$

$$H_{\nu}^{(2)}(k_1 b) H_{\nu}^{(1)}(k_1 a) \approx \frac{2}{\pi k_1 \sqrt{ab \sin \beta_a \sin \beta_b}} e^{-j\Psi(a,b,k_1)} \quad (B.9)$$

where $\Psi(a, b, k_1)$ is defined as

$$\Psi \equiv k_1 [b \sin \beta_b - a \sin \beta_a] - k_1 [\beta_b b \cos \beta_b - \beta_a a \cos \beta_a] \quad (B.10)$$

Therefore, we obtain

$$H_{\nu}^{(1)}(k_1 b) H_{\nu}^{(2)}(k_1 a) - H_{\nu}^{(2)}(k_1 b) H_{\nu}^{(1)}(k_1 a) \approx \frac{4j}{\pi k_1 \sqrt{ab \sin \beta_a \sin \beta_b}} \sin\{\Psi(a, b, k_1)\} \quad (B.11)$$

$$H_{\nu}^{(1)}(k_1 b) H_{\nu}^{(2)}(k_1 a) + H_{\nu}^{(2)}(k_1 b) H_{\nu}^{(1)}(k_1 a) \approx \frac{4}{\pi k_1 \sqrt{ab \sin \beta_a \sin \beta_b}} \cos\{\Psi(a, b, k_1)\}$$

(B.12)

Thus, it can be readily shown that

$$\begin{aligned}
 & H_{\nu}^{(1)'}(k_1 b) H_{\nu}^{(2)}(k_1 a) - H_{\nu}^{(2)'}(k_1 b) H_{\nu}^{(1)}(k_1 a) \\
 & \approx j \sin \beta_b \{ H_{\nu}^{(1)}(k_1 b) H_{\nu}^{(2)}(k_1 a) + H_{\nu}^{(2)}(k_1 b) H_{\nu}^{(1)}(k_1 a) \} \\
 & \approx \frac{4j \sin \beta_b}{\pi k_1 \sqrt{ab \sin \beta_a \sin \beta_b}} \cos \{ \Psi(a, b, k_1) \}
 \end{aligned} \tag{B.13}$$

Therefore, we obtain

$$C_s = -j \frac{Z_0}{Z_1} \sin \beta_b \cot \{ \Psi(a, b, k_1) \} \tag{B.14}$$

Incorporating this result into Equation (B.2) yields

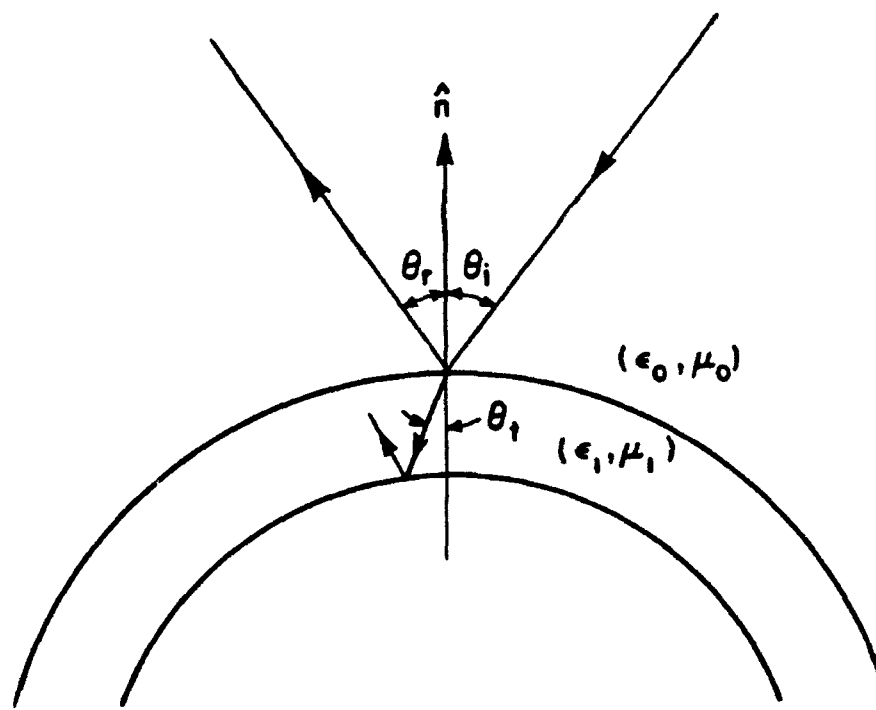
$$R_s = \frac{j \sin \alpha_s - \frac{Z_0}{Z_1} \sin \beta_b \cot \{ \Psi(a, b, k_1) \}}{j \sin \alpha_s + \frac{Z_0}{Z_1} \sin \beta_b \cot \{ \Psi(a, b, k_1) \}} \tag{B.15}$$

In the Chapter III, it has been proved that at the stationary point,

$$\nu = k_0 b \cos \alpha_s = k_0 b \sin \theta_i \tag{B.16}$$

Thus, β_a and β_b in Equation (B.7) can be expressed in terms of the incident angle θ_i .

$$\beta_a = \cos^{-1} \left(\frac{k_0 b \sin \theta_i}{k_1 a} \right) \tag{B.17}$$



$$k_0 \sin \theta_i = k_1 \sin \theta_1$$

$$\theta_i = \theta_r$$

Figure B.3: Snell's Law

$$\beta_b = \cos^{-1} \left(\frac{k_o b \sin \theta_i}{k_1 b} \right) \quad (B.18)$$

From the Snell's law, it is known that $k_o \sin \theta_i = k_1 \sin \theta_t$. As shown in Figure B.3, θ_i is the incident angle at the reflection point and θ_t is the angle of transmission into the dielectric/ferrite material. Therefore, we obtain

$$\sin \beta_b = \sqrt{1 - (\cos \beta_b)^2} = \sqrt{1 - \left(\frac{k_o}{k_1} \cos \theta_i \right)^2} = \cos \theta_t \quad (B.19)$$

$$\sin \beta_a = \sqrt{1 - (\cos \beta_a)^2} = \sqrt{1 - \left(\frac{k_o b}{k_1 a} \cos \theta_i \right)^2} \quad (B.20)$$

Consequently, we obtain

$$R_s = - \frac{Z_o - j Z_1 \cos \theta_i / \cos \theta_t \tan \{ \Psi(a, b, k_1) \}}{Z_o \cos + j Z_1 \cos \theta_i / \cos \theta_t \tan \{ \Psi(a, b, k_1) \}} \quad (B.21)$$

When the thickness of the coating d is very small compared to the radius of the cylinder (i.e. $d \ll b$), $\Psi(a, b, k_1)$ can be simplified as

$$\Psi(a, b, k_1) \approx k_1(b - a) \sin \beta_b = k_1 d \cos \theta_t \quad (B.22)$$

If we use this result,

$$R_s = - \frac{Z_o - j Z_1 \cos \theta_i / \cos \theta_t \tan(k_1 d \cos \theta_t)}{Z_o \cos + j Z_1 \cos \theta_i / \cos \theta_t \tan(k_1 d \cos \theta_t)} \quad (B.23)$$

Above result coincide with the reflection coefficient of the grounded dielectric/ferrite slab.

B.2 TE_z case

$$C_h(\nu) = -j \frac{Z_1}{Z_0} \frac{H_\nu^{(1)'}(k_1 b) H_\nu^{(2)'}(k_1 a) - H_\nu^{(2)'}(k_1 b) H_\nu^{(1)'}(k_1 a)}{H_\nu^{(1)}(k_1 b) H_\nu^{(2)'}(k_1 a) - H_\nu^{(2)}(k_1 b) H_\nu^{(1)'}(k_1 a)} \quad (\text{B.24})$$

It can be shown that

$$\begin{aligned} & H_\nu^{(1)}(k_1 b) H_\nu^{(2)'}(k_1 a) - H_\nu^{(2)}(k_1 b) H_\nu^{(1)'}(k_1 a) \\ & \approx -j \sin \beta_a \{ H_\nu^{(1)}(k_1 b) H_\nu^{(2)}(k_1 a) + A H_\nu^{(2)}(k_1 b) H_\nu^{(1)}(k_1 a) \} \\ & \approx \frac{-4j \sin \beta_a}{\pi k_1 \sqrt{ab} \sin \beta_a \sin \beta_b} \cos\{\Psi(a, b, k_1)\} \end{aligned} \quad (\text{B.25})$$

It can also be shown that

$$\begin{aligned} & H_\nu^{(1)'}(k_1 b) H_\nu^{(2)}(k_1 a) + H_\nu^{(2)'}(k_1 b) H_\nu^{(1)}(k_1 a) \\ & \approx -j \sin \beta_a \{ H_\nu^{(1)'}(k_1 b) H_\nu^{(2)}(k_1 a) - H_\nu^{(2)'}(k_1 b) H_\nu^{(1)}(k_1 a) \} \\ & \approx \frac{4 \sin \beta_a}{\pi k_1 \sqrt{ab} \sin \beta_a \sin \beta_b} \sin\{\Psi(a, b, k_1)\} \end{aligned} \quad (\text{B.26})$$

From Equation (B.25) and (B.26), it can be shown that

$$H_\nu^{(1)'}(k_1 b) H_\nu^{(2)'}(k_1 a) - H_\nu^{(2)'}(k_1 b) H_\nu^{(1)'}(k_1 a)$$

$$\begin{aligned}
&\approx j \sin \beta_b \{H_\nu^{(1)}(k_1 b) H_\nu^{(2)'}(k_1 a) + H_\nu^{(2)}(k_1 b) H_\nu^{(1)'}(k_1 a)\} \\
&\approx \frac{4j \sin \beta_a \sin \beta_b}{\pi k_1 \sqrt{ab \sin \beta_a \sin \beta_b}} \sin\{\Psi(a, b, k_1)\} \quad (B.27)
\end{aligned}$$

Substituting Equation (B.25) and (B.27) into Equation (B.24), we obtain

$$C_h(\nu) = j \frac{Z_1}{Z_0} \sin \beta_b \tan\{\Psi(a, b, k_1)\} \quad (B.28)$$

Incorporating this result into Equation (B.1) yield

$$R_h = \frac{j \sin \alpha_s + \frac{Z_1}{Z_0} \sin \beta_b \tan\{\Psi(a, b, k_1)\}}{j \sin \alpha_s - \frac{Z_1}{Z_0} \sin \beta_b \tan\{\Psi(a, b, k_1)\}} \quad (B.29)$$

As for the TM_z case α_s and β_b are replaced by θ_i and θ_t by using the relationship in Equation (B.18) and (B.19). Consequently, we obtain

$$R_h = \frac{Z_0 - j Z_1 \cos \theta_t / \cos \theta_i \tan\{\Psi(a, b, k_1)\}}{Z_0 + j Z_1 \cos \theta_t / \cos \theta_i \tan\{\Psi(a, b, k_1)\}} \quad (B.30)$$

For the small thickness of the coating t ,

$$R_h = \frac{Z_0 - j Z_1 \cos \theta_t / \cos \theta_i \tan(k_1 d \cos \theta_t)}{Z_0 + j Z_1 \cos \theta_t / \cos \theta_i \tan(k_1 d \cos \theta_t)} \quad (B.31)$$

Above result also coincides with the reflection coefficient of the grounded dielectric/ferrite slab.

In summary,

$$R_s = - \frac{Z_0 - j Z_1 \cos \theta_i / \cos \theta_t \tan\{\Psi(a, b, k_1)\}}{Z_0 + j Z_1 \cos \theta_i / \cos \theta_t \tan\{\Psi(a, b, k_1)\}} \quad (B.32)$$

$$R_h = \frac{Z_o - jZ_1 \cos \theta_t / \cos \theta_i \tan\{\Psi(a, b, k_1)\}}{Z_o + jZ_1 \cos \theta_t / \cos \theta_i \tan\{\Psi(a, b, k_1)\}} \quad (B.33)$$

where

$$\Psi \equiv k_1(b \sin \beta_b - a \sin \beta_a) - k_o b(\beta_b - \beta_a) \sin \theta_i \quad (B.34)$$

where

$$\sin \beta_b = \cos \theta_t \quad (B.35)$$

$$\sin \beta_a = \sqrt{1 - \left(\frac{b}{a} \sin \theta_t\right)^2} \quad (B.36)$$

REFERENCES

- [1] J.B. Keller, "*Diffraction by a convex cylinder*", IEEE Trans. on Antennas and Propagation, Vol. AP-24, pp. 312-321, 1956.
- [2] J.B. Keller, "*Geometrical theory of diffraction*", J. Opt. Soc. Amer., 52, pp. 116-130, 1962.
- [3] P.H. Pathak, "*An asymptotic analysis of the scattering of plane waves by a smooth convex cylinder*", Radio Science Vol 14. No. 3, pp. 419-435, 1979.
- [4] N. Wang, "*Regge poles, natural frequencies, and surface wave resonance of a circular cylinder with a constant surface impedance*", IEEE Trans. on Antennas and Propagation, Vol. AP-30, No. 6, pp. 1244-1247, November, 1982.
- [5] N. Wang and H.T. Kim, "*UTD Solution for the Electromagnetic Scattering from a Circular Cylinder with a Constant Surface Impedance*" -Part II of "*Ram and Inlet Modeling Studies*", Technical Report 716495-2, The Ohio State University, ElectroScience Lab., Dept. of Electrical Engineering. October 1985.
- [6] N. Wang, "*Electromagnetic scattering from a dielectric coated cylinder*", IEEE Trans. on Antennas and Propagation, Vol. AP-33, No. 9, pp. 960-963, September, 1985.

- [7] R. Paknys, "*High frequency surface fields excited by a line source on a dielectric coated cylinder*", The Ohio State University, Dept. of Electrical Engineering Ph.D. Dissertation, 1985.
- [8] R. Paknys and N. Wang, "*Creeping wave propagation constants and modal impedance for a dielectric coated cylinder*", IEEE Trans. on Antennas and Propagation, Vol. AP-34, No. 5, pp. 674-680, May, 1986.
- [9] G.N. Watson, "*A Treatise on the theory of Bessel Functions*", Second edition. Cambridge Univ. Press, London, 1962.
- [10] J.J. Bowman, T.B.A. Senior and P.L.E. Ushlenghi, eds "*Electromagnetic and Acoustic Scattering by Simple Shapes*", North Holland, 1969.
- [11] R.E. Collin, "*Field Theory of Guided Waves*", McGraw Hill, 1960.
- [12] M. Abramowitz and I. Stegun, eds "*Handbook of Mathematical Functions*", Dover, 1965.
- [13] L. Felson and N. Marcuvitz, "*Radiation and Scattering of Waves*", Prentice Hall, 1973.
- [14] N.A. Logan, (1959), "*General Research in Diffraction Theory*", Missiles and Space Division, Lockheed Aircraft Corp., Vol. 1, Rep. LMSD-288087 and Vol. 2, Rep. LMSD-288088, December 1959.
- [15] J.R. Wait, "*Electromagnetic Radiation from Cylindrical Structures*", Pergamon, New York, 1959.
- [16] G. Tyras, "*Radiation and Scattering of Electromagnetic Waves*", Academic Press 1969

- [17] J.R. Wait and A.M. Conda, "*Pattern of Antenna on a Curved Lossy Surface*" IRE Trans. on Antennas and Propagation, pp. 348-359, 1958.
- [18] W. Streifer, "*Creeping Wave Propagation Constants for Impedance Boundary Conditions*" IEEE Trans. Antennas Propagat., AP-12, pp. 312-321, 1964.
- [19] R.S. Elliott, "*Azimuthal Surface Waves on Circular Cylinders*" J. Appl. Phys., 26, No. 4, pp. 368-376, 1955.
- [20] N.A. Logan and K.S. Yee, "*A Mathematical Model for Diffraction by Convex Surface*", in "*Electromagnetic Waves*", edited by R.E. Langer, pp 139-180, The University of Wisconsin Press, 1962.
- [21] R.D. Kodis, "*The Radar Cross-Section of a Conducting Cylinder with Dielectric Sleeve at Optical Limit*", in "*Electromagnetic Theory and Antennas*": Part I, edited by E.C. Jordan, pp 127-132, Pergamon Press, N.Y. 1963.
- [22] C. W. Helstrom, "*Scattering from a Cylinder Coated with a Dielectric Material*", in "*Electromagnetic Theory and Antennas*": Part I, edited by E.C. Jordan, pp 133-144, Pergamon Press, N.Y. 1963.
- [23] T.C.K. Rao and M.A.K. Hamid, "*G.T.D. Analysis of Scattering from a Coated Conducting Cylinder*", IEE Proc. Vol 127, Pt. H. No. 3 June 1980.